Ultrafast Control and Tailoring of Surface Plasmon Generated Electron Pulses

by

Shawn Richard Greig

A thesis submitted in partial fulfillment of the requirements for the degree of

Doctor of Philosophy

in

Photonics and Plasmas

Department of Electrical and Computer Engineering
University of Alberta

Abstract

This thesis presents theoretical and experimental work on the generation and control of ultrashort electron pulses via surface plasmon (SP) waves. As such, new methods are presented to specifically control various beam parameters such as direction, kinetic energy, pulse duration, and current.

Employing a single, ultrashort, terahertz (THz) electric field pulse to a standard SP based electron source provides a method for ultrafast, all-optical control of the angular directivity and kinetic energy spectra of SP generated electron pulses. By introducing a second THz pulse and controlling its delay and phase with respect to the first THz pulse, greater control over the electron's temporal acceleration profile is afforded, allowing electrons to be accelerated to kinetic energies up to 3.5 keV.

The design of a compact, ultrafast nanoplasmonic based electron gun is presented. Harnessing the focusing capability of radially polarized light, conical surface plasmons are able to accelerate electrons to 1.2 keV. Through the use of magnetostatic and spatial filtering, electron packets with attosecond durations can be achieved.

Multiple methods of increasing the electron yield of surface plasmon based electron sources are studied. Reduction of the nonlinear emission order is achieved by introducing a dielectric layer beneath the plasmonic metal film. The dielectric layer allows for higher electric field confinement and thus higher acceleration gradients. To further increase the current, gating of secondary electrons generated by an external, continuous, electron beam is explored. This platform allows for an in-depth study of the

interaction of free electrons with strong SP fields for the next generation of ultrafast, high current SP based electron sources.

The knowledge gained from SP-electron interaction in a vacuum environment is transferred to a solid-state Si-based platform to investigate the next generation of optical computing devices. Utilizing the SP mode in a nanoplasmonic waveguide to accelerate electrons, and subsequently filtering them based on their energy produces a triode like behaviour useful for interfacing current nanoelectronics and nanoplasmonics. A similar effect is used to develop a solid-state detector for the carrier-envelope-phase of few-cycle pulses.

With the understanding of the effect that free electrons within a film can have on the various properties of a plasmonic system, a method to modulate the conductivity of an ensemble of Au particles using THz electric fields was explored. By utilizing all-THz pump-probe time-resolved spectroscopy, it was demonstrated that a low THz field strength can induce a measurable change to the Au particle's conductivity. This is the first step towards controlling the SP coupling and photoemission properties in the near-infrared, such that THz electric field enhanced photoemission can be realized.

Preface

Portions of Chapter 3 have been published as S.R. Greig and A.Y. Elezzabi, "On the Role of Terahertz Field Acceleration and Beaming of Surface Plasmon Generated Ultrashort Electron Pulses," *Appl. Phys. Lett.* **105**, 041115 (2014), S.R. Greig and A.Y. Elezzabi, "Electron Acceleration and Kinetic Energy Tailoring via Ultrafast Terahertz Fields," *Opt. Express* **22**, 29092 (2014), and S.R. Greig and A.Y. Elezzabi, "Generation of Attosecond Electron Packets via Conical Surface Plasmon Electron Acceleration," *Sci. Rep.* **6**, 19056 (2016). I was responsible for the numerical simulations, data analysis, and preparation of the manuscripts. A. Y. Elezzabi supervised the project and contributed to manuscript preparation and edits.

Chapter 4 describes the work that has been published as S.R. Greig, A. Morteza-Najarian, R.L. McCreery, and A.Y. Elezzabi, "Surface Plasmon Driven Lowering of the Electron Emission Order in a Carbon/Gold Bilayer Film," *Appl. Phys. Lett.* **109**, (2016). I was responsible for the experimental design, data collection, data analysis, and preparation of the manuscript. A. Morteza-Najarian prepared and characterized the films and contributed to manuscript edits. R. L. McCreery contributed to manuscript edits. A. Y. Elezzabi supervised the project and contributed to manuscript preparation and edits.

A portion of Chapter 5 has been published as S.R. Greig and A.Y. Elezzabi, "An Ultrafast Silicon Nanoplasmonic Ballistic Triode," *Appl. Phys. Lett.* **105**, 241115 (2014). I performed the numerical simulations, data analysis, and prepared the manuscript. A. Y. Elezzabi supervised the project and contributed to manuscript preparation and edits. A portion of the other section of Chapter 5 has been included in the review article: S.

Sederberg, C.J. Firby, S.R. Greig, and A.Y. Elezzabi, "Integrated Nanoplasmonic Waveguides for Magnetic, Nonlinear, and Strong-Field Devices," *Nanophotonics* **6**, (2017).

Chapter 6 has been published as A.Y. Elezzabi, P. Maraghechi, and S.R. Greig, "Terahertz Plasmonic Field-Induced Conductivity Modulation in Gold," *Sci. Rep.* 6 (2015). I was responsible for the numerical simulations, data analysis, and preparation of the manuscript. A. Y. Elezzabi supervised the project, helped with data analysis and manuscript preparation. A. Y. Elezzabi and P. Maraghechi performed the experiments and data collection.

Acknowledgements

First and foremost, I would like to thank my supervisor Dr. Abdul Elezzabi. Without his continued help and guidance, the work of this thesis would not have been possible. His ever-present optimism and encouraging words helped me push through the various hiccups and roadblocks that one encounters when doing novel experiments. The skills, both technical and non-technical, I learned while working in his lab will stay with me throughout my career.

The various experiments and experimental setups would not have been possible without assistance from the wonderful staff and technicians of both the NanoFab and the Electrical & Computer Engineering machine shop. Specifically, I would like to thank Herbert Dexel, Reiner Schwarze, and Terry Kugler from the machine shop for always being able to manufacture whatever bizarre piece we needed for the next experiment. I would like to thank Glenn Elaschuk from the NanoFab for all his help with the various problems I encountered while working on my vacuum chamber.

The time spent in the lab would not have been the same without the friends that I've made there. Whether it was discussions of how to set up a new experiment, or simply a friendly chat over lunch, my time spent in the lab would have been a lot less interesting without my labmates: Curtis Firby, Katherine Smith, Brett Carnio, Nir Katchinskiy, Shawn Sederberg, Ryan Boehnke, Liam McCrae, and Michael Nielsen.

Last but certainly not least, I am grateful and thankful to my loving family and close personal friends. They have always been there for me especially when experiments may not have been going as planned. Without their continued love and support, this PhD would not have been possible.

Contents

List of Tables

List of Figures

List of Abbreviations

1PA	single photon absorption
2D	two dimensional
2PA	two photon absorption
3D	three dimensional
3PA	three photon absorption
4D	four dimensional (space & time)
AFM	atomic force microscope
a.u.	arbitrary units
BSE	backscattered electron
CEP	carrier envelope phase
CMA	cylindrical mirror analyzer
CMOS	complementary metal oxide semiconductor
CPA	chirped pulse amplifier
DC	direct current
DLA	dielectric linear accelerator
eCarbon (eC)	electron beam evaporated carbon
EELS	electron energy loss spectroscopy
EM	electromagnetic
FC	faraday cup
FDA	field driven acceleration

FDTD	finite-difference time-domain
FWHM	full-width at half-maximum
HWHM	half-width at half-maximum
KE	weighted central kinetic energy
MOSFET	metal oxide semiconductor field effect transistor
MPI	multi-photon ionization
PIC	photonic integrated circuit
PML	perfectly matched layer
RE	reflected electron
RF	radio frequency
RPA	retarding potential analyzer
SE	secondary electron
SEM	scanning electron microscope
SP	surface plasmon
TEM	transmission electron microscope
THz	terahertz
TM	transverse magnetic
UED	ultrafast electron diffraction
UEM	ultrafast electron microscopy
UPS	ultraviolet photoelectron spectroscopy
UV	ultraviolet
WFWHM	weighted full-width at half-maximum

Chapter 1

Introduction

Within the last 10-15 years there has been great interest in time-resolved electron microscopy. Electron microscopy has allowed users to obtain images with high spatial resolution since the 1930's [1]. With resolution on the atomic scale, scientists and engineers have unprecedented access to study the nanoscale features of materials. However, the images produced are static, still-frame images that contain no temporal information. As such, researchers began to investigate ways to generate ultrashort electron pulses in order to achieve high temporal (~femtoseconds) resolution to complement the already achievable atomic spatial resolution. Using ultrafast electron pulses, it is possible to combine multiple atomic scale snapshots to capture the intricate dynamics of electrons on surfaces and in matter. Typical ultrafast electron sources can achieve resolutions of a few hundreds of femtoseconds (fs). Current research is attempting to push the resolution down to the 10 fs and ultimately the sub-fs regime [2–4]. By utilizing electron pulses on the order of tens of fs, researchers would be able to observe fundamental physical and chemical processes and truly understand what is occurring on the atomic level.

1.1. Methods of Generating Ultrashort Electron Pulses

To generate ultrashort electron pulses, lasers having pulse durations of ≤ 100 fs are used to photoemit electrons from a suitable material. To emit an electron from a material, the electron must gain enough energy to overcome the material's work function,

W_F. For optical excitation, this can be achieved in multiple ways. The simplest method is to choose a suitable material and laser wavelength such that the photon energy, hv, is greater than W_F. This, however, can be difficult to achieve in practice as most experiments employ ultrafast Ti:Sapphire lasers with photon energies ~1.55 eV and nearly all materials used have significantly higher W_F (>4 eV), thus requiring the laser output to be frequency doubled or tripled to match W_F. Without changing the photon energy, multiple photons are required to free an electron, making the emission process non-linear and requiring high intensities. To overcome this, W_F can be lowered through the application of a high strength electric field [5]. This high electric field can either be a DC field or can come from the high electric field of the laser pulse itself [6]. In either case, with sufficient electric field strength, W_F can be lowered by enough to allow electrons to tunnel over the Schottky barrier at the material-vacuum interface, reducing the number of photons required to free an electron. Within the category of laser-driven electron sources, there are various techniques for generating ultrashort electron pulses such as plasma wakefield accelerators, dielectric accelerators, photocathodes, and surface plasmon (SP) based sources.

1.1.1. Direct Laser Driven Electron Sources

The original method that was used for generating ultrashort electron pulses was a photocathode. Here, an ultrafast laser pulse is simply focused on a material to photoemit electrons. Photocathodes have the advantage of being compact and simple to operate as they only require focusing a laser pulse on to the material. However, the electron energy produced is quite low, ~ a few eV, and thus requires post acceleration in high electric fields to reach the energy range useful for electron microscopy (> 1 keV). This increases

the overall size of the electron source and introduces a larger source to sample distance that limits the minimum achievable pulse duration to 100's of fs due to dispersion (explained in greater detail in Section 1.2.).

The first pioneering work demonstrating sub-picosecond (ps) time resolution is that of R. J. D Miller in 2003 [7,8]. Their group was able to achieve 600 fs electron pulses from a photo-activated electron gun, which was subsequently used to probe the solid-liquid phase transition of aluminum via ultrafast electron diffraction (UED). The experimental setup used is depicted in Fig. 1.1(a). Here, the initial photoelectrons are generated by focusing the output of a Ti:Sapphire amplifier that has been frequency tripled to $\lambda_{tripled}$ = 256 nm (4.84 eV) on the back of a thin 40 nm silver film deposited on a sapphire substrate. These electrons are then accelerated in an external field to a kinetic energy of 30 keV before being focused by a magnetic lens on the sample as illustrated in Fig. 1.1(b). Notably, this electron source was specifically designed to operate with ~10^4 electrons per laser pulse to reduce measurement acquisition time. This work represents the first major stepping stone in achieving sub-ps temporal resolution for electron microscopy.

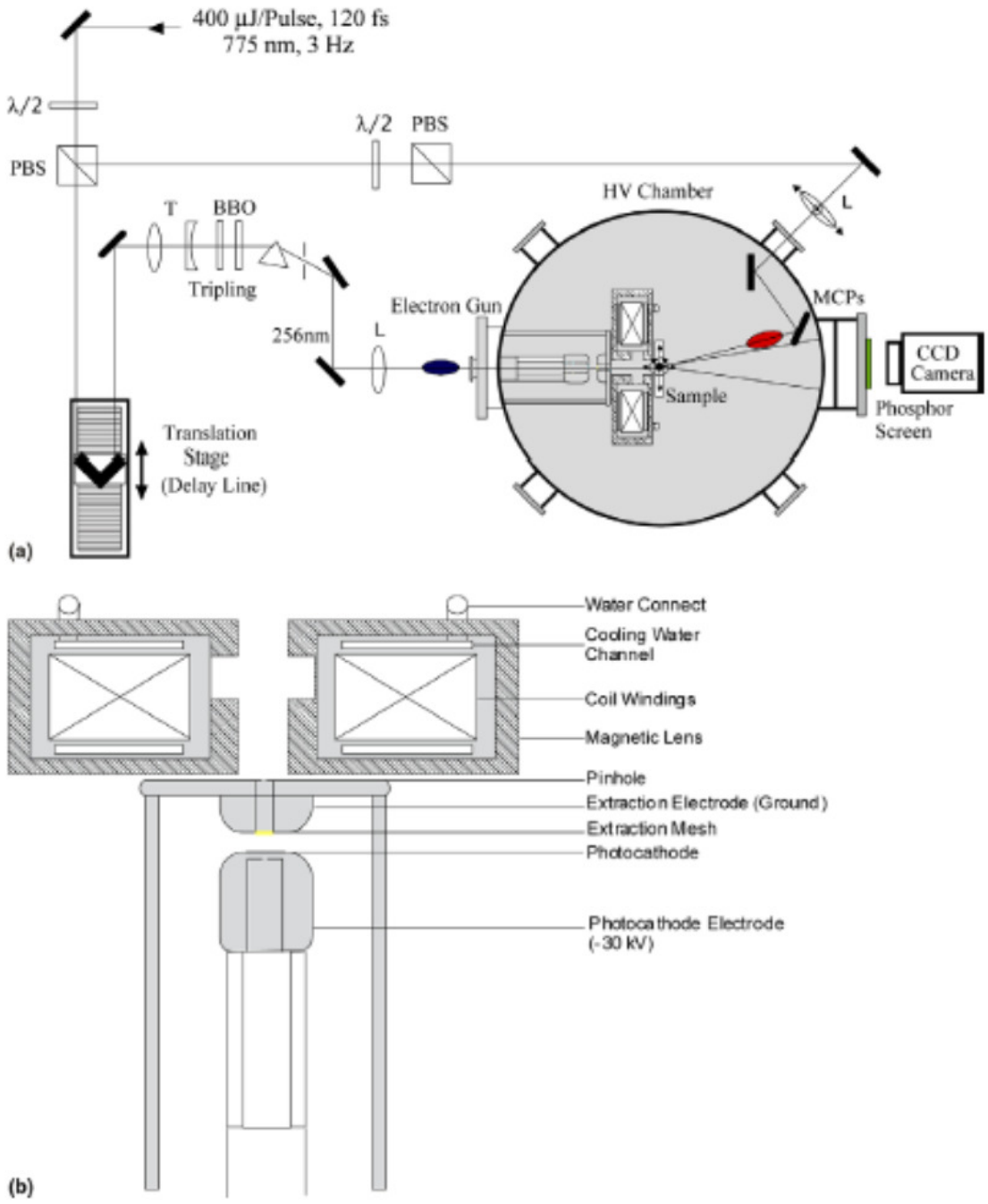

Figure 1.1. (a) Ultrafast electron diffractometer with Ag photocathode. (b) Schematic overview of the photo-activated gun capable of generating electron pulses having 600 fs pulse durations. [8]

Around the same time, A. H. Zewail's ultrafast electron microscopy (UEM) group was working towards achieving even higher temporal resolution [9]. Zewail et al.'s initial

work utilizes a modified transmission electron microscope (TEM) column, depicted in Fig. 1.2(a). Electrons are emitted by focusing a laser pulse on the standard lanthanum hexaboride (LaB_6) emitter of the TEM column. Here, the laser pulse used is the frequency doubled output of a sub-100 fs, 800 nm, Ti:Sapphire oscillator. By utilizing the second harmonic of the laser output (400 nm or 3.1 eV) and LaB_6 (W_F ~ 2.5 eV), the emission is a single-photon process. Remarkably, with an average of one electron per pulse, they can produce images with comparable resolution, contrast, and quality to those obtained with standard TEM techniques, Fig. 1.2(b)-(c), respectively.

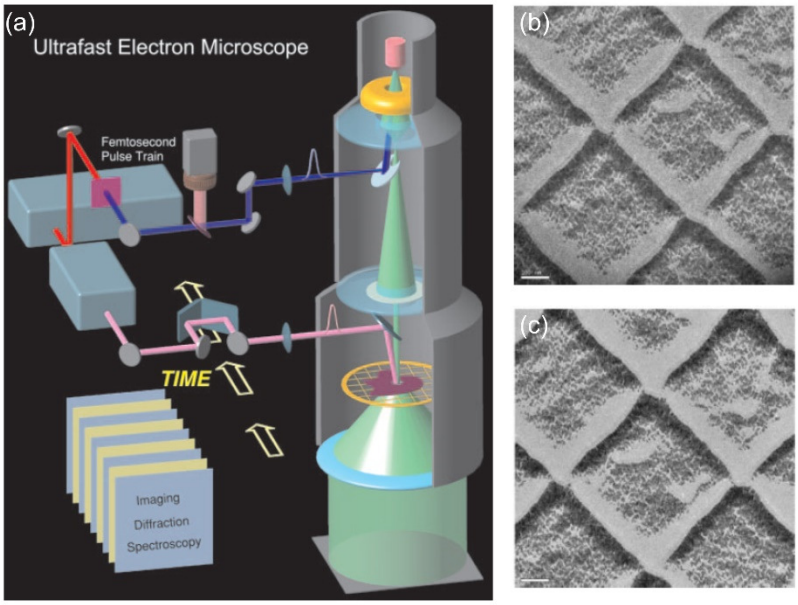

Figure 1.2. (a) Ultrafast TEM with photocathode. (b) UEM micrograph of diffraction grating, and (c) traditional TEM micrograph of the same diffraction grating. The scale bar is 100 nm. [9]

1.1.2. Electron Pulse Generation Driven by High Intensity Laser Fields

Operating in the high intensity regime, > 10^{15} W/cm^2, it is possible to generate high energy ultrashort electron pulses from plasmas. A few different geometries in this regime include laser wakefield acceleration and acceleration in the longitudinal field of a focused

radial laser beam. While these techniques can produce high energy, short electron pulses they necessitate the use of large, complex laser systems in order to reach the high laser intensities used.

Laser wakefield acceleration was proposed by Tajima and Dawson in 1979 as a method to produce laser-driven acceleration gradients significantly higher than state of the art particle accelerators [10]. The operation principle is quite simple, an intense laser pulse propagates through a plasma containing electrons and ions. The electrons are accelerated (in the transverse direction) by the large ponderomotive potential of the laser pulse, setting up a longitudinally oscillating plasma wakefield propagating behind the laser pulse. It is possible for some of these electrons to be trapped in this wakefield and experience significant longitudinal acceleration to high kinetic energies. This approach has been used to reach kinetic energies in the GeV range by Mo et al. [11]. Lundh et al. were able to achieve electron bunches with an estimated 1.4-1.8 fs pulse duration and kinetic energies of 84 MeV [12]. Their experimental setup is depicted in Fig. 1.3.

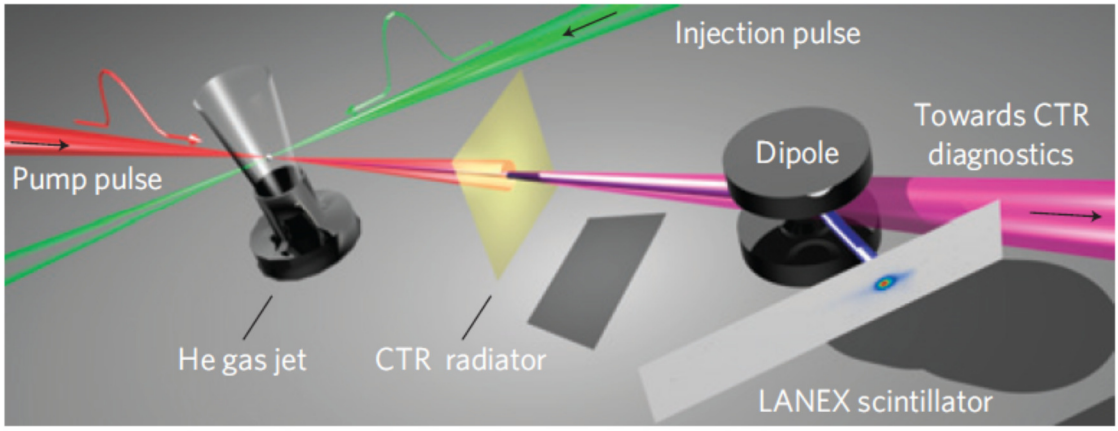

Figure 1.3. Laser wakefield acceleration setup used to achieve high energy, 84 MeV, 1.4 fs electron beams. [12]

Alleviating the need for a plasma, Payeur et al. were able to achieve electron pulses with kinetic energies ~23 keV by focusing a radially polarized laser beam with an intensity of 7.4×10^{17} W/cm^2 into a chamber filled with oxygen [13]. A depiction of their experimental setup is shown in Fig. 1.4. At the focus of the radial laser beam, a high longitudinal electric field component is realized. As such, the laser ionizes the oxygen to produce electrons that are subsequently accelerated in this intense longitudinal field to high kinetic energies. Payeur estimates the pulse duration to be ~20 fs at the electron beam waist. Theoretical work from the same group has proposed that this generation technique can be extended to achieve electron pulses with attosecond pulse durations [14–16].

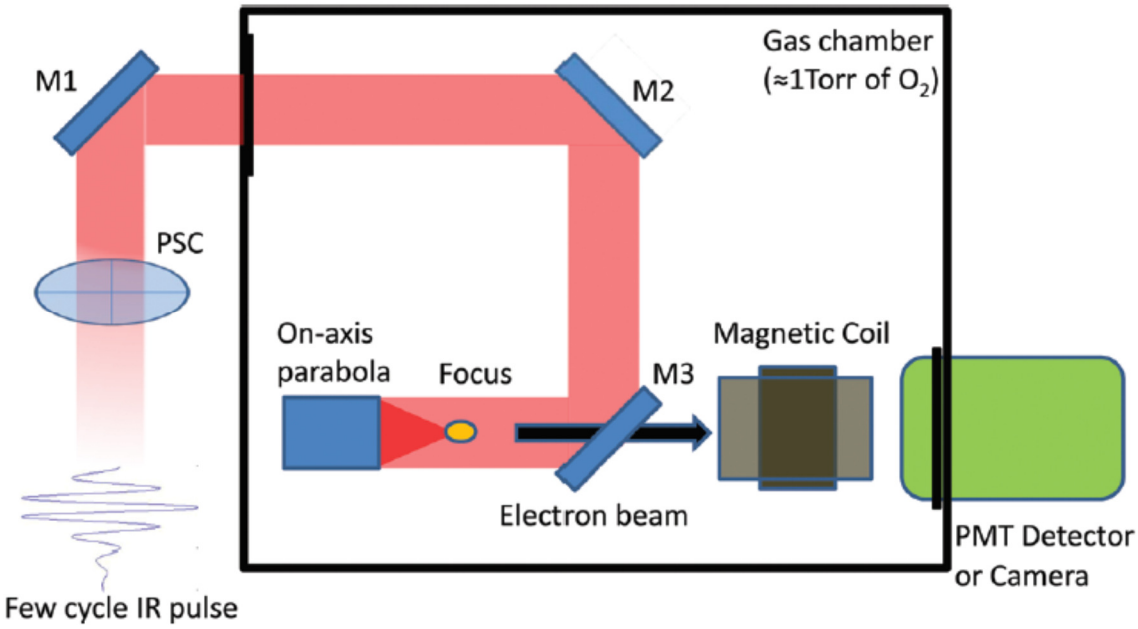

Figure 1.4. Experimental setup for electron pulse generation using intense radially polarized laser pulses [13].

1.1.3. Surface Plasmon Driven Electron Sources

Another widely used method of generating ultrafast electron pulses with tabletop laser sources, and the focus of this thesis, is using a surface plasmon (SP) based approach. Surface plasmons are the collective oscillation of conduction band electrons within a metal. The oscillating charges are coupled to electromagnetic waves that decay away from the surface. This evanescent decay results in confinement of the electromagnetic fields to the surface of the metal, which leads to strong enhancement of the electric field and makes this a promising platform for generation and acceleration of ultrafast electron pulses. A more comprehensive, electromagnetic explanation of surface plasmons and the various geometries used for excitation is presented in Section 2.3.

Surface plasmons can be excited on various geometries including prisms [6,17–20], gratings [21,22], nanoantennas [23,24], and nanotips [3,4]. After excitation, the SP photoemits electrons like photocathodes, i.e. through multiphoton absorption or tunnel ionization, but with the caveat that the materials used must support surface plasmons at the wavelength of the incident laser. For this reason, many of the sources utilize gold (Au) or silver (Ag) films when operating with ultrafast lasers such as Ti:Sapphire oscillators with central wavelengths around 800 nm. SP based electron sources offer several advantages over photocathodes including being more compact due to the nanoscale confinement, higher electric field enhancement leading to built-in electron acceleration instead of post acceleration, carrier-envelope-phase (CEP) sensitivity, and they have demonstrated the shortest pulse durations to date [3,4]. Owing to the high electric field enhancement of the SP, these electron sources are also able to enter the strong-field regime of laser-matter interaction while utilizing low energy laser pulses

from Ti:Sapphire oscillators [20]. This strong-field interaction allows for the acceleration or deceleration of electrons. SP based electron acceleration has been shown to be able to achieve high energy, >1 keV, electrons and sub-30 fs pulse durations [6]. They are not without their drawbacks though. Notably, SP waves cannot be excited by free-space radiation and require specific geometries to be excited, thus increasing the complexity of the electron source.

The initial work that motivated this research area was the observation of increased photoemission current due to surface plasmons on various metallic films in the Kretschmann geometry by Tsang et al. [25]. It was demonstrated that SP photoemission resulted in a 3500× increase in current from Ag compared to non-resonant photoemission. This opened the way for utilizing SP based sources to generate ultrashort, high-energy electron pulses.

The first use of an SP based source to generate high-energy electrons was carried out in a similar configuration by Zawadzka et al., Fig. 1.5(a) [17]. Incident laser pulses with a pulse duration of 150 fs were used to excite the surface plasmons. Initially, kinetic energies up to 40 eV were achieved for incident laser intensities up to 21 GW/cm^2 (Fig. 1.5(b)). However, by significantly increasing the laser intensity to 40 TW/cm^2, kinetic energies up to 0.4 keV were achieved [18].

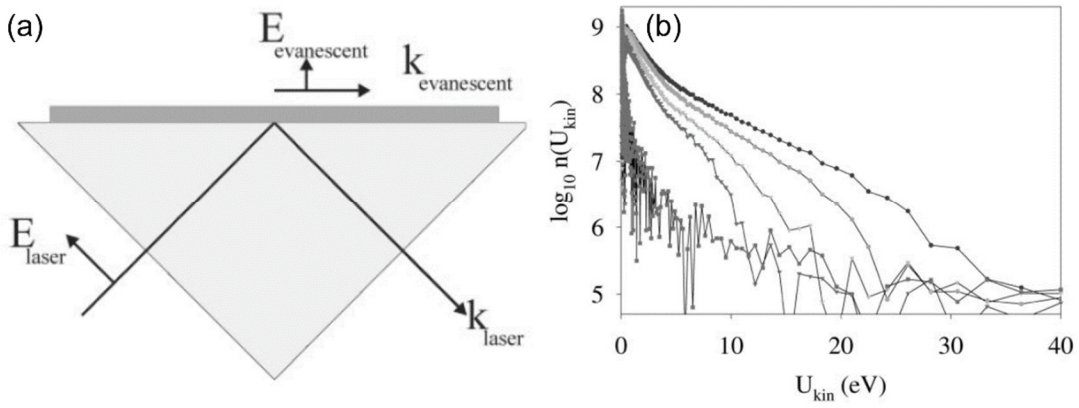

Figure 1.5. (a) Kretschmann geometry. (b) Kinetic energy spectra for SP accelerated electrons with incident laser intensities of 0.7, 4.2, 5.5, 8.3, and 21 GW/cm^2. [17]

It was demonstrated by our group (Irvine et al.) that similar, high kinetic energies could be achieved using significantly lower laser intensities [19]. Figure 1.6(a) depicts kinetic energies up to 0.4 keV that were observed when exciting SP waves with 27 fs, 1.5 nJ laser pulses from a Ti:Sapphire oscillator focused to an intensity of 1.8 GW/cm^2. As the plasmon lifetime is ~48 fs, utilizing a shorter laser pulse duration allows for a more efficient transfer of the ponderomotive energy from the SP wave to the accelerated electrons, thus allowing for higher kinetic energies at lower laser intensities. Furthermore, Fig. 1.6(b) depicts correlation experiments that were carried out to demonstrate that the electron pulses generated have a pulse duration ≤ 27 fs at the surface of the Ag film. Irvine et al. also observed kinetic energies up to 2 keV at a laser intensity of 30 GW/cm^2, by utilizing 30 fs laser pulses obtained from a Ti:Sapphire amplifier [6]. Operating at these high laser intensities also brought the photoemission process from the multiphoton regime into the tunneling regime due to the high electric field enhancement on the surface of the metallic film. This meant that a single photon could be used to free an electron from the metal instead of requiring multiple photons in order to excite an electron over

the Schottky barrier at the metal-vacuum interface. The various excitation regimes are discussed in greater detail in Section 2.4.

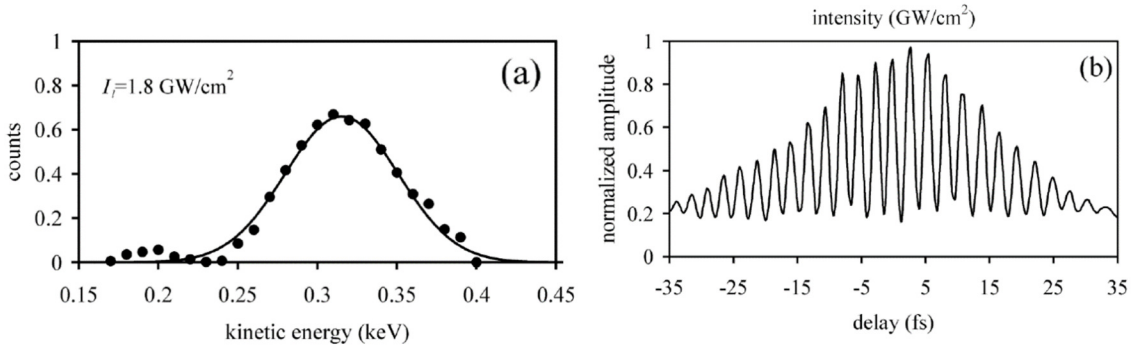

Figure 1.6. (a) Kinetic energy spectrum of SP generated electrons at a laser intensity of 1.8 GW/cm^2. (b) Corresponding interferometric 3-photon correlation trace indicating 27 fs electron pulse duration. [19]

Within the last five years, other geometries utilizing nanoparticles are beginning to be explored [23,24]. Nanoparticle based sources represent a unique opportunity because, unlike prisms or gratings, they do not require the incident laser pulse to arrive at a specific angle, only the laser polarization direction is important. Additionally, the particle geometries can be tuned to achieve greater control over the characteristics of the emitted electron pulse. Kinetic energies up to 140 eV are observed for arrays of 100 nm diameter Au nanopillars when excited with a laser intensity of 140 GW/cm^2, Fig. 1.7 [23]. This is an increase of 3× compared to a flat Au film irradiated at the same laser intensity. Notably, the non-linear emission order of the nanopillars is observed to be second-order as opposed to the expected third order process determined by the W_F of the Au film (4.8 eV) and the incident photon energy (1.55 eV). The decrease in emission order is attributed to an 18× electric field enhancement from the nanopillars, causing a shift from the multi-photon regime to the tunnel ionization regime.

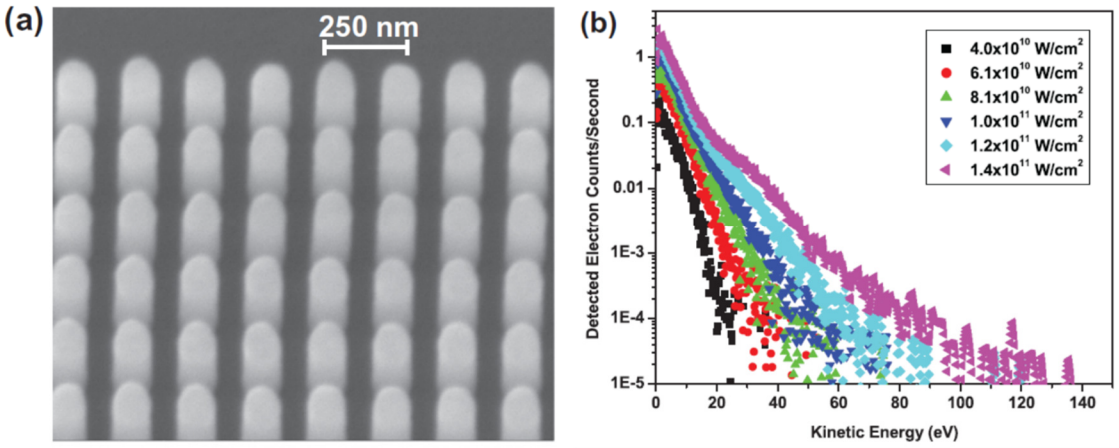

Figure 1.7. (a) Scanning electron microscope (SEM) image of Au nanopillar array. (b) Kinetic energy spectra of electrons emitted from the array at various incident laser intensities. [23]

A similar study was carried out using various shapes of nanoparticles [24]. Here, arrays of different length nanorods or resonant bowties were illuminated with ~100 fs laser pulses with a central wavelength of 805 nm. Figures 1.8(a)-(d) depict the kinetic energy spectra for resonant nanorods, nanorods with a red-shifted resonance, nanorods with a blue-shifted resonance, and resonant bowties, respectively. SEM images of each of the corresponding arrays are shown in Fig. 1.8(e)-(h). The highest kinetic energy of 19 eV was obtained for a bowtie sample irradiated with 25.1 GW/cm^2. It was found that to obtain similar kinetic energies with the nanorod samples required the laser intensity to be increased to 45.6 GW/cm^2. The increased performance of the bowtie structures can be directly attributed to the increased electric field enhancement in the gap between the two halves of the bowtie. While nanoparticles have the advantage of less stringent coupling requirements they necessitate the use of nanofabrication techniques to pattern the particles, as well as their maximum achievable kinetic energies for a given laser intensity are significantly less than Kretschmann based electron sources.

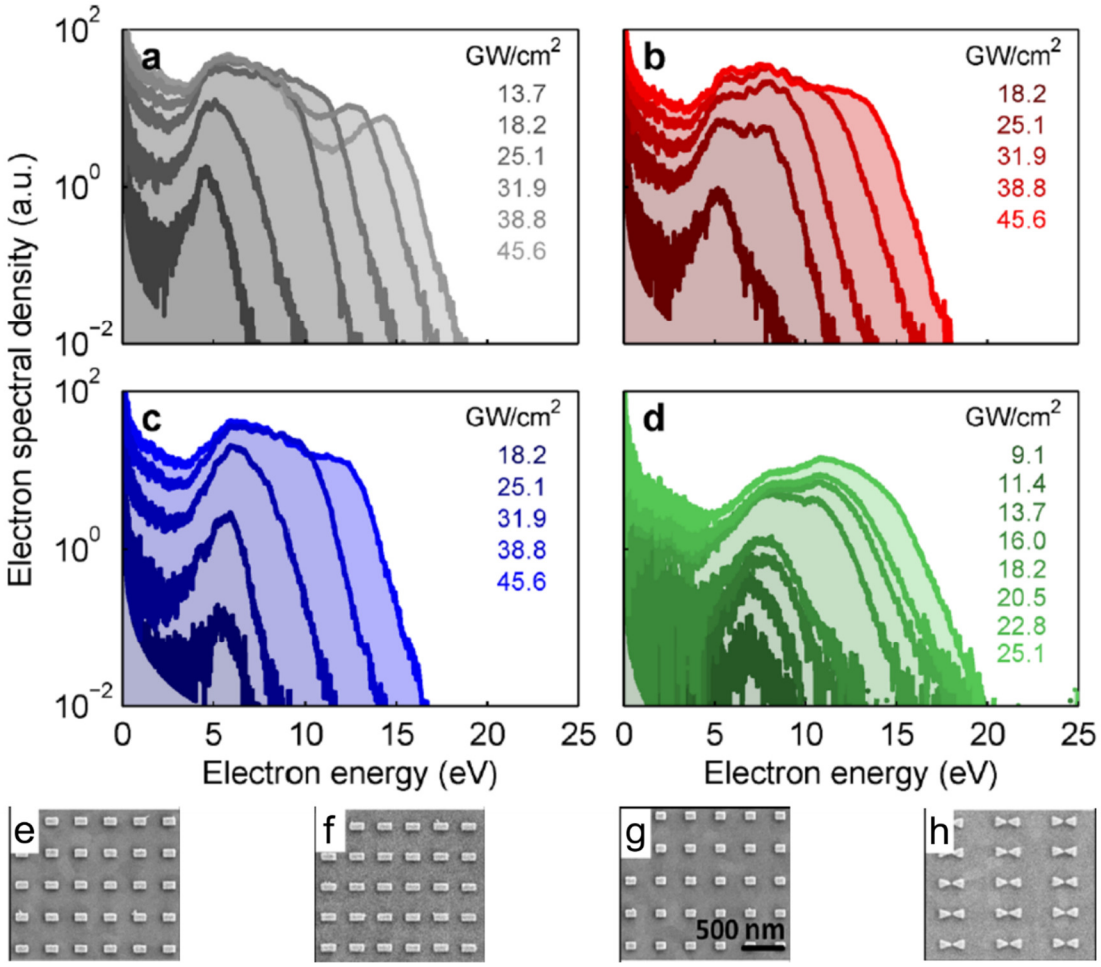

Figure 1.8. Kinetic energy spectra at various incident laser intensities from nanoparticle arrays of (a) resonant nanorods, (b) red-shifted nanorods, (c) blue-shifted nanorods, and (d) resonant bowties. Corresponding SEM images of (e) resonant nanorods, (f) red-shifted nanorods, (g) blue-shifted nanorods, and (h) resonant bowties. [24]

More recently, there has been a great interest in utilizing nanotips to generate femtosecond electron pulses. The first work on nanotip based sources operated on similar principles to photocathodes by focusing a high intensity pulse on the apex of the nanotip and observing the emitted photoelectrons [26–28]. However, in order to further increase the temporal resolution, groups have begun utilizing plasmonic based nanotips [3,4].

Initial work was carried out on electrochemically etched single-crystal tungsten (W) tips with an applied DC bias by Hommelhoff et al. [27]. The DC bias acts to reduce the Schottky barrier at the tungsten-vacuum interface and allows for a DC tunneling current to be observed. When the tip is excited by a laser pulse, the laser electric field adds to the applied DC bias and thus increases the photoemitted current. Notably, they were able to ascertain that the photoemission process is prompt with the laser excitation and occurs from a small 2 nm diameter region. Therefore, electron pulses with durations similar to the pulse duration of the driving laser pulse can be achieved. For higher current applications, it was shown that blunt tips can be utilized to increase the photoemitted current from 100 fA to 40 nA at the same laser intensity of 30 GW/cm^2. The same nanotips can also be used to produce low energy ultrafast electron pulses with kinetic energies up to 19 eV, however this requires laser intensities up to 230 GW/cm^2, Fig. 1.9 [28]. A similar approach by Li et al. utilizing ultrashort, single-cycle, terahertz (THz) pulses to excite tungsten tips has been demonstrated to achieve kinetic energies up to 5 keV, Fig. 1.10 [29]. The advantage of using single-cycle THz pulses is that due to the THz photon energy (~ a few meV) being much less than the W_F of the tungsten tip, the process is entirely field-driven, allowing researchers to study purely field-driven processes without any competing multi-photon effects.

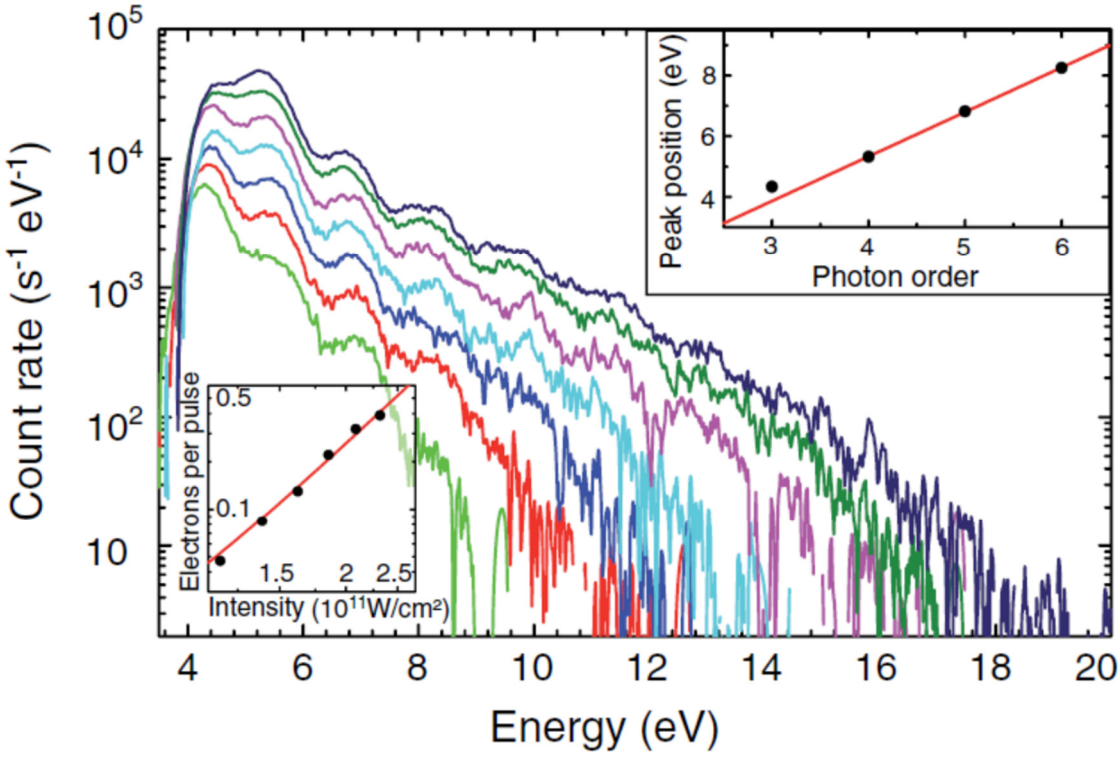

Figure 1.9. Kinetic energy spectra from W nanotip irradiated by laser intensities of {90, 120, 140, 160, 190, 210, 230} GW/cm^2 (curves from bottom to top). The top inset depicts the position of the energy peaks in the spectrum obtained at 120 GW/cm2. The lower inset illustrates the measured number of electrons per pulse for the given intensities. [28]

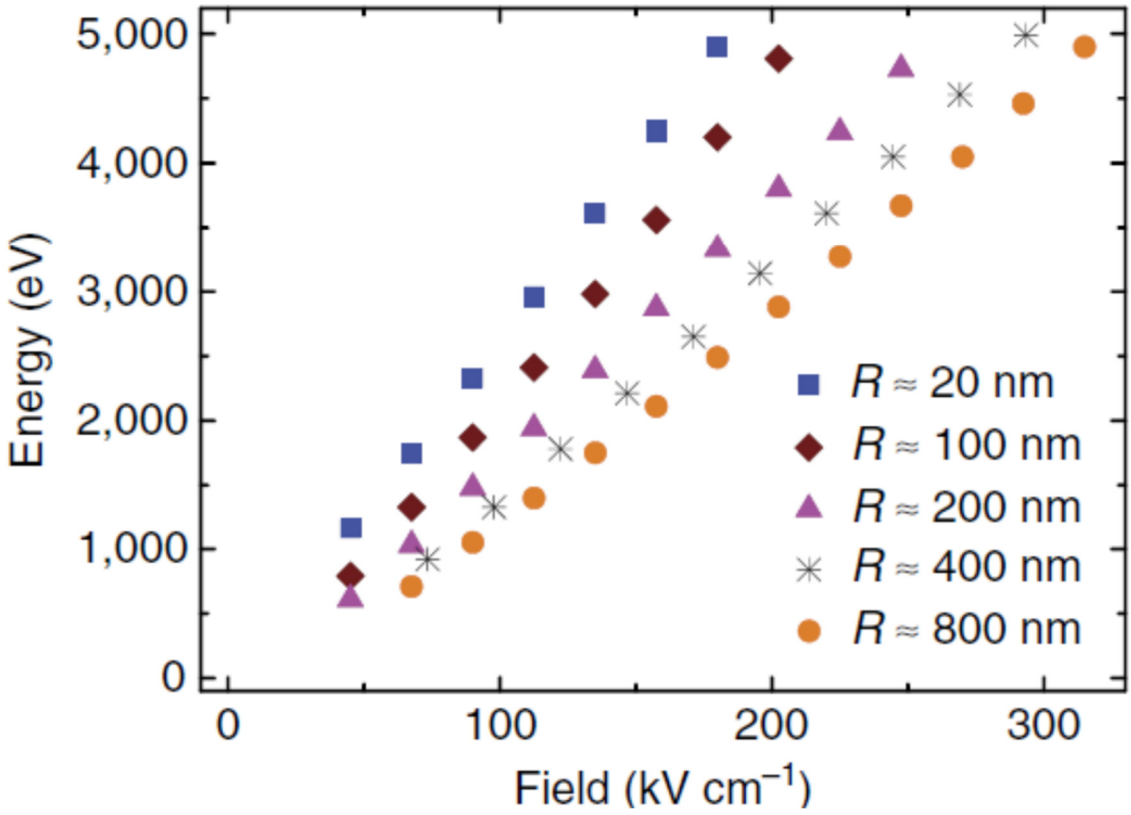

Figure 1.10. Maximum electron kinetic energy from W tips as a function of incident THz electric field strength and tip radius, *R*. [29]

The most recent advances in nanotip based electron sources is using nanoplasmonic focusing to generate ultrafast electron pulses. This offers a large advantage over excitation of the apex directly as the nanotip source can now be placed significantly closer to the sample under test as the laser is focused far from the sample. This improves the achievable temporal resolution due to a reduction in temporal pulse broadening. The setup is very similar to that of the other nanotip arrangements, except a grating is ion milled into the side of Au nanotips (Fig.1.11) to allow for the incident laser pulse to couple to a SP wave that travels towards and focuses at the apex of the nanotip. Vogelsang et al. were able to achieve an electron pulse duration of 27 fs at the tip by

exciting the grating with a 16 fs laser pulse with a central wavelength of 1.6 µm [4]. They successfully used the electron source to image a silver nanowire with a diameter of 100 nm using point projection microscopy. Müller et al. developed a similar plasmonic focusing nanotip based source around the same time. They were able to achieve a sub-10 fs temporal resolution [3]. The increased temporal resolution is attributed to excitation by a 5 fs laser pulse with 800 nm central wavelength. This source was used to successfully image an InP nanowire.

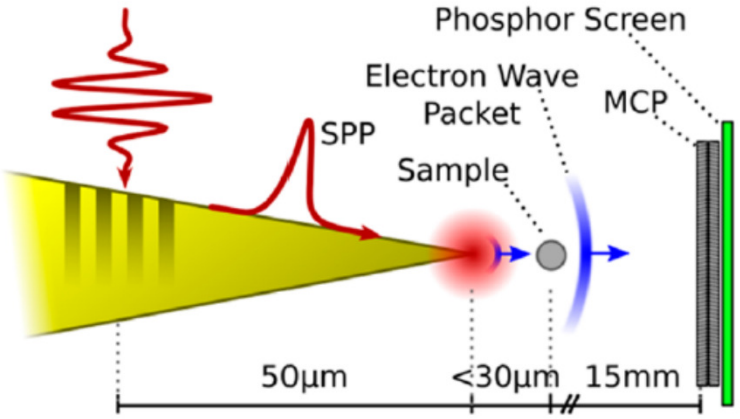

Figure 1.11. Nanoplasmonic Au nanotip electron source. [4]

To reach high kinetic energies for a compact electron source, Hommelhoff et al. have been pursuing nanoscale dielectric linear accelerators (DLA) [30]. Initial work focused on the acceleration of nonrelativistic continuous electron beams, as shown in Fig. 1.12(a). Here, an ultrafast laser is used to excite evanescent fields on a dielectric grating structure. Subsequently, a continuous beam of 28 keV electrons is passed above the grating and interacts with the fields resulting in acceleration. Notably, electrons gain up to 300 eV over a distance of 11.2 µm, resulting in an acceleration gradient of 25 MeV/m that is comparable to modern RF accelerators. The next step that Hommelhoff et al.

explored is the incorporation of a laser-driven nanotip emitter to generate the initial seed electron pulse [31]. The proposed electron gun is schematically depicted in Fig. 1.12(b), where a nanotip emitter is used to seed cascaded DLAs. It is envisioned that this cascaded approach is capable of accelerating the electrons to kinetic energies reaching 1 MeV within a few mm. This combination of a laser-driven nanotip source and the cascaded DLAs could be used for an extremely compact source of high energy, femtosecond electron pulses.

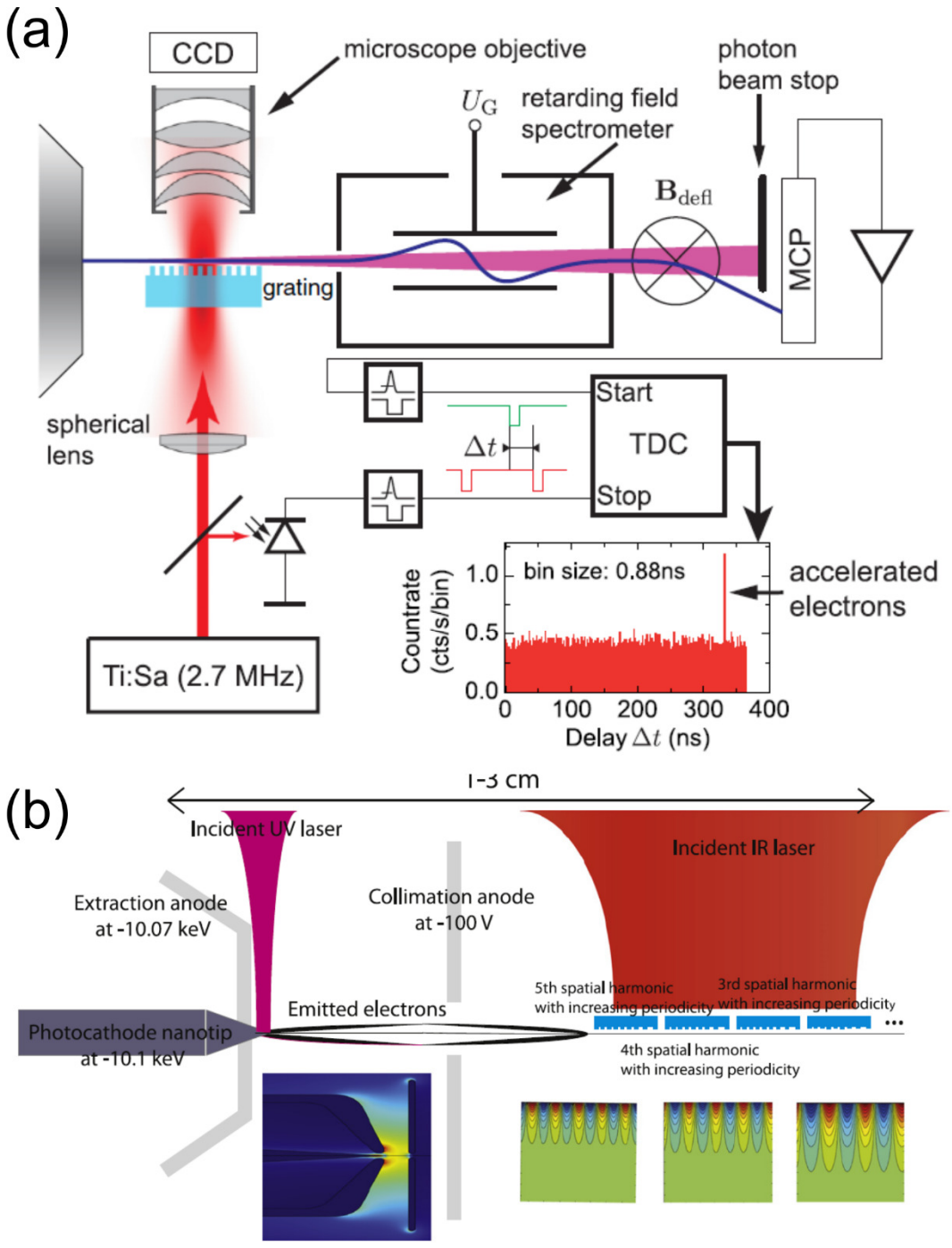

Figure 1.12. (a) Experimental setup for acceleration of continuous electron beams using a dielectric linear accelerator. [30] (b) Proposed schematic of a compact high energy, 1 MeV, femtosecond electron gun based on cascaded dielectric linear accelerators seeded by electron pulses from a laser-driven nanotip emitter. [31]

1.2. Obstacles Facing Generation of Ultrafast Electron Pulses

The biggest challenge in generating electron pulses with durations < 100 fs is temporal pulse broadening. Pulse broadening can occur due to two different factors, space-charge induced broadening, or kinetic-energy induced broadening. In both cases, the broadening gets worse as the distance between the generation point and sample under test increases. Space-charge induced broadening occurs due to the coulombic repulsion between all of the electrons within the pulse [32]. To overcome this, fewer electrons must be generated per laser pulse, which can be achieved by lowering the incident laser pulse energy. However, with fewer electrons per pulse in hand, obtaining a suitable image may require more pulses and hence a longer acquisition time. For most currently developed sources, space charge broadening is not an issue as the sources are typically operated to deliver a few electrons per pulse. Kinetic-energy induced pulse broadening occurs due to the broad range in kinetic energies within a given electron pulse [33]. When electrons are photoemitted from a material, they will have excess kinetic energy corresponding to the difference between W_F and the (multi-)photon energy. In addition, as discussed previously, for SP based sources, the electrons will be accelerated and therefore, the electron pulse will have a very broad kinetic energy spectrum. When this happens, the higher energy electrons will be at the front of the pulse leading the lower energy ones. As each kinetic energy corresponds to a different velocity, the electron pulse will begin to disperse in time as it propagates to the sample under test. A number of methods to combat this pulse broadening have been proposed and demonstrated, with the majority of them falling into a few categories: filtering of the electron pulse [34,35], compressing the electron pulse [36,37], optically gating the pulse [38–40], or simply shrinking the source-sample distance by utilizing nanoscale emitters [3,4].

The first method that was employed to combat pulse broadening was compression or bunching of the electron beam using a radio-frequency (RF) cavity [36]. A schematic depiction of the setup is shown in Fig. 1.13(a). In this configuration, generated electron beams enter an RF cavity at the correct phase such that the higher energy electrons leading the pulse will be decelerated and the lower energy electrons at the end of the pulse will be accelerated. In doing so, the electron pulse will compress (bunch) as it propagates towards the sample. With suitable selection of injection time and spacing between the RF cavity and the sample, the shortest duration electron pulse can be achieved. This method has been used to generate sub-100 fs, 95 keV electron pulses with enough electrons to allow for single-shot imaging [37]. However, there is a drawback to RF compression, namely the timing jitter between the RF source and the laser generating the electron pulse. For this experiment, the lowest attainable jitter was 80 fs. Instead of RF fields, high power ultrafast THz pulses can be used to provide the necessary electric fields as depicted in Fig. 1.13(b) [41]. Here, 950 fs electron pulses are passed through the gap of an inverse THz bowtie structure which provides electric field enhancement. By controlling the time delay between the arrival of the electron pulse and the arrival of the THz pulse, the electron pulse was compressed to a 75 fs pulse duration, similar to the RF compression, but with a timing jitter of only 4 fs.

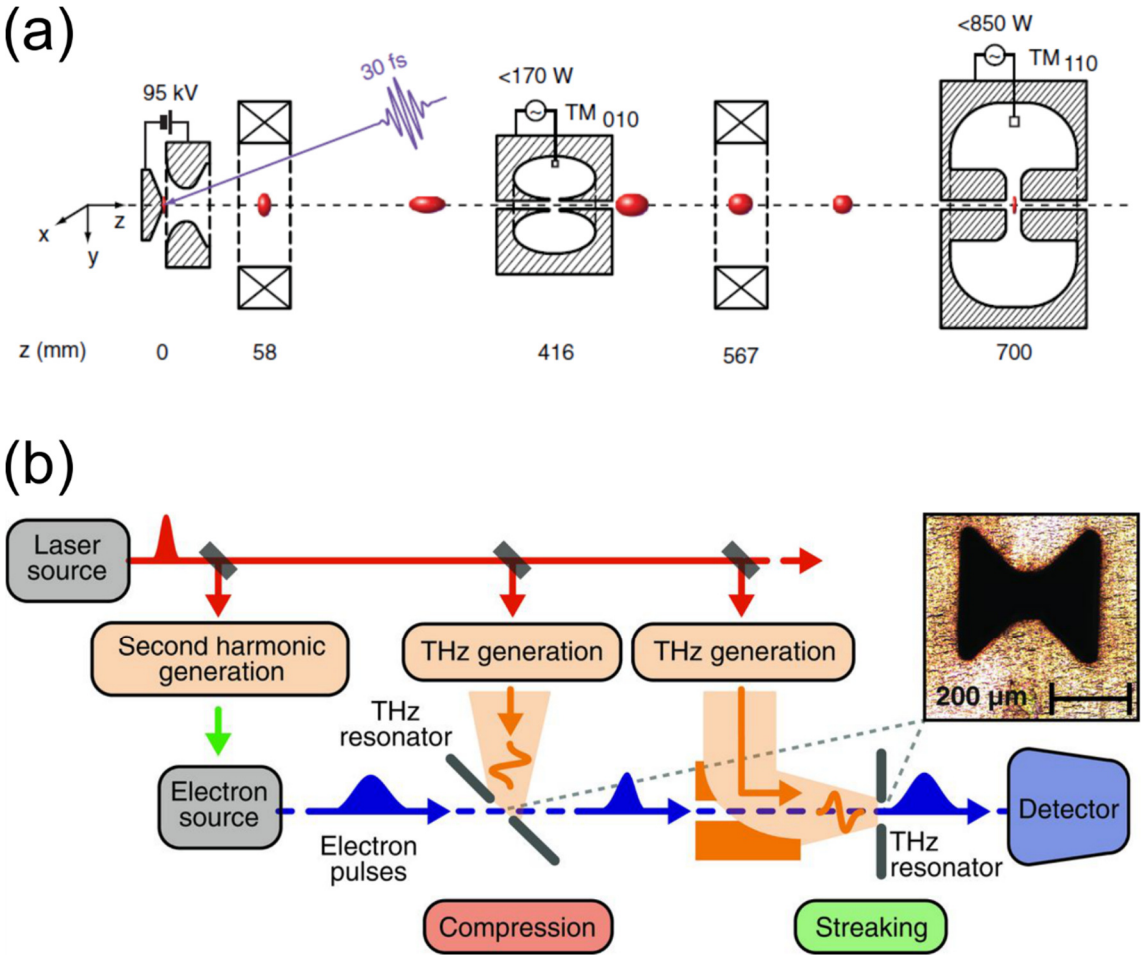

Figure 1.13. Electron pulse recompression techniques using (a) RF cavities [37], and (b) THz electric fields [41].

A similar method has been proposed that would utilize ultrafast laser pulses to perform the compression [2]. The proposed scheme for generating attosecond electron pulses is shown in Fig. 1.14. By utilizing the same laser to initially generate the electron pulse and to recompress it, time synchronization is guaranteed. This method utilizes a moving intensity grating provided by focusing a laser and its second harmonic to provide the actual recompression. It was theorized that starting with a 30 keV, 300 fs electron pulse, it can be compressed to a duration of 15 attosecond (as). Remarkably, this can be achieved with a long laser pulse duration of 300 fs but requires an intensity of 800

GW/cm^2. Recently, this proposed scheme has been experimentally demonstrated by Kozák et al. [42]. The experimental setup used is depicted in Fig. 1.15(a)-(b). Here, two separate optical traveling waves are generated by focusing counterpropagating laser pulses in free space. The first traveling wave provides the compression while the second is used to characterize the compressed electron pulse. The initial electron pulse is generated by laser excitation of the Schottky emitter in a field emission electron gun followed by acceleration to achieve a seed pulse duration of 460 fs and a central kinetic energy of 23.5 keV. Remarkably, this setup allows for a compressed pulse duration of 260 attoseconds, Fig. 1.15(c)-(d).

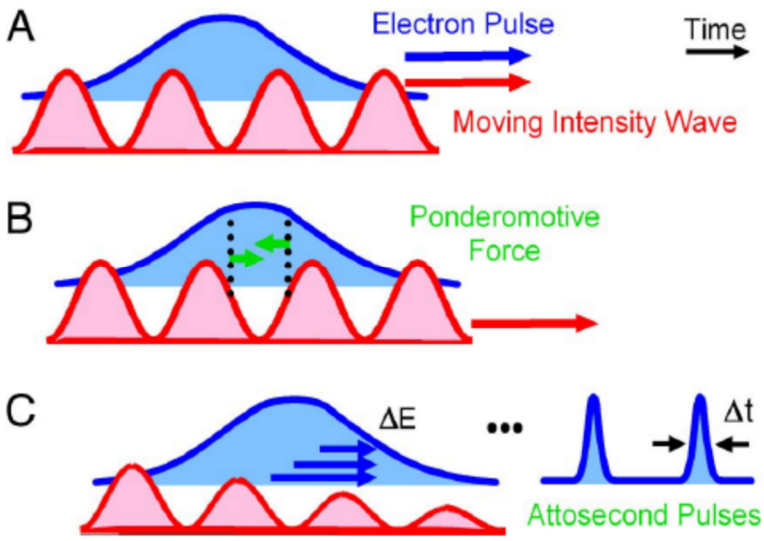

Figure 1.14. Proposed laser-driven compression scheme for generating attosecond electron pulses. (a) An electron packet (blue curve) propagates along the same direction as a moving intensity wave (red curve) excited by counterpropagating laser pulses at different frequencies. (b) The ponderomotive force (green arrows) push electrons away from regions of high laser intensity. Electrons on the falling slope are accelerated while those on the rising slope are decelerated. (c) Over many cycles this acceleration/deceleration leads to self-compression of the electron pulse to an attosecond duration. [2]

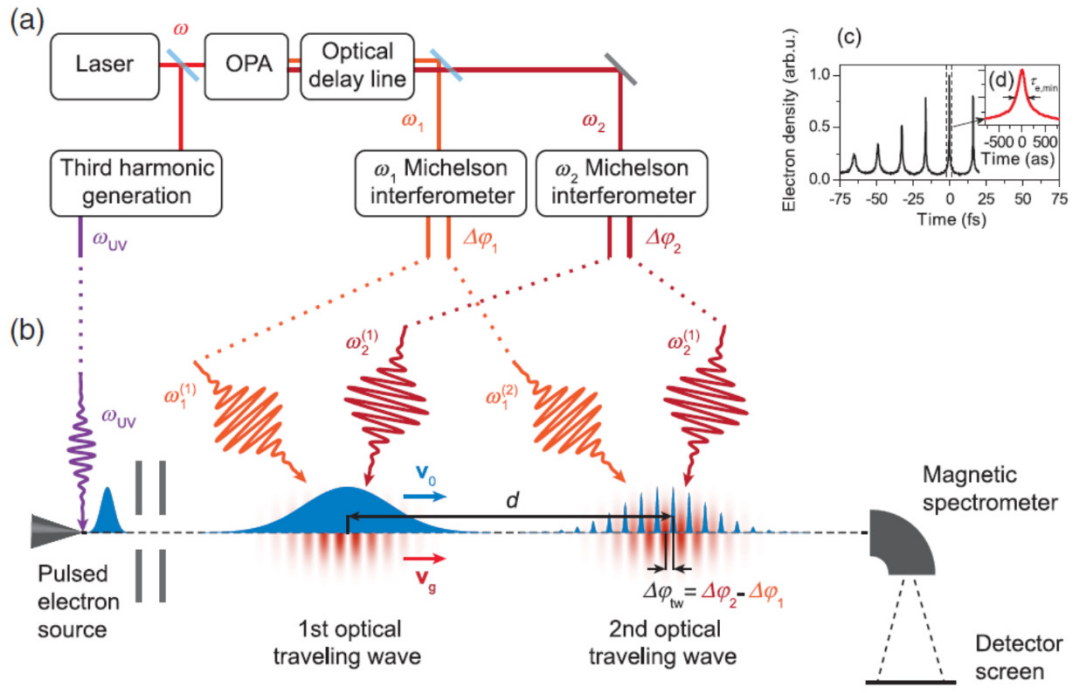

Figure 1.15. Experimental setup used to generate and detect attosecond electron pulses with schematic depiction of (a) laser setup and (b) electron pulse generation, compression, and detection setup. (c) Temporal evolution of the electron pulse. (d) Expanded view demonstrating 260 attosecond electron pulse duration. [42]

A more recent method used to generate ultrashort pulses within a TEM column utilizes multiple laser pulses to generate electron pulses with a 30 fs temporal resolution [35]. Figure 1.16 depicts the experimental setup used to achieve this. The fundamental laser pulse used has a central wavelength of 1040 nm. This pulse is then frequency doubled twice to produce a UV pulse at 260 nm which is then focused on a photocathode to produce the initial electron pulse with a duration of 500 fs. As the pulse propagates down the TEM column it is accelerated to 200 keV. At the sample, the second laser pulse (gating pulse produced from a non-collinear optical parametric amplifier) with a 30 fs pulse duration overlaps (in time and space) the electron pulse, giving rise to a modulation in the energy spectrum of the electron pulse. By filtering the electron signal based on

these modulations, the time resolution of the imaging technique will correspond to the interaction time of the gating pulse and the initial electron pulse. As such, they are able to achieve a temporal resolution of ~30 fs. It is important to note that actual electron pulse duration is > 30 fs. It is also theorized that this method can be extended to the attosecond regime by using gating pulses with attosecond duration on pre-compressed electron pulses of ~75 fs pulse duration.

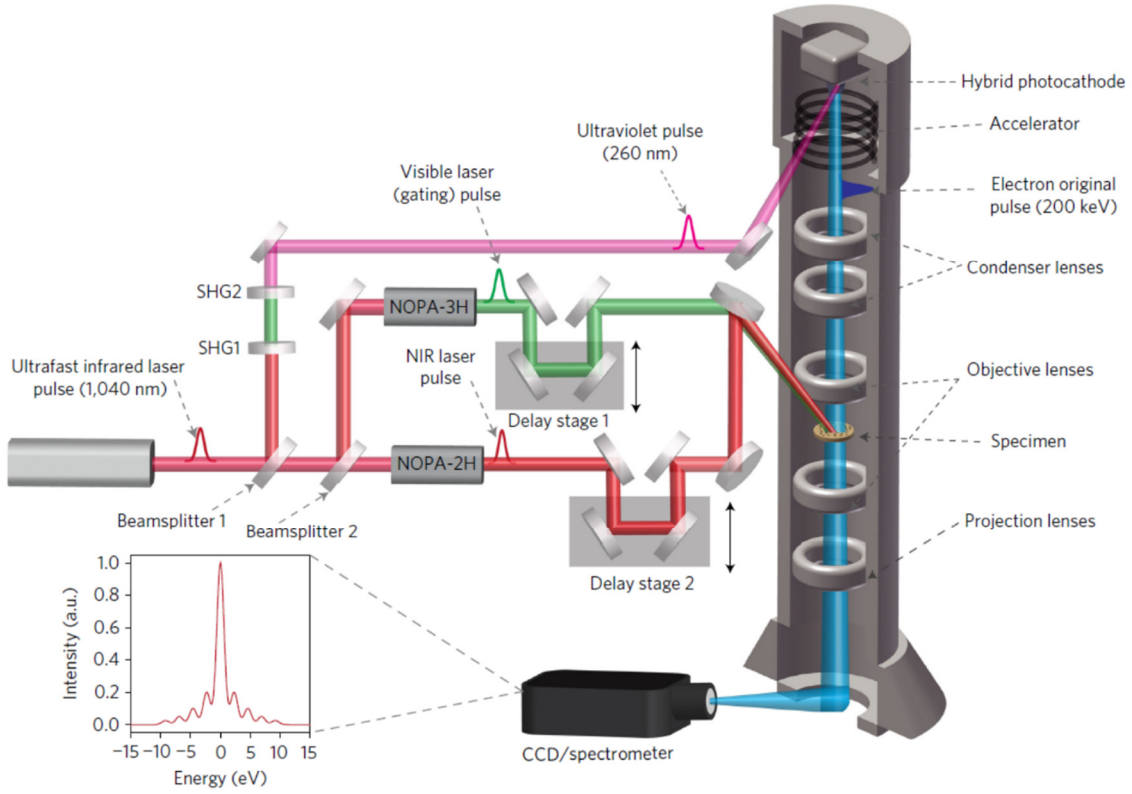

Figure 1.16. Experimental setup for optical gating of electron pulses in an ultrafast electron microscope. [35]

A similar arrangement using laser fields to modulate the energy spectrum of a free electron beam has been demonstrated to achieve pulse durations down to 1.2 fs [39]. This method uses a pair of gratings on which surface plasmons are excited by laser pulses with 600 fs pulse durations, as shown in Fig. 1.17. The first grating introduces a periodic

energy modulation to the 28 keV free electrons which is either enhanced or suppressed by controlling the arrival time of the second laser pulse at the second grating. Then, by selecting only those electrons that have gained energy, an electron pulse train with durations dependent on the time delay is achieved. This dual grating arrangement can also be employed for transverse streaking to temporally characterize the electron pulses.

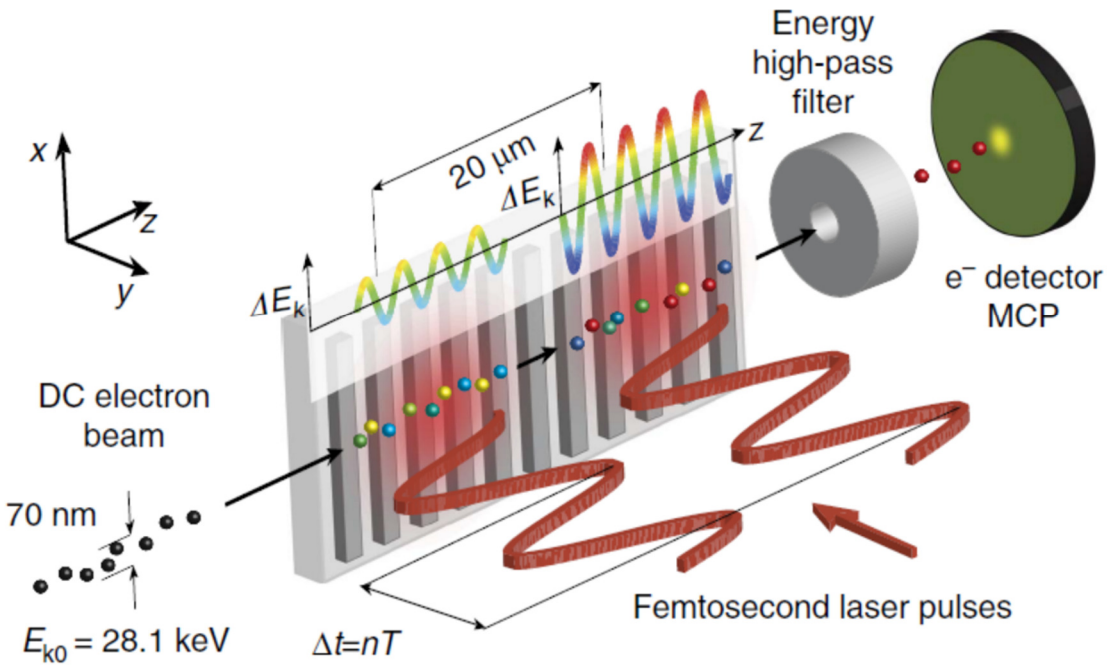

Figure 1.17. Dual grating setup for optical modulation of continuous electron beams. [39]

In addition to aiding the recompression process, and specifically for SP based electron sources, it would be beneficial to generate electron pulses that do not have a broad kinetic energy spectrum, and in fact possess a quasi-monoenergetic energy spectrum. One proposed method to do this is by introducing openings in a thin dielectric layer deposited on the plasmonic metal in the Kretschmann geometry [34]. Electron emission will then be confined to specific regions. As such, electrons will only be

generated at locations that produce favorable kinetic energies. By restricting emission to a 300 nm region at the center of the laser excitation region, it was theorized that electron pulses with kinetic energies of 60 eV and a minimal spread of 1.8 eV can be generated.

With all of the attempts to recompress or modulate the electron pulses from direct laser driven sources, there has been very little attention paid to SP based sources. To date, there exist very few methods for control and tuning of the characteristics of SP generated electron pulses such that the electron pulses can be tailored to their specific applications. As SP based sources have demonstrated greater performance than direct laser driven sources, it is of utmost importance to develop these methods for SP based electron sources.

1.3. Thesis Objectives

The main goal of this thesis is the generation and control of ultrashort electron pulses via surface plasmon waves. SP based electron sources is an emerging area, but many of the SP based methods still suffer from inherent lack of control, both in electron beam characteristics (kinetic energy, pulse duration, number of electrons per pulse, etc.) and spatial directionality. As such, this thesis aims to develop new methods to specifically control the kinetic energy and pulse duration of the generated electron pulses while also providing a mechanism for controlling the emission direction. Techniques to significantly increase the current of SP based electron sources are also demonstrated. The outcomes of this thesis will open new pathways for the next generation of compact, ultrafast, SP based electron sources for use in all areas such as ultrafast electron microscopy, ultrafast electron diffraction, and seeding of nanoscale particle accelerators. The specific goals are outlined below:

1. Develop a method for ultrafast, all-optical, control of SP generated electron pulses utilizing terahertz pulses.
2. Develop high-energy, ultrafast, compact SP based sources.
3. Develop methods to increase the electron yield from SP based sources at low laser intensities.
4. Gain a fundamental understanding of the interaction of an external electron beam with strong SP fields.
5. Demonstrate a high current SP based source by gating secondary electrons from Au.
6. Apply the insight gained from vacuum electron sources for novel solid-state devices.
7. Demonstrate the direct, all-optical, THz modulation of conduction electrons in Au as a stepping stone to ultrafast control of SP coupling and photoemission in the near-infrared.

1.4. Thesis Organization

This thesis includes 7 chapters that present a combination of theoretical and experimental work demonstrating ultrafast control of SP generated electron pulses. Chapter 2 includes the relevant background information necessary to understand the work presented in this thesis.

When working with electrons interacting with electromagnetic fields, it is necessary to be able to model the laser-electron interaction to fully understand what is happening. To this end, a particle tracking code was developed and used to study various methods of ultrafast control in Chapter 3. The particle tracking code is used to model

single-cycle, ultrafast THz pulses as a method for all-optical control of SP generated electron beams. The THz pulses allow for increased kinetic energy and angular tuning. Notably, the THz pulses are found to not destroy any carrier-envelope-phase (CEP) dependence of the initial SP generated electron beam. Although the THz allows for control of the energy and angle, it does not help with generating ultrashort electron pulses. To do so requires some method of filtering which can be achieved using a combination of magnetostatic and spatial filtering. The second half of Chapter 3 discusses a compact method to generate isolated attosecond electron pulses with kinetic energies > 0.5 keV while maintaining a low laser intensity that can be accessed with a tabletop laser oscillator.

Chapter 4 discusses various methods of increasing the current yield of SP based sources. A thin dielectric layer of eCarbon is added to act as a reservoir of electrons for the Au plasmonic film and reduce the nonlinear emission order of the SP based source. Gating of continuous electron beams to significantly increase the current of SP based electron sources is also demonstrated. The second half of Chapter 4 additionally details the systematic study of the interaction of a free, continuous, external electron beam passing through a strong plasmonic field on a metal.

With a greater understanding of the interaction of electrons with SP fields in vacuum, attention is turned to solid-state plasmonic electron devices. Chapter 5 explores such solid-state hybrid plasmonic/electronic devices. A nanoplasmonic triode that is the optical analogue of a standard three-terminal electronic device such as a transistor is investigated. This device can be used to bridge the gap between nanoplasmonics and nanoelectronics. Subsequently, a compact solid-state CEP detector that would allow for

the in-situ measurement of the CEP of few-cycle phase-stabilized laser pulses is presented.

Chapter 6 presents the experimental demonstration of the modulation of the conductivity of Au using THz electric fields. This modulation can be harnessed to control the SP coupling, electric field enhancement, and photoemission in the near-infrared regime opening a new pathway towards THz electric field enhanced photoemission.

Chapter 7 summarizes the major outcomes from this thesis as well as discusses the future directions of this research.

Chapter 2

Background

The work presented in this thesis explores various methods for ultrafast control and tailoring of ultrashort electron pulses usable for the next generation of time-resolved ultrafast electron microscopy. Both the generation and control of electron beams are presented and incorporate various different areas of science and engineering including ultrafast laser-matter interaction, optical surface plasmons, and ponderomotive electron acceleration. This chapter explores each area in detail and helps to develop the background necessary for the experiments and investigations laid out in the rest of the thesis. First, classical electromagnetics is discussed along with the Drude theory of metals. This leads to the concept of surface plasmon waves excited at dielectric-metal interfaces. Next, various methods of electron emission are discussed including secondary electron emission.

2.1. Classical Electromagnetics

All of classical electromagnetics is governed by four simple equations referred to as Maxwell's equations:

$$\nabla \cdot \vec{D} = \rho \tag{2.1}$$

$$\nabla \cdot \vec{B} = 0 \tag{2.2}$$

$$\nabla \times \vec{E} = -\frac{\partial \vec{B}}{\partial t} \tag{2.3}$$

$$\nabla \times \vec{H} = \vec{J} + \frac{\partial \vec{D}}{\partial t} \tag{2.4}$$

Here, $\vec{E}$ is the electric field, $\vec{D}$ is the electric flux density, $\vec{H}$ is the magnetic field, $\vec{B}$ is the magnetic flux density, ρ is the free charge density, and $\vec{J}$ is the free current density. The relationship between $\vec{D}$, $\vec{E}$ and $\vec{B}$, $\vec{H}$ is given by the following constituent equations:

$$\vec{D} = \varepsilon_r \varepsilon_0 \vec{E} \tag{2.5}$$

$$\vec{B} = \mu_r \mu_0 \vec{H} \tag{2.6}$$

Here, ε_r is the relative material permittivity, ε_0 is the permittivity of free space (8.854×10^{-12} F/m), μ_r is the relative material permeability, and μ_0 is the permeability of free space ($4\pi\times10^{-7}$ H/m). When equations (2.1) to (2.6) are combined, the interaction of electromagnetic waves with matter can be fully described.

2.2. Drude Theory of Metals

To fully understand the interaction of electromagnetic waves with metallic films, such as those used for surface plasmon experiments, it is important to understand the Drude theory of metals as proposed by Paul Drude [43,44]. This theory governs the behaviour of electrons within a metal. When the atoms within the metal are brought together (such as in a film or in bulk), the light and mobile valence electrons detach from their atoms and are free to move throughout the material while the heavy and immobile positively charged atoms stay in place. Drude modelled the electrons by applying the kinetic theory of gases to the "gas" of free electrons within the metal. This theory has two

main assumptions: (1) The electrons are solid identical spheres that travel in straight lines until they collide with the immobile ions, and (2) the only forces present are those that momentarily arise during collisions. As such, any electron-electron or electron-ion interactions except during collisions are neglected. These interactions can be neglected due to the short electron mean-free path, and hence short transit time between collisions, of the electrons within the material. This assumption fails when considering film thicknesses on the order of the mean-free path. For these films, the interaction is better modeled with the Lindhard dielectric function [45,46]. The density of these free electrons per cm^3 within a metal is given by [47]:

$$n_e = \frac{N_A n_v \rho_m}{m_a} \tag{2.7}$$

Where, N_A is Avogadro's Number (6.022×10^{23} atoms/mole), n_v is the number valence electrons contributed per atom, ρ_m is the mass density in g/cm^3, and m_a is the atomic mass of the material. For most metals, n_e is on the order of 10^{22}-10^{23} cm^{-3}. The main plasmonic metals used when working with laser pulses having wavelengths ~800 nm are Ag and Au which have n_e of 5.86×10^{22} cm^{-3} and 5.90×10^{22} cm^{-3}, respectively. Another commonly used metric to describe the density of conduction electrons in a material is the so-called Wigner-Seitz radius, r_s, defined as the volume of a sphere equal to the volume per conduction electron and typically given in units of Bohr radius. The Wigner-Seitz radius is given by [47]:

$$r_s = \left(\frac{3}{4\pi n_e}\right)^{1/3} \times a_0 \tag{2.8}$$

Where a_o is the Bohr radius (5.29×10^{-11} m). This gives r_s = 3.02 for Ag and 3.01 for Au.

These conduction electrons will respond to an external electromagnetic field that is oscillating at an angular frequency, ω. The motion of the electron (in one dimension) can be described by:

$$\frac{d^2x}{dt^2} + \nu_d \frac{dx}{dt} = -\frac{qE(t)}{m_e} \tag{2.9}$$

Where $x(t)$ is the electron displacement, ν_d is the material damping rate, q is the elementary electric charge, m_e is the electron mass, and $E(t)$ is the externally applied electric field driving the electron's motion. The relationship between the electron displacement and the external field can be found using the standard harmonic time dependence which assumes the forms for $x(t)$ and $E(t)$:

$$x(t) = x_0 \exp(i\omega t) \tag{2.10}$$

$$E(t) = E_0 \exp(i\omega t) \tag{2.11}$$

Substituting equations (2.10) and (2.11) into (2.9) results in:

$$x_0 = \frac{qE_0}{m_e} \frac{1}{\omega^2 - i\nu_d \omega} \tag{2.12}$$

The polarization of the material can then be written as the sum of all electric dipoles per unit volume as $P(t) = -n_e q x(t)$. When combined with equation (2.12), the electric susceptibility of the material can be derived:

$$\chi = \frac{P(t)}{E(t)} = -\frac{n_e q^2}{m_e} \frac{1}{\omega^2 - i\nu_d \omega} \tag{2.13}$$

The frequency dependent dielectric function of the material is then:

$$\varepsilon = \varepsilon_0 + \chi = \varepsilon_0 \left(1 - \frac{\omega_p^2}{\omega^2 - i\nu_d \omega} \right) \tag{2.14}$$

Where $\omega_p = \sqrt{n_e q^2 / \varepsilon_0 m_e}$ is the so-called plasma frequency or the natural collective oscillation frequency of the electrons within the material.

2.3. Surface Plasmons

A plasmon wave is the coherent oscillation of conduction band electrons within a metal. The quantized quasi-particle of these coherent oscillations is referred to as a plasmon. Plasmons come in two forms, *bulk* plasmons and *surface* plasmons. Bulk plasmons are excited within a bulk film when the lightweight, mobile, conduction electrons are displaced from the static, heavy, background atoms. This displacement can occur due to an external electric field such as the wakefield behind an electron traveling through the material. As such, bulk plasmons are typically probed with techniques such as electron energy loss spectroscopy (EELS) [48]. On the other hand, surface plasmons exist at, and are confined to, the very surface of a metal. Specifically, at a metal-dielectric interface. This concept is illustrated in Fig. 2.1, which depicts the charge oscillations and coupled electromagnetic fields of a SP wave confined at the interface between two infinite half spaces. For $z > 0$, the space is filled with a dielectric having a dielectric constant ε_1, while for $z < 0$ the space is filled with a metal having dielectric constant ε_2. For a surface charge density oscillation (plasmon) to exist at the dielectric-metal interface, it must obey Maxwell's equations. Assuming that region 1 is free-space and by following the prescription in [49], the electric field distribution of the surface plasmon at the interface can be derived. Here, we seek a wave solution to Maxwell's equations that

is confined to the interface at $z = 0$ and is propagating in the $+x$ direction. Starting with E and H fields of the form:

$$\vec{E}_1 = (E_{x1}, 0, E_{z1}) \exp[i(k_{x1}x - \omega t)] \exp[-k_{z1}z] \tag{2.15}$$

$$\vec{E}_2 = (E_{x2}, 0, E_{z2}) \exp[i(k_{x2}x - \omega t)] \exp[k_{z2}z] \tag{2.16}$$

$$\vec{H}_1 = (0, H_{y1}, 0) \exp[i(k_{x1}x - \omega t)] \exp[-k_{z1}z] \tag{2.17}$$

$$\vec{H}_2 = (0, H_{y2}, 0) \exp[i(k_{x2}x - \omega t)] \exp[k_{z2}z] \tag{2.18}$$

Where k is the wavevector. Here, the subscript numbers correspond to the medium in which the field is contained (i.e. 1 for free space, and 2 for metal), and both k_z are taken to be positive in order to have exponential decay away from $z = 0$ to confine the plasmon wave to the interface. The boundary conditions at the interface dictate that $\vec{D}$ must be continuous giving $\varepsilon_1 E_{z1} = \varepsilon_2 E_{z2}$, and as the material is assumed to be non-magnetic, the continuity of the normal component of $\vec{B}$ gives $H_{z1} = H_{z2}$. This combined with the fact that $\nabla \cdot \vec{B} = 0$ at the interface, necessitates that only the H_y component must exist.

Furthermore, $\nabla \times \vec{H} = \vec{J} + \dfrac{\partial \vec{D}}{\partial t}$ with only an H_y component dictates that E_y must be zero, indicating that the surface plasmon wave is a transverse magnetic (TM) wave. As such, surface plasmons can only be excited with *p*-polarized light in order to satisfy the boundary conditions. Substituting equations (2.15) to (2.18) into Ampere's Law (equation (2.4)), and assuming that there is no surface current, yields:

$$(k_{z1}H_{y1}, 0, ik_{x1}H_{y1}) = -i\varepsilon_1\omega(E_{x1}, 0, E_{z1}) \tag{2.19}$$

$$(-k_{z2}H_{y2}, 0, ik_{x2}H_{y2}) = -i\varepsilon_2\omega(E_{x2}, 0, E_{z2}) \tag{2.20}$$

The next step is to look at the boundary conditions of the tangential fields at the interface, which must be continuous, giving $E_{x1} = E_{x2} = E_x$, and $H_{y1} = H_{y2} = H_y$. This also implies that $k_{x1} = k_{x2} = k_x$. Substituting these boundary conditions and looking at the *x*-components of equations (2.19) and (2.20) yields $k_{z1}H_y = -i\varepsilon_1\omega E_x$ and $k_{z2}H_y = i\varepsilon_2\omega E_x$, dividing the two gives:

$$\frac{k_{z1}}{k_{z2}} = -\frac{\varepsilon_1}{\varepsilon_2} \tag{2.21}$$

As we have already assumed that both k_z are positive, and that ε_1 is free space (i.e. positive and equal to ε_0) the only way to satisfy the above result is to have ε_2 be negative. This result indicates that for a surface plasmon wave to exist at the metal-dielectric interface, the dielectric function of the metal must be negative, which will only occur for frequencies below the plasma frequency (i.e. $\omega_p = \sqrt{n_e q^2 / \varepsilon_0 m_e}$).

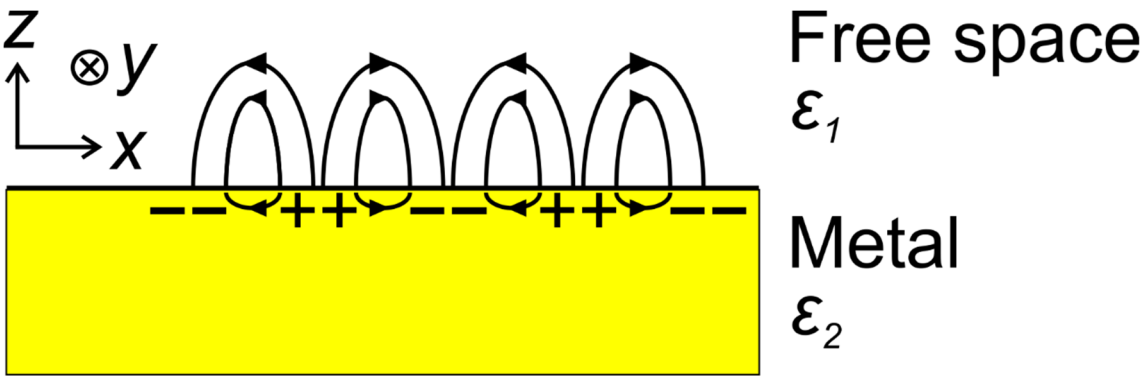

Figure 2.1. Surface plasmon confined to the interface between infinite half spaces of metal and free space. The SP consists of charge oscillations coupled to electromagnetic fields.

The wave equation can be used to obtain the dispersion relation of the propagating surface plasmon mode:

$$\nabla^2 \vec{E} = \varepsilon\mu \frac{\partial^2 \vec{E}}{\partial t^2} \tag{2.22}$$

Substituting equations (2.15) to (2.18) into equation (2.22) gives the following expressions:

$$-k_x^2 + k_{z1}^2 = -\varepsilon_1 \mu_0 \omega^2 \tag{2.23}$$

$$-k_x^2 + k_{z2}^2 = -\varepsilon_2 \mu_0 \omega^2 \tag{2.24}$$

Rearranging and dividing these equations gives:

$$\frac{k_{z1}^2}{k_{z2}^2} = \frac{k_x^2 - \varepsilon_1 \mu_0 \omega^2}{k_x^2 - \varepsilon_2 \mu_0 \omega^2} \tag{2.25}$$

Substituting equation (2.21) into equation (2.25) gives the relationship between the frequency of the surface plasmon and its wavevector (i.e. the SP dispersion relation):

$$\omega = c k_x \sqrt{\frac{\varepsilon_1 + \varepsilon_2}{\varepsilon_1 \varepsilon_2}} \tag{2.26}$$

Where c is the speed of light in vacuum. Figure 2.2 illustrates the dispersion relation for a surface plasmon wave at the interface between an Au film and vacuum. The red curve in Fig. 2.2 depicts the dispersion relationship of a photon traveling in free space:

$$\omega = c k_{photon} \tag{2.27}$$

Where ω is the angular frequency of the photon, and k_{photon} is the wavevector of the photon. The Au dielectric function is taken to be the Drude model using parameters from [50]. Notably, at high wavevectors the dispersion curve approaches an asymptote equal to $\omega_p / \sqrt{2}$, the so-called surface plasmon frequency. At low wavevectors, it is observed that the SP dispersion curve behaves similar to the light line. However, it should be noted that the two curves do not actually cross, which is an important point in plasmonics. Consequently, it is not possible to directly couple free space electromagnetic waves to surface plasmon excitations since the momentum of the electromagnetic wave is not matched to that of the plasmon wave.

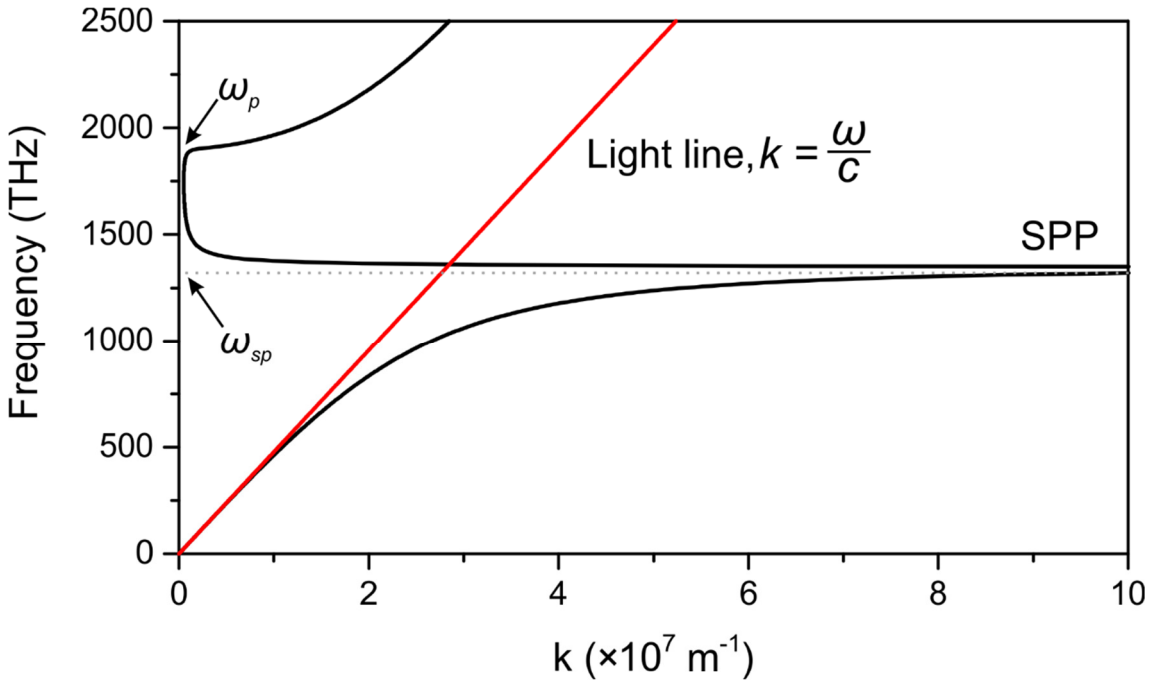

Figure 2.2. Surface plasmon dispersion curve for a lossy Au film. The red light line depicts the dispersion curve for a photon, indicating no coupling between the SP mode and light.

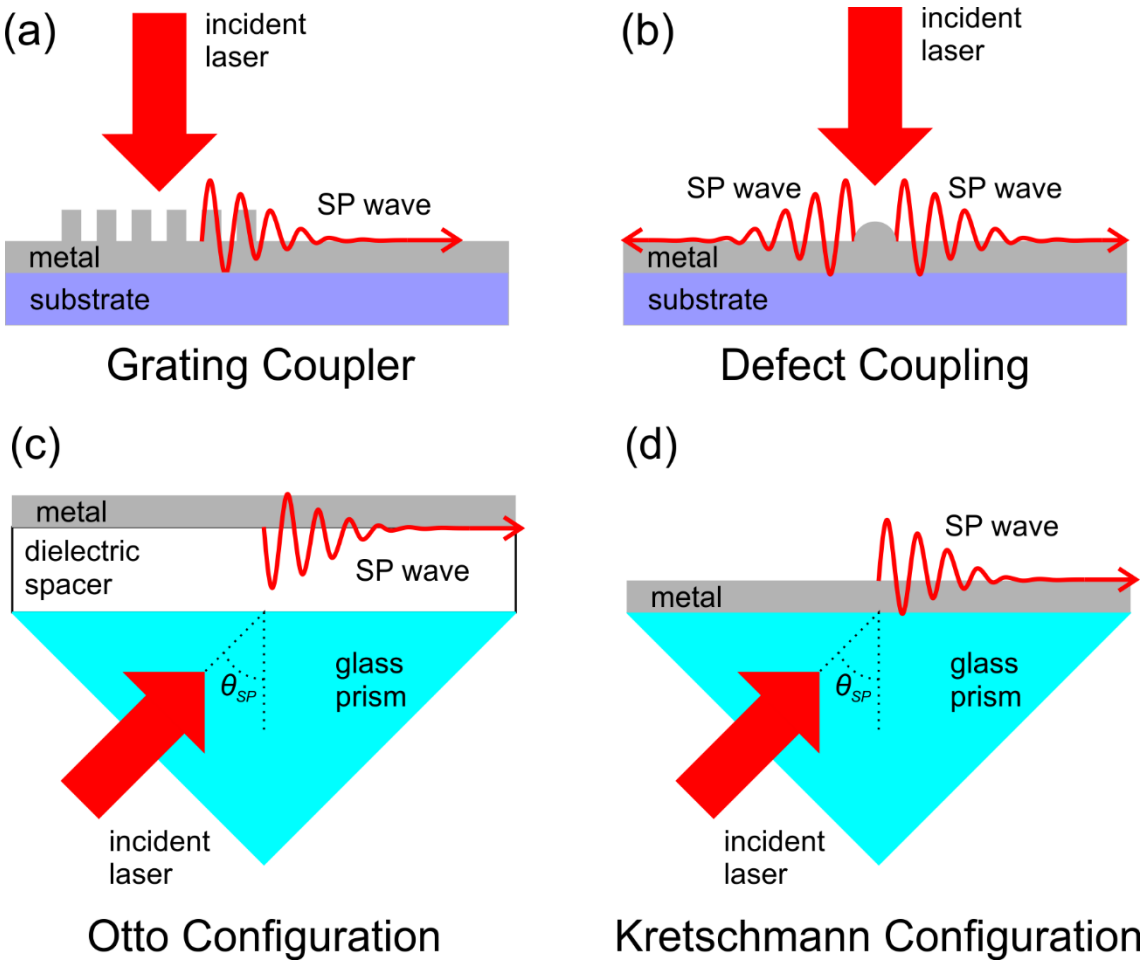

Figure 2.3. Schematic depiction of various geometries used for coupling lasers to surface plasmons: (a) grating coupling, (b) defect coupling, (c) Otto configuration, and (d) Kretschmann configuration. Each method provides the necessary momentum matching between incident laser photons and the propagating SP wave.

To couple a free space electromagnetic wave to a surface plasmon wave, the dispersion curves must cross such that both the energy and momentum is conserved when the plasmon is excited by a photon. There are multiple ways to enable the momentum conservation, such as grating couplers (Fig. 2.3(a)), defect couplers (Fig. 2.3(b)), the Otto configuration (Fig. 2.3(c)), and the Kretschmann configuration (Fig. 2.3(d)). The grating and defect couplers increase the incident photons momentum via diffraction while the

Otto and Kretschmann configurations increase the momentum by passing the incident photons through a prism. The Kretschmann geometry is used throughout this thesis due its simplicity, (i.e. it only requires the deposition of a thin metal film). In this geometry, a thin metallic film is deposited on the hypotenuse side of a right-angle glass prism. Light is coupled to a surface plasmon at the metal-free space interface by illuminating the glass side of the metal film. As the incident photon is now traveling in the glass prism, its dispersion curve will have a different slope inversely proportional to the refractive index of the glass prism, n_{prism}. When the photon passes through the glass prism, its dispersion relation obeys:

$$\omega = \frac{ck_{photon}}{n_{prism}} \tag{2.28}$$

This, in effect, increases the momentum of the photon ($\hbar k_{photon}$, where $\hbar$ is reduced Planck's constant) at a given frequency, causing the dispersion curves to cross and the momentum to be conserved between the incident photon and the plasmon, as depicted in Fig. 2.4. However, to excite the surface plasmon, the component of the incident photon wavevector, k_{photon}, must match that of the propagating surface plasmon wavevector, k_x according to:

$$k_x = k_{photon} \sin(\theta_{SP}) \tag{2.29}$$

Where θ_{SP} is the surface plasmon resonance angle.

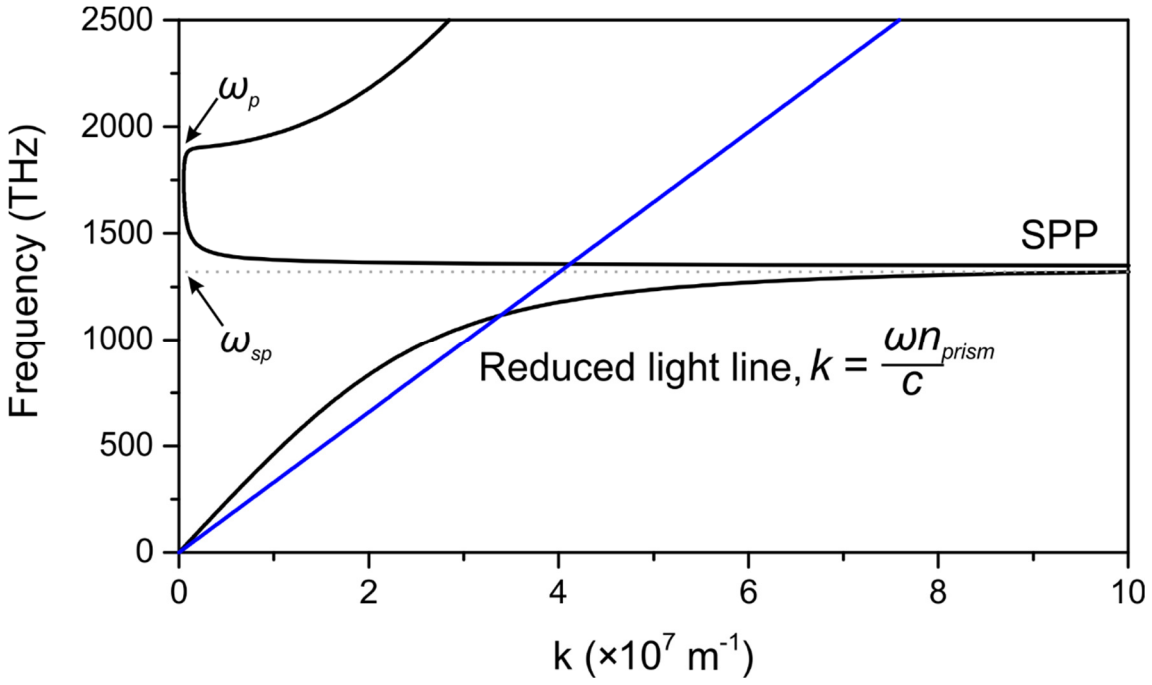

Figure 2.4. Surface plasmon dispersion curve with reduced light line for light incident on the Au film from the glass prism with refractive index n_{prism}.

Substituting equation (2.28) into (2.29) we get the momentum of the propagating surface plasmon wave:

$$k_x = \frac{\omega}{c} n_{prism} \sin(\theta_{SP}) \tag{2.30}$$

To find θ_{SP}, one must consider the thickness, d_2, and the permittivity, ε_2, of the metal film. The plasmon coupling angle occurs when light is most efficiently coupled to the SP wave, i.e. when the reflection from the surface exhibits a sharp dip having no reflection. Figure 2.5 shows the arrangement of prism, metal film, and free-space used to calculate the reflection. The amplitude reflectivity of the multilayer stack is thus given by:

$$r_{321} = \frac{\sum_{n=1}^{\infty} E_n}{E_0} \tag{2.31}$$

Where E_n represents the multiple reflections of the electric field from the interface and is given by:

$$\begin{aligned} E_1 &= r_{32} \\ E_2 &= t_{32} r_{21} t_{23} e^{-i2\phi_r} \\ E_3 &= t_{32} r_{21}^2 r_{23} t_{23} e^{-i4\phi_r} \\ &\ldots \end{aligned} \tag{2.32}$$

Where $\phi_r = (\omega / c)(\varepsilon_2 - \varepsilon_3 \sin^2 \theta_1)^{1/2} d_2$ is the phase change on reflection, and r_{ij}, t_{ij} are the Fresnel reflection and transmission coefficients given by [25]:

$$\begin{aligned} r_{ij} &= \frac{\varepsilon_j k_i - \varepsilon_i k_j}{\varepsilon_j k_i + \varepsilon_i k_j} \\ t_{ij} &= \frac{2\varepsilon_i k_i}{\varepsilon_j k_i + \varepsilon_i k_j} \end{aligned} \tag{2.33}$$

Where i is the index of the material the electric field is incident from, j is index of the material on the other side of the boundary, and $k_i = (\omega / c)(\varepsilon_i - \varepsilon_3 \sin^2 \theta_1)^{1/2}$. Carrying out the summation of equation (2.31) one arrives at the closed form solution:

$$r_{321} = \frac{r_{32} + r_{21} e^{-i2\phi_r}}{1 + r_{32} r_{21} e^{-i2\phi_r}} \tag{2.34}$$

The amplitude reflectance is simply $\left| r_{321} \right|^2$ and is plotted in Fig. 2.6(a) for a λ = 800 nm light wavelength incident on Au films of various d_2 deposited on a fused silica prism using permittivity data from [50]. Figure 2.6(b) depicts the amplitude reflectance for a Ag film using permittivity data from [51]. The plasmon coupling angle shifts from 45° for a 45 nm Au film to 44.7° for a 45 nm Ag film. The thickness has quite a profound affect on the efficiency of the coupling process with only 40-50% of the incident light being

coupled to the SP for films thinner or thicker than 45 nm. Notably, θ_{SP} is above the angle for total-internal reflection at the glass-metal interface. As such, the use of a prism is necessary as the 45° angle of the input face results in minimal refraction for the incident laser. If the photon was incident on a rectangular glass block, there is no angle of incidence that could be found that would result in (after refraction at the input face) θ_{SP} at the glass-metal interface, thus making it impossible to couple to a SP wave.

Based on Fig. 2.6, surface plasmons can be efficiently excited on both Ag and Au films with similar angular sensitivities (0.6° full-width at half-maximum (FWHM) for Au and 0.3° FWHM for Ag), the choice of metal comes down to additional factors. Au was selected over Ag for experiments in this thesis for one main reason: Ag films begin to tarnish and form Ag_2S when exposed to air [52]. As such, the performance of Ag films severely degrades within a short time frame (~ a day) and cannot be used for experiments over a long period of time.

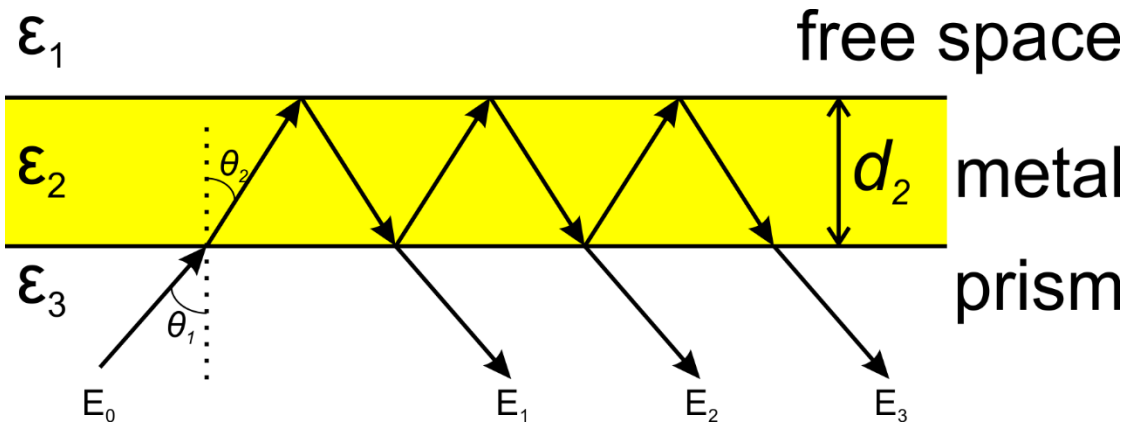

Figure 2.5. Multilayer system for calculating Fresnel reflectance.

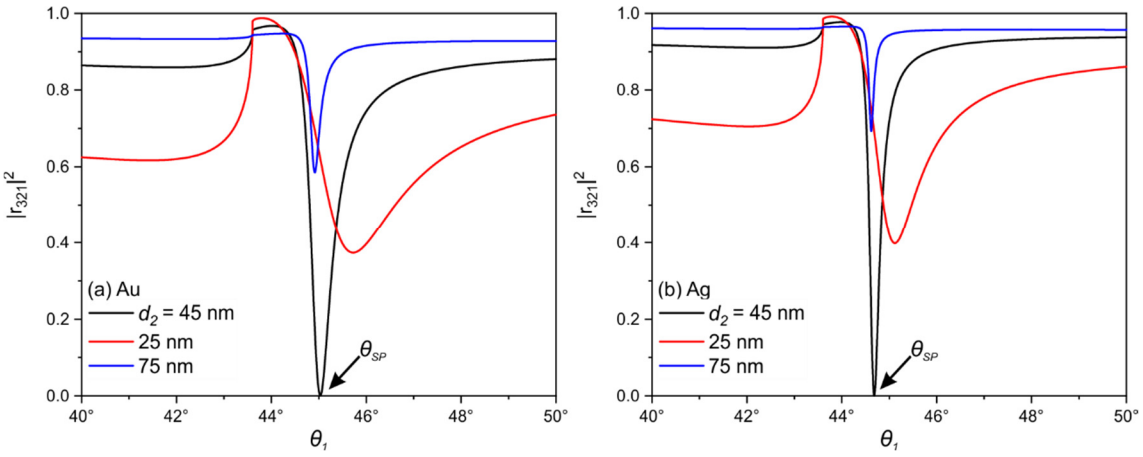

Figure 2.6. Reflectance of λ = 800 nm light for a multilayer stack composed of (a) fused silica/Au/Air at different metal thicknesses, d_2, and (b) fused silica/Ag/Air at different metal thicknesses, d_2.

2.4. Electron Emission from Metal Surfaces

When a photon is incident on a metallic surface, it may free an electron from the conduction band via the photoelectric effect, given that the photon energy is greater than the work function of the metal. Typically, this corresponds to photons in the ultraviolet (UV) as the work function of most metals is in the range of 4-5 eV. Albert Einstein first theorized the photoelectric effect in 1905 while trying to explain the results of Hertz previous experiments by proposing that packets of light have quantized energy given by:

$$E_{photon} = h\nu \tag{2.35}$$

Where E_{photon} is the photon energy, h is Planck's constant, and ν is the frequency of the light. Notably, Einstein realized that there is an energy threshold (work function) for the ejection of electrons and that the number of electrons generated is linearly proportional to the intensity of the incident light. However, for intense enough light, such as that from a laser, multiple photons can be absorbed to free an electron, termed multi-photon

absorption. In this case, each photon is absorbed to a virtual state and can be thought of as "stacking" their individual energies such that when the sum of their energies is above the work function, a single electron will be freed. Both single photon absorption and multi-photon absorption are depicted in Fig. 2.7. The number of photons required can be determined by:

$$m = \mathrm{mod}(W_F, h\nu) \tag{2.36}$$

Where m is the number of photons required, W_F is the work function of the metal, and mod is the modulus. The electron that is ejected will have an excess of kinetic energy given by:

$$E_k = mh\nu - W_F \tag{2.37}$$

Where E_k is the initial kinetic energy of the generated electron. In addition, as the process now relies on multiple photons, the number of generated electrons, and hence, the current density, J, will scale nonlinearly with the incident intensity given by:

$$J \propto I_{laser}^{m} \tag{2.38}$$

Where I_{laser} is the incident laser intensity.

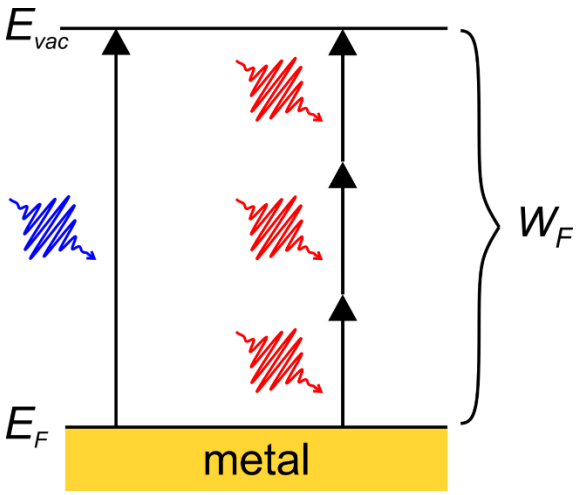

Figure 2.7. Single photon absorption (left) and multi-photon absorption (right) to free electrons from a metallic film. Electrons are excited from the Fermi energy (E_F) to energies exceeding the vacuum energy (E_{vac}).

Another method of electron emission from metallic surfaces is optical field emission. Optical field emission occurs when there is a high electric field present at the surface of the metal such that the potential barrier ($\phi(x)$), is lowered to a level that electrons can overcome it by absorbing a single photon's energy, as depicted in Fig. 2.8(a). The source of the electric field can either be from an externally applied DC field or from the electric field of a laser pulse. A similar effect is tunnel ionization, in which the applied electric field distorts the potential barrier such that electrons within a material have a greater probability to tunnel through it. These electrons typically tunnel from energy states close to the Fermi energy, E_F, as shown in Fig. 2.8(b). Externally applied DC fields have widely been used for electron sources in high-resolution electron microscopes (i.e. field emission microscopes).

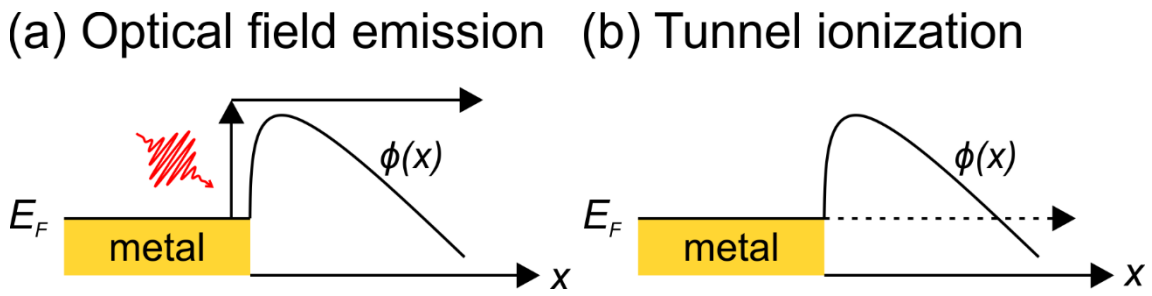

Figure 2.8. Schematic depiction of (a) optical field emission and (b) tunnel ionization. $\phi(x)$ is the potential barrier at the metal-vacuum interface.

The value of the electric field necessary to induce tunnel ionization is generally calculated via the Keldysh parameter that was derived for an electric field ionized atom [53]. The Keldysh parameter is given by:

$$\gamma = \frac{\omega\sqrt{2m_e W_F}}{qE_{laser}} \tag{2.39}$$

Where E_{laser} is the peak laser electric field value. For values of $\gamma > 1$, multi-photon absorption will be the dominating electron emission mechanism, and for $\gamma < 1$, tunnel ionization will dominate. To give a sense of the of the electric fields required for tunnel ionization, an electric field of 1.7×10^{10} V/m or 17 V/nm is required for an Au film (W_F = 4.8eV) being excited by a Ti:Sapphire laser ($\omega = 2.4\times10^{15}$ rad/s).

2.5. Secondary Electrons

Electrons may also be freed from a material through means other than photoemission, namely secondary electron emission. A section of Chapter 4 explores the control of these secondary electrons with plasmonic fields. As such, it is important to understand what happens when an energetic primary electron (PE) having kinetic energy E_P collides with atoms in a material. Figure 2.9 depicts the four main outcomes that arise. During the

collision, the four outcomes that may occur are: (1) The primary electron is elastically reflected from an atom of the material. This electron will have an energy of E_p and is deemed a reflected electron (RE). (2) The primary electron will undergo inelastic collisions within the material and becomes directed back out of the material. This electron will have an energy between 50 eV and E_p and is deemed a backscattered electron (BSE). (3) The material is thin enough and E_p is high enough such that the primary electron is transmitted through the material. These electrons will have kinetic energies between 50 eV and E_p and are typically used in transmission electron microscopes (TEM) and EELS. (4) The primary electron will undergo inelastic collisions with the shell electrons of the atoms and ionizes them to generate new electrons. These new electrons travel randomly through the material and if they have enough energy to overcome the material work function they will be ejected from the material. These electrons are the secondary electrons (SE) with kinetic energies < 50 eV (by definition) and will be the focus of this background section as well as the second half of Chapter 4. Secondary electrons provide the main signal for scanning electron microscopes (SEM).

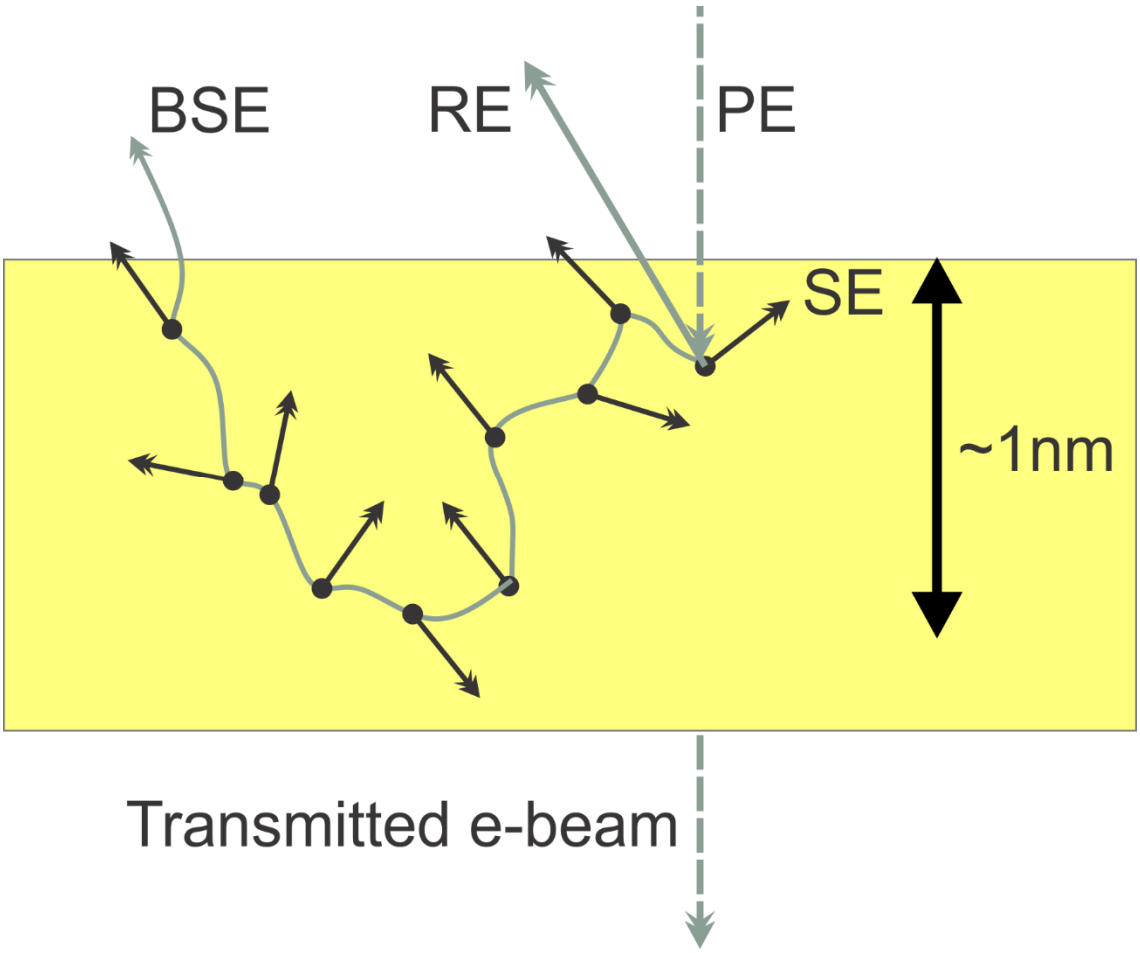

Figure 2.9. When a primary electron (PE) interacts with a material there are four possible outcomes: (1) The electron is reflected with no energy loss (RE). (2) The electron undergoes multiple collisions, loses energy and is directed back out of the material (BSE). (3) The electron is transmitted through the sample and may or may not lose energy (transmitted e-beam). (4) The electron undergoes multiple collisions knocking off secondary electrons (SE) that are emitted from the sample with kinetic energies < 50 eV.

As secondary electrons, by definition, have kinetic energies less than 50 eV, it is important to understand the shape of their kinetic energy spectrum and how it might be influenced for different primary beam or material characteristics. The kinetic energy spectrum is given by [54]:

$$\frac{dN_{SE}}{dE_{SE}} = \frac{q^4 k_F^3 14.7 (E_F \beta)^{3/2} (E_{SE} - E_F - W_F)}{12\pi E_p (m_e^*)^{1/2} [atan(1/\beta)^{1/2} + \beta^{1/2}/(1+\beta)](E_{SE} - E_F)^4} \quad (2.40)$$

Where N_{SE} is the number of secondary electrons, E_{SE} is the secondary electron energy, k_F is the Fermi wavevector, E_F is the Fermi energy, $\beta = (4/9\pi)^{1/3}(r_s/\pi)$, and m_e^* is the electron effective mass. Notably, from (2.40) the shape of the spectrum is entirely determined by:

$$\frac{dN_{SE}}{dE_{SE}} = \frac{E_{SE} - E_F - W_F}{(E_{SE} - E_F)^4} \quad (2.41)$$

The remainder of (2.40) only determines the magnitude of the spectrum. Remarkably, the shape is independent of E_p [55]. Figure 2.10 depicts the SE energy spectrum for Au assuming E_F = -5.53 eV [47], and W_F = 5.2 eV.

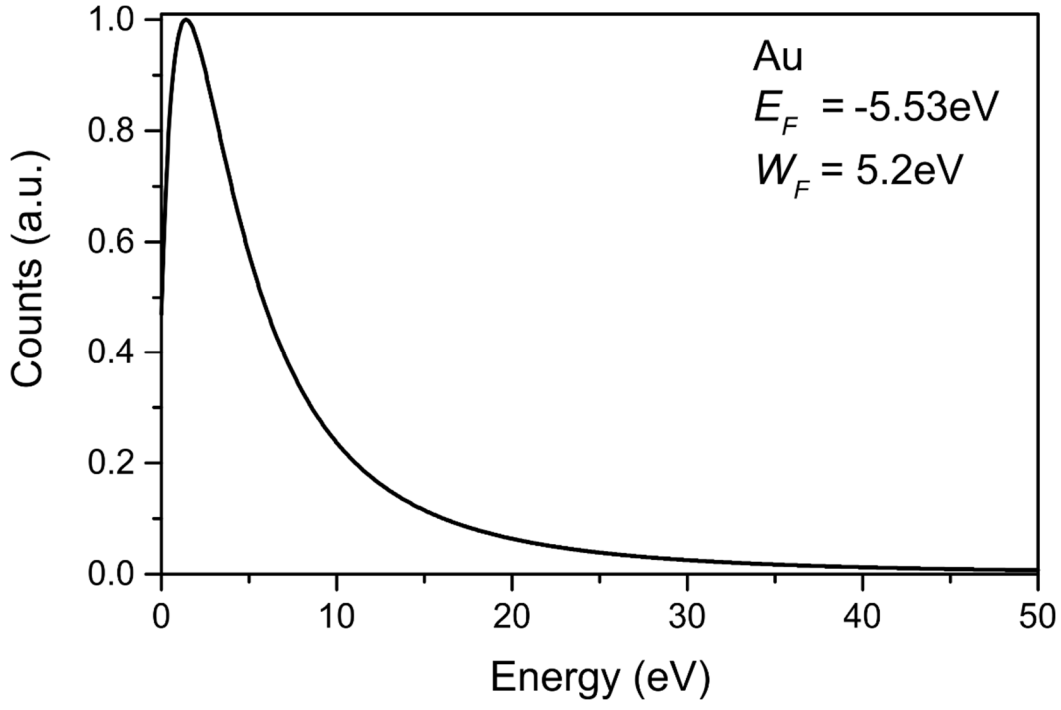

Figure 2.10. Secondary electron energy spectrum for Au. Note that the energy is referenced to the vacuum level.

As SE are generated by inelastic collisions of the primary electron within a material, there is the possibility that multiple SE will be generated for a given primary electron. This is deemed the SE yield, $\delta = i_{SE} / i_p$, where i_{SE} is the measured SE current and i_p is the primary electron beam current. The SE yield increases for increasing E_p until a maximum δ_m is reached, at which point δ decreases for increasing E_p. The increase at low E_p is attributed to the primary electrons penetrating farther into the material and thus exciting more SE. Due to their low energy, SE have a very low escape depth, meaning that only SE excited within the escape depth will be able to reach the surface of the material and contribute to the measured i_{SE}. As such, at a certain value of E_p, the penetration depth of the primary electron exceeds the escape depth of the SE, leading to a reduction in δ [56]. The escape depth of most metals is ~0.5-1.5 nm with a maximum escape depth of ~5 nm [55]. To calculate δ, a few assumptions must be made [57]:

1. The number of SE generated in a material is determined by the energy loss per unit length of the primary electron along its path ($-dE_k / dx$) divided by the energy required to produce a single SE (Ω_{SE}).
2. The probability of a SE produced at depth x reaching the surface is given by $\exp(-\alpha x)$, where α is the inverse extinction length.
3. The escape probability for SE leaving the surface is B_{SE}.
4. The constant loss approximation is used for the primary electrons. This assumes that the average loss of primary energy is independent of the depth, i.e. $dE_k / dx = -E_p / R$, where R is the primary electron penetration depth. This accounts for the angular scattering of the primary electron beams once they have penetrated the material.

5. The penetration depth, *R*, is determined by primary electrons that do not undergo angular scattering and follows a power law, i.e. $dE_k / dx = -\Gamma / E_k^{b-1}$, where Γ is a material constant determined from experiment, and *b* is experimentally determined to be ~1.35 for E_p < 10keV. [58]

From these assumptions, the secondary electron yield is given by [56]:

$$\delta(E_p) = B_{SE} \times \frac{E_p}{\Omega_{SE} R} \times (1 - e^{-\alpha R}) / \alpha \tag{2.42}$$

It has been found that there is a somewhat universal curve for δ as a function of E_p that is normalized to the peak values. The equation governing this universal curve is [56]:

$$\frac{\delta}{\delta_m} = \exp\left[-\frac{\left(\ln \frac{E_p}{E_m} \right)^2}{2\sigma_{yield}^{\ 2}} \right] \tag{2.43}$$

Where δ_m is the value of the maximum SE yield, E_m is the kinetic energy value that δ_m occurs at, and σ_{yield} has a value of 1.6. Figure 2.11 depicts the theoretical universal SE yield as a function of E_p for a Au film using parameters from [55]. The value of δ_m and the corresponding E_m for some common metals are listed in Table 2.1. Notably, experimental values reported for E_m and δ_m vary significantly between published works. For example, the value of E_m for Au has been reported ranging from 300 eV up to 875 eV [55,59,60].

It also important to understand how the yield changes with the primary electron beam angle of incidence. Due to the short escape depth of SE, the SE yield increases at

oblique angles. This is due to the fact that a large portion of the primary electron penetration depth is now projected parallel to the surface of the material (within the SE escape depth) as opposed to normal to it (beyond the SE escape depth). The adjusted SE yield is given by [55]:

$$\delta(\theta) = \delta_0(\cos\theta)^u \tag{2.44}$$

Where, δ_0 is the SE yield at normal incidence, θ is measured from the normal to the surface, and u is found to be ~1.3 for materials with atomic number, Z, < 30, and ~0.8 for Z > 30 [55].

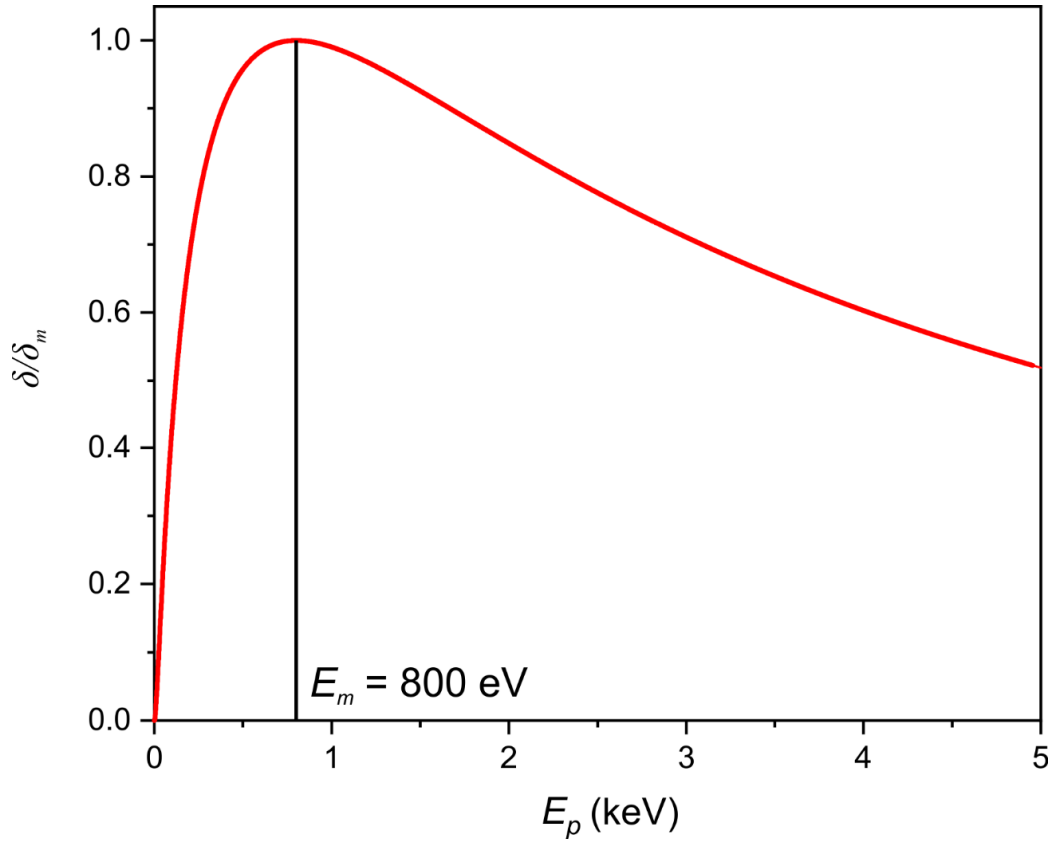

Figure 2.11. Secondary electron yield for an Au film as a function of primary electron energy, E_p.

Atom	Z	δ_m	E_m (eV)
Al	13	0.9 – 1.0	250 – 300
Ti	22	0.7 – 0.9	300
Cr	24	1.0	470
Cu	29	1.1 – 1.3	500 – 600
Ag	47	1.2 – 1.4	700 – 800
Pt	78	1.35 – 1.7	700 – 750
Au	79	1.2 – 1.6	700 – 875

Table 2.1. Maximum of SE yield, δ_m, and the corresponding kinetic energy, E_m for common metals. Adapted from [55].

To determine the angular distribution of the SE electrons, one can consider the situation depicted in Fig. 2.12. Here, the primary electron is assumed to be impinging normal to the surface. A portion of the SE current, di_{SE}, originates from a point along the path of the primary electron location, dx, and travels to the surface along the path l at an angle θ. The internal SE distribution is assumed to be isotropic such that di_{SE} is independent of angle. The SE must then traverse a distance of $l = x / \cos\theta$. The SE yield as a function of angle is then given by [61]:

$$\delta(\theta) = (K/2)\int_0^R (dE/dx)\exp[-\alpha x/\cos\theta]dx \tag{2.45}$$

Where K is a constant. This can be integrated to achieve:

$$\delta(\theta) = (K/2g)(CA/\alpha)^{1/g}(f_p'(A') + \eta f_b'(A')) \tag{2.46}$$

Where g is a fitting parameter depending on the energy range of E_p [61], C is the energy range coefficient, $A = (\alpha/C)E_p^g$, $A' = A/cos\theta$, f_p' is the contribution to the SE from the primary electrons, f_b' is the contribution from the backscattered electrons, η is the backscatter coefficient, and with:

$$f_p'(A') = \int_0^1 [\exp(-A'y) / g(1-y)^{-1/g+1}]dy$$
$$f_b'(A') = \int_0^{1/2} [\exp(-A'y) / g(\Phi^g + y)^{-1/g+1}]dy \quad (2.47)$$

Where $y = x / R$ is the reduced penetration depth, and $\Phi = 0.45 + 2\times10^{-3}Z$ is the relative mean energy of the backscattered electrons. Using equations (2.46) and (2.47), and the fact that the peak yield (δ_m) is related to the primary energy at the peak yield (E_m) by $\delta_m / E_m = 2.4\times10^{-3}\text{eV}^{-1}$ the normalized angular distribution for SE is as follows:

$$\delta(\theta) / \delta_m = (26.2 / g)(E_p / E_m)(f_p'(A') + \eta f_b'(A')) \quad (2.48)$$

From equation (2.48), the angular distribution approximates a cosine distribution as depicted in Fig. 2.13. The curve in Fig. 2.13 uses parameters from [61] for an Au film and assumes E_p is 300 eV. Furthermore, the angular distribution of SE is found to be essentially independent of E_p and angle of incidence [62].

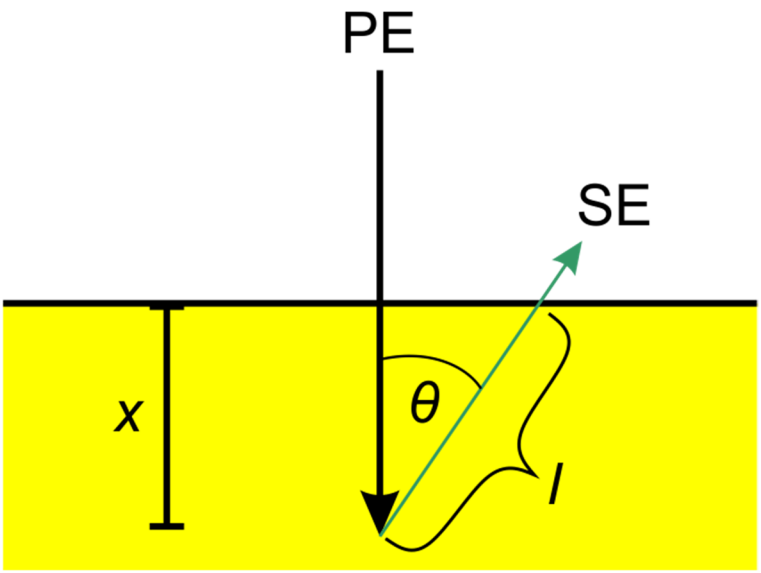

Figure 2.12. Schematic depiction of secondary electron angular distribution. PE is the primary electron and SE is the generated secondary electron.

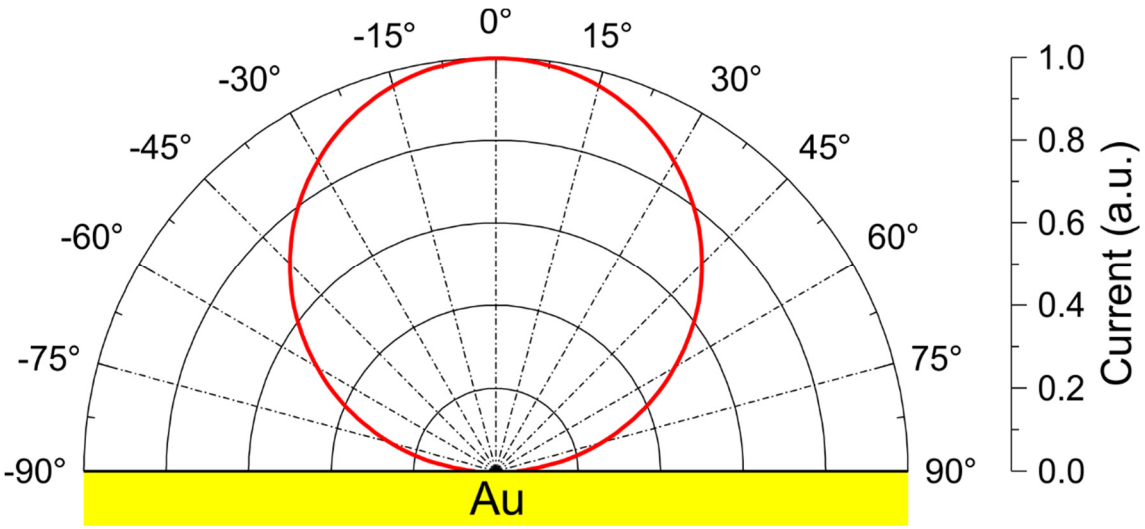

Figure 2.13. Secondary electron angular distribution indicating a cosine-like distribution.

2.6. Electron Acceleration in a Surface Plasmon Field

Now that multiple methods of electron generation have been discussed, it is essential to understand how these free electrons will interact with the surface plasmon fields present at the metal-vacuum interface. One of the characteristic behaviours of a surface plasmon mode is the tight confinement of the electromagnetic radiation to this interface. This is evidenced by the fact that the electric field of the surface plasmon decays exponentially away from the metal film in the normal direction. This high confinement gives rise to two very interesting phenomena, electric field enhancement, and the ponderomotive force.

As the electric field exponentially decays from the metal film, this sets up a large spatial gradient in the strength of the electric field. It is this spatial gradient that produces acceleration of free electrons. On the positive half-cycle of the electric field, electrons will be accelerated while on the subsequent negative half-cycle, the electrons will be

decelerated. In a spatially homogeneous electric field, over multiple cycles, this acceleration and deceleration will cancel out resulting in no net increase or decrease of the kinetic energy of the electron.

For a spatially inhomogeneous electric field, such as that of a surface plasmon, the result is significantly different. During the positive half-cycle, the electrons are accelerated from areas of high electric field to areas of lower electric field, i.e. along the gradient of the field. In addition, due to the high electric field strength, the electron traverses to the area of lower electric field faster than the electric field polarity can reverse. As such, on the negative half-cycle, the electron will be decelerated, but by an amount less than it was accelerated on the positive half-cycle, resulting in a net acceleration over a single cycle. Over multiple cycles, this acceleration accumulates, resulting in a significant increase in the electron kinetic energy, as well as the electron being guided from an area of high electric field (close to the metal-vacuum interface) towards an area of lower electric field (away from the interface into vacuum). Effectively the electron is 'pushed' farther towards an area of weaker field strength during the positive half-cycle than it is 'pulled' back during the negative half-cycle. This is schematically depicted in Fig. 2.14. This interaction is referred to as ponderomotive electron acceleration and constitutes one of the major sources of electron acceleration during laser-electron interaction.

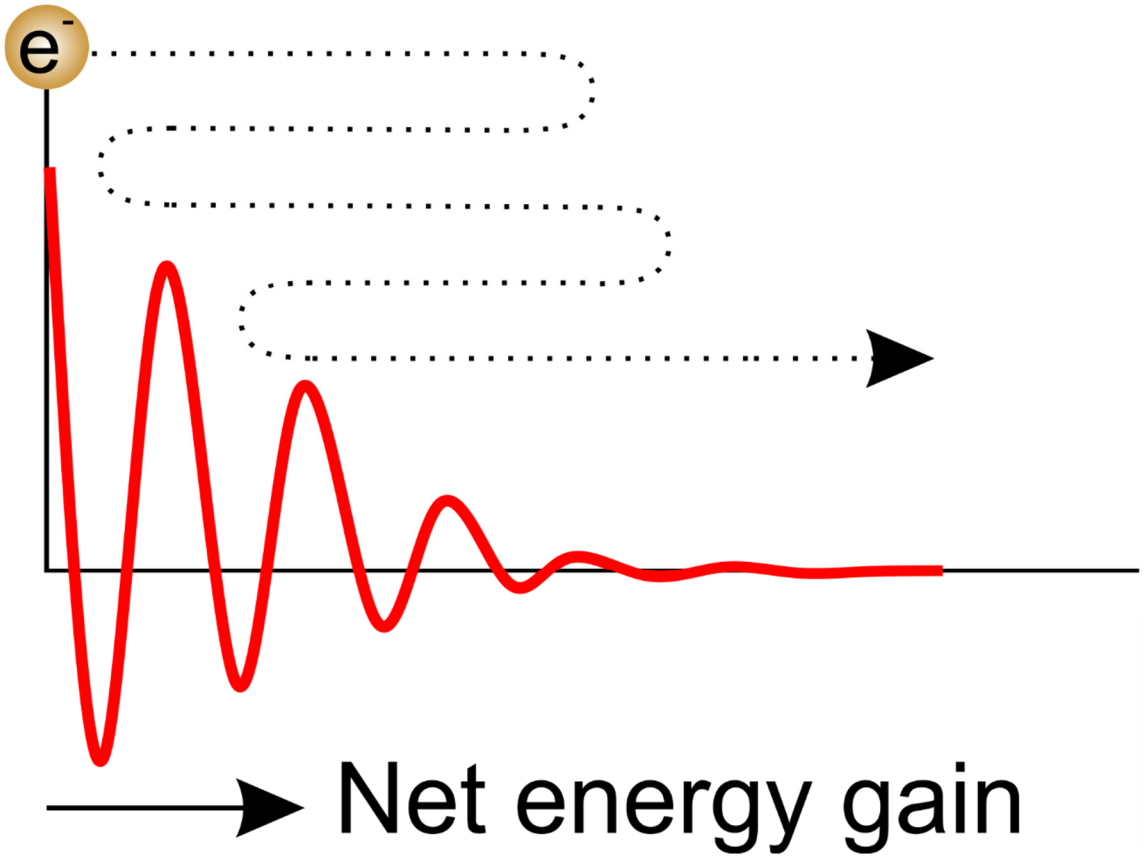

Figure 2.14. Schematic depiction of cycle-by-cycle ponderomotive electron acceleration in an SP field.

The ponderomotive force can be derived by considering the equation of motion for an electron placed in an oscillating electric field, i.e. the Lorentz force:

$$\frac{dv}{dt} = -\frac{q}{m_e}\left[\vec{E} + \vec{v} \times \vec{B}\right] \tag{2.49}$$

Where $\vec{v}$ is the velocity of the electron. Initially, only the electric field is considered as a first order contribution and then the magnetic field contribution is introduced as a second order perturbation. Assuming that the oscillating electric field has the form $\vec{E} = \vec{E}_0(r)cos(\omega t)$, the first order Lorentz force is:

$$\frac{d\vec{v}_1}{dt} = \frac{-q}{m_e} E_0(\vec{r}_0) cos(\omega t) \tag{2.50}$$

Which can be integrated to obtain the velocity

$$\vec{v}_1 = -\frac{q}{m_e \omega} \vec{E}_0(\vec{r}_0) \sin(\omega t) \tag{2.51}$$

And the incremental change in position is then:

$$\delta\vec{r} = \frac{q}{m_e \omega^2} \vec{E}_0(\vec{r}_0) cos(\omega t) \tag{2.52}$$

Next, the second order contribution of the magnetic field can be introduced by using Maxwell's equation to yield:

$$\vec{B}_1 = -\frac{1}{\omega} \nabla \times \vec{E}_0(\vec{r}_0) \sin(\omega t) \tag{2.53}$$

The second order Lorentz force equation is given by:

$$\frac{d\vec{v}_2}{dt} = -\frac{q}{m_e} \left[(\delta\vec{r}_1 \cdot \nabla)\vec{E} + v_1 \times \vec{B}_1 \right] \tag{2.54}$$

Substituting equations (2.51) to (2.53) in to equation (2.54) yields:

$$\frac{d\vec{v}_2}{dt} = -\frac{q^2}{m_e^2 \omega^2} \begin{bmatrix} ((\vec{E}_0(\vec{r}_0) cos(\omega t)) \cdot \nabla)\vec{E}_0(r) cos(\omega t) \\ +(-\vec{E}_0(\vec{r}_0) sin(\omega t)) \times (-\nabla \times \vec{E}_0(\vec{r}_0) sin(\omega t)) \end{bmatrix} \tag{2.55}$$

The high frequency $\sin^2(\omega t)$ and $\cos^2(\omega t)$ terms are time-averaged to yield ½, resulting in the rearranged form of:

$$\left\langle \frac{d\vec{v}_2}{dt} \right\rangle = -\frac{q^2}{2m_e^2 \omega^2} [(\vec{E}_0 \cdot \nabla)\vec{E}_0 + \vec{E}_0 \times (\nabla \times \vec{E}_0)] \tag{2.56}$$

The vector identity $\nabla E_0^2 = 2(\vec{E}_0 \cdot \nabla)\vec{E}_0 + \vec{E}_0 \times (\nabla \times \vec{E}_0)$ can be used to reduce the right hand side of equation (2.56) to a single term:

$$\frac{d\vec{v}_2}{dt} = -\frac{q^2}{4m_e^2\omega^2}\nabla E_0^2 \tag{2.57}$$

Which results in the final expression for the ponderomotive force:

$$F_{pond} = -\frac{q^2}{4m_e\omega^2}\nabla E_0^2 \tag{2.58}$$

And the corresponding ponderomotive potential

$$U_{pond} = \frac{q^2}{4m_e\omega^2}E_0^2 \tag{2.59}$$

From equations (2.58) and (2.59), it can be concluded that for a large ponderomotive interaction, high electric field strengths, as well as, steep gradients are favoured. Therefore, the high spatial confinement of SP waves affords an ideal environment for ponderomotive acceleration. It can also be concluded that the ponderomotive force scales with the wavelength of the driving laser light.

Chapter 3

Theoretical Control and Tailoring of Electron Pulses

3.1. Introduction

In this chapter, numerical simulations are presented that explore various methods to control and tailor SP generated electron pulses. The first section introduces the theoretical model used for these simulations and discusses additions that were necessary to include THz electric fields. The following sections present results that were obtained using this model that demonstrate the application of external THz electric fields for kinetic energy and angular tuning of SP generated electron pulses. The final section introduces multiple filtering techniques to achieve attosecond electron pulses with ~0.5 keV kinetic energy.

3.2. Particle Tracking Model

This section describes the theoretical model used to simulate the interaction of free electrons with intense laser and surface plasmon fields both in materials and in vacuum. The model implemented consists of a two-step algorithm. First, electromagnetic (EM) fields are calculated using the commercial finite-difference-time-domain (FDTD) software package *FDTD Solutions* from *Lumerical Inc.* [63]. Next, test electrons are tracked in space and time as they interact with the FDTD calculated fields. A description of the MATLAB source code and the overall flow of the particle tracking simulation can be found in Appendix A.

3.2.1. Electron Interaction with Electromagnetic Fields

The particle tracking code is a fully home-developed program using MATLAB and can be broken down into two major components. The first component is the generation of the electrons before they interact with the electromagnetic fields, and the second component is the interaction of the generated electrons with the EM fields.

The source of electrons within my particle tracking code can take several forms and will be described below. Each source calculates the electron's initial position, velocity, starting time and statistical weight. The statistical weight is implemented to sample the behaviour of the electrons without having to simulate a large number of electrons. For this reason, the weight is a relative probability of an electron possessing that specific characteristic.

The most common electron source used is the plasmon source. This source represents electrons that are freed from a material through multi-photon ionization (MPI). As such, their weight will be dependent on the multi-photon absorption probability of the material which is proportional to $I_{SP}^{m}(x, y, z, t)$, where m is the order of the emission process (typically 3 for Ag, and 4 for Au), and I_{SP} is the intensity of the SP field. The MPI electrons may also possess initial kinetic energies from the multiphoton absorption given by equation (2.37). This excess kinetic energy is randomly directed away from the metallic film, as depicted in Fig. 3.1(a). The electrons are placed along the metallic film's surface and their initial starting time is typically set to correspond to the peak of the SP electric field. This electron source can also be used to model multi-photon absorption within a material such as two-photon absorption in Si (see results presented in Chapter 5) or eC (see eC/Au bilayer in Chapter 4).

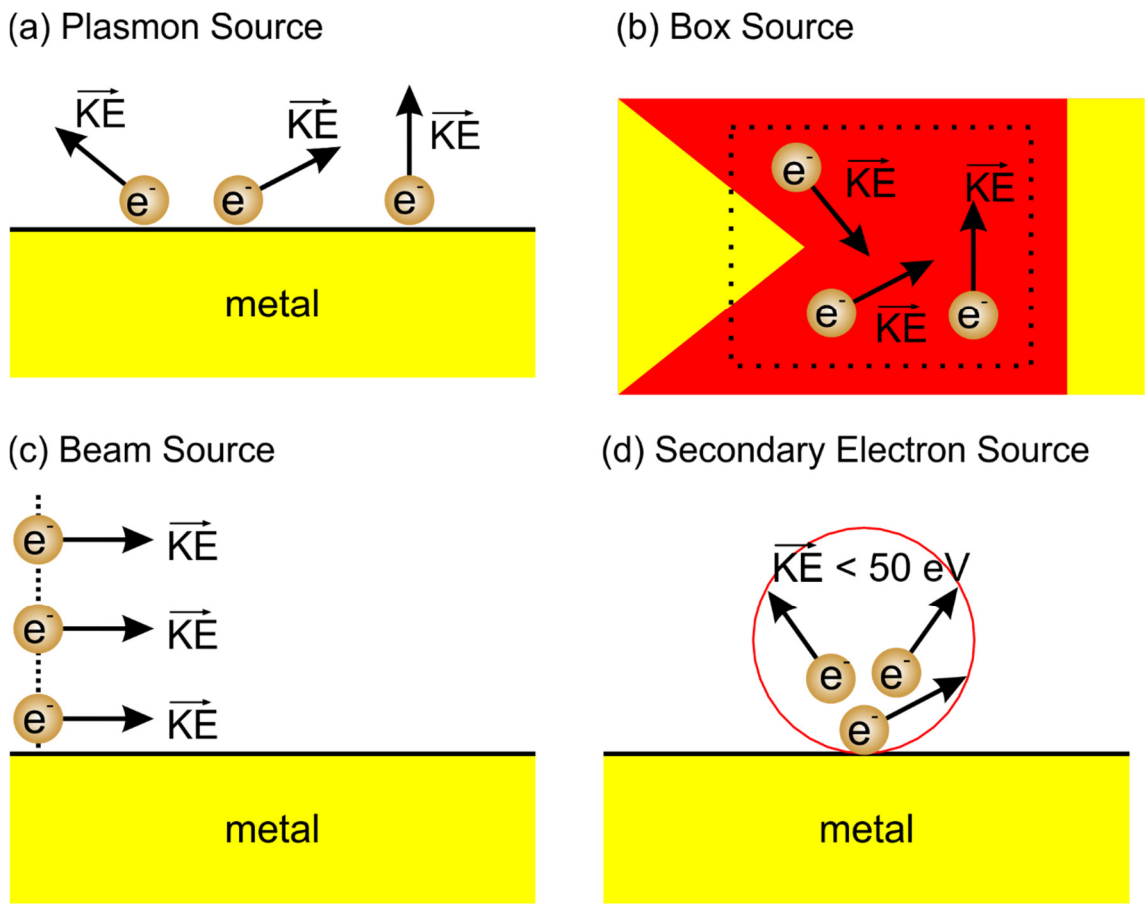

Figure 3.1. Schematic depictions of the different types of electron sources available. (a) Surface plasmon source where electrons are ejected from the metal via multi-photon ionization. (b) Box electron source where electrons are injected within the dotted box region. (c) Beam source whose electrons are distributed in a plane and are all directed along the same direction. (d) Secondary electron source where electrons are injected with kinetic energies <50 eV and are directed in a cosine angular distribution (red circle).

The simplest source of electrons is the so-called "box source," depicted in Fig. 3.1(b). Here, free electrons are placed within a defined spatial box, 2D or 3D where appropriate, within the simulation region. The electron's initial position, starting time, and velocity can be randomized or set as needed. As the physical source of these electrons is ambiguous, they are assigned a statistical weight of 1. This source is useful for modelling electrons within a material.

The next source is an electron beam source, useful in modelling a continuous electron beam such as that used for the electron beaming experiments presented in Chapter 4. Figure 3.1(c) depicts this source which introduces a plane of electrons having a given velocity and direction that are injected at times specified. To emulate a continuous electron beam, electrons are injected at equally spaced times throughout the entire duration of the simulation. As each electron is identical to the others within the electron beam, they are assigned a weight of 1.

The final electron source that was required for the electron beaming simulations was the secondary electron source, depicted in Fig. 3.1(d). SE electrons are generated with initial kinetic energies up to 50 eV, with their initial angular direction corresponding to a cosine distribution. As such, their weight is proportional to $\frac{E_{SE} - E_F - W_F}{(E_{SE} - E_F)^4} \times \cos\theta$, where θ is the angle measured from the surface normal (See Chapter 2 for more details on characteristics and theory of SE). Again, to emulate the effect of continuous SE emission, these electrons are generated at equally spaced times throughout the simulation.

Once the electrons have been introduced to the simulation region, they must be tracked as they interact with the electromagnetic fields from the FDTD simulation. This interaction is modelled through the non-relativistic equation of motion for the Lorentz force:

$$\frac{d\vec{v}}{dt} = \frac{q}{m_e}(\vec{E} + \mu_0 \vec{v} \times \vec{H}) \tag{3.1}$$

Equation (3.1) is discretized using finite difference and the particle-tracking code steps through time to calculate the position and velocity at the same time steps that the FDTD

fields were calculated at. Because the FDTD fields are discretized in space, linear interpolation is implemented to calculate the fields at the specific positions of the various test electrons. It is important to note that the particle tracking code does not include any electron-electron interactions and thus can only be used for simulations below the space charge limit.

The THz fields necessary for the simulations presented in following sections are included by appending the THz field terms to equation (3.1). The updated equation of motion becomes:

$$\frac{d\vec{v}}{dt} = \frac{q}{m_e}[\vec{E}_{SP} + \vec{E}_{THz} + \mu_0 \vec{v} \times (\vec{H}_{SP} + \vec{H}_{THz})] \tag{3.2}$$

Where $\vec{E}_{SP}$, $\vec{H}_{SP}$ are the FDTD calculated fields, and $\vec{E}_{THz}$, $\vec{H}_{THz}$ are the analytically calculated THz fields. For all simulations considered in this thesis, the THz electric field pulse is assumed to be a single-cycle pulse centred around $\lambda_{THz} = 600$ μm and having a pulse duration of 1 ps. Figures 3.2(a) and 3.2(b) depict the THz signal in the time domain and frequency domain, respectively. Due to the wavelength and timescale of the THz electric field being significantly larger than that of the SP field, the THz electric field is implemented analytically as opposed to being calculated via FDTD. A spatial gaussian with a full-width at half-maximum (FWHM) diameter of 600 μm is assumed. The equation for the THz electric field is given by:

$$E_{THz}(r,t) = -2\frac{t - t_{center}}{2\Delta t_{THz}} \exp\left[\frac{-(t - t_{center})^2}{2\Delta t_{THz}^2}\right] \exp\left[\frac{-r^2}{2\sigma_{THz}^2}\right] \tag{3.3}$$

Where t is the time, t_{center} is the time of the center of the THz electric field pulse, Δt_{THz} is the THz electric field sideband, r is the spatial coordinate, and σ_{THz} is the spatial FWHM parameter.

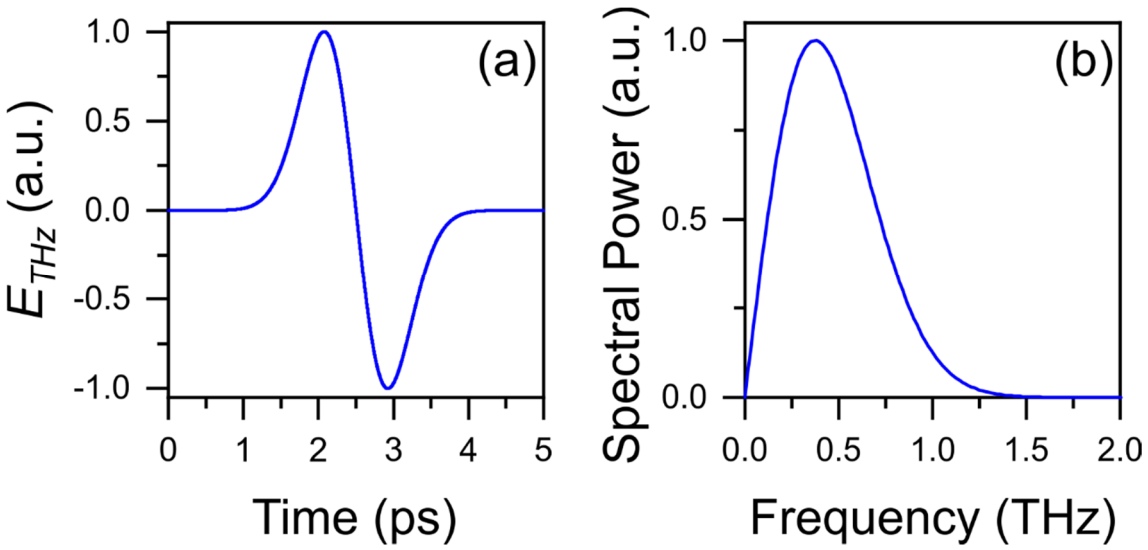

Figure 3.2. (a) Time domain trace of the single cycle THz electric field pulse used for particle tracking simulations and (b) corresponding frequency domain spectrum.

3.3. Terahertz Electric Field Control and Acceleration of Surface Plasmon Generated Electrons

This section explores the use of THz electric fields in various configurations to control and tailor surface plasmon generated electron beams through detailed model calculations. While SP based electron beam generation has shown great strides towards creating high energy electron beams, these are inherently broadband, possessing a large range of kinetic energies. This, in turn, makes the beams less desirable for ultrafast electron pulse applications. Yet, it has proven very challenging to control and tune the various characteristics of the generated electron beam, such as peak kinetic energy, kinetic energy spread, angular directivity, and angular spread. This lack of control arises from the electrons being photogenerated at different spatial and temporal phases within

the SP field. As such, each electron experiences a different temporal acceleration profile ultimately resulting in a wide spread of kinetic energies and emission angles. For the next generation of SP based electron sources, it is crucial to find a mechanism that can modify the trajectory of each electron on an ultrafast timescale to tailor the resulting ultrafast electron pulse for its intended application. In addition, generating high kinetic energies, > 500 eV, requires electric fields strengths approaching the material damage threshold. Therefore, it is beneficial to decrease the optical electric field and introduce a secondary source of acceleration. To satisfy these stringent requirements, an all-optical technique is necessary.

THz electric field pulses represent a unique approach for acceleration and manipulation of electron pulses. The difference in wavelength ($\lambda_{THz} >> \lambda_{SP}$) allows the THz electric field, E_{THz}, to interact with the electron pulse in a quasi-static manner over the length scale of interest. Due to the timescale mismatch between E_{THz} and E_{SP} (picoseconds vs. femtoseconds), the electrons will interact with the slowly-varying E_{THz} and either be accelerated or decelerated, dependent on their initial phase with respect to the SP field. Furthermore, as the THz electric field pulse can be generated from the same laser as the optical pulse, low jitter timing synchronization can be achieved between the SP generated electron pulse and the THz electric fields, providing ultrafast control. This all-optical THz electric field control not only provides the tuning of kinetic energy to a specific range, but also facilitates the generation of high energy electron pulses possessing narrow kinetic energy bands, while simultaneously maintaining a low incident optical field below the material damage threshold. The angular directivity and spread can also be controlled, allowing for active steering of ultrafast electron beams.

3.3.1. Single Terahertz Electric Field Pulse Control[1]

The first configuration that was investigated was a single THz electric field pulse acting on the electrons that are generated from SP waves in the Kretschmann geometry, as depicted in Fig. 3.3(a). The geometry consists of a 50 nm Ag film on the hypotenuse side of a silica prism. A 30 fs duration optical pulse, with peak electric field strength E_{laser}, centred at λ_{laser} = 800 nm is coupled from the prism side to the vacuum side of the Ag film as a surface plasmon wave with peak electric field, E_{SP}. Here, electrons are generated through multi-photon absorption. Subsequently, the ejected electrons experience a cycle-by-cycle acceleration as they quiver in the E_{SP} field (Fig. 3.3(b)-(c)), allowing them to either gain or lose kinetic energy.

The peak of the first half-cycle of the THz electric field pulse coincides with the peak of the optical pulse in time. Test electrons are introduced and allowed to interact with both E_{SP} and E_{THz}. Here, electrons are accelerated in a fixed E_{SP} of 5×10^8 V/cm and are collected 1 mm away from the Ag film for various E_{THz} field strengths and initial polarities.

In the absence of E_{THz}, the majority of accelerated electrons are emitted perpendicular to the Ag film, as shown in Fig. 3.3(a). Therefore, the initial polarity of the E_{THz} is crucial in determining the optimal configuration for achieving kinetic energy and ejection angle tuning. The two configurations that are investigated are: $E_{THZ}^{(+)}$ and $E_{THZ}^{(-)}$, as depicted in Fig. 3.3(b), where the superscript indicates the initial polarity. $E_{THZ}^{(+)}$ and

[1] A version of this section has been published as S.R. Greig and A.Y. Elezzabi, "On the Role of Terahertz Field Acceleration and Beaming of Surface Plasmon Generated Ultrashort Electron Pulses," *Appl. Phys. Lett.* **105**, 041115 (2014).

$E_{THZ}^{(-)}$ are 180° out of phase with respect to each other. At E_{SP} = 5×10^8 V/cm, and with no E_{THz} present, electrons are accelerated to a peak kinetic energy of 180 eV (FWHM of 300 eV). Introducing a THz pulse with field strength ~ 10^5-10^6 V/cm significantly alters the situation.

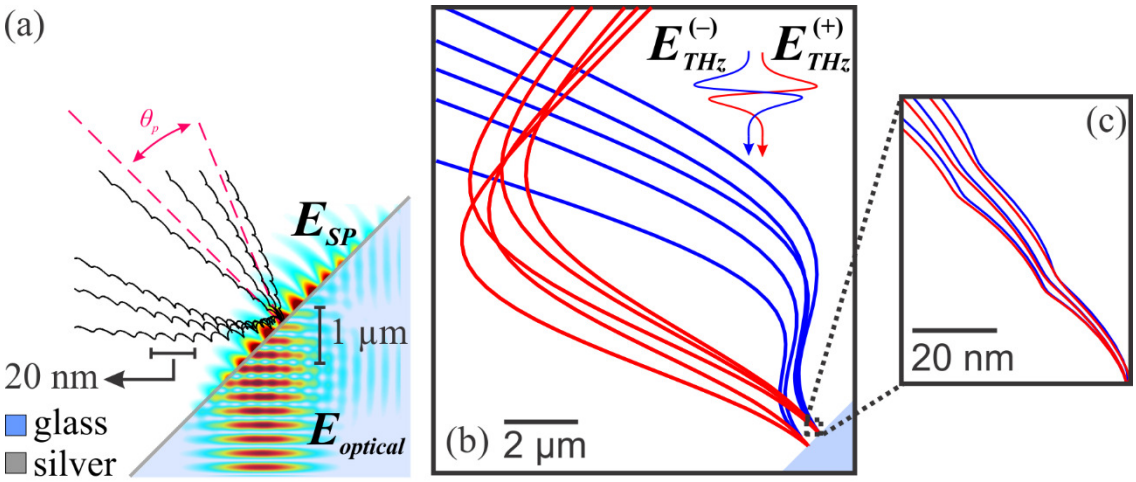

Figure 3.3. (a) Schematic depiction of Kretschmann configuration with a 50 nm Ag film on hypotenuse side of a glass prism. E_{laser} is the electric field of the incident 30 fs pulse. E_{SP} is the electric field of the excited surface plasmon. θ_p is the pitch angle, subtended to the normal of the metal film, of the emitted electrons. The black lines show representative electron trajectories due to acceleration from E_{SP} = 5×10^8 V/cm, with ~10 nm between inflection points as they quiver in the field. The 1 μm scale bar corresponds to the E_{SP} and E_{laser} electric fields. The 20 nm scale bar corresponds to the electron trajectories (black lines). (b) The $E_{THZ}^{(+)}$ and $E_{THZ}^{(-)}$ pulses represent the different initial starting polarity for the applied THz electric field. The red and blue curves depict representative electron trajectories for $E_{THZ}^{(+)}$ and $E_{THZ}^{(-)}$ = 3×10^6 V/cm, respectively. Electrons directed to the right (red lines) are under the influence of $E_{THZ}^{(+)}$. Electrons directed to the left are under the influence of $E_{THZ}^{(-)}$ (blue lines). (c) Magnified electron trajectories under the influence of $E_{THZ}^{(+)}$ and $E_{THZ}^{(-)}$, as they quiver in both the E_{SP} and E_{THz} electric fields.

The kinetic energy spectra for various $E_{THZ}^{(+)}$ field strengths are depicted in Fig. 3.4(a). When $E_{THZ}^{(+)} \approx< 1\times10^6$ V/cm, the force on the electrons from the first half-cycle of $E_{THZ}^{(+)}$ acts to further accelerate the E_{SP} accelerated electrons outward, away from the Ag film (i.e. acting with the ponderomotive force of the plasmonic field), while the second half-cycle attempts to decelerate the electrons and direct them back toward the Ag film. However, during this second half-cycle, the E_{SP} has propagated to a different location along the Ag film and thus the electrons experience only the force due to $E_{THZ}^{(+)}$. As such, these electrons experience a net decrease in their kinetic energy from the time-varying ponderomotive potential and the 'quasi-static' potential from the THz field. However, when $E_{THZ}^{(+)} > 1\times10^6$ V/cm, the whole spectrum translates to higher energies (peaks at 0.49 keV (FWHM of 0.27 keV) for $E_{THZ}^{(+)} = 3\times10^6$ V/cm). Here, a combination of E_{SP} and the first half-cycle of $E_{THZ}^{(+)}$ alters the trajectory of the electron such that it is nearly perpendicular to $E_{THZ}^{(+)}$, thus reducing the force experienced due to the second half-cycle of the THz electric field. This allows the electron to retain a greater portion of its kinetic energy gained during the first half-cycle. Exemplary trajectories are depicted in Fig. 3.3(b).

Reversing the polarity of the E_{THz} (i.e. from $E_{THZ}^{(+)}$ + to $E_{THZ}^{(-)}$) produces more interesting results. The kinetic energy spectra at various $E_{THZ}^{(-)}$ are depicted in Fig. 3.4(b). For this configuration, the first half-cycle of $E_{THZ}^{(-)}$ forces the electrons back towards the metal film (i.e. acting against the ponderomotive force), thus allowing them to experience the ponderomotive force over a greater number of E_{SP} cycles. Acting in opposition to the

first half-cycle of $E_{THZ}^{(-)}$, the ponderomotive force prevents the electrons from reaching the metal. This allows the electrons to be accelerated on the subsequent second half-cycle of $E_{THZ}^{(-)}$ to higher kinetic energies. At the same E_{SP} field, higher peak kinetic energies up to 1.56 keV (FWHM of 0.5 keV) are realized, without the inherent broadband energy spectrum typically associated with E_{SP} accelerated electrons. Notably, to achieve similar energy results from E_{SP} acceleration alone would require the E_{SP} field strength to be 5× higher, while producing an extremely broad FWHM of 1.8 keV [64].

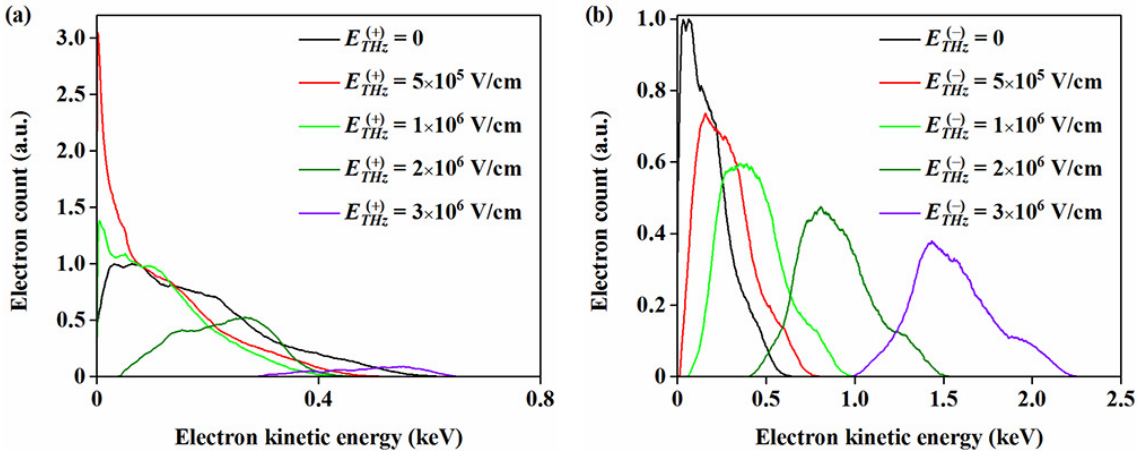

Figure 3.4. Electron kinetic energy spectra calculated at detector located 1 mm away from the Ag film at a fixed $E_{SP} = 5\times10^8$ V/cm and at various: (a) $E_{THZ}^{(+)}$ and (b) $E_{THZ}^{(-)}$ field strengths. Note the kinetic energy scale difference between (a) and (b).

At high $E_{THZ}^{(-)}$ strengths, the peak kinetic energy for $E_{THZ}^{(-)}$ is ~3× higher than that of $E_{THZ}^{(+)}$, as depicted in Fig. 3.5. While the electron's kinetic energy tunability can be demonstrated via the application of E_{THz}, a crucial factor to consider is the fraction of electrons that reach the detector, ψ. Fig. 3.5 depicts ψ as a function of E_{THz}. For $E_{THZ}^{(+)}$, ψ decreases significantly for increasing $E_{THZ}^{(+)}$ where only 7% of the electrons are collected

for $E_{THZ}^{(+)}$ = 3×10^6 V/cm. This is because electron trajectories are being increasingly directed parallel to the Ag film and therefore either miss the detector or collide with the Ag film. On the contrary, for $E_{THZ}^{(-)}$, 72% of the electrons are collected for $E_{THZ}^{(-)}$ = 3×10^6 V/cm. This increase in collected electrons is directly attributed to the E_{SP} field acting in unison with $E_{THZ}^{(-)}$ during the first half-cycle of $E_{THZ}^{(-)}$.

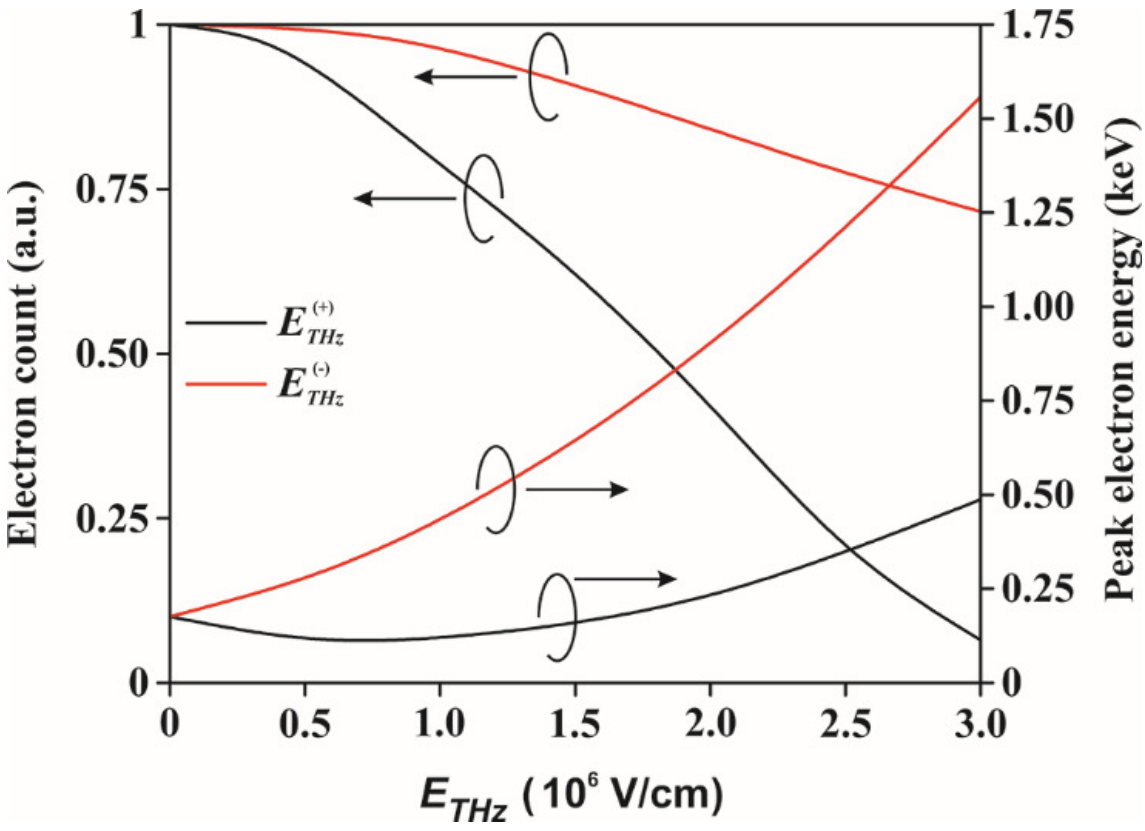

Figure 3.5. Electron count and peak electron kinetic energy at detector, at a fixed E_{SP} = 5×10^8 V/cm.

The introduction of E_{THz} also affords control over the trajectories of the electron pulse (Fig. 3.3(b)-(c)) and, hence, the pitch angle subtended normal to the metal film, θ_p.

Fig. 3.6 shows θ_p as a function of kinetic energy at $E_{THZ}^{(+)} = 0$, 5×10^5, 2×10^6, and 3×10^6 V/cm. The color bar represents the electron count at that specific kinetic energy and θ_p. The insets in Fig. 3.6 depict the total electron count versus θ_p. At $E_{THZ}^{(+)} = 0$ V/cm, the electrons exhibit a peak θ_p =10° with the majority of electrons spread between θ_p = -60° and θ_p = 20° (Fig. 3.6(a)). This angular spread and the location of the peak in the positive direction is due to the E_{SP} accelerating the electrons along its direction of propagation. By introducing $E_{THZ}^{(+)} = 5\times10^5$ V/cm, the location of the energy peak becomes θ_p = 20°, while maintaining a similar angular spread between θ_p = -50° and θ_p = 45° (Fig. 3.6(b)). Figure 3.6(c) depicts the peak θ_p = 58° for $E_{THZ}^{(+)} = 2\times10^6$ V/cm, with all of the electrons spread between θ_p = 55° and θ_p = 90°. At $E_{THZ}^{(+)} = 3\times10^6$ V/cm the majority of the electrons are now directed parallel to the Ag film surface, with electrons spread between θ_p = 80° and θ_p = 90° (Fig. 3.6(d)). The increase in θ_p as $E_{THZ}^{(+)}$ increases is due to the fact that during the first half-cycle of the THz pulse, $E_{THZ}^{(+)}$ is accelerating the electrons towards θ_p = -45°, in opposition to the E_{SP} field which is attempting to direct the electrons to θ_p = 10° (inset of Fig. 3.6(a)). As such, the first half-cycle works with the E_{SP} field to accelerate the electrons away from the metal film; therefore, the net θ_p is directed negative. Subsequently, during the second half-cycle of $E_{THZ}^{(+)}$, the E_{SP} field has propagated to a new region and now only the second half-cycle of $E_{THZ}^{(+)}$ is acting to decelerate the electron back towards the metal film. This deceleration results in increasing θ_p for increasing $E_{THZ}^{(+)}$ field strength up to the peak of nearly 90°, almost parallel to the Ag film, at $E_{THz}^{(+)} = 3\times10^6$ V/cm.

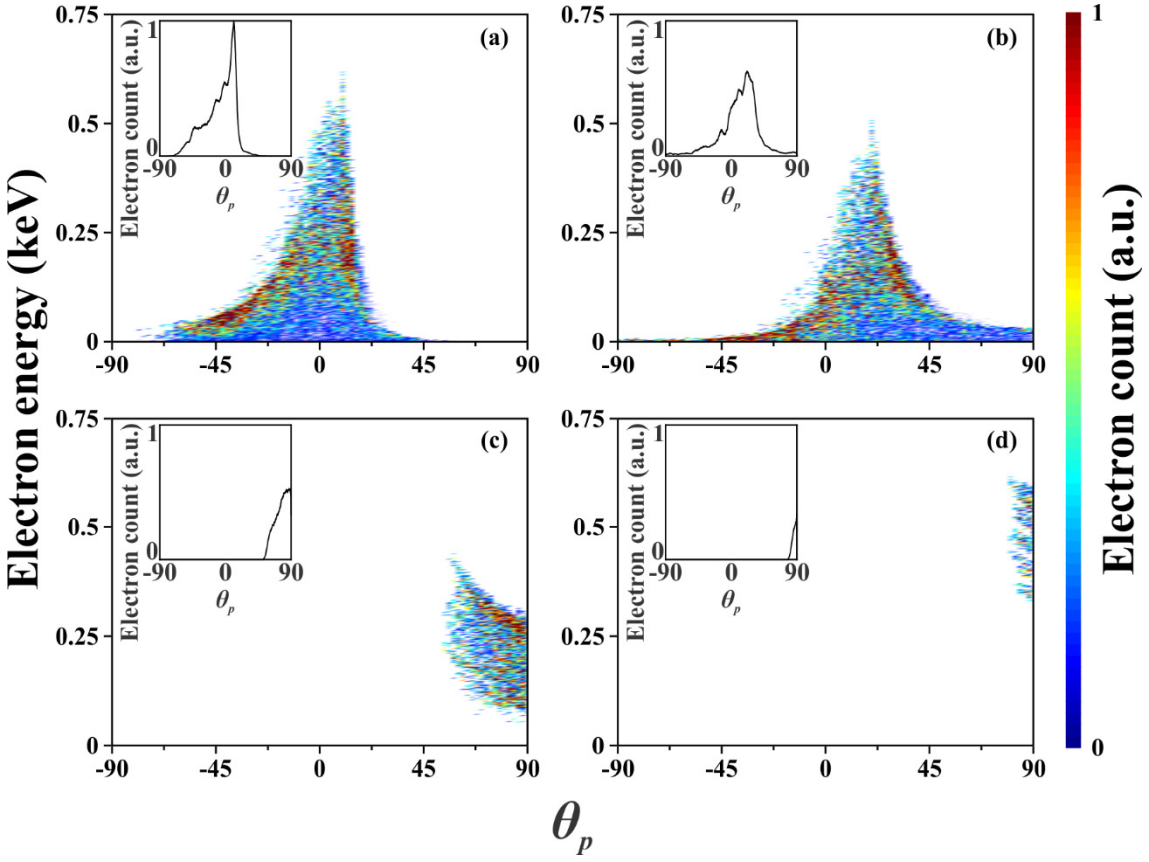

Figure 3.6. Electron kinetic energy as a function of pitch angle measured 1 mm away from the Ag film. Color represents the electron count. $E_{THZ}^{(+)}$ = (a) 0, (b) 5×10^5 V/cm, (c) 2×10^6 V/cm, (d) 3×10^6 V/cm. Insets show pitch angle versus electron count, normalized to $E_{THZ}^{(+)} = 0$.

Reversing the polarity of E_{THz} allows θ_p to be directed in the opposite direction. Figure 3.7 depicts θ_p as a function of kinetic energy at $E_{THZ}^{(-)} = 0$, 5×10^5, 2×10^6, and 3×10^6 V/cm. When $E_{THZ}^{(-)} = 5\times10^5$ V/cm, the energy peak is directed to $\theta_p = 2°$ with a reduced θ_p spread between $\theta_p = -50°$ and $\theta_p = 2°$. The kinetic energy also begins to reach higher energies (Fig. 3.7(b)). Figure 3.7(c) depicts that at $E_{THZ}^{(-)} = 2\times10^6$ V/cm, the majority of

electrons have gained an energy between 0.65 keV to 1.1 keV and are directed to a θ_p between θ_p = -45° and θ_p = -15° with the peak energy at θ_p = -15°. At $E_{THZ}^{(-)} = 3\times10^6$ V/cm, the electron's energy increases further to between 1.3 keV and 1.7 keV, while only slightly shifting θ_p between θ_p = -42° and θ_p = -22° (Fig. 3.7(d)), thus providing a narrower angular directivity. This angular control is shown in the insets in Fig. 3.7 and is attributed to the first half-cycle of $E_{THZ}^{(-)}$ that initially decelerates the electrons toward the Ag film within the range θ_p = -45° and θ_p = 10°. Here, the electrons reside in the E_{SP} field for a longer time and experience more cycles of the E_{SP} field. Subsequently, the second half-cycle accelerates the electrons away from the Ag film towards θ_p = -45°. This outward acceleration leads to a peak θ_p = -26.7° when $E_{THZ}^{(-)} = 3\times10^6$ V/cm.

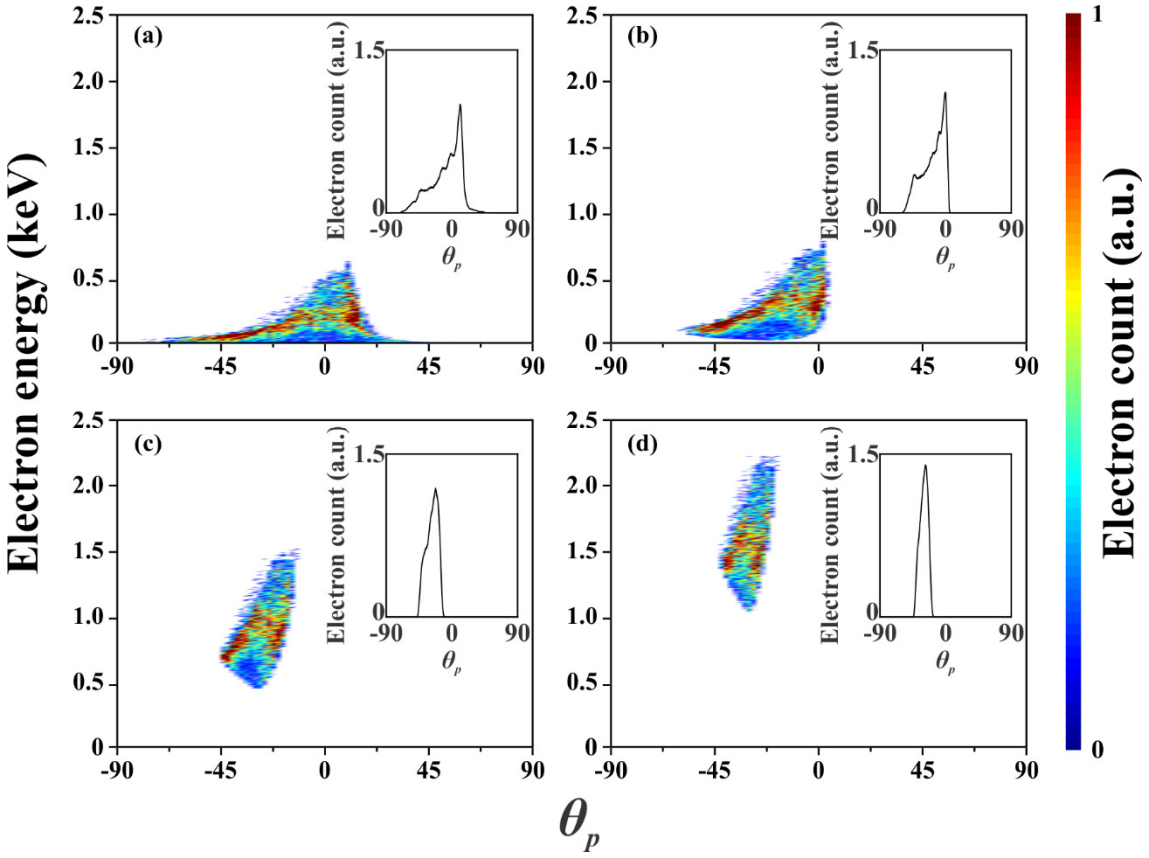

Figure 3.7. Electron kinetic energy as a function of pitch angle measured 1 mm away from the Ag film. Color represents the electron count. $E_{THZ}^{(-)}$ = (a) 0, (b) 5×10^5 V/cm, (c) 2×10^6 V/cm, (d) 3×10^6 V/cm. Insets show pitch angle versus electron count, normalized to $E_{THZ}^{(-)} = 0$.

Clearly, a single THz electric field pulse allows for tailoring of two of the generated electron beam characteristics, namely kinetic energy and angular directivity. The next logical step is to add a second THz pulses such that a gating effect can be achieved by altering the time delay and phase between the two pulses.

3.3.2. Two Terahertz Electric Field Pulses for Electron Pulse Gating[2]

Adding a second THz electric field pulse introduces two new parameters to work with: the phase, φ, and time delay, Δt, between the two THz electric field pulses. The dual THz electric field configuration is implemented to translate, narrow, or broaden the kinetic energy spectrum of the electron pulse.

The simulation setup is similar to that of the single THz electric field configuration but with a few minor adjustments, as depicted in Fig. 3.8. Now, the THz electric fields are directed normal to the Ag film and E_{THz} is fixed at 1.5×10^6 V/cm for each pulse, while E_{SP} is fixed at 5×10^8 V/cm as before. Throughout the calculations, the time delay between $E_{THz}^{(a)}$ and E_{SP} is fixed while the time delay, Δt, between $E_{THz}^{(b)}$ and $E_{THz}^{(a)}$ is varied to allow for control over the central energy and the width of the kinetic energy spectrum of the accelerated electron pulse. Further control can also be realized through alteration of the phase relationship between $E_{THz}^{(a)}$ and $E_{THz}^{(b)}$. The time delay is varied from -500 fs to 500 fs, where negative delay corresponds to $E_{THz}^{(b)}$ arriving prior to $E_{THz}^{(a)}$. The effect of the relative phase difference between $E_{THz}^{(a)}$ and $E_{THz}^{(b)}$ is also investigated for $E_{THz}^{(b)}$ in-phase ($\varphi = 0$) and out-of-phase ($\varphi = \pi$) with $E_{THz}^{(a)}$.

[2] A version of this section has been published as S.R. Greig and A.Y. Elezzabi, "Electron Acceleration and Kinetic Energy Tailoring via Ultrafast Terahertz Fields," *Opt. Express* **22**, 29092 (2014).

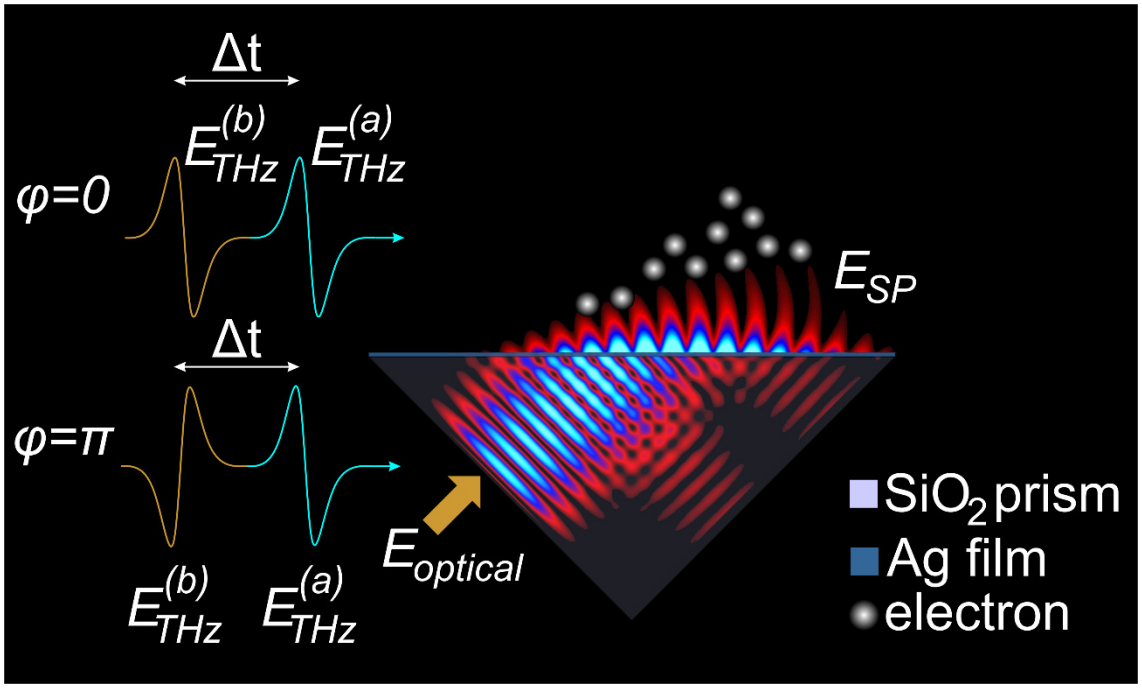

Figure 3.8. Schematic illustration of the Kretschmann configuration consisting of a 50 nm Ag film on a right-angle silica prism. E_{laser} and E_{SP} represent the optical and plasmonic electric fields, respectively. The $E_{THz}^{(a)}$ and $E_{THz}^{(b)}$ depict the two THz electric fields with a delay of Δt between them. φ represents the relative phase difference between $E_{THz}^{(a)}$ and $E_{THz}^{(b)}$. The spatial full width at half maxima of the THz and optical pulses are 600 µm and 4 µm, respectively.

3.3.3. Two Terahertz Electric Field Pulse Electron Kinetic Energy Control

The kinetic energy spectra of the in-phase ($\varphi = 0$) case at various positive and negative Δt are depicted in Figs. 3.9(a) and 3.9(b). Here, the first half cycles of $E_{THz,\varphi=0}^{(a)}$ and $E_{THz,\varphi=0}^{(b)}$ act to decelerate the electrons against the outward ponderomotive force of the E_{SP}. Subsequently, on the reversed second half-cycle, $E_{THz,\varphi=0}^{(a)}$ and $E_{THz,\varphi=0}^{(b)}$ accelerate the generated electron pulse outward, away from the Ag film, resulting in higher kinetic energies. Examining first the $\Delta t = 0$ case, $E_{THz,\varphi=0}^{(a)}$ and $E_{THz,\varphi=0}^{(b)}$ temporally overlap and the

electrons effectively experience a single THz pulse with field strength $2\times E^{(a)}_{THz,\varphi=0} = 3\times10^6$ V/cm. This electron pulse achieves a broad weighted full-width-at-half-maximum (WFWHM) of 0.62 keV which is centered at 1.8 keV. Varying Δt provides marked kinetic energy selectivity. Figure 3.9(a) depicts the electrons' kinetic energy spectra for $\Delta t > 0$. At $\Delta t = 500$ fs, the central kinetic energy has shifted to 0.94 keV having a narrower WFWHM of 0.49 keV. As Δt decreases from 500 fs to 100 fs, the central energy shifts from 0.94 keV to 1.65 keV. The WFWHM, however, exhibits a decreasing trend where the minimum WFWHM of 0.43 keV is achieved at $\Delta t = 200$ fs, followed by broadening as Δt decreases further to $\Delta t = -500$ fs, where a much wider WFWHM of 1.56 keV (centered at 1.85 keV) is observed, as shown in Fig. 3.9(b).

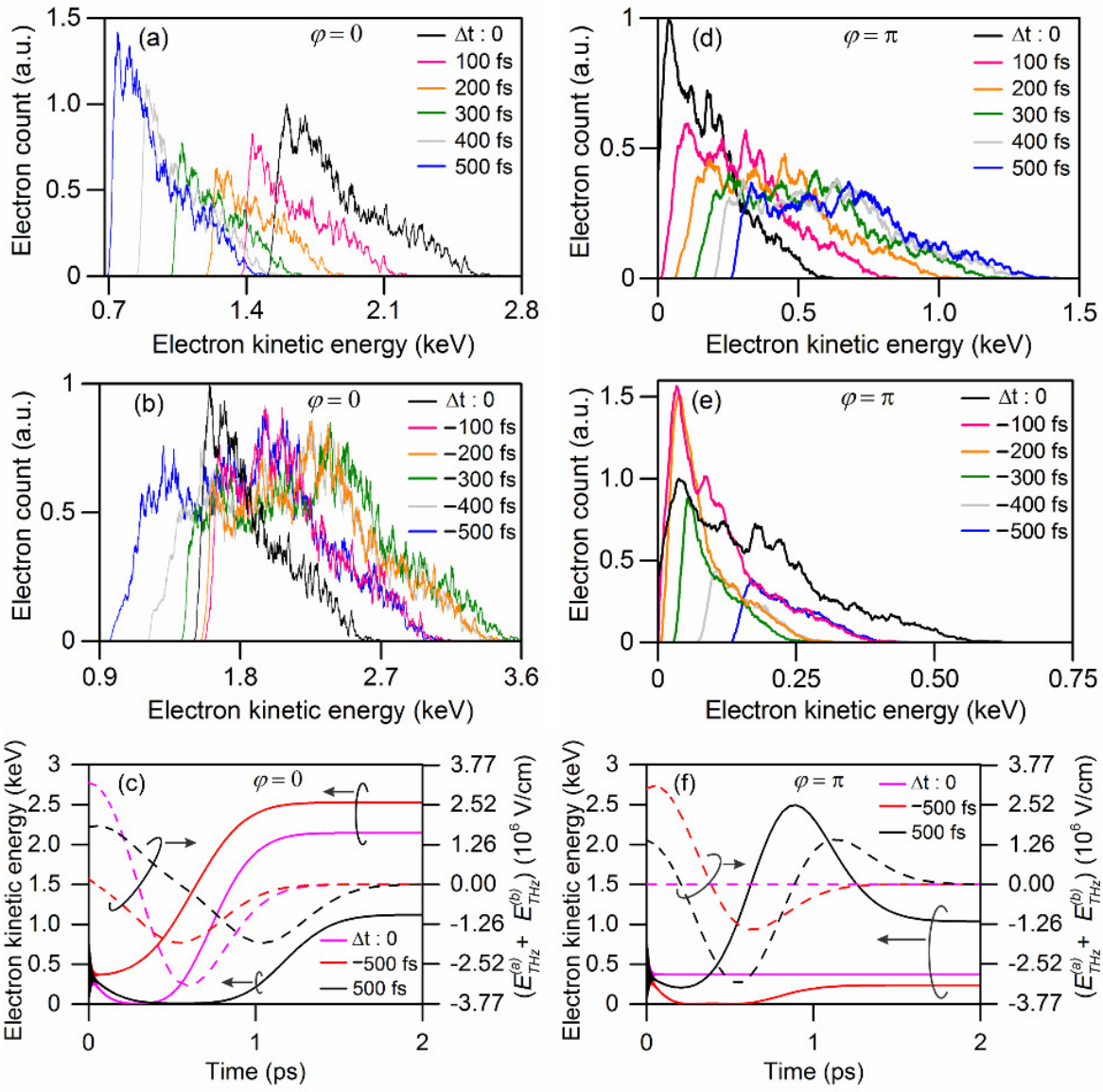

Figure 3.9. Kinetic energy spectra for $\varphi = 0$ at (a) $\Delta t > 0$ and (b) $\Delta t < 0$. (c) Kinetic energy and combined THz electric field strength as a function of time for $\varphi = 0$ at $\Delta t = 0$ (pink line), Δt = -500 fs (red line), and Δt = 500 fs (black line). Kinetic energy spectra for $\varphi = \pi$ at (d) $\Delta t > 0$ and (e) $\Delta t < 0$. (f) Kinetic energy and combined THz electric field strength as a function of time for $\varphi = \pi$ at $\Delta t = 0$ (pink line), Δt = -500 fs (red line), and Δt = 500 fs (black line).

The energy selectivity is ascribed to the two THz electric field pulses interfering with each other to create different temporal acceleration potential profiles at various Δt.

This can more easily be illustrated with the aid of Fig. 3.9(c) where an electron's kinetic energy, and the combined THz electric field it experiences, are tracked as a function of time at Δt = -500 fs, 0 fs, and 500 fs. Within the first 25 fs the electrons at various delays gain the same energy of 0.35 keV from the E_{SP} field. Afterwards, the electron corresponding to Δt = -500 fs experiences a greater outward (away from the Ag film) force from the combined $E^{(a)}_{THz,\varphi=0}$ and $E^{(b)}_{THz,\varphi=0}$ compared to the Δt = 500 fs and Δt = 0 cases. This leads to a higher final kinetic energy of the electron. As the electron interacts and gains more energy from the E_{SP} field at various locations along the SP wave propagation direction, it simultaneously experiences only a unipolar THz electric field due to the overlapping of $E^{(a)}_{THz,\varphi=0}$ and $E^{(b)}_{THz,\varphi=0}$ (i.e. the second half-cycle of $E^{(b)}_{THz,\varphi=0}$ overlaps with the first half-cycle of $E^{(a)}_{THz,\varphi=0}$, effectively cancelling it out). However, for Δt = 0 or 500 fs, the THz field overlap increases the combined THz electric field strength (Δt = 0) or extends the duration of the first half-cycle (Δt = 500fs). Here, the electron is decelerated to the point where it possesses almost zero kinetic energy (~10 eV). This low energy point coincides with the combined THz electric field reversing polarity. For Δt = 500 fs, the effective electron deceleration duration is much longer (i.e. 570 fs), resulting in significantly lower final kinetic energy (1.1 keV vs 2.15 keV) when compared to Δt = 0. This significant difference in kinetic energy allows for a specific energy range to be selected based on the time delay between the two THz electric fields.

A distinct behavior is achieved when $E^{(b)}_{THz}$ is 180 degrees out of phase with $E^{(a)}_{THz}$. The kinetic energy spectra at various Δt are depicted in Figs. 3.9(d) and 3.9(e). Here, the two THz electric field pulses ($E^{(a)}_{THz,\varphi=0}$ and $E^{(b)}_{THz,\varphi=\pi}$) are applying opposite forces on the

electrons, depending on their half-cycle field polarity. At $\Delta t = 0$, $E^{(a)}_{THz,\varphi=0}$ and $E^{(b)}_{THz,\varphi=\pi}$ completely overlap, and thus, effectively cancel out any acceleration due to the THz electric fields. Here, the electrons only gain kinetic energy from the E_{SP} field. As Δt decreases from Δt = 500 fs towards Δt = -200 fs, the central kinetic energy is shifted from 0.66 keV (WFWHM of 0.61 keV) (Fig. 3.9(d)) to lower kinetic energies until a minimum of 83 eV is achieved at Δt = -200 fs (Fig. 3.9(e)). Below Δt = -200 fs, the kinetic energy begins to translate towards higher values. The WFWHM follows a similar trend when going from Δt = 500 fs to Δt = -500 fs, with the narrowest WFWHM of 111 eV coinciding with the lowest central kinetic energy at Δt = -200 fs.

The difference in behavior for the out of phase case is more easily seen in Fig. 3.9(f) where an electron's energy and combined THz electric field experienced is tracked through time for Δt =-500fs, 0 fs, and 500fs. At Δt =0 the combined THz electric field experienced by the electron is zero; therefore, the electron's kinetic energy reaches its maximum of 0.37 keV during its interaction with the E_{SP} field alone. At Δt = -500 fs, since the first half-cycle of the effective THz electric field is twice the strength of the second half-cycle, the net deceleration experienced by the electron is greater than its acceleration. This leads to a final kinetic energy of 0.24 keV. On the contrary, at Δt = 500 fs, the electron is initially decelerated to 0.2 keV and subsequently accelerated to its maximum kinetic energy of 2.5 keV as the THz electric field reverses its polarity. However, the net THz electric field reverses polarity again, greatly decelerating the electron to its final energy of 1.1 keV.

The results presented in Figs. 3.9(c) and 3.9(f) help to enforce the need for control over the temporal characteristics of the applied THz electric field pulse. Clearly, the most

advantageous configuration is a unipolar THz electric field as the electron is continually accelerating to higher kinetic energies, i.e. none of the energy imparted to the electron from the THz electric field is lost.

3.3.4. Carrier Envelope Phase Effects of Electrons in Terahertz Fields[3]

When working with few-cycle laser pulses having durations of ~5-10 fs (with a central wavelength of 800 nm), the carrier envelope phase (CEP) starts to become important for electric field dependent processes such as electron acceleration. The carrier envelope phase represents the phase difference between the peak of the envelope of the pulse and actual peak of the electric field, or carrier wave. Figure 3.10 shows the electric field of a 5 fs, 800 nm laser pulse with CEP ranging from 0 to $3\pi/2$. In this regime there are only a few cycles of the electric field within the pulse duration and therefore the phase difference between the carrier wave and the envelope of the pulse plays a major role in laser-matter interactions. As the distinct signature of CEP has been previously reported for SP based electron acceleration [65]**,** it is important that any modification to the acceleration process, such as the addition of THz pulses used here, preserve this CEP dependence.

[3] A version of this section is published in S.R. Greig and A.Y. Elezzabi, "Electron Acceleration and Kinetic Energy Tailoring via Ultrafast Terahertz Fields," *Opt. Express* **22**, 29092 (2014).

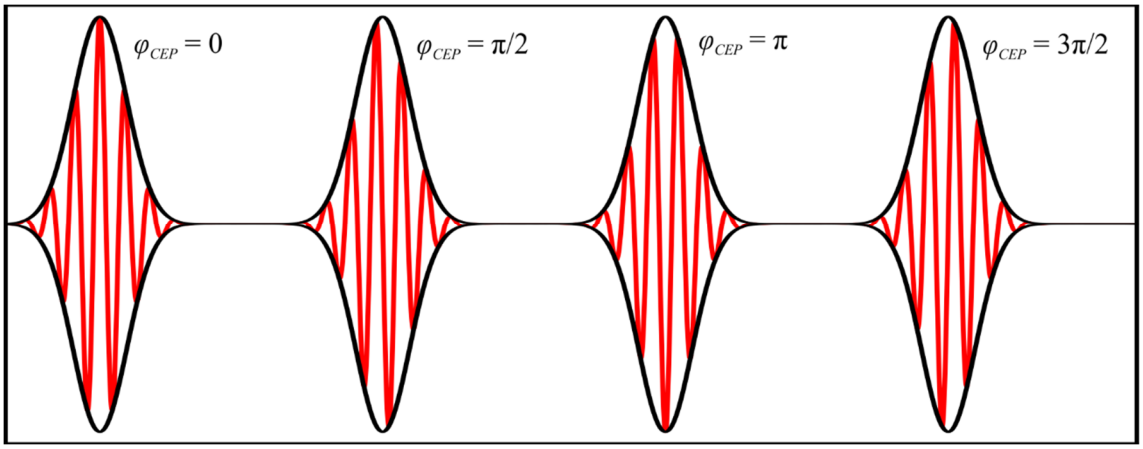

Figure 3.10. Few cycle pulse train depicting four values of carrier-envelope-phase at a carrier wavelength of 800 nm.

To observe prominent CEP effects, the E_{SP} field must consist of only a few cycles, otherwise any effect is averaged out over the pulse duration. As such, the surface plasmon is now excited by an optical pulse having a pulse duration of 5 fs while keeping the 800 nm central wavelength. A single E_{THz} pulse is introduced to observe how it will affect the kinetic energy characteristics of the electron packets generated at various values of CEP. The setup, shown in Fig. 3.11, is again the standard 50 nm Ag film in the Kretschmann geometry with a single THz pulse directed at 45° to the surface normal. Throughout the simulations, the E_{SP} and E_{THz} field strengths are fixed at 6.5×10^{8} V/cm and 3×10^{6} V/cm, respectively.

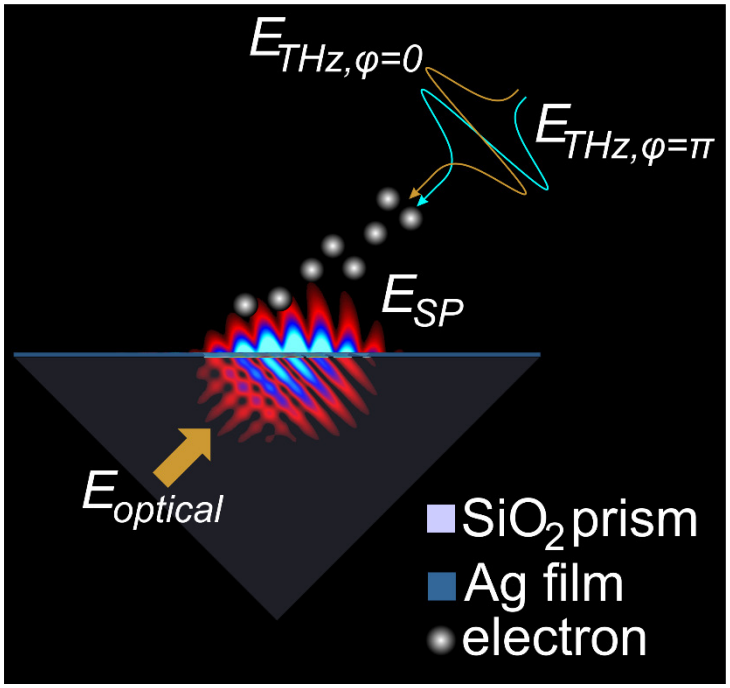

Figure 3.11. Simulation setup for CEP dependence using a 5 fs optical pulse. $E_{THz,\varphi=0}$ and $E_{THz,\varphi=\pi}$ represent the different phases of the THz electric field. The spatial full width at half maxima of the THz and optical pulses are 600 μm and 4 μm, respectively.

Of particular interest is the influence of the initial phase of the E_{SP} field on the energy of the accelerated electrons as they interact with the THz field. The CEP effects on the kinetic energy spectra, in the presence of $E_{THz,\varphi=0}$, at various values of φ_{CEP} are shown in Fig. 3.12(a). Each spectrum exhibits a similar trend at energies < K_0 = 1.6 keV. Above K_0, each of the spectra exhibit a discernible drop (δ_1) in the number of electrons collected, often followed by a plateau and second drop (δ_2) [65]. For $0 < \varphi_{CEP} < \pi$, δ_1 is shifted to lower energy for increasing φ_{CEP}, exhibiting similar behavior to electron pulses generated in the absence of $E_{THz,\varphi=0}$ [65]. However, for $\varphi_{CEP} > \pi$, only δ_1 is present. Clearly, the electron's interaction with the ponderomotive force from the E_{SP} is highly dependent upon the phase of E_{SP} during its generation.

Utilizing the opposite polarity, $E_{THz,\varphi=\pi}$, different behavior is observed. The energy spectra for $E_{THz,\varphi=\pi}$ at various φ_{CEP} values are depicted in Fig. 3.12(b). The energy spectra exhibit similar low energy behavior for energies < K_0 = 0.37 keV. However, the shift in δ_1 is significantly less pronounced than the $\varphi = 0$ case. This is ascribed to the fact that the deceleration from the second half-cycle of $E_{THz,\varphi=\pi}$ reduces the overall number of electrons collected at the detector (36% compared to the $E_{THz,\varphi=0}$ case). As such, the E_{SP} field imparts its phase on fewer electrons. Additionally, the φ_{CEP} effects are obscured due to the lower spread of kinetic energies. For 0 < φ_{CEP} < π, the number of collected electrons is increasing for increasing φ_{CEP}. Above $\varphi_{CEP} = \pi$, δ_1 occurs at lower energies for increasing φ_{CEP}.

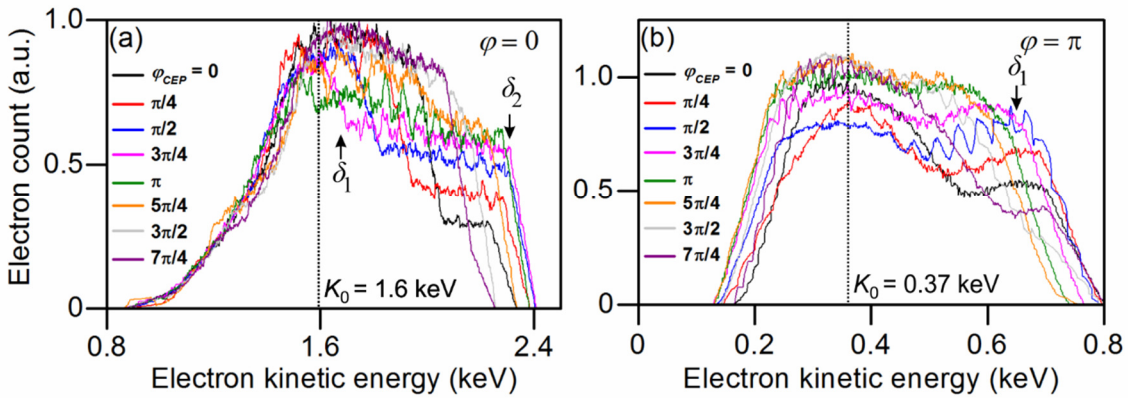

Figure 3.12. Kinetic energy spectra for $E_{THz,\varphi=0} = 3\times10^6$ V/cm and $E_{SP} = 6.5\times10^8$ V/cm for (a) $\varphi = 0$ and (b) $\varphi = \pi$ at various values of φ_{CEP}. Note that the kinetic energy scales are different between (a) and (b).

Due to the marked difference in the number of collected electrons above K_0, a useful measure is to investigate the percentage of collected electrons above K_0 versus

φ_{CEP}. Figures 3.13(a) and 3.13(b) depict a distinctive sinusoidal relationship between K_0 and φ_{CEP}, similar to the case in the absence of E_{THz} [65]. Clearly, introduction of E_{THz} maintains any CEP information present in the generated electron pulse. A characteristic to note is that the curves for $E_{THz,\varphi=0}$ and $E_{THz,\varphi=\pi}$ are exactly 180° out of phase, affirming the fact that not only can the CEP information be recovered from the electron pulse, but also the polarity of the applied E_{THz}.

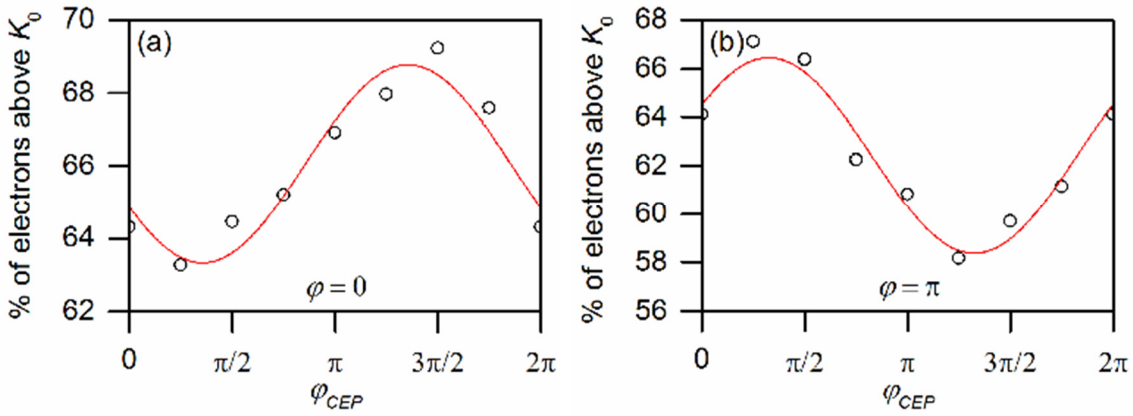

Figure 3.13. Percentage of electrons collected above (a) K_0 = 1.6 keV for $\varphi = 0$ and (b) K_0 = 0.37 keV for $\varphi = \pi$. The red lines represent sinusoidal fits to the data.

3.4. Generation of Attosecond Electron Packets via Conical Surface Plasmon Electron Acceleration and Post-Acceleration Filtering[4]

From the kinetic energy plots of the previous section it can be ascertained that THz electric field electron acceleration works well for generating high kinetic energies, but the electron pulses still possess a broad range of energies. This will ultimately destroy the ultrafast time duration of the electron pulses. As such, this section explores the combination of various electron filtering methods in order to greatly reduce this kinetic

[4] A version of this section is published as S.R. Greig and A.Y. Elezzabi, "Generation of Attosecond Electron Packets via Conical Surface Plasmon Electron Acceleration.," *Sci. Rep.* **6**, 19056 (2016).

energy spread to produce ultrafast electron packets. Combining these filtering techniques with a unique approach to electron generation, a compact, high-energy nanoplasmonic electron gun capable of producing attosecond electron packets is developed and simulated. By harnessing the unique focusing property of radially polarized light, and magnetostatic spatial filtering, extremely short electron packets of attosecond durations and keV kinetic energies are produced. Additionally, it is demonstrated that by varying the magnetic field strength and the parameters of a physical aperture, electron packets with various kinetic energies and temporal packet lengths can be tailored to a specific need.

3.4.1. Electron Acceleration via Conical Surface Plasmon Waves

The geometry used for generating the keV attosecond electron packets is depicted in Fig. 3.14. The electron source consists of a 50 nm Ag film deposited on a conical silica lens with a diameter of 10 μm, an apex angle of 91°, and a refractive index n = 1.45. To ensure that the findings are generalizable to a realistic situation, the Ag film is modelled to have a surface roughness of 2.8 nm rms [20] such that the influence of enhanced SP fields localized at random spots is captured. A traveling SP wave is excited by a λ = 800 nm radially polarized laser pulse with pulse duration of 5 fs and an electric field strength, E_{laser}. It should be noted that all values of E_{laser} refer to the peak value of the incident field. The use of a radially polarized beam affords the benefit of having the electric field polarization oriented such that it is *p*-polarized with respect to the Ag film along the entire azimuthal angle of the conical lens. This leads to the excitation of traveling SP waves encompassing the entire conical surface of the Ag film, a so-called conical SP wave. Consequently, this results in a greater peak enhancement of the electric field (63

times) at the apex than for the case of linear polarization (11 times). Figure 3.15 depicts the electric field intensity profile when the tip is excited by a radially polarized 5 fs laser pulse. The high intensity electric fields that are present within the silica lens itself are due to the interference of out-of-plane reflections from the glass-metal interface along the entire azimuthal angle of the lens. The polarization of the SP wave is given by the two-headed arrows in Fig. 3.15. Notably, at the very apex of the conical lens, the SP waves from each azimuthal direction constructively interfere and the polarization is along the axis of the cone. This is what gives rise to the increased enhancement of 63 times.

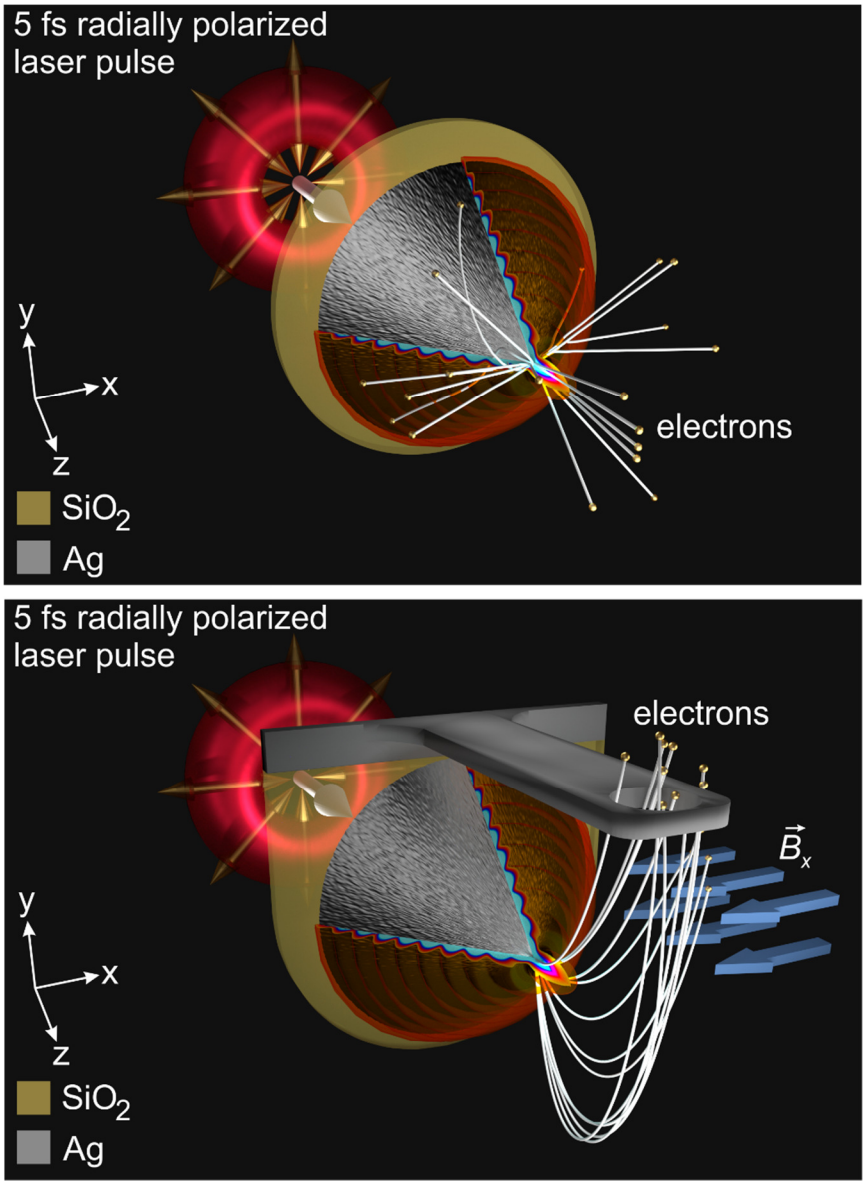

Figure 3.14. Schematic depiction of a nanoplasmonic attosecond electron source consisting of a 50 nm Ag film deposited on a conical silica lens. The electrons are generated by a 5 fs radially polarized laser pulse with a central wavelength of 800 nm and are accelerated by the nanoplasmonic field. (a) Configuration in the absence of a static magnetic field, where the electron packet generated has no defined direction, as shown by an ensemble of electron trajectories. (b) Configuration in the presence of a static magnetic flux density at $\bar{B}_x$ = -1T. Here, the electron trajectories show that the generated electron packet is now directed towards the detector placed 50 µm away and pass through the aperture for energy filtering.

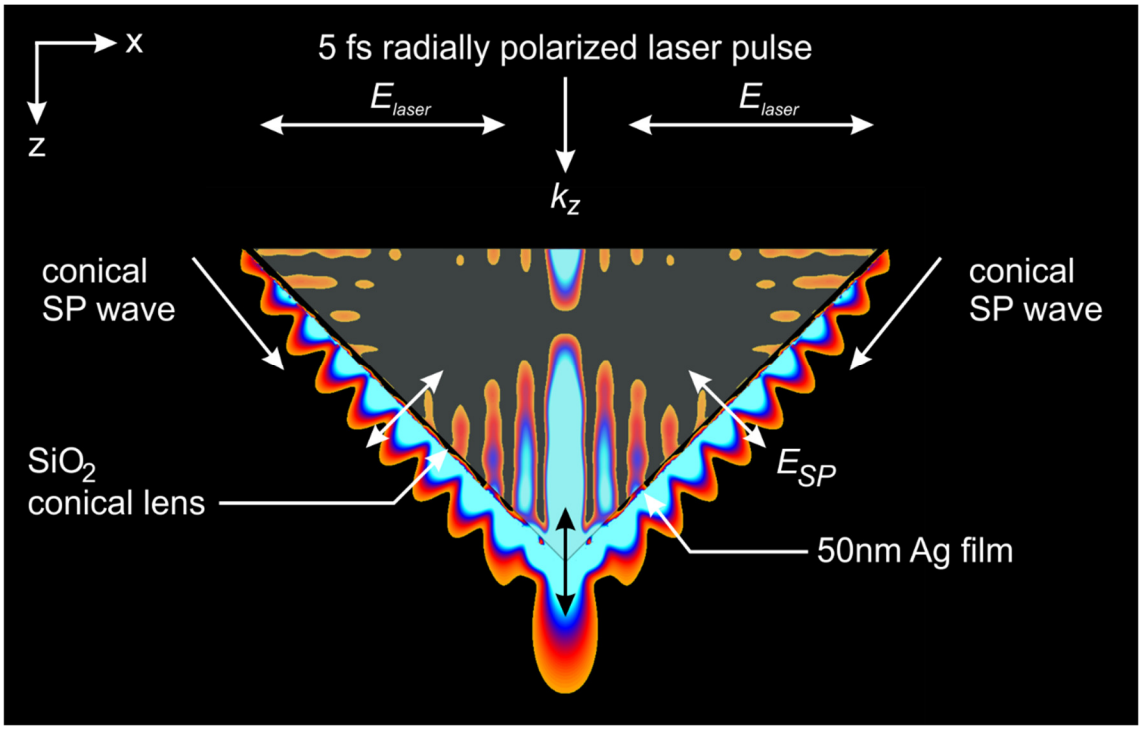

Figure 3.15. Two-dimensional slice of the electric field intensity profile of the conical SP wave on the Ag coated conical lens when excited by a 5 fs radially polarized laser pulse with electric field strength E_{laser}. The two-headed arrows represent the electric field oscillation direction of the laser field, E_{laser}, and the SP field, E_{SP}.

The behaviour of the electron gun is modelled using the standard particle tracking code. Free electrons are ejected through a three-photon absorption process from the film and interact with the SP electric field, E_{SP}. To verify that multi-photon absorption will be the dominate generation mechanism, the Keldysh parameter is calculated. For our operating parameters, and with the average surface enhancement of 3, a value of γ=1.83 is calculated, indicating that electron emission will occur through a multi-photon process. The calculated average surface enhancement considers the enhancement along the entire azimuthal Ag surface. Note that due to the surface roughness of the Ag film, there will be hotspots of electric field enhancement greater than 3. However, these localized hotspots

will not significantly contribute to the total electron count and thus the statistical weighing used above will remain valid. Throughout the calculations, the peak intensity of the optical pulse is kept below 1.2×10^{12} W/cm^2 which is below the experimentally determined damage threshold of a thin Ag film on a silica prism [20]. At this intensity, and with a spot size diameter of ~6 μm for a radially polarized beam, the corresponding energy per laser pulse is calculated to be ~1 nJ. Such a low laser pulse energy can be achieved with a typical ultrafast laser oscillator. It is estimated that at the highest intensities considered (1.2×10^{12} W/cm^2), there will be ~10^4 electrons/packet [20]. However, after passing through the aperture, the number is significantly reduced to 4% of its initial value. As this value is well below 10^7 electrons/packet, space charge effects will not be encountered [20]. It should also be noted that due to the lack of tight focussing of the laser field, the Gouy phase shift can be neglected.

3.4.2. Electron Simulation Parameters

To reduce the computational requirements, the conical lens is simulated with a base diameter of 10 μm, which is larger than the laser spot size used. Symmetric boundary conditions are utilized in the *x* and *y*-directions with Berenger perfectly-matched-layer (PML) boundary conditions in the *z* direction. The conical lens is placed 5 μm away from the boundary in the *x, y*-direction and 8 μm away in the *z*-direction. Furthermore, the source is placed 2.5 μm back from the lens. The 50 nm Ag film is simulated with a random surface roughness of 2.8 nm rms [20]. The spatial electric field profile of the incident radially polarized laser beam is given by the following:

$$\vec{E}(r) = E_0 \exp(-(r/w_0)^2)\,\mathrm{J}_1(r)\ \hat{r} \tag{3.4}$$

where E_0 is amplitude, r is the radial distance from the center of the beam, w_0 is the beam waist, J_1 is the first order Bessel function, and $\hat{r}$ is a unit vector directed in the radial direction. For the linear polarization configuration, the spatial electric field profile is that of a standard Gaussian laser beam polarized in the x direction. For both configurations, the spatial electric field profiles are modulated in time by a 5 fs temporal Gaussian pulse having a central wavelength of 800 nm.

The static magnetic field utilized for filtering the electrons is introduced by appending a static magnetic field term to the equation of motion used in the standard particle tracking code. To characterize the effect of the aperture on the electrons arriving at the detector, the aperture diameter, d_a, thickness, t_a, and location, l_a, are swept to select exemplary sets of parameters. The diameter and thickness of the aperture act to limit the acceptance angle of the aperture. From the parametric sweeps, representative electron packets are chosen based on their kinetic energies and temporal lengths. For all simulations, the detector is placed a fixed 50 μm away, in the +y-direction (Fig. 3.14(b)), from the tip of the conical lens. A total of 825,000 electrons are considered for each different magnetic field strength.

3.4.3. Generation of Attosecond Electron Packets

The kinetic energy spectra for a linearly polarized excitation laser pulse at various values of E_{laser} are depicted in Fig. 3.16(a). At the maximum $E_{laser} = 3\times10^7$ V/cm, a peak electron kinetic energy of 15 eV is achieved, with the majority of electrons (85%) being accelerated to energies below 2 eV. Lowering E_{laser} shifts the electron kinetic energy spectrum towards lower energies with a maximum at 2.2 eV, achieved at $E_{laser} = 1\times10^7$ V/cm. Clearly, utilizing linearly polarized laser pulses at these field strengths limits the

electron's energy to only a few eVs. The poor performance of the linearly polarized configuration can be directly attributed to the laser pulse only coupling to an SP wave in one plane (i.e. the *xz* plane at the center of the conical lens in Fig. 3.14(a)), leading to a reduction in the electric field enhancement occurring at the apex of the conical lens.

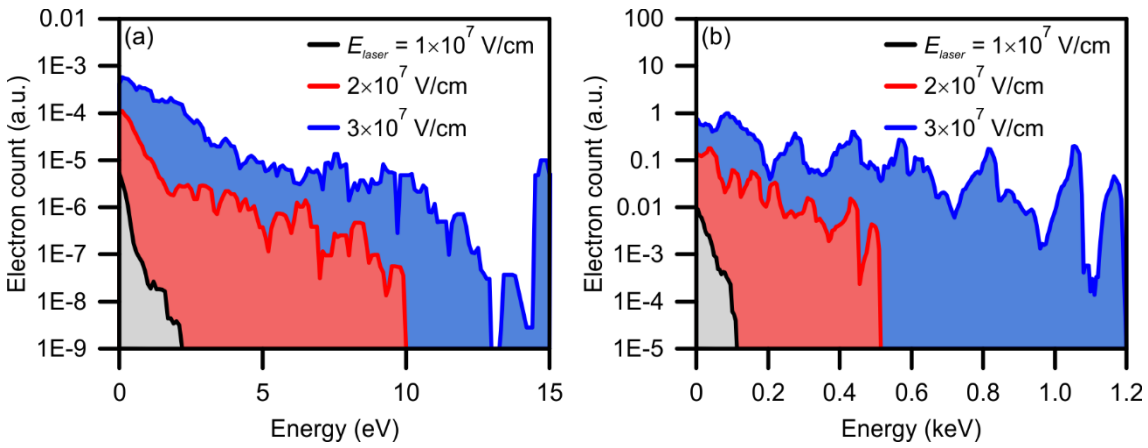

Figure 3.16. Electron kinetic energy spectra for an excitation with (a) linear polarization and (b) radial polarization. The electron count scale is normalized to the radial polarization configuration at E_{laser} = 3×10^7 V/cm. Note the difference in the electron count and kinetic energy scales between (a) and (b).

A radially polarized incident laser pulse can be utilized to increase the maximum attainable kinetic energy of the generated electrons. As discussed earlier, this leads to conical SP waves that are directed towards and focused at the tip where they constructively interfere. Therefore, a peak electric field enhancement of 63× is achieved at the tip, compared to 11× for the case of linear polarization.

The electron kinetic energy spectra for excitation with a radially polarized laser pulse at various E_{laser} are depicted in Fig. 3.16(b). Owing to the increased electric field enhancement from the radially polarized configuration, a maximum kinetic energy of 1.2 keV can be achieved at E_{laser} = 3×10^7 V/cm, 80 times higher than for excitation with

linear polarization at the same electric field strength. Remarkably, at this excitation field strength, a large number of electrons (45% of the total electrons) have kinetic energies above 0.25 keV. The maximum kinetic energy drops to 0.11 keV at $E_{laser} = 1\times10^7$ V/cm.

The high kinetic energy gain can also be attributed to a non-ponderomotive source of acceleration deemed sub-cycle acceleration. If an electron experiences a high electric field strength during its first half-cycle, the electron will be essentially "ejected" from the surface plasmon field, meaning it will not experience the second half-cycle and thus will not be decelerated. This can result in significant energy gain in an extremely short period of time (~fs). Figure 3.17(a) depicts the kinetic energy of an electron as a function of time during its interaction with an intense electric field of 3 V/nm for the radially polarized case. Notably, the electron achieves a final kinetic energy of 0.96 keV within 7 fs of it being ejected from the metal into the intense SP field. Figure 3.17(b) depicts the energy vs. time for an electron that is ejected at a different point, in space and time, and achieves a final kinetic energy of 13 eV within 40 fs. This electron experiences a more ponderomotive like acceleration evidenced by the multiple kinetic energy gain/loss cycles as a function of time, which correspond to the period of the driving laser pulse, ~2.7 fs (λ = 800 nm). In the ponderomotive interaction, electrons experience a significant difference in electric field strength on the positive and negative half-cycles. Thus, over multiple cycles, the electron is accelerated or decelerated, dependent on the polarity of the E_{SP} field. However, for short pulse durations, there is additional energy gained by non-ponderomotive acceleration due to the SP field [21]. This energy gain can occur over less than an oscillation cycle and depends on the phase of the SP field that the electron experiences when it is generated.

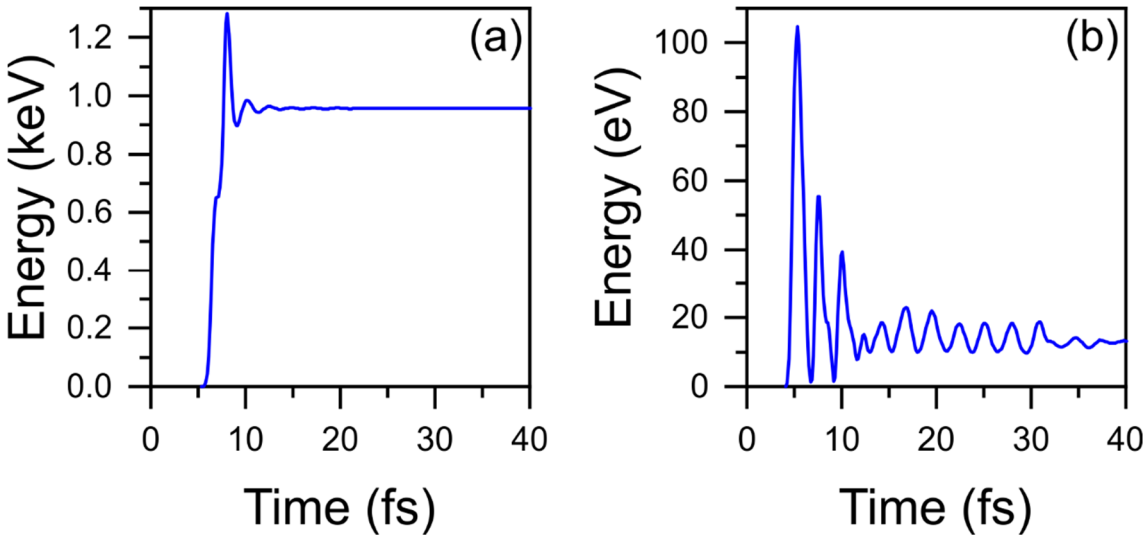

Figure 3.17. Kinetic energy as a function of simulation time for electrons experiencing (a) sub-cycle acceleration, and (b) ponderomotive acceleration.

In addition to the increased kinetic energy of the generated electrons, employing a radially polarized configuration greatly increases the total number of photogenerated electrons. This is evidenced by comparing the electron counts between Fig. 3.16(a) and Fig. 3.16(b), where the maximum total number of electrons for the radial polarization is ~4,300 times that of the linear case at $E_{laser} = 3\times10^7$ V/cm. This can be attributed to excitation of the conical SP waves along the entire conical surface of the Ag film.

From the broad kinetic energy spectra present in Fig. 3.16, it can be ascertained that any electron packet generated from either configuration (linear or radial polarization) would result in an extremely long packet duration due to the inherent time dispersion. Therefore, it is of paramount importance to implement a mechanism that can either tune or filter the kinetic energies of the electrons to produce electron packets with a minimal spread in kinetic energy. One such configuration that is presented here is kinetic energy filtering of the electrons through the introduction of a static magnetic field. In this

manner, the accelerated electrons will be directed away from the tip towards a detector placed in the +*y*-direction (Fig. 3.14(b)) and spatially dispersed in accordance to their kinetic energy. The introduction of the magnetic field causes the electrons to travel in a circular trajectory with a radius given by:

$$R_e = (q / m_e)^{-1} \left|\vec{v}\right| \Big/ \left|\vec{B}\right| \tag{3.5}$$

where $\left|\vec{v}\right|$ is magnitude of the electron velocity, and $\left|\vec{B}\right|$ is the strength of the magnetic flux density. Since the radius is proportional to the velocity, and hence the kinetic energy of the electron, the electrons will spread out along the *z*-axis of the detector. A sample of 500 electron trajectories in the absence of any external magnetic field is shown in Fig. 3.18(a), with the color of the trajectory representing the kinetic energy of that electron. Since the accelerating force from the SP field acts in both the outward radial and the longitudinal directions, the accelerated electrons are spread accordingly. While these generated electrons have kinetic energies up to 1.2 keV, the lack of directionality in this arrangement makes it inadequate for UED and UEM applications. Conversely, applying a magnetic field breaks the symmetry of the trajectories of the electrons being accelerated via the conical SP wave. Figure 3.18(b) illustrates such action, where the electrons are now directed in one direction (towards the detector) along a circular, velocity-dependent path. Notably there are two distinct path types. The first path type corresponds to electrons that are initially directed in the negative *y* direction. These electrons experience a greater bending radius due to the increased interaction with the magnetic field. The second path type are those electrons that are initially directed more towards the positive *y*

direction. These electrons have a reduced bend radius and arrive significantly earlier than the other electrons.

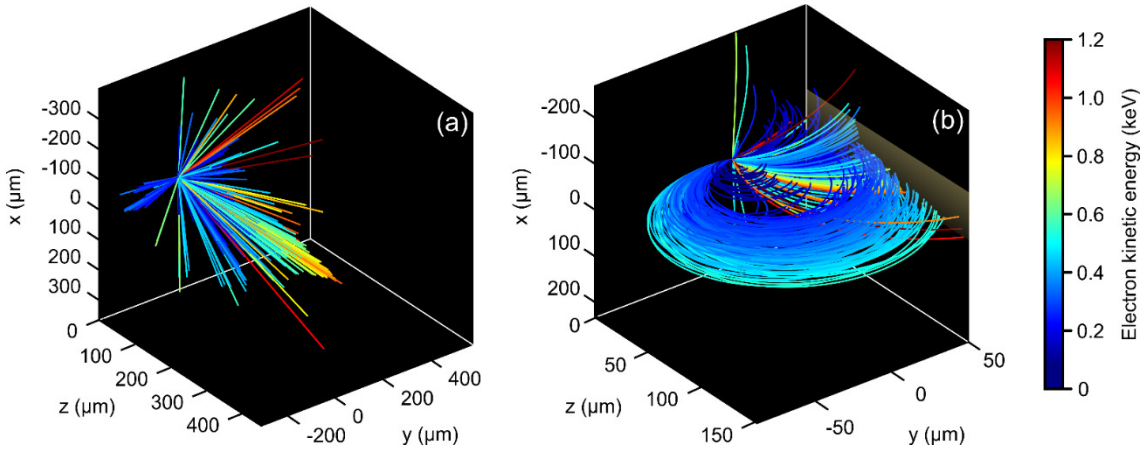

Figure 3.18. Representative electron trajectories (a) in the absence of the magnetostatic field, and (b) with an applied $\vec{B}_x$ = -1 T. The color scale represents the electron kinetic energy.

Varying the strength of the applied magnetic field results in the tuning of the packet length of the generated electron packet and offers a scheme for accessing the attosecond regime. This can be illustrated with the following representative arrangement, where the detector is placed 50 μm away from the tip in the +*y* direction, E_{laser} is fixed at 3×10^7 V/cm, and $\vec{B}$ is directed in the –*x* direction. Figure 3.19 depicts a 2-dimensional map of the arrival time of the electrons as a function of their final position along the *z*-axis of the detector for $\vec{B}_x$ = -0.5 T, -1 T, -1.5 T, and -2 T, with the color representing the normalized electron count on a logarithmic scale. The spatial spreading afforded by the magnetic field can distinctly be seen in Fig. 3.19 where the electrons spread out in space as they reach the detector. Here, electrons arrive up to 420 μm away from the tip for $\vec{B}_x$ = -0.5 T. For increasing $\left|\vec{B}_x\right|$, electrons will arrive at the detector closer to z = 0,

thus reducing the spatial spreading of the packet. Additionally, the inherent time dispersion of the electron packet is also evident in Fig. 3.19. In the case of $\vec{B}_x$ = -0.5 T, electrons can take up to 47 ps to arrive at the detector, but only 12 ps for $\vec{B}_x$ = -2 T. Notably, at a given $\vec{B}_x$, there are specific locations along the detector's surface where the duration of the electron packets is <1 ps, and others where the duration is extremely long (>10 ps). The reason for the wide spread in the electron packet durations is due to the fact that each electron experiences a different spatial and temporal electric field strength as it gets accelerated within the SP field. That is, the SP acceleration process is sensitive to the local magnitude of the SP field and the phase of the generation of the electron with respect to the phase of the conical SP wave. When the magnetic field is introduced, it acts to curve the trajectory of the electrons in a circular fashion where their initial trajectory ultimately dictates where and when they will arrive at the detector. Each electron will have its velocity oriented in a different direction based on its specific interaction with the SP field. As such, electrons will arrive at the detector at different locations, resulting in the spread of both kinetic energy and arrival time at a distinct position along the detector. Clearly, the introduction of a static magnetic field is the first step in filtering the electrons to achieve ultrashort electron packets.

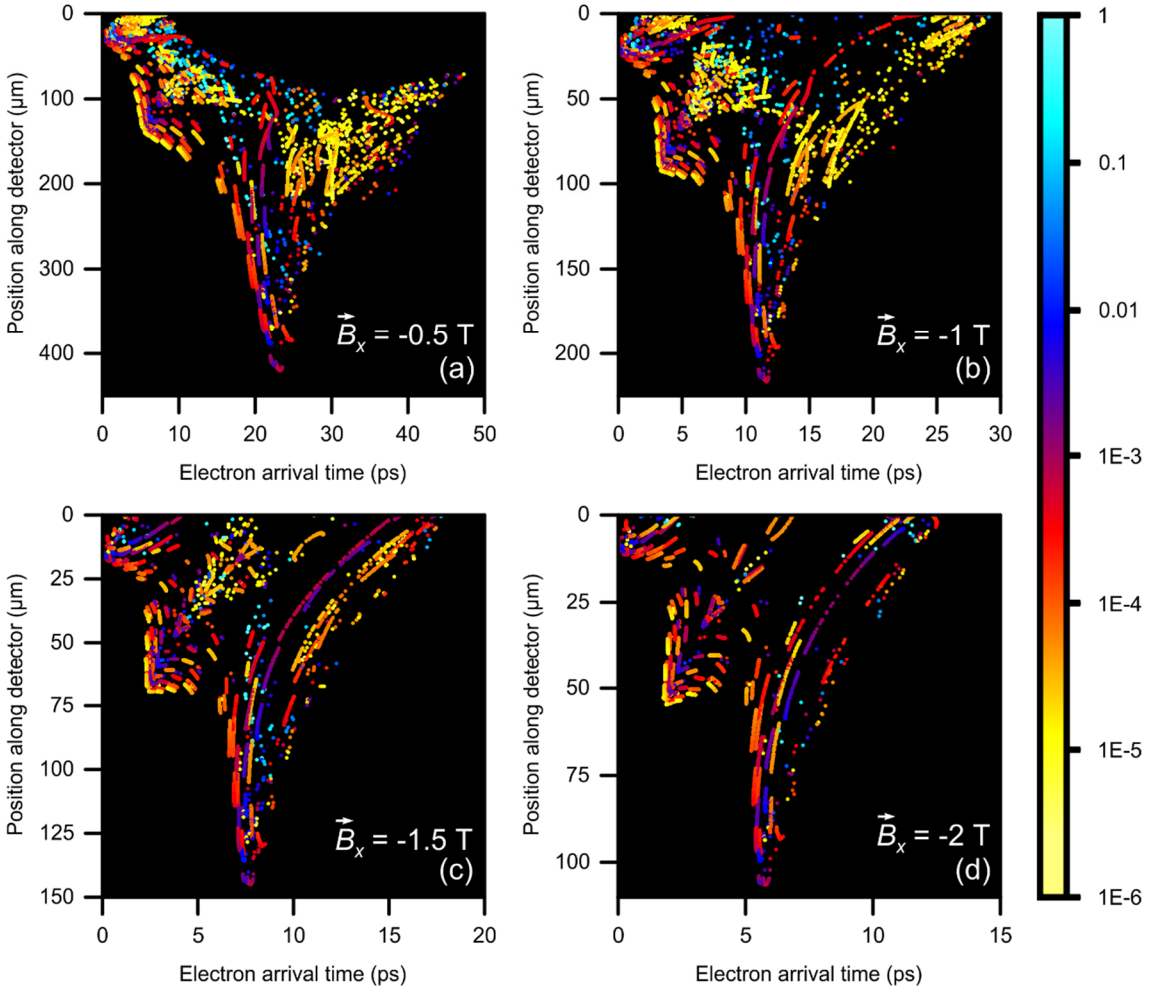

Figure 3.19. Electron arrival time as a function of position along a detector placed 50 μm away from the tip, for E_{laser} = 3×10^7 V/cm and with an applied static magnetic flux density $\vec{B}_x$ = (a) -0.5 T, (b) -1 T, (c) -1.5 T, and (d) -2 T. The color scale represents the normalized logarithmic electron count. Note the difference in axis scales.

To spatially gate the electrons at the detector, an aperture is placed in front of the detector (depicted in Fig. 3.14(b)). This opening defines the position along the detector that is exposed to electrons, as well as, the arrival angles of the electrons. By varying the diameter (d_a), thickness (t_a), and location (l_a) of the aperture, the kinetic energy and the packet length of the electron packet can be controlled. This aperture and the magnetic field strength introduce four different parameters that can be used to tailor the final

electron packet. To explore the extremely large parameter space, each parameter was given realistic bounds and swept to determine the characteristics of the final electron packet. Through predetermined selection of these parameters, the electron packet can be tailored to the specific needs for a given application.

The key characteristics defining an ultrafast electron packet are the temporal length (τ_p), and the weighted central kinetic energy (KE). Figure 3.20 depicts electron packet arrival times chosen for two illustrative sets of aperture parameters and for $\vec{B}_x$ = -0.5 T, -1 T, and -1.5 T with the corresponding τ_p and KE, labelled on the respective electron packets. The kinetic energy spread (ΔKE) has also been included for completeness. Choosing the aperture thickness to be 25 μm, the diameter to be 1 μm, and locating it 45 μm from the tip, we obtain electron packets with kinetic energies varying from 0.06 keV at $\vec{B}_x$ = -0.5 T (Fig. 3.20(a)) to 0.49 keV at $\vec{B}_x$ = -1.5 T (Fig. 3.20(c)). For $\vec{B}_x$ = -0.5 T, the packet length is 50 fs, while a packet length of 52 fs is achieved for $\vec{B}_x$ = -1 T. Notably, an ultrashort packet length of 912 as is observed at $\vec{B}_x$ = -1.5 T. The characteristic square shape of the generated electron packets depicted in Fig. 3.20 arises due to the magnetic field acting to effectively map electrons from a location on the tip to a position along the detector based on their interaction with the SP field. As such, the electrons within the detected packet will have experienced similar acceleration due to the localized SP field (i.e. resulting in similar kinetic energies and electron counts). Selecting a different set of aperture parameters (d_a = 1 μm, t_a = 9 μm, l_a = 57 μm) results in increased kinetic energies, albeit with longer duration packets, as shown in Fig. 3.20(d) - 3.20(f). Figure 3.20(d) depicts the 0.06 keV, 265 fs electron packet which is observed for

$\vec{B}_x$ = -0.5 T. Varying $\vec{B}_x$ to -1 T or -1.5 T results in 0.25 keV, 161 fs and 0.61 keV, 30 fs electron packets, respectively. The generated electron packets exit the aperture with central angles, θ_a, ranging from -8.19° to 5.69° with angular spreads, $\Delta\theta_a$, from 0.01° to 0.93°. Table 3.1 lists the central angle and the angular spread for each representative electron packet presented. It should be noted that the two sets of aperture parameters discussed above are chosen as illustrative examples and that electron packets with various desired characteristics can be chosen by modifying the parameters of the aperture.

t_a (μm)	d_a (μm)	l_a (μm)	$\vec{B}_x$ (T)	θ_a (°)	$\Delta\theta_a$ (°)
25	1	45	-0.5	-1.34	0.09
25	1	45	-1	0.49	0.19
25	1	45	-1.5	0.40	0.42
9	1	57	-0.5	-1.59	0.30
9	1	57	-1	-3.32	0.71
9	1	57	-1.5	-5.95	0.25
25	2	131.5	-1	1.31	0.17
24	5	75.5	-1	5.69	0.93
4	1	207	-1	-8.19	0.01
7	1	166	-1	-5.20	0.02
25	1	137.5	-1	-1.20	0.03
15	1	140.5	-1	-1.59	0.07

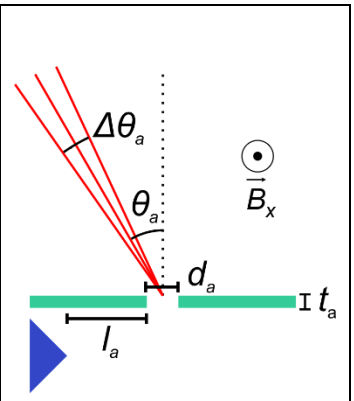

Table 3.1. Electron packet angular spread after leaving the aperture. θ_a is the central angle of the electrons and $\Delta\theta_a$ is the angular spread.

As increasing $\left|\vec{B}_x\right|$ leads to a reduction in the spatial spreading of the electrons along the length of the detector, it becomes more challenging to select aperture parameters that result in desirable electron packets at various magnetic field strengths. Therefore, it is also possible to fix $\vec{B}_x$ and examine different aperture parameters to achieve various electron packets. Figure 3.21(a)-(c) depict three illustrative femtosecond electron packets arriving at the detector for different aperture parameters at a fixed $\vec{B}_x$ = -1

T. For d_a = 2 μm, t_a = 25 μm, and l_a = 131.5 μm, an electron packet KE = 0.50 keV, and τ_p = 52 fs is observed (Fig. 3.21(a)). With d_a = 5 μm, t_a = 24 μm, and l_a = 75.5 μm, an electron packet with KE = 0.24 keV and τ_p = 25 fs is achieved (Fig. 3.21(b)). An ultrashort, high energy electron packet with KE = 1.15 keV and τ_p = 4 fs is achieved for d_a = 1 μm, t_a = 4 μm, and l_a = 207 μm (Fig. 3.21(c)). Remarkably, attosecond electron packets with kinetic energies >0.5 keV (Fig. 3.21(d)- 3.21(f)) can be achieved through proper choice of the aperture parameters. With d_a = 1 μm, t_a = 7 μm and l_a =166 μm a high energy (KE = 0.76 keV) attosecond (τ_p = 775 as) packet can be achieved. An electron packet with τ_p = 195 as and KE = 0.54 keV can be achieved with d_a = 1 μm, t_a = 25 μm and l_a = 137.5 μm. Notably, an ultrashort electron packet with τ_p = 140 as packet and KE = 0.56 keV is observed for the aperture parameters d_a = 1 μm, t_a = 15 μm and l_a = 140.5 μm. Again, the electron packet characteristics can be tuned for a specific need by tailoring the aperture parameters.

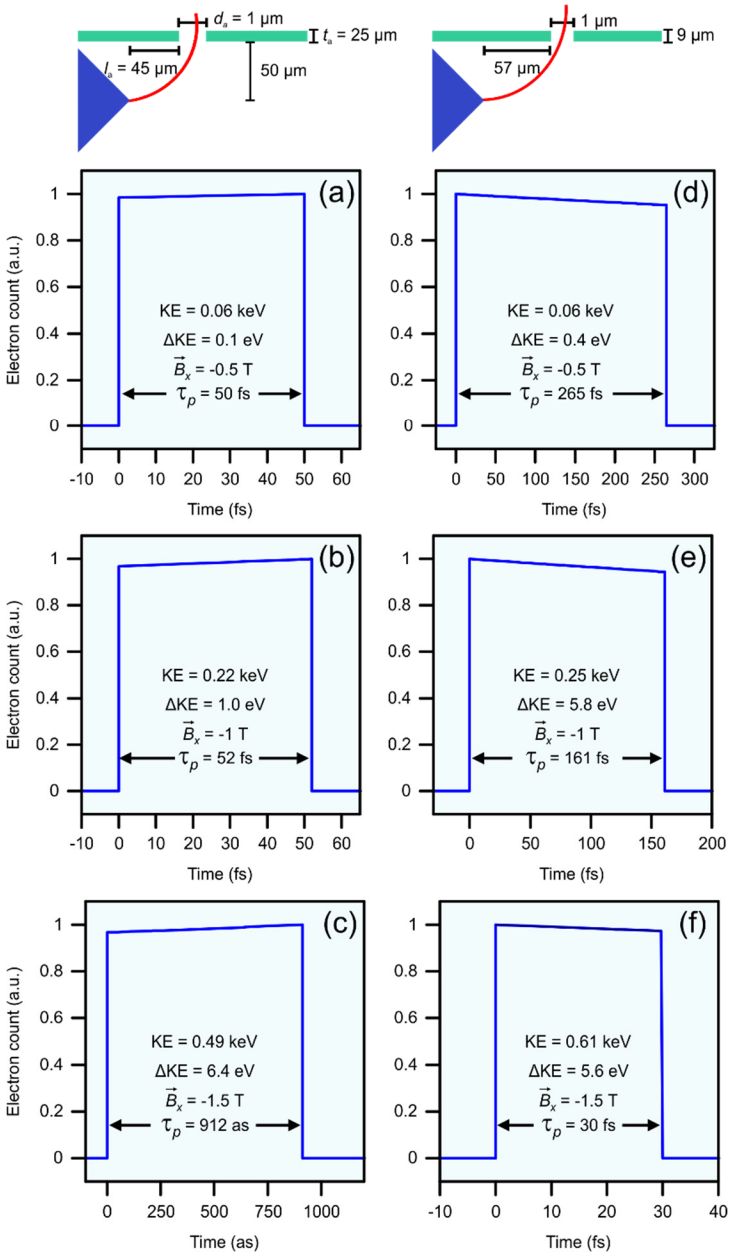

Figure 3.20. Electron packet duration at a detector placed 50 µm away from the tip, with schematic depictions of aperture parameters used at: $\vec{B}_x$ = (a) -0.5 T, (b) -1 T, and (c) -1.5 T for aperture parameters d_a = 1 µm, t_a = 25 µm, and l_a = 45 µm; $\vec{B}_x$ = (d) -0.5 T, (e) -1 T, and (f) -1.5 T for aperture parameters d_a = 1 µm, t_a = 9 µm, and l_a = 57 µm. KE is the weighted central kinetic energy, ΔKE is the kinetic energy spread, and τ_p is the temporal duration of the electron packet. Note that the schematic depictions of the aperture parameters are not to scale.

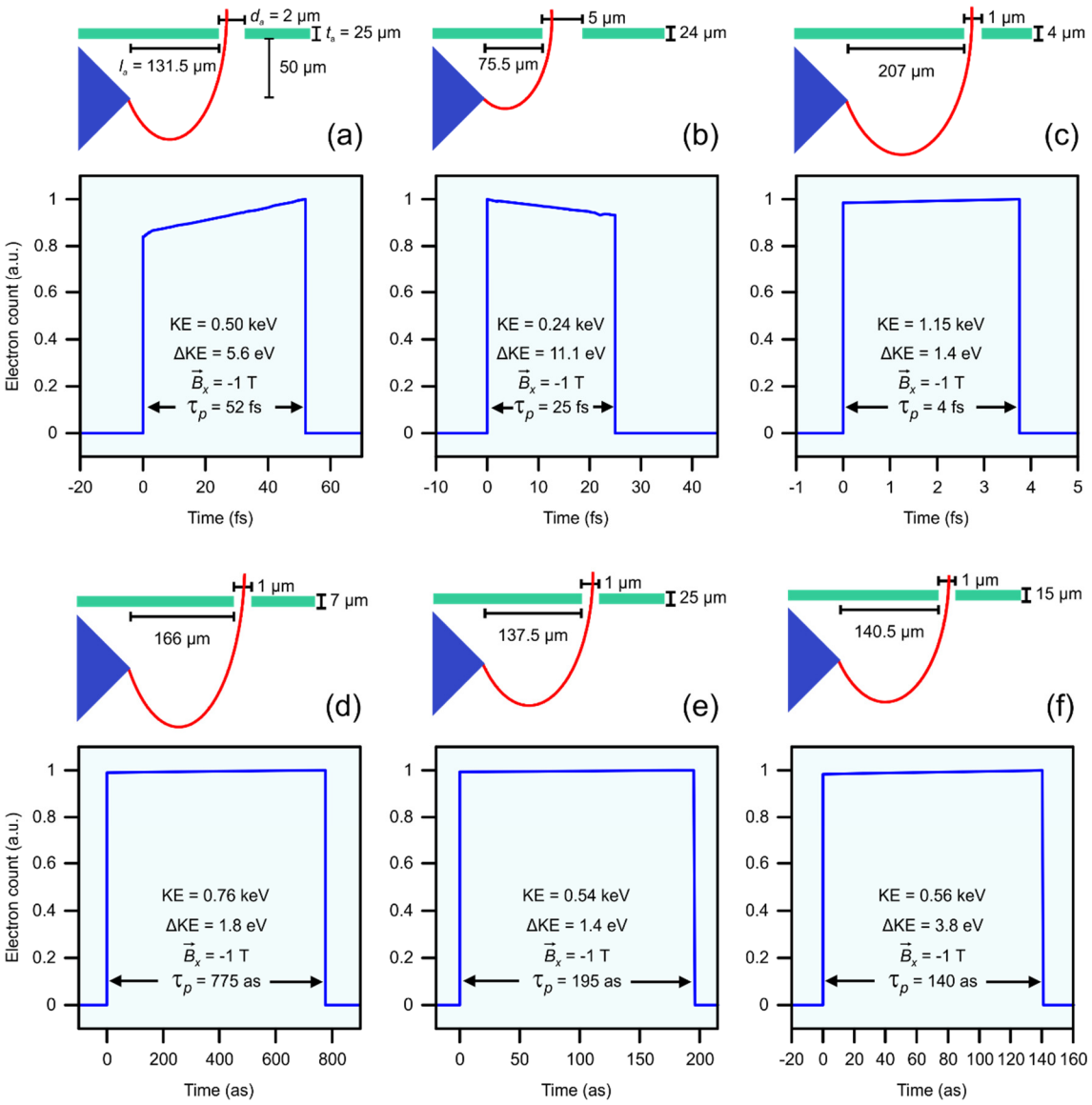

Figure 3.21. Electron packet duration at a detector placed 50µm away from the tip, at a fixed $E_{laser} = 3\times10^7$ V/cm and $\vec{B}_x = -1$ T with aperture parameters (a) $d_a = 2$ µm, $t_a = 25$ µm, $l_a = 131.5$ µm, (b) $d_a = 5$ µm, $t_a = 24$ µm, $l_a = 75.5$ µm, (c) $d_a = 1$ µm, $t_a = 4$ µm, $l_a = 207$ µm, (d) $d_a = 1$ µm, $t_a = 7$ µm, $l_a = 166$ µm, (e) $d_a = 1$ µm, $t_a = 25$ µm, $l_a = 137.5$ µm, and (f) $d_a = 1$ µm, $t_a = 15$ µm, $l_a = 140.5$ µm. KE is the weighted central kinetic energy, ΔKE is the kinetic energy spread, and τ_p is the temporal duration of the electron packet. Note that the schematic depictions of the aperture parameters above each electron packet are not to scale.

3.5. Summary

The results of this chapter demonstrate that there are multiple methods that can be employed to achieve control of electron pulses and ultimately tailor them to their intended applications. A mechanism utilizing THz pulses to control the kinetic energy spectrum of surface plasmon generated electron pulses was presented. Utilizing a single THz electric field pulse, control of the angular and energy characteristics of the generated electron pulse can be achieved. Through control of the time delay between a second ultrashort THz electric field pulse, the kinetic energy spectrum can be selectively tuned to the required range. It was also shown that carrier envelope phase information of the optical pulse can be recovered in the presence of a THz electric field. Although the THz electric field pulses can control the kinetic energy of the electrons, they still produce broad kinetic energy spectra. To overcome this limitation, a method that utilizes magnetostatic and physical filtering to generate attosecond keV electron packets was designed and modelled. By varying the strength of the applied magnetic field or modification of the parameters of an aperture placed in front of the detector, both the kinetic energy of the electrons and the duration of the electron packet can be tailored. This compact attosecond, nanoplasmonic, keV electron source opens the pathway for time-resolved electron microscopy of physical, biological, and chemical processes with sub-nanometer and sub-femtosecond resolution such as real-time imaging of the formation and breaking of chemical bonds, imaging of protein folding, and imaging of intra-atomic processes. Attosecond electron pulses can also be used for the next generation of vacuum electronics that harness the switching speed of electrons in vacuum to extend operating frequencies into the terahertz regime.

Chapter 4

Experimental High Current Electron Sources

4.1. Introduction

In this chapter, experimental demonstration of multiple methods to increase the electron yield of SP based electron sources is presented. The main drawback to using SP to generate electron pulses is that at low intensities, the electron generation mechanism occurs in the multi-photon regime. As such, 3 or more photons are required to liberate an electron from the plasmonic metal, resulting in a very low electron yield or requiring high intensity laser pulses. The number of photons required can be reduced by lowering the potential energy barrier at the metal-vacuum interface via application of a strong enough electric field either from a DC bias or the electric field of the laser pulse itself. Both approaches have drawbacks though, namely the DC electric field breakdown or the laser induced damage threshold of the materials involved. To develop the next generation of ultrafast electron sources, it is important to reduce the number of photons required while utilizing low laser light intensities.

The first section of this chapter details the experimental setup that is used to carry out the experiments. The following sections explore the use of a non-metallic/metallic bilayer film to reduce the nonlinear electron emission order, thus increasing the electron yield. The final section details work on an ultrafast high current plasmon driven secondary electron source that harnesses the increased current of an external electron beam. Also

included in this chapter is a detailed investigation of the interaction of free, non-SP generated, electrons with strong SP fields.

4.2. Experimental Setup

This section aims to describe the various experimental setups that were used throughout this chapter. The base setup used for the experiments consists of three distinct sections, the laser system, the vacuum system, and the detection setup. Briefly, laser pulses from either a laser oscillator or a chirped-pulse-amplifier (CPA) are directed through a chopper and variable neutral density filter before being directed towards the vacuum chamber where electrons are detected with the detection setup. The following subsections describe each separate subsystem in detail.

4.2.1. Laser System

Figures 4.1(a)-(b) depict a photograph and a schematic of the laser system, respectively. Laser pulses are obtained from a commercial FemtoLasers Kerr-lens mode-locked Ti:Sapphire laser oscillator capable of supplying 15 fs duration pulses with a central wavelength of 800 nm and a maximum pulse energy ~5 nJ at a repetition rate of 76 MHz. The pulse train from the oscillator passes through an optical chopper and a variable neutral density filter before being directed to the experimental setup. Flipper mirror F3 can be used to direct the pulse train to a few beam diagnostic tools such as a GRENOUILLE ultrafast pulse measurement tool (Swamp Optics GRENOUILLE 8-9-USB), or an optical spectrometer (Ocean Optics USB4000). Figures 4.2(a)-(b) depict the measured and retrieved FROG traces, respectively, of the output of the Ti:Sapphire oscillator. The corresponding extracted time and spectral plots including phase are depicted in Fig. 4.3(a)-(b), respectively. From the FROG trace, a pulse duration of 17.4 fs

(FWHM) is obtained as well as a FWHM bandwidth of 58 nm. This specific model of GRENOUILLE is unable to correctly measure the entire broadband frequency spectrum of the laser pulse. As such, a full spectrum was obtained from the optical spectrometer as depicted in Fig. 4.4, demonstrating a broad FWHM bandwidth of 122 nm.

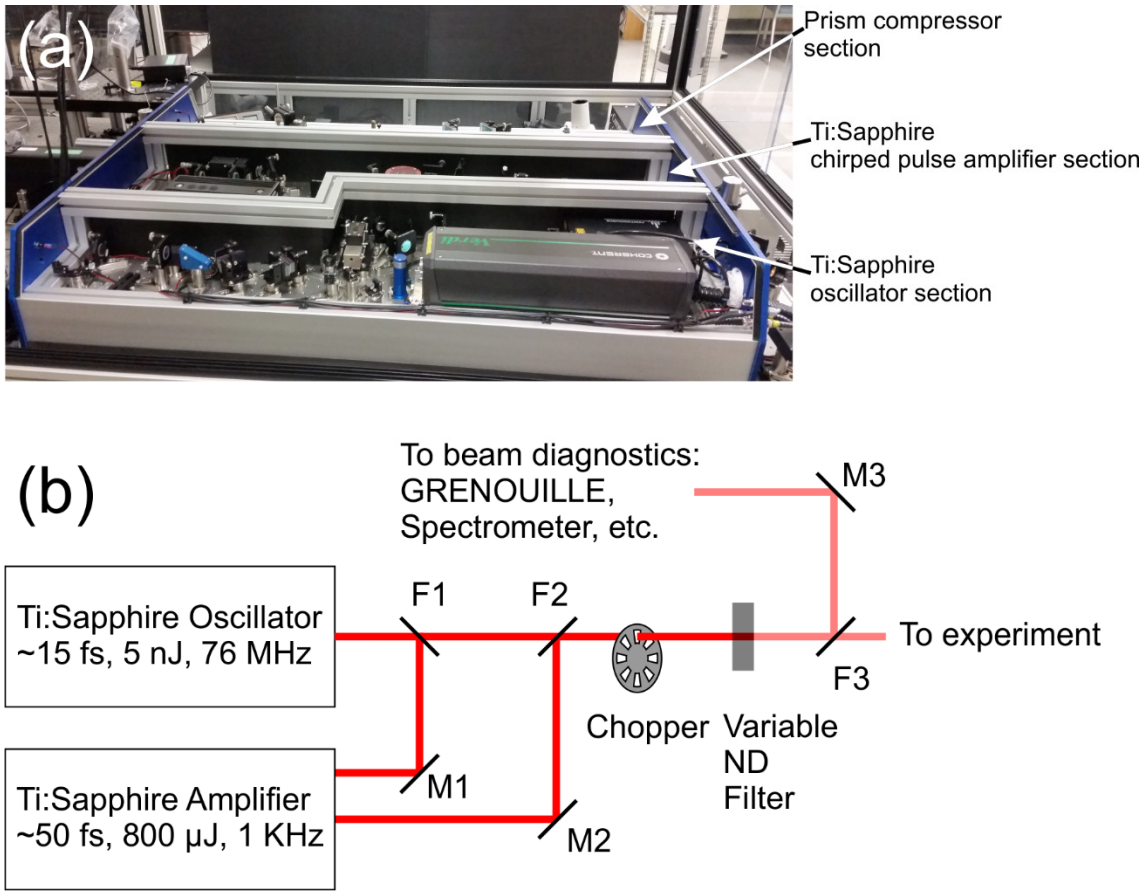

Figure 4.1. (a) Photograph of the three sections of the laser system used: the Ti:Sapphire oscillator, the Ti:Sapphire chirped-pulse-amplifier, and the prism compressor. (b) Schematic depiction of the laser setup used throughout the experiments. F: flipper mirror, M: fixed mirror, ND: neutral density filter. F1 and F2 are placed in the beam path to use the pulse train from the oscillator as the seed for the amplifier. F3 is used to direct the pulse train to either the GRENOUILLE or optical spectrometer for diagnostics.

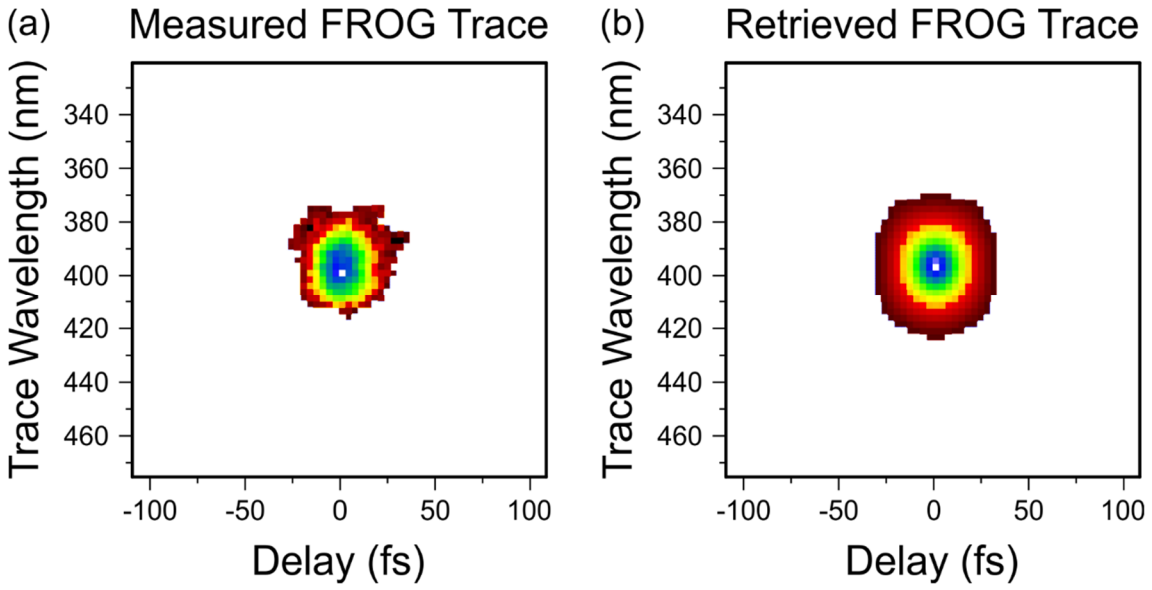

Figure 4.2. (a) Measured and (b) Retrieved FROG traces obtained from the GRENOUILLE 8-9-USB.

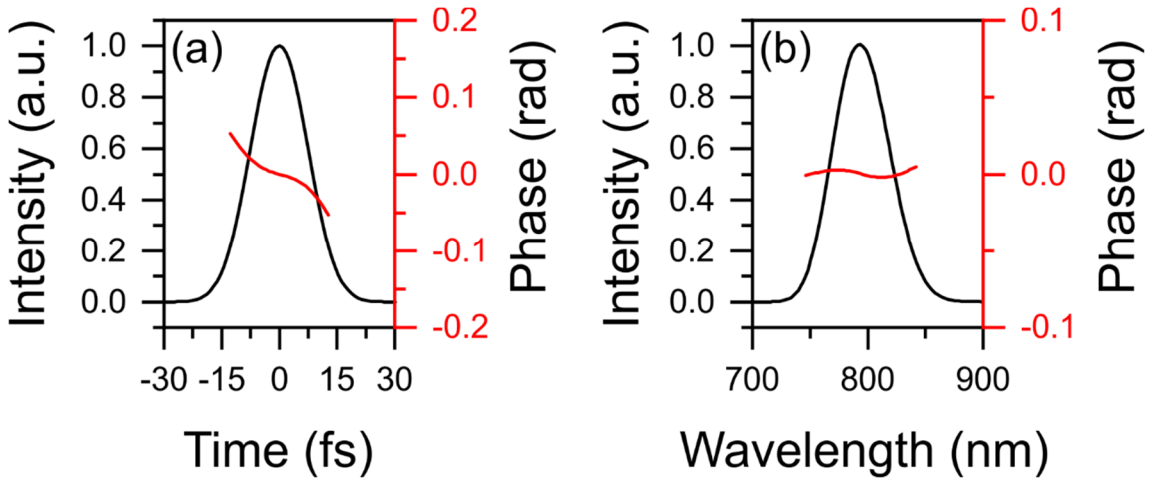

Figure 4.3. Extracted (a) temporal and (b) spectral traces from the FROG results. The red curves depict the phase.

To obtain higher intensities, the output from the laser oscillator can be used to seed a FemtoLasers Ti:Sapphire chirped-pulse-amplifier (CPA) by moving flipper mirrors F1 and F2 into the beam path. Using a prism compressor at the output, the CPA can supply 25 fs pulses with pulse energies up to ~800 μJ at a repetition rate of 1 KHz.

Due to the high pulse energy at the location of the sample, the FROG trace could not be measured. Figures 4.5(a)-(b) depict the intensity autocorrelation and frequency spectrum of the output of the CPA, indicating a FWHM pulse duration of 21 fs and a FWHM bandwidth of 36.8 nm. As the output beam diameter of the CPA is ~10 mm, the beam is directed through a two-lens telescope to reduce the beam size to ~4 mm diameter. This disperses the amplified laser pulse to a final pulse duration of ~50 fs.

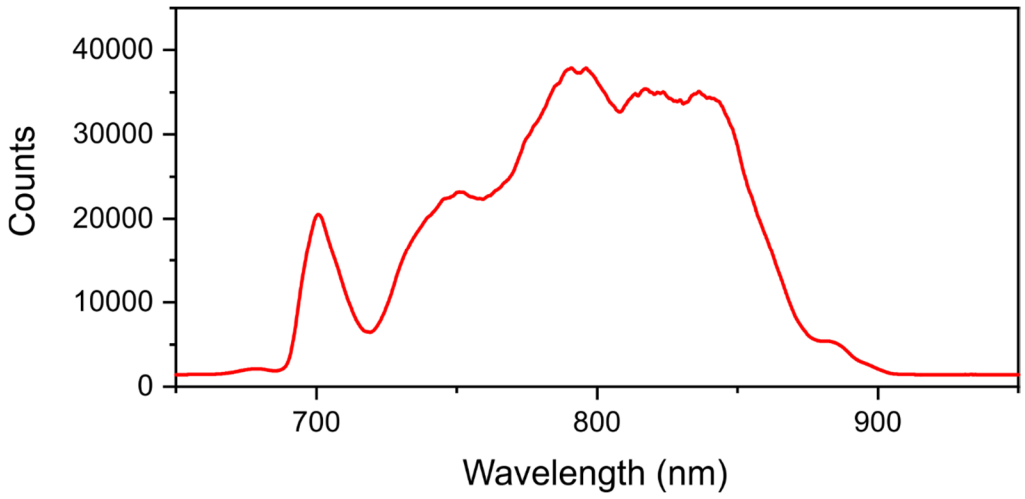

Figure 4.4. Broadband laser pulse spectrum from mode-locked Ti:Sapphire oscillator obtained with optical spectrometer.

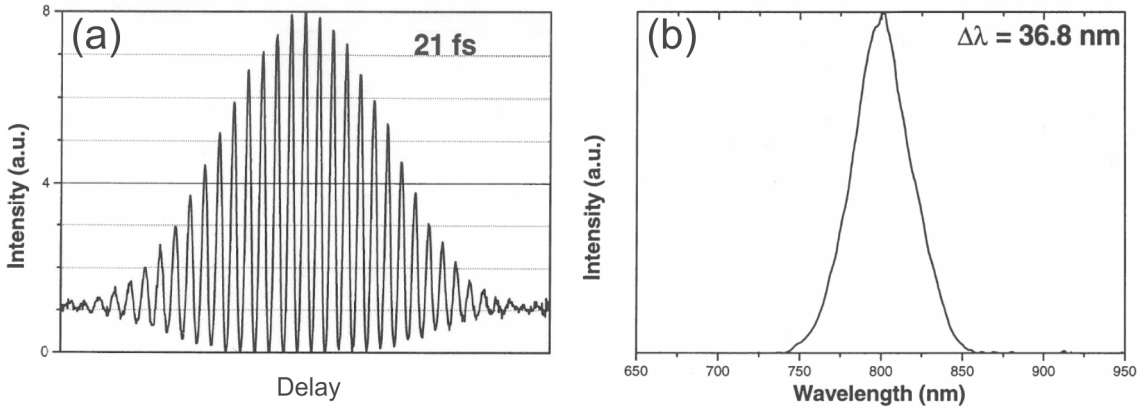

Figure 4.5. (a) Intensity autocorrelation trace and (b) laser pulse spectrum of the chirped pulse amplifier.

4.2.2. Vacuum Chamber

A few iterations of the vacuum chamber have been used for experiments, but for brevity only the most recent configuration will be discussed below. Figure 4.6 depicts a photograph of the vacuum chamber. It consists of a main 12" diameter chamber with various ConFlat vacuum flanges around the perimeter and protruding from the bottom. To allow for optical components to be mounted inside, a round steel optical breadboard is mounted inside the main chamber. A top down schematic diagram of the interior of the vacuum chamber (without electrical connections) is shown in Fig. 4.7(a) with corresponding photograph in Fig. 4.7(b). Laser pulses are coupled into the vacuum chamber through a thin glass window, after which they pass through a lens, L1, and are directed by a mirror towards the sample holder in the middle of the chamber. L1 is mounted on a translation stage that is controllable from outside the vacuum chamber. This allows for tuning of the laser spot size while the chamber is under vacuum. The sample holder was designed by me and consists of a circular platform mounted on a mechanical feedthrough from the bottom of the chamber. Figures 4.8(a)-(b) depict a photograph of the sample holder and the mechanical feedthrough, respectively. This allows the sample to be translated in 3-dimensions as well as rotated about the central axis. As many of the experiments being carried out in this setup use the Kretschmann geometry to excite surface plasmons, the rotation allows for the highest plasmon coupling, and hence highest photoemission to be achieved. A rack and pinion system driven by a stepper motor (Oriel Motor Mike 18212) can be mounted on the sample holder, as shown in Fig. 4.9, to allow for angularly resolved measurements with various detectors. A commercial electron gun (VG Electronics LEG32) is mounted on one of the vacuum chamber flanges and is directed towards the center of the chamber as shown in

Fig. 4.7(b). The electron gun supplies a continuous electron beam with an energy of 0.1-5 keV in discrete 0.1 keV steps and a beam current up to 2 microamps. Deflectors within the electron gun allow for x-y steering and an electrostatic lens allows for focusing of the electron beam. The entire vacuum chamber is pumped with a turbomolecular pump (Adixen Alcatel ATP80) backed by a dry membrane roughing pump (Leybold EcoDry M15). This setup can achieve pressures of ~10^{-5} Torr.

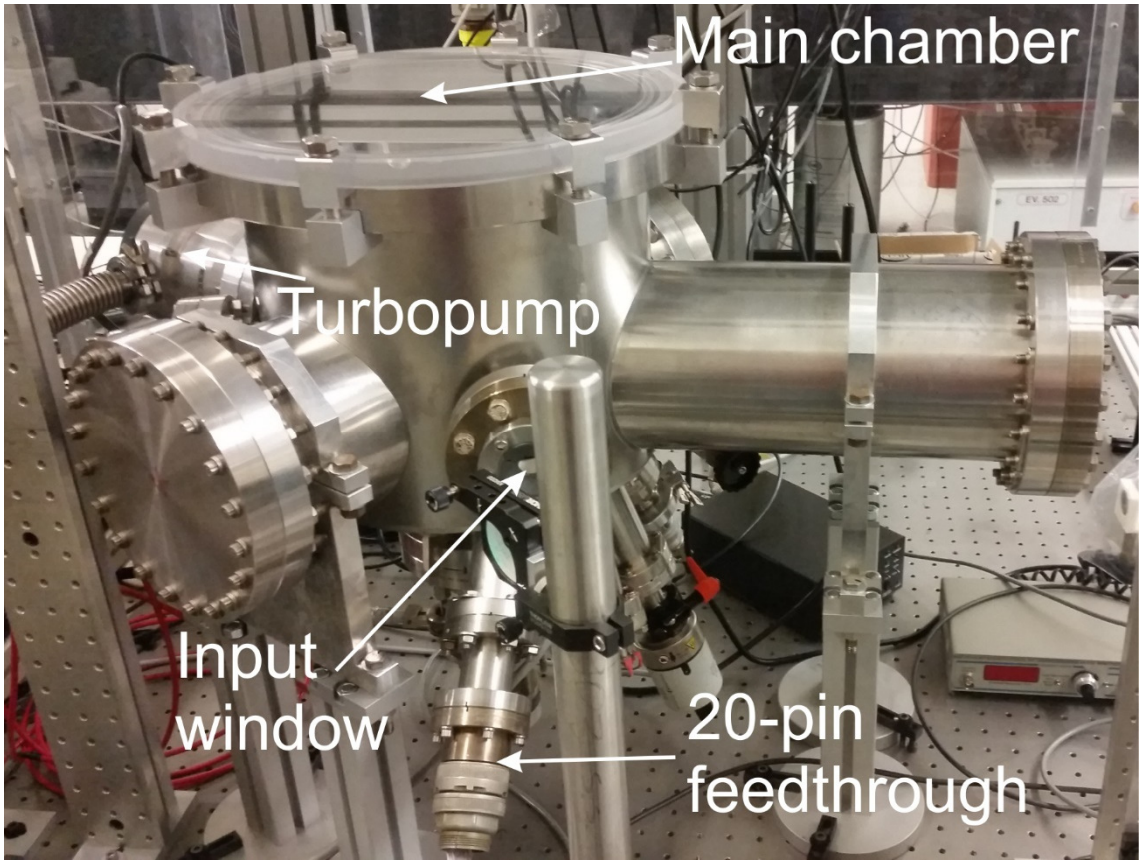

Figure 4.6. Photograph of current vacuum chamber exterior.

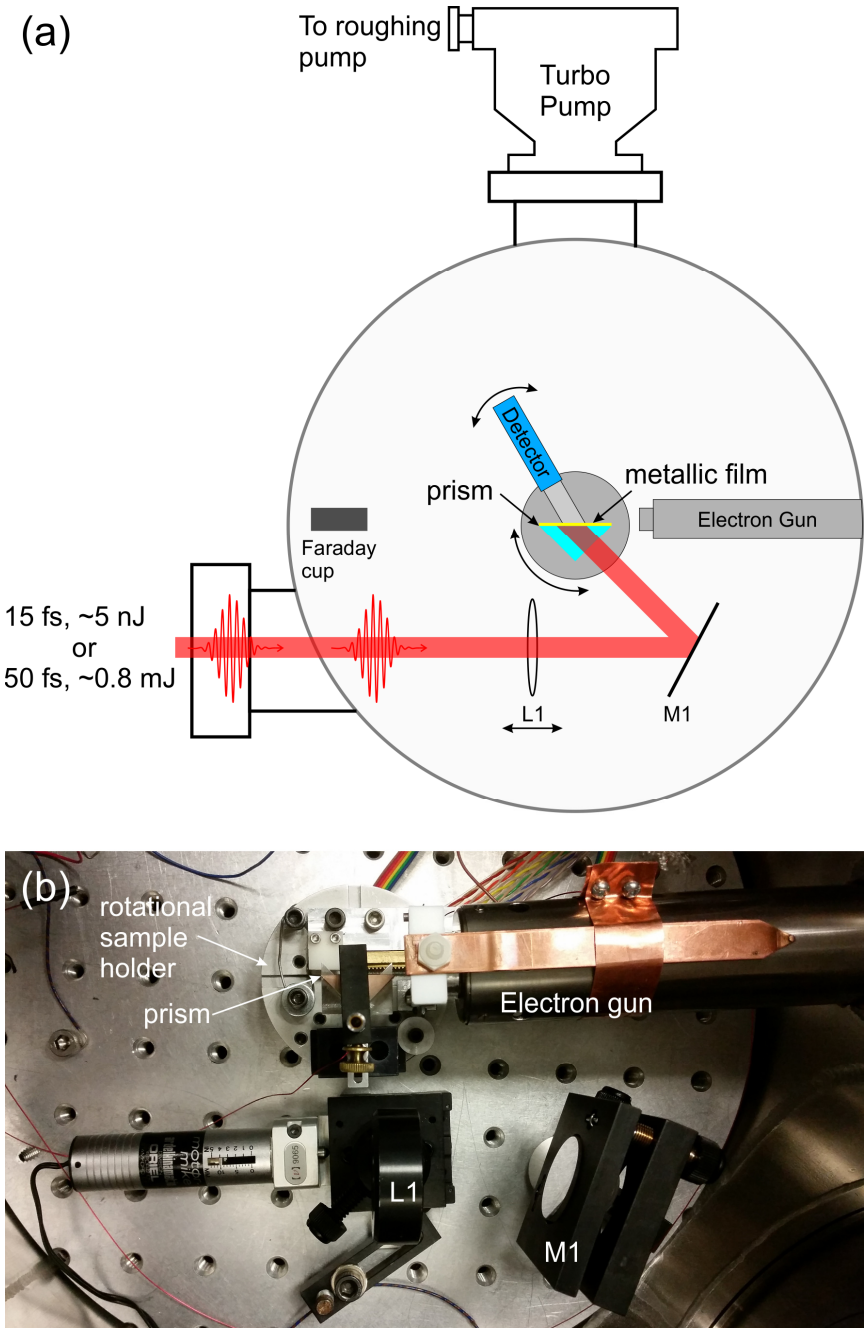

Figure 4.7. (a) Schematic depiction of the vacuum chamber setup. Different detectors can be used as needed and can be swept angularly for angle-resolved measurements. The focusing lens L1 is mounted on a translation stage operated from outside the vacuum. The Faraday cup allows for on-line monitoring of the electron gun current. The turbopump allows for base pressures ~10^{-5} Torr. (b) Photograph of the interior of the vacuum chamber, note that the Faraday cups are not pictured.

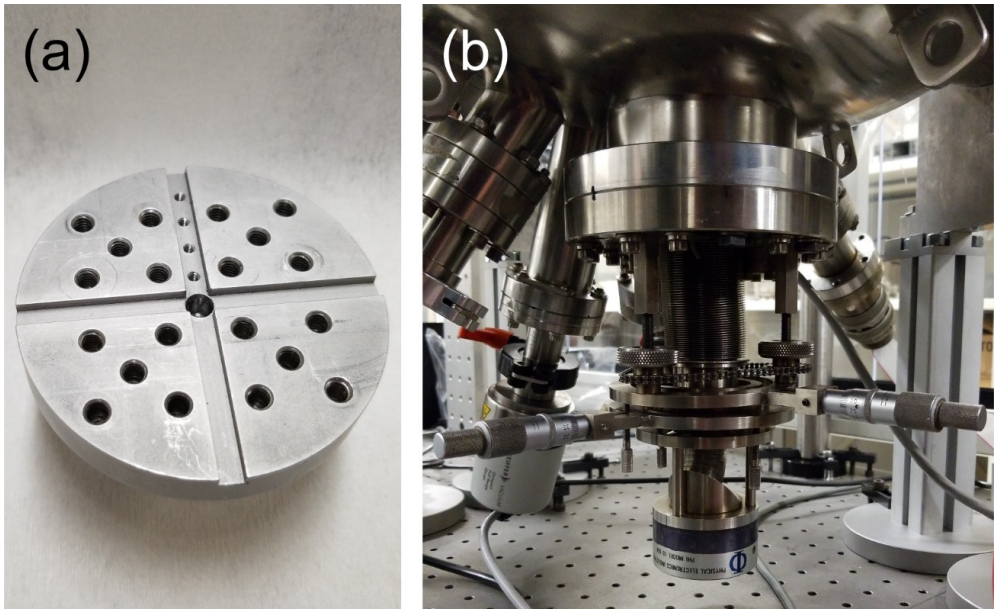

Figure 4.8. Photograph of (a) circular sample holder, and (b) 3-axis rotational feedthrough.

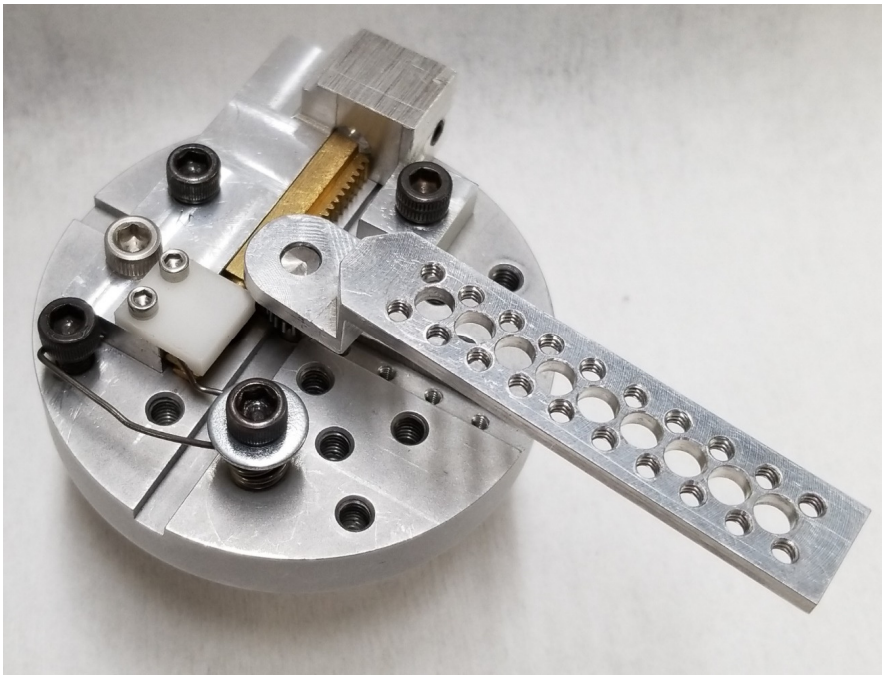

Figure 4.9. Rack and pinion system for angularly resolved measurements. Note that the stepper motor is not pictured.

4.2.3. Detection System

Multiple detectors are used for the photoemission experiments and are interchanged as necessary, they include a Ceremax 7596m channeltron electron multiplier (Fig. 4.10(a)), a Hamamatsu R5150-10 discrete dynode electron multiplier (Fig. 4.10(b)), and various copper (Fig. 4.10(c)) and steel (Fig. 4.10(d)) Faraday cups. The output of the detector is connected to either an electrometer (Keithley 619) or a lock-in amplifier (Stanford Research SR830) depending on the given experiment. An optical chopper (Stanford Research SR540) in the laser beam path provides the reference signal for the lock-in amplifier. To increase the sensitivity of the detection setup, a low-noise current amplifier (Stanford Research SR570) is used when needed. Electrical connections are provided by three electrical feedthroughs mounted on the bottom of the chamber. Detailed wiring diagrams for the electrical feedthroughs and detector connections can be found in Appendix B.

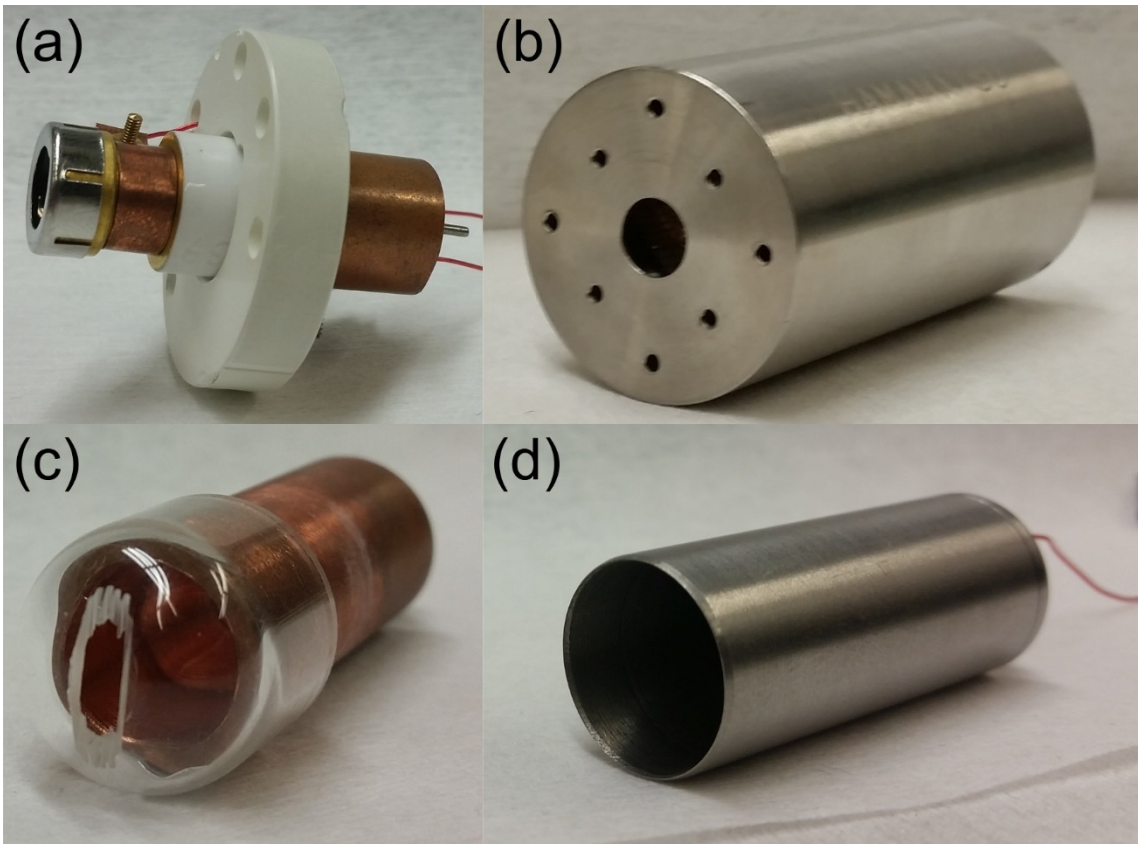

Figure 4.10. Various electron detectors used throughout the experiments: (a) Ceremax 7596m channeltron electron multiplier, (b) Hamamatsu R5150-10 discrete dynode electron multiplier, (c) copper Faraday cup with glass slit to reduce acceptance angle, and (d) steel Faraday cup.

To measure kinetic energy spectra, the retarding potential method is used, which utilizes a grid connected to a voltage, V_{RP} to act as a high pass filter for the electrons, as depicted in Fig. 4.11. Only electrons with kinetic energies greater than qV_{RP} will pass through the grid to be collected by the detector. As such, the measured signal is the integral of kinetic energy and must be differentiated to obtain the true kinetic energy spectrum. Although the retarding potential approach is simple its resolution is ultimately limited by the stability of V_{RP} and the uniformity of the electric field on the grid. To improve the uniformity of the electric field, I designed and built a compact retarding

potential analyzer (RPA) based on designs from [66,67] that could be mounted directly to the front of the electron multiplier or channeltron (with an adapter). The RPA consists of two sections separated by a dielectric (acrylic) spacer and is shown in Fig. 4.12. The front piece is grounded and has a small input aperture (1-3 mm depending on the mounted front piece). The rear cylinder is connected to V_{RP} and is covered at the back by a standard retarding potential grid. This cylinder helps to create a more uniform field distribution between the grounded front piece and the retarding potential grid. Mechanical drawings of the RPA are included in Appendix C. The major disadvantage of the RPA is that due to its physical size it is not always the appropriate choice for kinetic energy measurements, as such a standard retarding potential grid is used for some experiments.

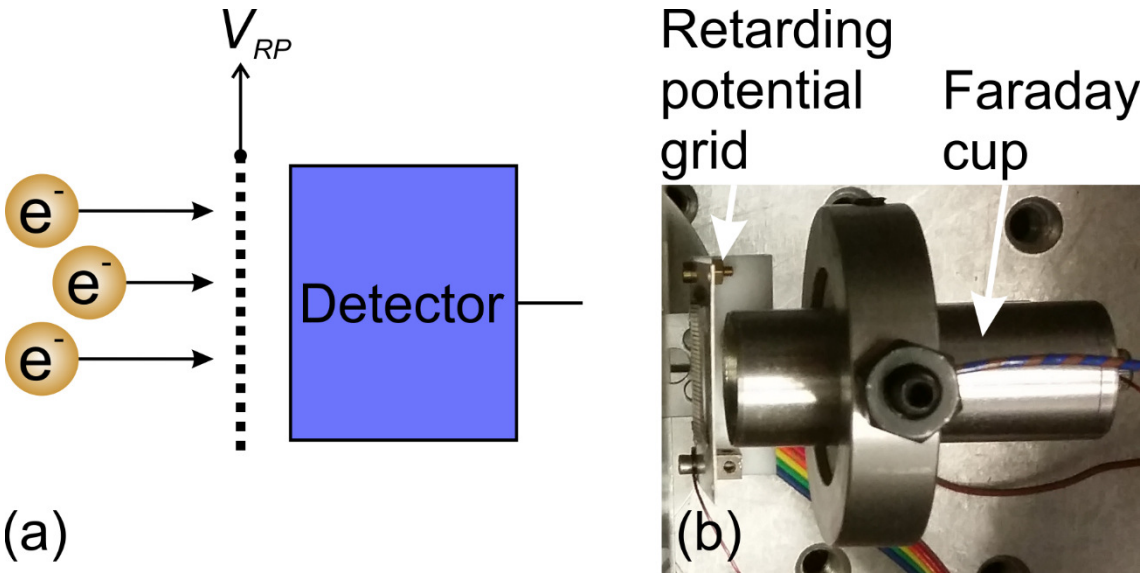

Figure 4.11. (a) Schematic depiction and (b) photograph of retarding potential setup used for measuring electron kinetic energy.

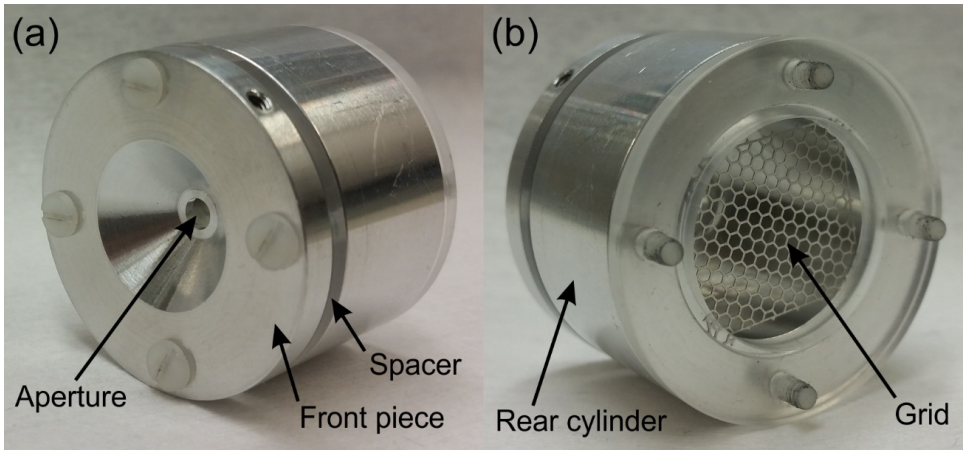

Figure 4.12. Retarding potential analyzer (RPA) (a) front, and (b) rear.

In order to achieve a higher kinetic energy resolution, I also designed and built a double-pass cylindrical mirror analyzer (CMA) based on the work in [68,69]. The completed CMA is depicted in Fig. 4.13. Details of the mechanical design and electromagnetic/particle tracking simulations are discussed in Appendix D.

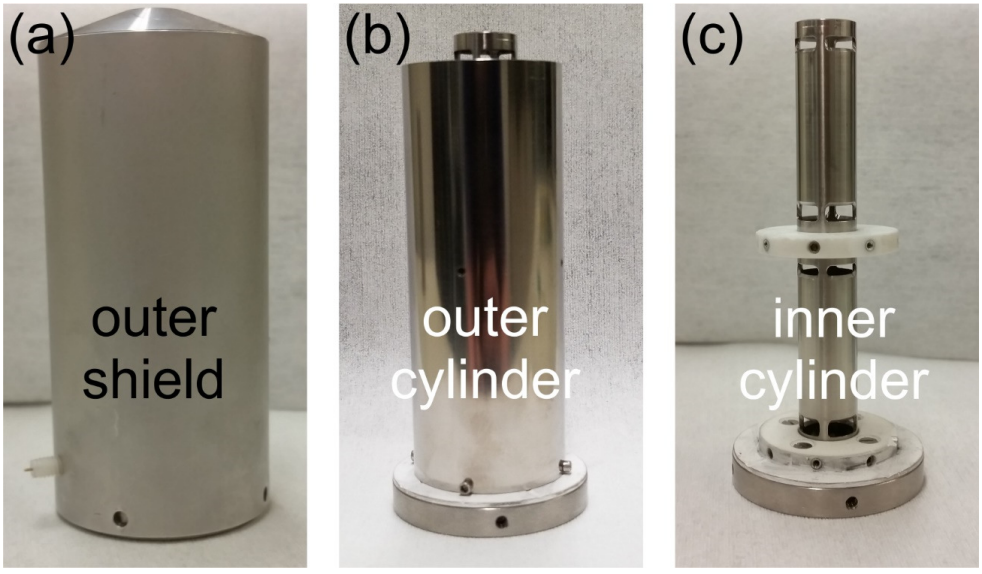

Figure 4.13. Double-pass cylindrical mirror analyzer (CMA). (a) Fully assembled CMA. (b) Outer shield removed. (c). Outer cylinder removed revealing the electron slits in the inner cylinder.

4.2.4. Graphical User Interface for Electron Experiments

To correctly identify small signals on the lock-in amplifier, such as the output from a Faraday cup, it is necessary to accumulate data points for long periods of time and compute the median value. This is easily automated, so I designed and developed a MATLAB based graphical user interface (GUI). Figure 4.14 depicts a screenshot of the GUI. The program allows the user to select various lock-in settings such as time constant, sensitivity and data sampling rate. The user can then select the type of experiment they are doing such as energy, power scaling, angle, shutter time series, or other. When a new data point is taken, the program instructs the lock-in amplifier to accumulate data at the specified sampling rate for the time specified. Once the time has elapsed, the raw data from the lock-in (R and θ) is transferred to the computer and the median value is calculated. The data is then added to the table and the plot. The value displayed in the table and plot can be selected to be either R, X, or Y. To use the shutter controls or the shutter experiment type, a shutter controller (Uniblitz VCM-D1) is connected to the lock-in amplifier with the shutter being placed in the laser beam path. When using the shutter experiment type, the shutter is opened before the point is taken and closed when it is finished. The program then waits the specified step size (in minutes) before taking another measurement.

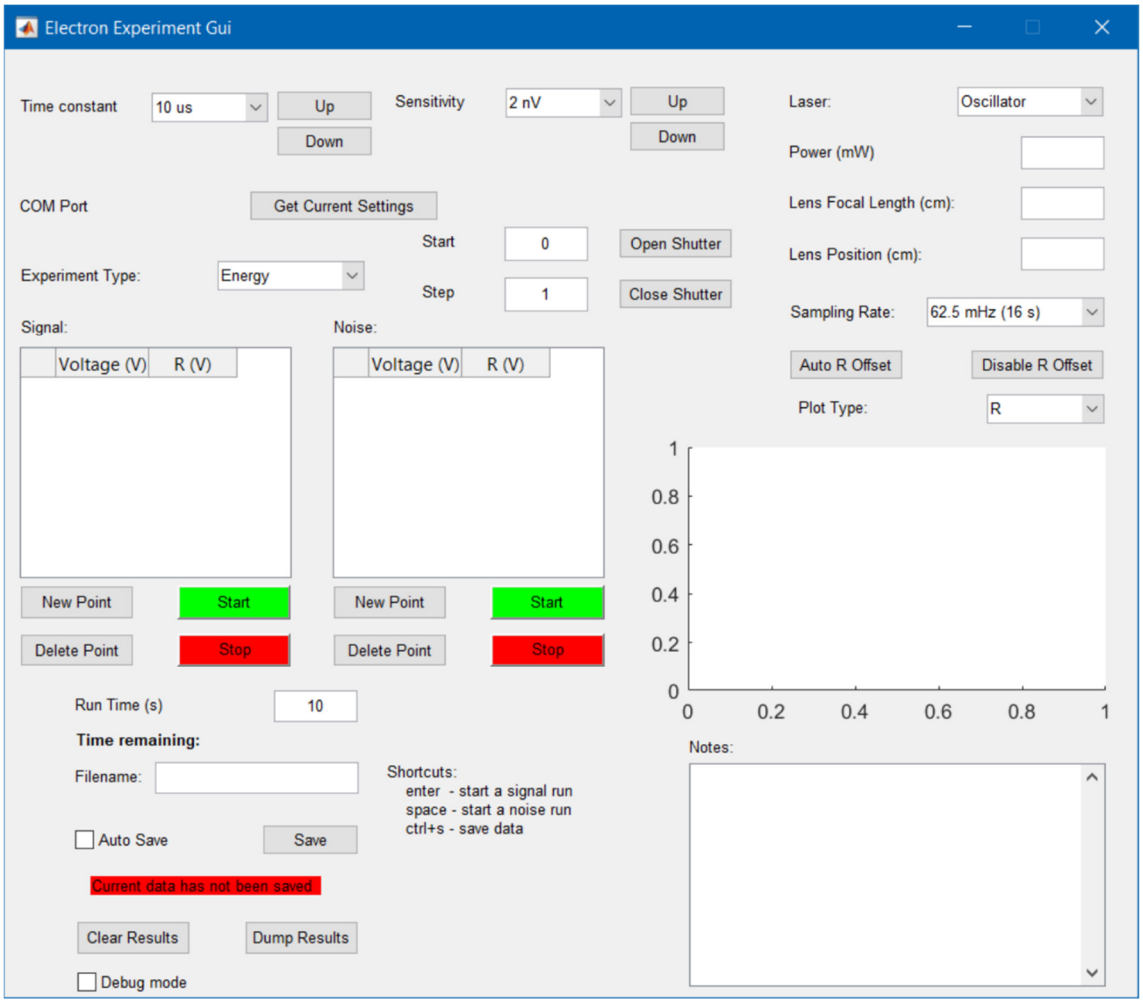

Figure 4.14. Electron experiment GUI for control of data collection using the lock-in amplifier.

4.3. Surface Plasmon Driven Lowering of the Electron Emission Order in an eCarbon/Gold Bilayer[5]

To increase the electron yield of a SP based electron source, one requires an alternative source of electrons that acts in unison with the plasmonic metal. As such, a nonmetallic material can be introduced that acts as a source/reservoir of electrons. However, there are two issues that need to be addressed using this approach: a

[5] A version of this section is published as S.R. Greig, A. Morteza-Najarian, R.L. McCreery, and A.Y. Elezzabi, "Surface Plasmon Driven Lowering of the Electron Emission Order in a Carbon/Gold Bilayer Film," *Appl. Phys. Lett.* **109**, (2016).

nonmetallic/metallic surface interface can introduce an inversion/depletion region that will impede the flow of electrons into the metal layer; and the nonmetallic material can interfere with the coupling and propagation of the SP at the metal-vacuum interface. This limits the choices of nonmetallic materials to dielectrics with low absorption so as not to disturb the SP field at the metal-vacuum interface and whose Fermi level lines up exactly with that of the metal. This section explores the use of a thin dielectric film composed of electron beam evaporated carbon (eCarbon or eC) as a reservoir of electrons beneath an Au plasmonic film to reduce the nonlinear electron emission order of a SP based electron source.

4.3.1. eCarbon

Before studying the effects of introducing eCarbon into a plasmonic system, it is important to understand some physical and optical properties of the material itself. The eCarbon films used in these experiments were deposited in Dr. Richard McCreery's lab in the National Institute for Nanotechnology (NINT) at the University of Alberta. The films were deposited by standard electron beam evaporation at a rate of <0.01 nm/sec using a target of spectroscopic graphite rods (SPI Supplies, PA). eCarbon is an amorphous form of carbon and the deposited films consist of approximately 30% sp^3 hybridized carbon, with the remainder sp^2 [70]. The sp^2 corresponds to a graphite like structure while the sp^3 is closer to a diamond-like structure.

eCarbon's most important feature is that it produces extremely flat films with RMS surface roughness <1 nm. Remarkably, this flatness is maintained for films deposited on top of the eCarbon, meaning it can be used as a sort of buffer layer to

produce smooth metallic films. Figures 4.15(a)-(b) show atomic force microscope (AFM) images of a 45 nm Au layer deposited on a fused-silica prism at two different locations. The RMS surface roughness of each location is 1.19 nm and 0.85 nm. For a 10 nm eCarbon layer beneath a 45 nm Au layer on a similar prism, the surface roughness is reduced to 0.88 nm and 0.81 nm as seen in Fig. 4.15(c)-(d). For SP based electron sources, the lower surface roughness of the eC/Au bilayer should allow for reduced radiative scattering loss as the SP propagates along the film, potentially increasing the various performance characteristics of the source.

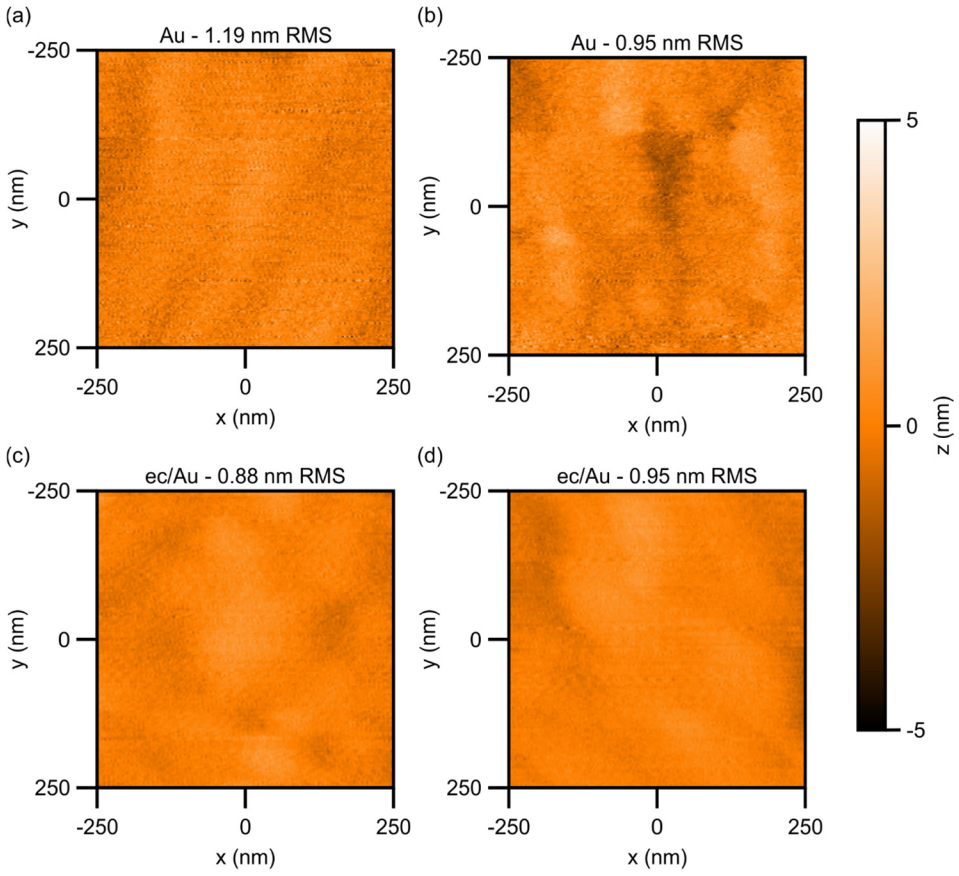

Figure 4.15. AFM images for (a) Au film location 1, (b) Au film location 2, (c) eC/Au location 1, and (d) eC/Au film location 2 indicating the reduced surface roughness for the eC/Au film.

It is important to understand the optical characteristics of all materials employed in a plasmonic system. As such, spectroscopic ellipsometry was used to determine the complex refractive index of the eCarbon film. By fitting the ellipsometry data to a model for Al_2O_3 (a diamond-like structure), the complex refractive index for eCarbon over the range of 600-1000 nm was determined. The refractive index of eCarbon at 780 nm is $n = 3.26 + i0.53$ and refractive index over the spectral range 600-1000 nm is depicted in Fig. 4.16. This model was used for FDTD simulations throughout this section.

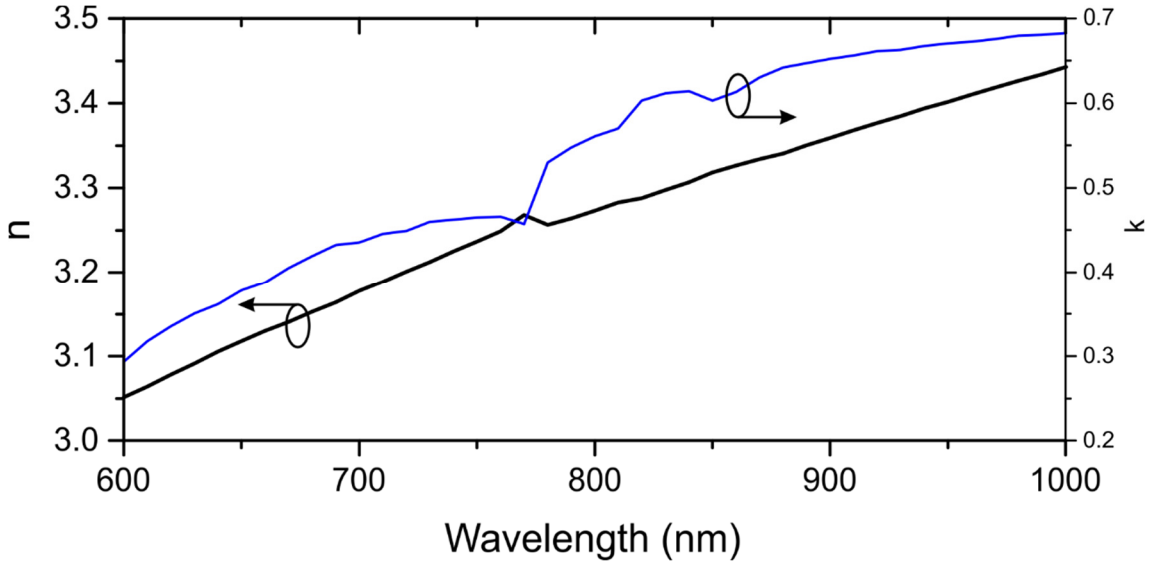

Figure 4.16. eCarbon refractive index and extinction coefficient from 600-1000 nm.

4.3.2. Electron Emission from an eCarbon/Gold Bilayer

Two samples were prepared, one with a 45 nm Au film on a UV fused silica prism, and the second with a 10 nm layer of eC underneath a 45 nm Au film. To determine the nonlinear electron emission order of each sample, they were placed in a vacuum chamber and SP waves were excited using 15 fs laser pulses having a central wavelength of 780 nm focused to a 140 μm diameter spot size. The photoemitted current

is measured using the channeltron electron multiplier connected to a lock-in amplifier through a current amplifier. The channeltron is operated at a bias of +2.4 kV, the current amplifier provides 20 nA/V gain, and a 3 second time constant was used on the lock-in amplifier to reduce signal fluctuations.

As previously mentioned, introducing a dielectric layer beneath the Au film may introduce a built-in potential difference due to a difference in the Fermi levels of the two materials. Figure 4.17(a) depicts the ultraviolet photoemission spectroscopy (UPS) spectra for a 10 nm eC film, a 20 nm Au film, and an eC/Au bilayer film. The onset of electron photoemission from all three films arises at 4.8 eV (inset of Fig. 4.17(a)), indicating that the Au, eC, and eC/Au films have the same work function of 4.8 eV. Therefore, the Fermi levels of the eC and Au line up and will not create an inversion layer that would produce a built-in potential. This is confirmed by measuring the current-voltage behavior of the eC/Au contact. The linear behavior of a four-point current-voltage electrical measurement, shown in Fig. 4.17(b), of the eC/Au contact junction confirms the absence of a built-in field at the eC/Au interface [5].

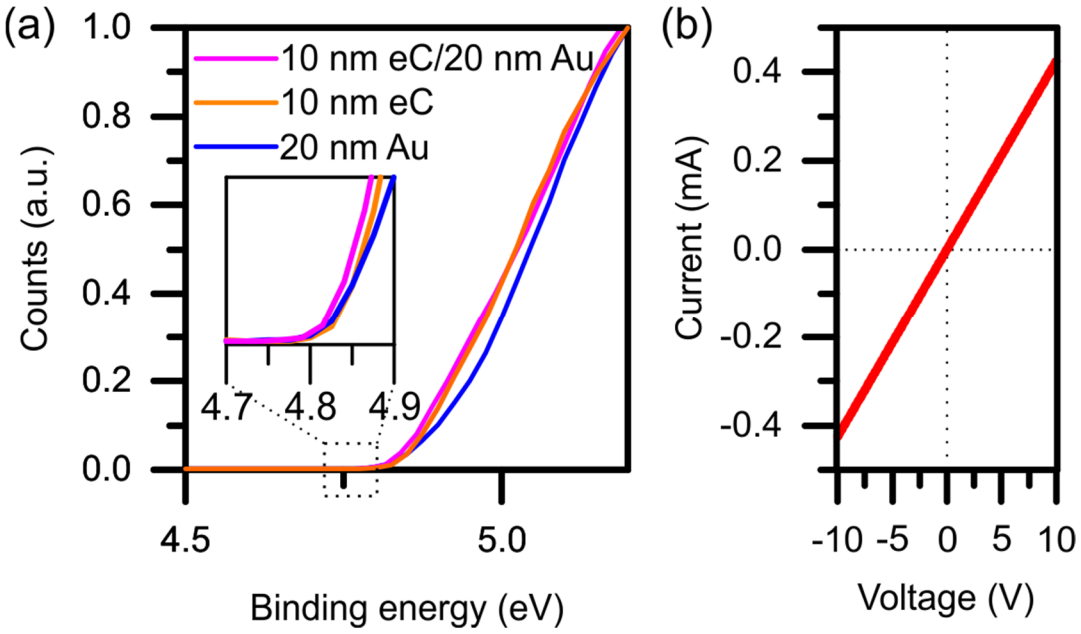

Figure 4.17. (a) Measured ultraviolet photoemission spectroscopy spectra for a 10 nm eC film, a 20 nm Au film, and a 10 nm eC film beneath a 20 nm Au film, indicating a 4.8 eV work function for eC and Au alone, and the eC/Au bilayer. (b) Four-point current vs. voltage measurement indicating the absence of a built-in field at the eC/Au interface.

After confirming that there will be no detrimental electrical effects introduced by the eC layer, the plasmonic performance of the eC/Au bilayer was studied. Figure 4.18 shows the measured reflected laser pulse spectrum at the SP resonance of each film. The spectrum was measured with an Ocean Optics USB4000 optical spectrometer. As the pulse used for excitation is quite broadband, a lens was used after the prism to collect all the wavelengths of the pulse as they would normally disperse in space. At the SP resonance approximately 8-10% of the incident light is reflected. It should be noted that the spectra are normalized, as such their counts cannot be directly compared. The black curve illustrates the spectrum of the laser pulse reflected off an Au mirror. The results indicate that the eC layer does not affect the plasmonic coupling compared to a standard Au film. Furthermore, these results indicate that the entire spectrum of the laser pulse is

being coupled into the SP wave. This is confirmed by performing FDTD simulations that find the SP electric fields at the Au-vacuum interface are within 5% of each other for each sample. A cut of the laser electric field squared, $|E_{laser}|^2$, along a direction normal to the surface of the films, determined by FDTD simulations, is depicted in Fig. 4.19(a)-(b) for the Au layer by itself and the eC/Au bilayer, respectively. The material parameters for eC and Au were determined by spectroscopic ellipsometry. Clearly, the introduction of the thin eC layer does not alter the SP coupling.

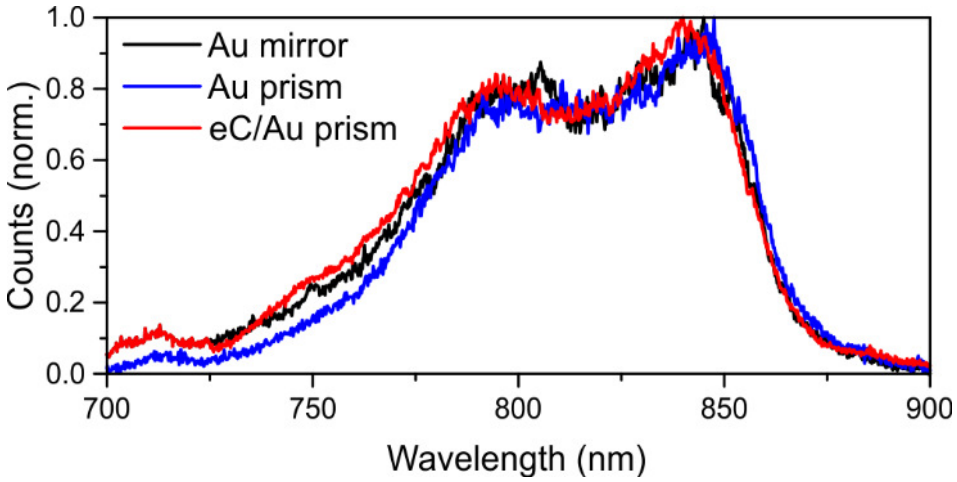

Figure 4.18. Spectrum of reflected laser pulse from Au and eC/Au films at the SP resonance. The black curve shows the spectrum of the laser pulse reflected from an Au mirror. Note that the counts are normalized.

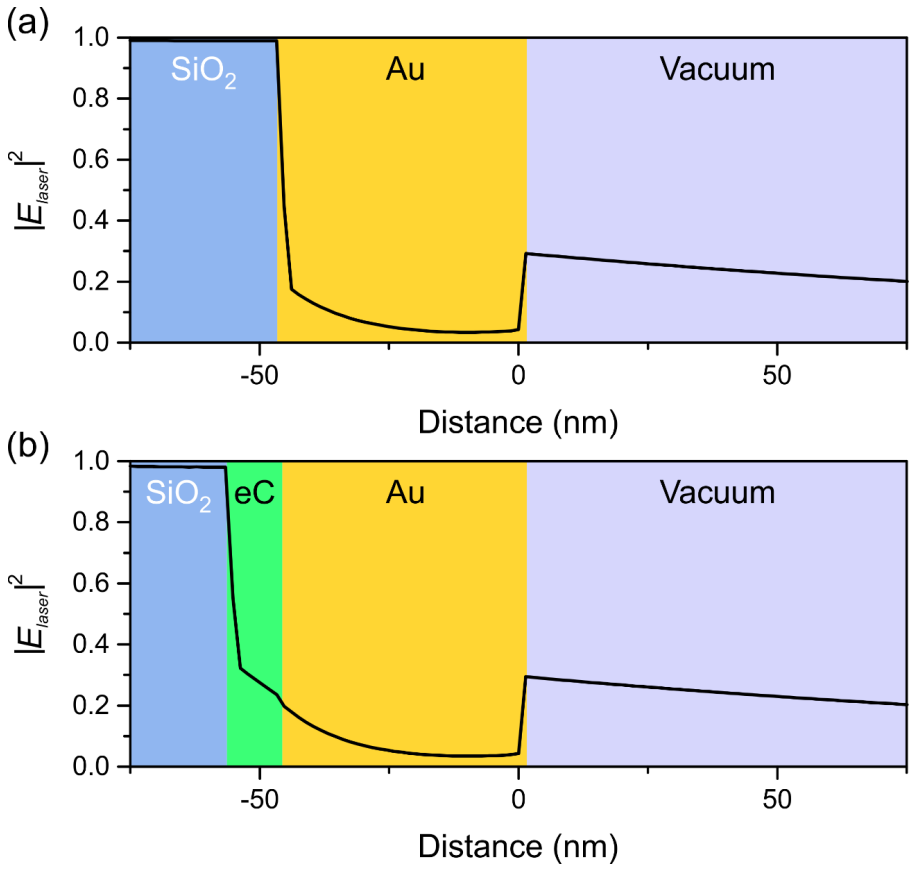

Figure 4.19 Cut of the laser electric field squared from FDTD simulations along a direction normal to the film for (a) Au and (b) eC/Au films.

For the duration of the experiment, the laser intensity is kept below 9.9 GW/cm^2 such that the emission process is occurring fully within the multi-photon absorption regime [6]. This provides a platform to study the effect of the eC/Au bilayer on the number of photons required to free an electron. Based on the work function of 4.8 eV for Au and eC (see inset of Fig. 4.17(a)), and with each photon of the incident laser pulse possessing an energy of ~1.4-1.7 eV, freeing an electron from an Au or an eC/Au film requires a minimum of a three-photon absorption (3PA) process to take place. At the laser intensities used here, the Keldysh parameter is calculated to be $\gamma = 21$ at the lowest

intensity of 0.37 GW/cm^2, and $\gamma = 11$ at 1.35 GW/cm^2, assuming a surface electric field enhancement of 21 times [20].

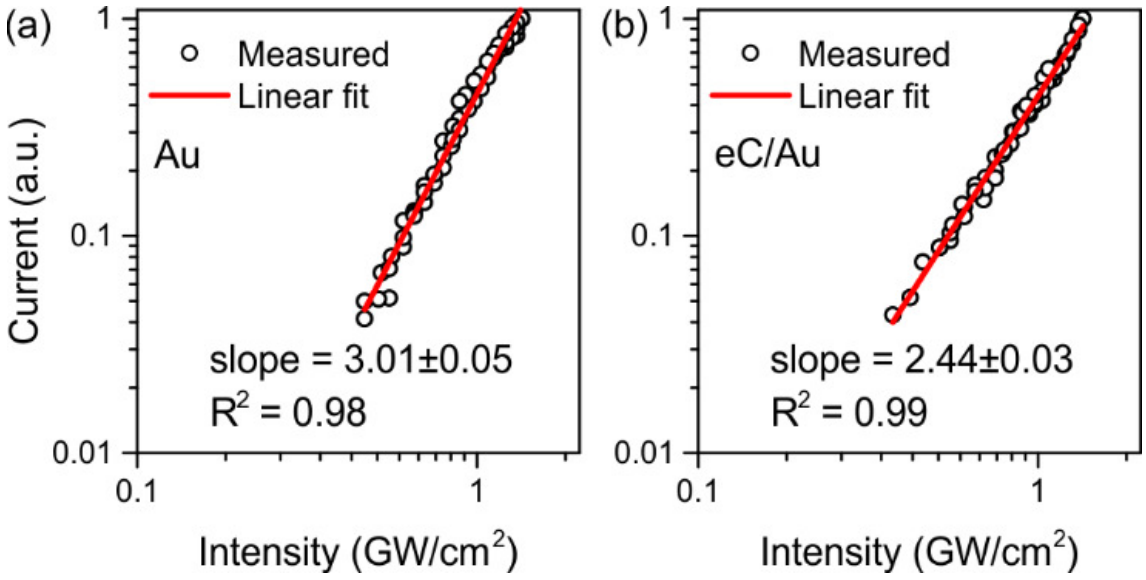

Figure 4.20. Measured current as a function of incident laser intensity indicating (a) three-photon ionization in the Au sample, and (b) a combination of absorption processes of different orders with different probabilities in the eC/Au sample.

To experimentally verify the electron emission order, the incident laser intensity was varied between 0.37 GW/cm^2 and 1.35 GW/cm^2. By operating with a maximum intensity of 1.35 GW/cm^2, thermal effects within the metallic films are avoided [22]. The measured photocurrent, J, for the Au and the eC/Au samples, as a function of laser intensity, I_{laser}, are depicted in Fig. 4.20(a) and Fig. 4.20(b), respectively. A slope of m = 3.01±0.05 is found for the Au sample, and a slope of m = 2.44±0.03 is found for the eC/Au sample. In an ideal multiphoton absorption photoemission process, one would expect the order, m, to be an integer number corresponding to the power dependence of the measured photocurrent, i.e. $J \propto I_{laser}^{m}$. While the m = 3 is expected for the Au film (Fig. 4.21), the m = 2.44 for the eC/Au bilayer suggests that electrons must be originating

from another, lower order emission process. However, the work function of eC was measured to be identical to that of Au, i.e. 4.8 eV. As such, any electron released would require the absorption of at least three photons (i.e. $m = 3$). Examining the absorbance of a 10 nm eC film, and a 15 nm Au film over the ultraviolet-visible wavelength range (Fig. 4.22), shows a broadband absorption in eC, indicating many possible local optical transitions between a range of states present in the disordered carbon matrix [71]. Notably, the absence of any strong absorption peaks indicates that there is no direct two-photon ionization of the eC layer. Evidently, the electron emission for the eC/Au sample must be originating from absorption processes of different orders with different probabilities.

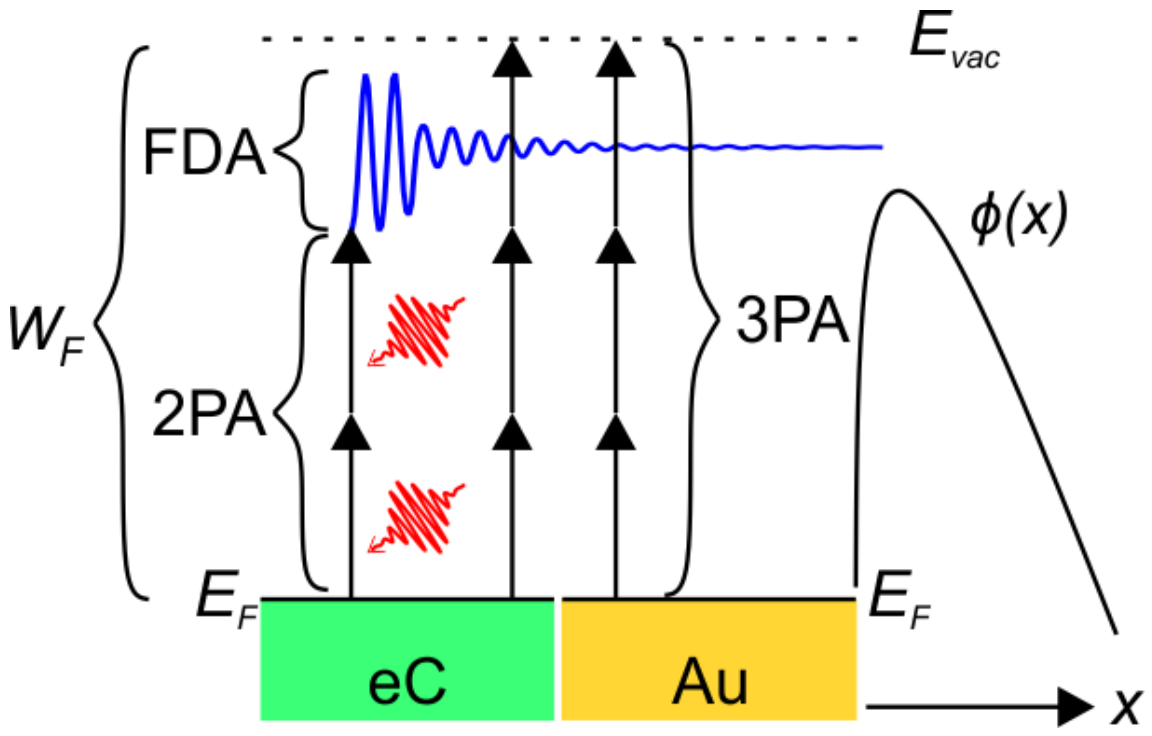

Figure 4.21. Energy band diagram at the eC/Au interface representing the two emission processes; two-photon absorption (2PA) followed by field-driven acceleration (FDA) and emission over the lowered ϕ; and direct three-photon absorption (3PA). Each arrow

represents a single photon with 1.6 eV energy. E_F is the fermi level, E_{vac} is the vacuum energy level, and x is directed away from the Au-vacuum interface.

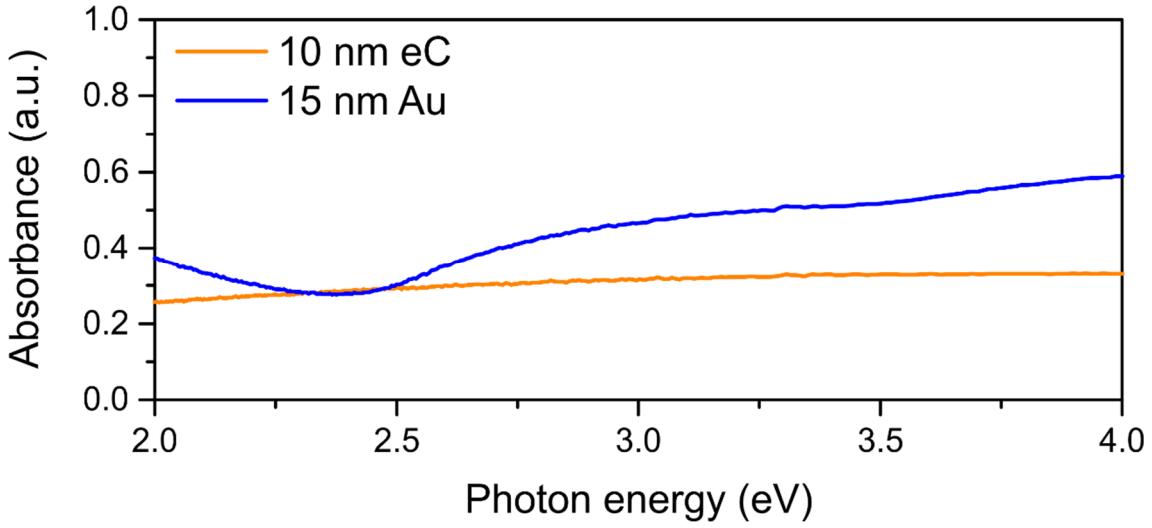

Figure 4.22. Measured absorbance for a 10 nm eC film and a 15 nm Au film.

To discern the low order of the photoemission process, the effect of the SP field must be considered. It is well known that in the presence of high electric fields, the vacuum potential barrier, ϕ, can be lowered via the Schottky effect [5,72]. The potential barrier under influence of an electric field is given by [5]:

$$\phi(x) = W_F - q^2/16\pi\varepsilon_0 x - qE_{laser}x \tag{4.1}$$

where x is the distance from the interface into the vacuum. Therefore, the lowered barrier at the surface is given by [5]:

$$\phi_l = W_F - \sqrt{\frac{qE_{laser}}{4\pi\varepsilon_0}} \tag{4.2}$$

In the current experiment, at the lowest incident field of $E_{laser} = 5.3\times10^5$ V/cm (or $I_{laser} =$ 0.37 GW/cm^2), and at an average SP electric field enhancement of 21 times, ϕ is lowered

by 1.1 eV to ϕ_l = 3.7 eV. However, this value of ϕ_l is not low enough to allow for two-photon absorption. Additionally, if ϕ_l was low enough, the reduction would be observed for both samples (i.e. Au and eC/Au) as this barrier is located at the Au-vacuum interface. Therefore, another mechanism must be responsible for the observed m = 2.44 in the eC/Au bilayer sample.

Just as electrons are accelerated in the SP field present at the Au-vacuum interface [6,19,20], electrons are also accelerated by the electric fields within the materials themselves [73]. Here, only electrons that are generated by one-photon absorption (1PA) and two-photon absorption (2PA) are considered, corresponding to initial kinetic energies of 1.6 eV and 3.2 eV, respectively. Electrons that have absorbed three photons are already freed from the metal. The electrons are then subsequently accelerated (decelerated) to higher (lower) kinetic energies by the electric fields present within the materials. Clearly, at the electric field strengths here, one-photon generated electrons will not be able to gain enough energy to overcome ϕ_l and thus cannot contribute to J. However, for completeness their simulation results are included below. On the contrary, for 2PA generated electrons, the minimal kinetic energy gain is quite achievable to overcome ϕ_l. Figure 4.21 illustrates the field-driven acceleration of 2PA generated electrons over ϕ_l.

4.3.3. Simulation of Electrons in an eCarbon/Gold Bilayer

To verify that the kinetic energy of the field-accelerated electrons is enough to overcome ϕ_l, particle tracking simulations are performed with electromagnetic fields calculated from FDTD simulations. For the single-photon absorption simulations, each electron is given an initial kinetic energy in the range of 1.4-1.7 eV, corresponding to the

bandwidth of the incident 15 fs laser pulse. The kinetic energy spectra of $m = 1$ generated electrons at the Au-vacuum interface after they have interacted with the internal fields in the Au sample are depicted in Fig. 4.23(a) for three values of incident laser intensity over the experimental range. The quasi-symmetric shape of the kinetic energy spectra can be ascribed to the fact that the acceleration process is highly dependent on the phase of the SP field when the electron is generated. As such, a similar number of electrons that are accelerated will be decelerated. As the maximum energy gained by any of the $m = 1$ electrons is only 0.25 eV at the highest laser intensity (1.35 GW/cm^2), none of these electrons can overcome ϕ_I.

For the eC/Au sample, even with only a 10 nm eC layer, the situation is markedly different. Firstly, there is a significant increase in electric field strength within the eC layer compared to the Au layer. This can readily be seen in Fig. 4.19 above. Calculating the average magnitude of the electric field obtained from FDTD simulations in each layer indicates 2.2 times higher average electric field in the eC layer of the eC/Au sample compared to the Au sample. Secondly, the effective mass of electrons within eC is 78% that of the effective mass in Au. Therefore, at a given E_{laser}, the relative acceleration, a_{rel}, experienced by an electron in eC compared to an electron in Au will be higher. The relative acceleration is given by:

$$a_{rel} = \eta_{confinement}\, m^*_{Au} / m^*_{eC} \tag{4.3}$$

where m^*_{Au} = 1.12 is the electron effective mass in Au [74], m^*_{eC} = 0.87 is the electron effective mass in eC [75], and $\eta_{confinement}$ = 2.2 is the aforementioned ratio of electric fields between the eC film and Au film. This results in 2.8 times higher electron acceleration in

the eC film compared to that in the Au film. Furthermore, in addition to the electric field enhancement from the SP, there is also field enhancement from the composition of the eC film itself. It is well known that for field emission from carbon films, the nanoclusters of conductive, graphitic, sp^2 bonds embedded in insulating, diamond-like, sp^3 bonds leads to increased localized electric field enhancement within the carbon [76–79]. It is also possible that at the interface between eC and Au, sp^3 bonds are converted to sp^2 bonds [80], resulting in further increase of sp^2 clustering directly at the interface, and hence, an increase in the electric field enhancement at the eC/Au interface. At an SP electric field enhancement of 21 times, combined with an eC electric field enhancement of 56 times [76], photogenerated electrons from the eC can gain significantly more kinetic energy compared to those in the Au film. Note that ϕ will only be lowered due to the SP field enhancement directly at the Au-vacuum interface and will not be affected by the localized sp^2/sp^3 clustering field enhancement.

Figure 4.23(b) depicts the kinetic energy spectra at the Au-vacuum interface for $m = 1$ electrons originating in the thin eC layer at three incident laser intensities. Only at the highest incident intensity (1.35 GW/cm^2) are electrons able to gain enough kinetic energy to overcome ϕ_l. These electrons only account for <2% of the total $m = 1$ electrons and therefore do not contribute to the measured J. From these results it is clear that the contribution from the $m = 1$ electrons can be ignored and it is more important to consider what happens to the 2PA generated electrons within each material.

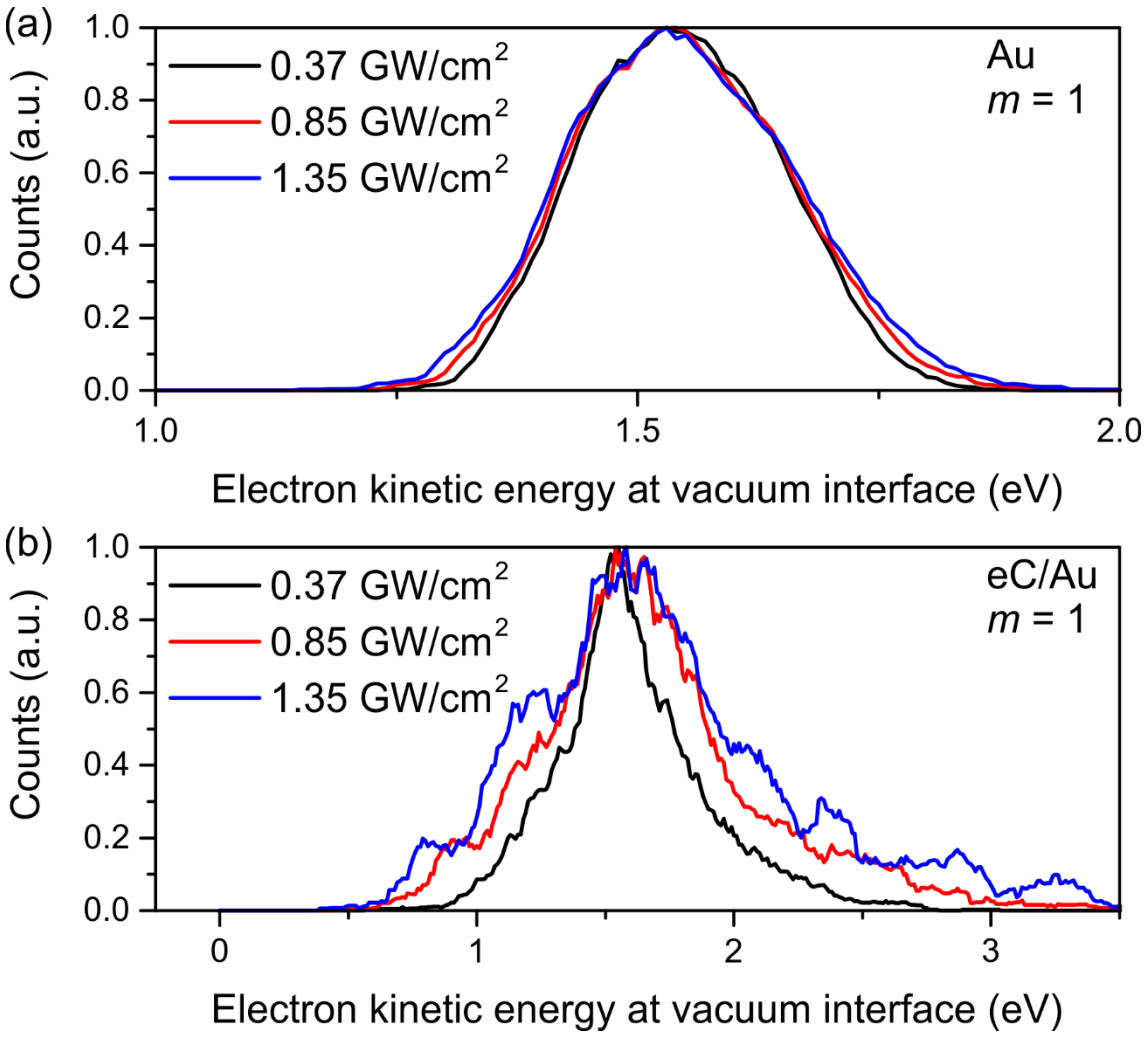

Figure 4.23. Simulated electron kinetic energy spectra at the Au-vacuum interface at various incident laser intensities for the (a) Au layer by itself, and (b) eC/Au bilayer. The electrons are given an initial kinetic energy in the range of 1.4-1.7 eV, corresponding to an electron generated by single-photon absorption of the incident laser pulse. The eC/Au spectrum is broader than the Au spectrum due to the higher accelerating SP field in the eC layer. Note that all electron counts are normalized and there is a difference in energy scales between (a) and (b).

For the $m = 2$ simulations, each electron is given an initial kinetic energy in the range of 2.8-3.4 eV, corresponding to 2PA of the laser pulse. Figure 4.24(a) depicts the kinetic energy of $m = 2$ generated electrons at the Au-vacuum interface for the Au sample at

three incident intensities (0.37, 0.85, and 1.35 GW/cm^2). At the lowest electric field of 5.3×10^5 V/cm, (i.e. I_{laser} = 0.37 GW/cm^2), no electron can gain enough kinetic energy to overcome ϕ_l. As the electric field strength increases, the barrier continues to lower, and electrons will gain enough kinetic energy to overcome the lowered barrier at the Au-vacuum interface. At $E_{laser} = 8\times10^5$ V/cm (i.e. I_{laser} = 0.85 GW/cm^2) only 2% of 2PA generated electrons will have enough energy to overcome the ϕ_l = 3.45 eV barrier, this increases to 19% at $E_{laser} = 1\times10^6$ V/cm (i.e. I_{laser} = 1.35 GW/cm^2) for the ϕ_l = 3.3 eV barrier. Due to the low number of m = 2 generated electrons reaching the vacuum, the normal m = 3 absorption process will completely dominate the emission process and results in the observed order of m = 3.01. Fig. 4.25(a) depicts exemplary electron trajectories for m = 2 generated electrons within the Au film.

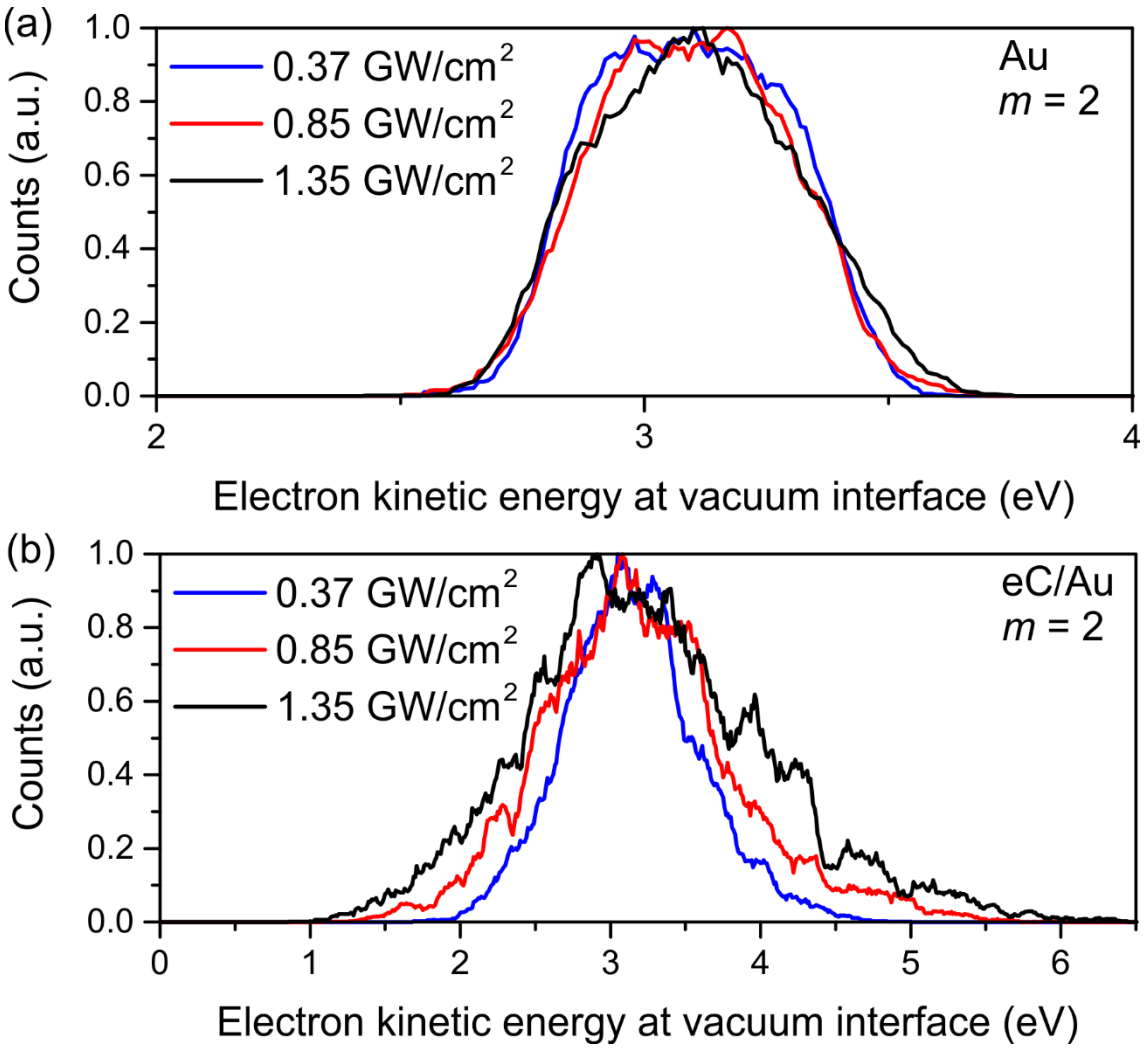

Figure 4.24. Simulated electron kinetic energy spectra at the Au-vacuum interface at various incident laser intensities for the (a) Au layer by itself, and (b) eC/Au bilayer. The electrons are given an initial kinetic energy in the range of 2.8-3.4 eV, corresponding to an electron generated by two-photon absorption of the incident laser pulse. The eC/Au spectrum is broader than the Au spectrum due to the higher accelerating SP field in the eC layer. Note that all electron counts are normalized and there is a difference in energy scales between (a) and (b).

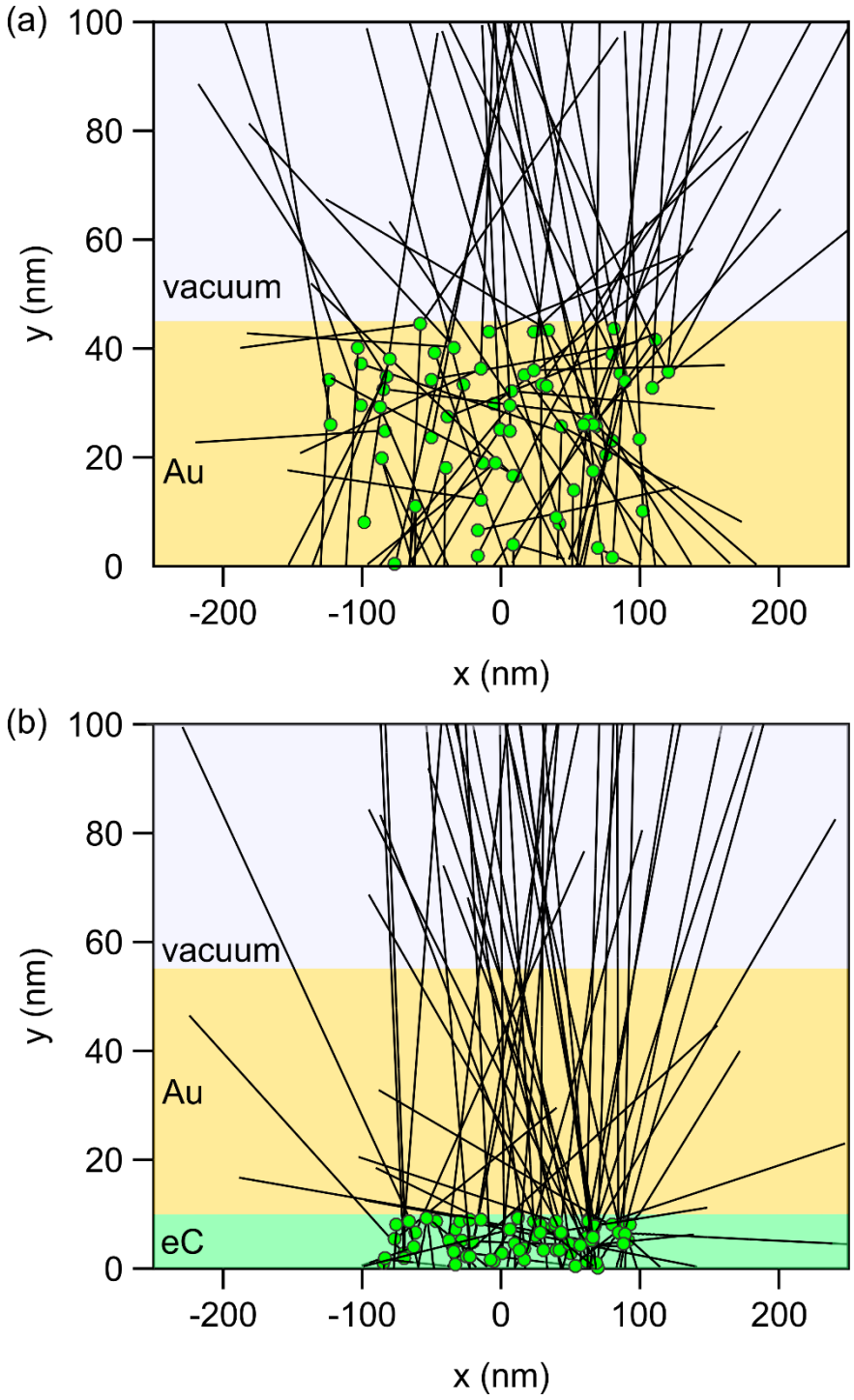

Figure 4.25. Exemplary trajectories of two-photon absorption generated electrons interacting with the E_{laser} = 1×10^6 V/cm in (a) the Au film, and (b) the eC/Au bilayer film calculated from the particle tracking model. Note that a green dot represents the start of an electron's trajectory.

Figure 4.24(b) depicts the kinetic energy of $m = 2$ accelerated electrons at the Au-vacuum interface at various incident laser intensities for the eC/Au bilayer. Notably, at the lowest electric field of 5.3×10^5 V/cm, (i.e. $I_{laser} = 0.37$ GW/cm^2), 11% of the electrons possess enough kinetic energy to overcome the barrier. This increases to 33% at $E_{laser} = 8\times10^5$ V/cm (i.e. $I_{laser} = 0.85$ GW/cm^2) and 45% at $E_{laser} = 1\times10^6$ V/cm (i.e. $I_{laser} = 1.35$ GW/cm^2). Note that the model used does not take in to account the local density of states of the eC. As such, the percentages do not correspond directly to an absolute number of electrons. Evidently, approximately half of the 2PA generated electrons originating from the eC layer will be emitted from the sample. Given that an $m = 2$ absorption process has a higher probability of occurring than an $m = 3$ absorption process, it can be concluded that the $m = 2$ accelerated electrons dominate the observed current, as exhibited by the lowering of the emission order to $m = 2.44$. Exemplary trajectories of the $m = 2$ electrons generated in the eC and passing through the Au layer to the vacuum are depicted in Fig. 4.25(b).

4.4. Ultrafast High Current Plasmon Driven Secondary Electron Sources

Based on the promising results of the eC/Au bilayer, it became obvious that introducing electrons through a method other than SP electron generation could be used to realize high current electron sources. This section explores the use of ultrafast plasmonic fields to gate continuous electron beams. By gating continuous electron beams it is envisioned that high current, ultrafast electron pulses can be generated without having to operate at high laser intensities. While the idea has been proposed in the past by our group [38], no experimental work has been done towards understanding the interaction of a free electron beam with a plasmonic field, especially in the presence of a

metallic film. Before an electron source can be built around this concept it is of utmost importance to fully understand this interaction between free electrons and the surface plasmon field. The following sections of this chapter explore this interaction as well as the interactions of a free electron beam passing above a metallic surface. The subsequent section details the experimental results that demonstrate the generation of a high current secondary electron based electron source.

4.4.1. Experimental Setup

Multiple experimental configurations were used to collect the data presented within this section. The main configuration is depicted schematically in Fig. 4.26(a) with the corresponding photograph in Fig. 4.26(b). Surface plasmons are excited on a 45 nm Au film in the Kretschmann geometry by laser pulses from the Ti:Sapphire CPA. The laser pulses have a pulse duration of 50 fs, a central wavelength of 780 nm, and arrive at a repetition rate of 1 KHz. The continuous electron beam is passed parallel to the Au film, along the same direction as the propagating SP wave. The electron beam current is measured in-situ by a Faraday cup (FC2) placed away from the prism. Experiment electrons are detected by a separate Faraday cup (FC1) that is placed on the angular translation stage so that the angular distribution of the electrons can be measured. Due to the placement and proximity of the electron gun to the prism, only angles between 0° and 90° can be measured. In order to only observe electrons that have interacted with the plasmonic field, the output of FC1 is connected through a low-noise current amplifier to a lock-in amplifier that takes its reference from an optical chopper placed in the laser beam path. To ensure the largest possible region of interaction, the laser spot size on the Au film has a 4 mm diameter.

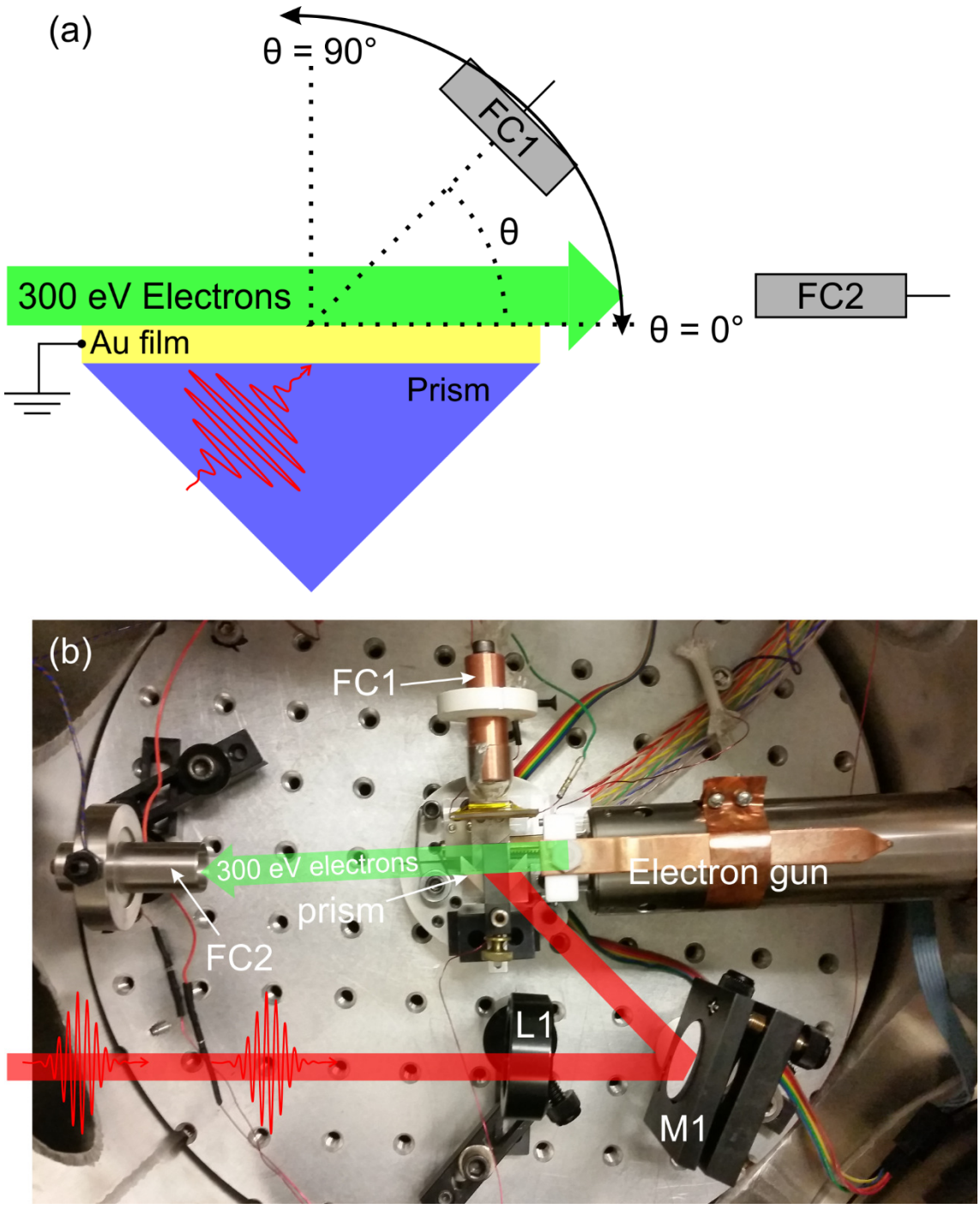

Figure 4.26. (a) Schematic depiction and (b) photograph of experimental setup. Surface plasmons are excited on a 45 nm Au film deposited on a fused-silica prism. A 300 eV continuous electron beam propagates parallel to the Au film. FC1 is a Faraday cup with 5° acceptance angle mounted on an angular translation stage. FC2 is a Faraday cup for monitoring the continuous electron beam current.

The first important experimental consideration to be made was the use of a Faraday cup detector instead of the standard channeltron electron multiplier for detection of the electrons. Although the channeltron provides high electron gain, it also introduces a source of high voltage (>2 kV) in to the vacuum chamber. It was determined that even with electrical shielding, the introduction of the high voltage was enough to act on the electrons from the continuous electron beam and alter the trajectory of the electrons. For this reason, a Faraday cup (FC1) was used. To increase the angular resolution of FC1, an insulating glass slit was placed in front of FC1 to limit the acceptance angle to 5°, as shown in Fig. 4.10(c).

4.4.2. Beaming of Continuous Electron Beams

The first measurements were designed to study the angular distribution of electrons as a function of electron beam current, I_{beam}, at a primary electron energy of 300 eV. This energy was selected due to it being the experimentally determined peak for secondary electron yield from Au films [59]. Here, the incident laser intensity is fixed at 25 GW/cm^2 as this is the maximum achievable intensity from the CPA while maintaining a large, 4 mm spot size, that is below the damage threshold of the Au film. Figure 4.27 depicts the measured angular distribution. When the electron gun is off, the electron emission peaks in a direction perpendicular to the Au film and has a half-width-at-half-maximum (HWHM) of ~17.5°. The peak emission current is 5.3pA at 90° with a total emission current of 37.2pA. Since the electron gun is off, these electrons can only be originating from the Au film and the laser field, exactly the same as a standard plasmonic emission experiments [6,19]. Once the electron gun is turned on, and even at a low I_{beam} of 5 nA, the situation is markedly different.

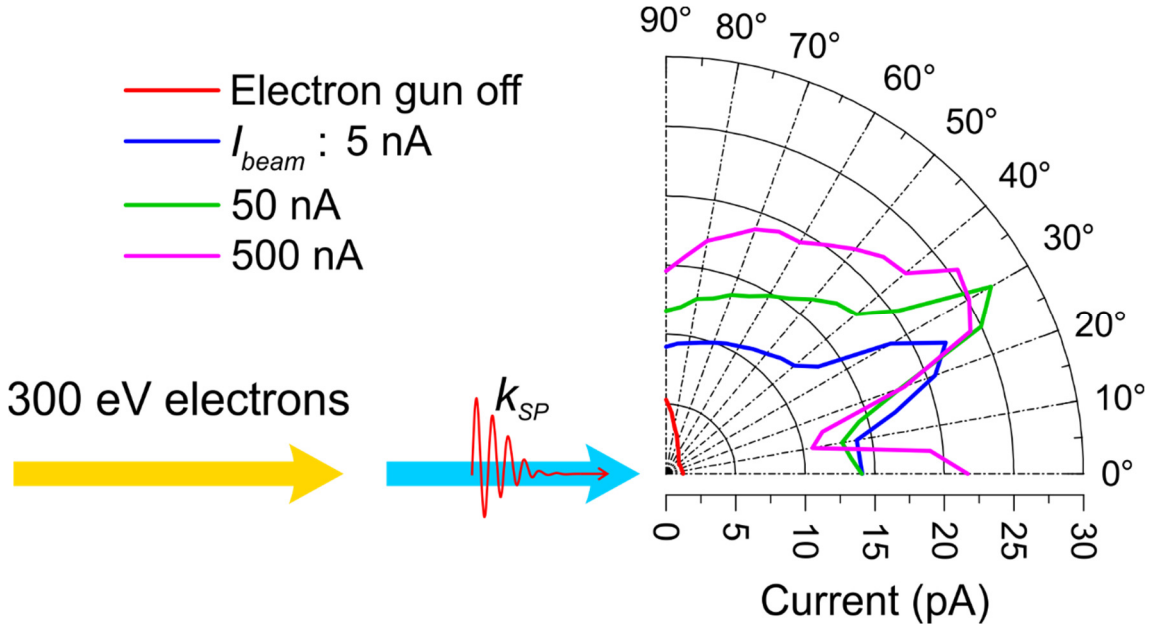

Figure 4.27. Angular distribution of measured electrons for Electron gun off, and I_{beam} of 5 nA, 50 nA, and 500 nA.

The first noticeable difference with the presence of the continuous electron beam is the significant increase in total collected current. At I_{beam} = 5 nA, the total collected current is 248 pA, a 6.7× increase compared to when the electron gun is off. Increasing I_{beam} to 50 and 500 nA results in total currents of 304 pA and 364 pA, respectively. In addition to the increase in collected current, there is a distinct beaming of the electrons to approximately 30° away from the Au film. At I_{beam} = 5 nA, the current peaks to 22.2 pA at 25°. At I_{beam} = 50 nA the peak shifts to 30° with 27 pA of measured current and 35° at 25.6 pA for I_{beam} = 500 nA.

There are a few possible explanations for the observed increase in collected current. At first glance, one might be inclined to think that when the electron gun is on, the detector is merely picking up electrons directly from the continuous electron beam. However, this cannot be the case since the measurement is done using phase sensitive

detection with a lock-in amplifier and only those electrons that have interacted with either the laser or plasmonic field will be detected. Further, only the change in current when the laser beam is incident compared to when the laser beam is blocked is measured at a given angular position due to the physical chopping. Meaning that if an electron from the 300 eV electron beam is not deflected away from or onto the detector when the laser pulse is present, it will not be registered. This is evidenced by the lack of a peak in the measured current at 0°.

The next possibility to look at is how the presence of the 300 eV electron beam may be affecting the SP wave and thus the SP generated electrons. When the electron beam passes above the Au film, it will induce positive image charges in the metal, as depicted in Fig. 4.28. However, the presence of the positive image charges will attract the escaping electrons, which would in-turn reduce the total emitted current, not provide an up to ten-fold increase as measured. These image charges will also set up a static electric field within the Au film. To calculate the strength of this field, the electron beam can be approximated as a line charge with a charge per unit length given by:

$$\frac{Q}{L} = \frac{I_{beam}}{v_{electron}} \tag{4.4}$$

Where Q/L is the charge per unit length, and $v_{electron}$ is the electron beam velocity (1×10^7 m/s at 300 eV). The electric field directly beneath the electron beam can then be calculated as a line charge above a conducting surface:

$$E_{induced} = \frac{Q/L}{\pi\varepsilon_0 r} \tag{4.5}$$

Where $E_{induced}$ is the electric field induced by the electron beam, and r is the distance between the Au film and the electron beam. At I_{beam} = 500 nA and assuming that the electrons are passing 1 nm above the Au film, the induced electric field strength is calculated to be ~10^6 V/m compared to the ~10^8 V/m of the SP electric field. As such, this field is much lower than the SP electric field and therefore the induced field will play a negligible role in the emission of electrons from the Au film.

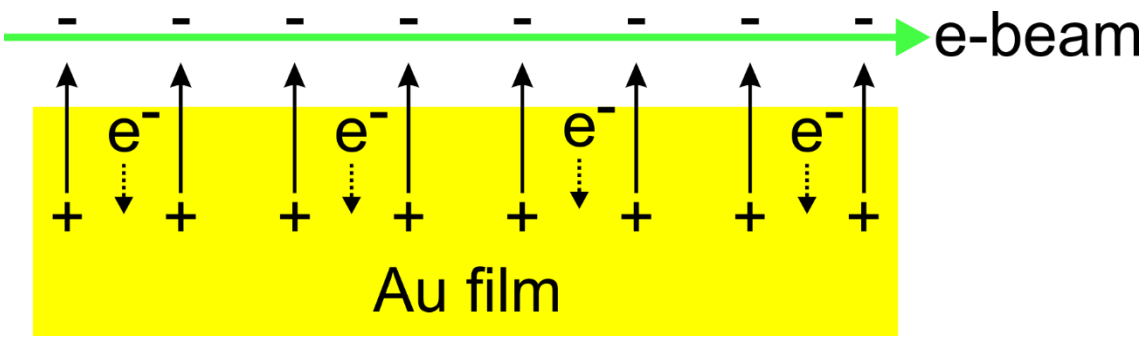

Figure 4.28. Induced charges and electric field lines from an electron beam passing above the Au film. The + and – indicate positive and negative charges, respectively.

The final and most likely scenario is that the 300 eV electron beam is not travelling completely parallel to the Au film, (i.e. it has some angular spread), and therefore some of the electrons will collide with the film. The spread of the beam was determined by angularly sweeping FC1 and measuring the detected beam current with an electrometer (Keithley 619). Note that the prism was still left in place for these measurements. Figure 4.29 depicts the normalized angular distribution for I_{beam} = 5 nA, 50 nA, and 500 nA. Notably, within the sensitivity of the detection setup, the angular distribution does not change for changing I_{beam} and maintains an approximately 5° spread. This spread indicates that a portion of the 300 eV electron beam is colliding with the Au film. When an energetic electron collides with a material, it may produce secondary

electrons (SE). Secondary electrons and their generation process are described in detail in Section 2.5. Briefly, secondary electrons are electrons that are freed from a material during a collision with a primary electron beam and, by definition, possess kinetic energies below 50 eV [55], and their angular distribution is a cosine distribution centered perpendicular to the material. Of importance for our situation is the secondary electron yield, or the fact that for a single primary electron it is possible to generate multiple secondary electrons through an avalanche process. For a 300 eV electron striking a Au film, the secondary electron yield is 1.14 [59]. Therefore, it is possible that our 300 eV electron beam is colliding with the Au film and generating secondary electrons that subsequently interact with the plasmonic field and are collected in the total current measurement.

To ascertain where the increased current is coming from, it is beneficial to measure the total collected current as a function of incident laser intensity. As in previous experiments presented in this thesis, this will indicate the order of the emission process, i.e. multi-photon absorption, single-photon absorption, or tunnel ionization. Figure 4.30 depicts the total measured current as a function of incident laser intensity with the electron gun off and at I_{beam} = 5, 50, and 500 nA. When the electron gun is off, we observe a nonlinear emission order of 4.23 (Fig. 4.30(a)). This is the standard multi-photon absorption of 1.55 eV (λ = 800 nm) photons in an Au film having a work function of 5.2 eV. This confirms that we are operating strictly in the multi-photon regime for electron generation. Notably, once the electron gun is turned on and at each value of I_{beam} employed, the total current scales linearly with the incident intensity, Fig. 4.30(b)-(d).

The slope and intercept change between the three cases simply due to the increase in total measured current as I_{beam} increases. Notably, the ratio between the slopes is the same, i.e.:

$$\frac{\text{slope}_{50\text{ nA}}}{\text{slope}_{5\text{ nA}}} = \frac{\text{slope}_{500\text{ nA}}}{\text{slope}_{50\text{ nA}}} = 1.17 \tag{4.6}$$

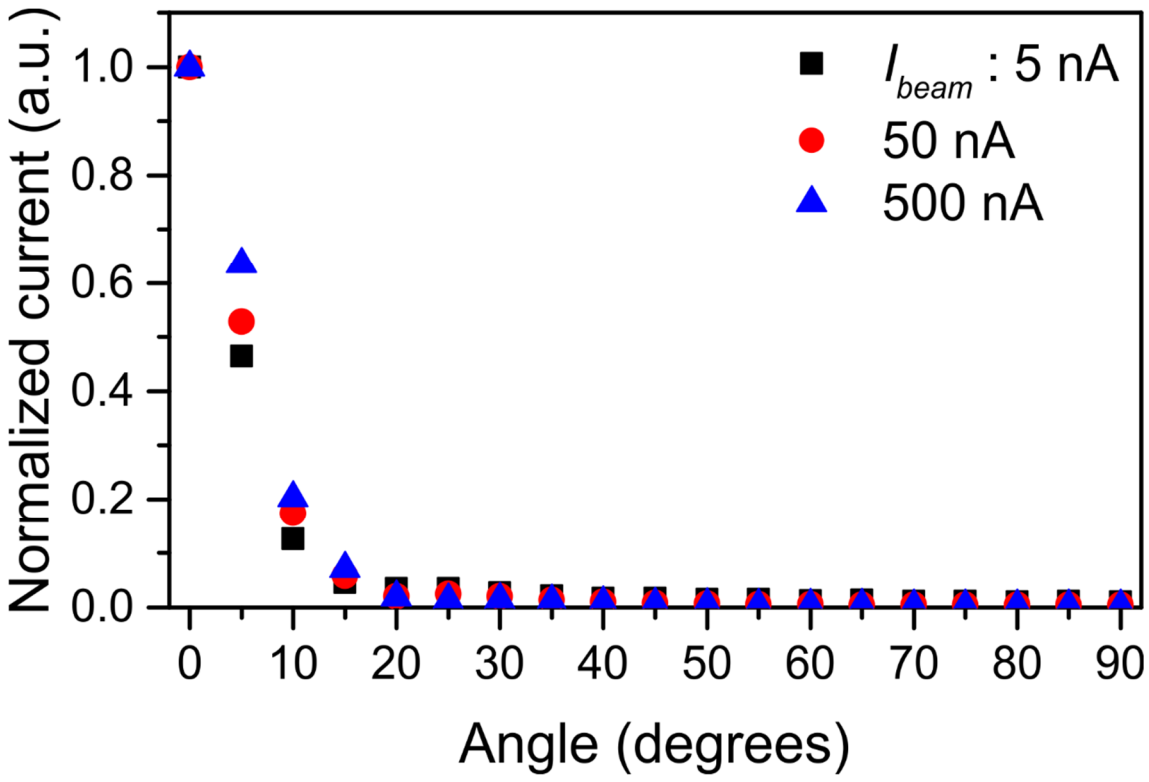

Figure 4.29. Continuous electron beam spread for I_{beam} = 5 nA (black square), 50 nA (red circle), and 500 nA (blue triangle) indicating a constant 5° spread in the 300 eV electron beam.

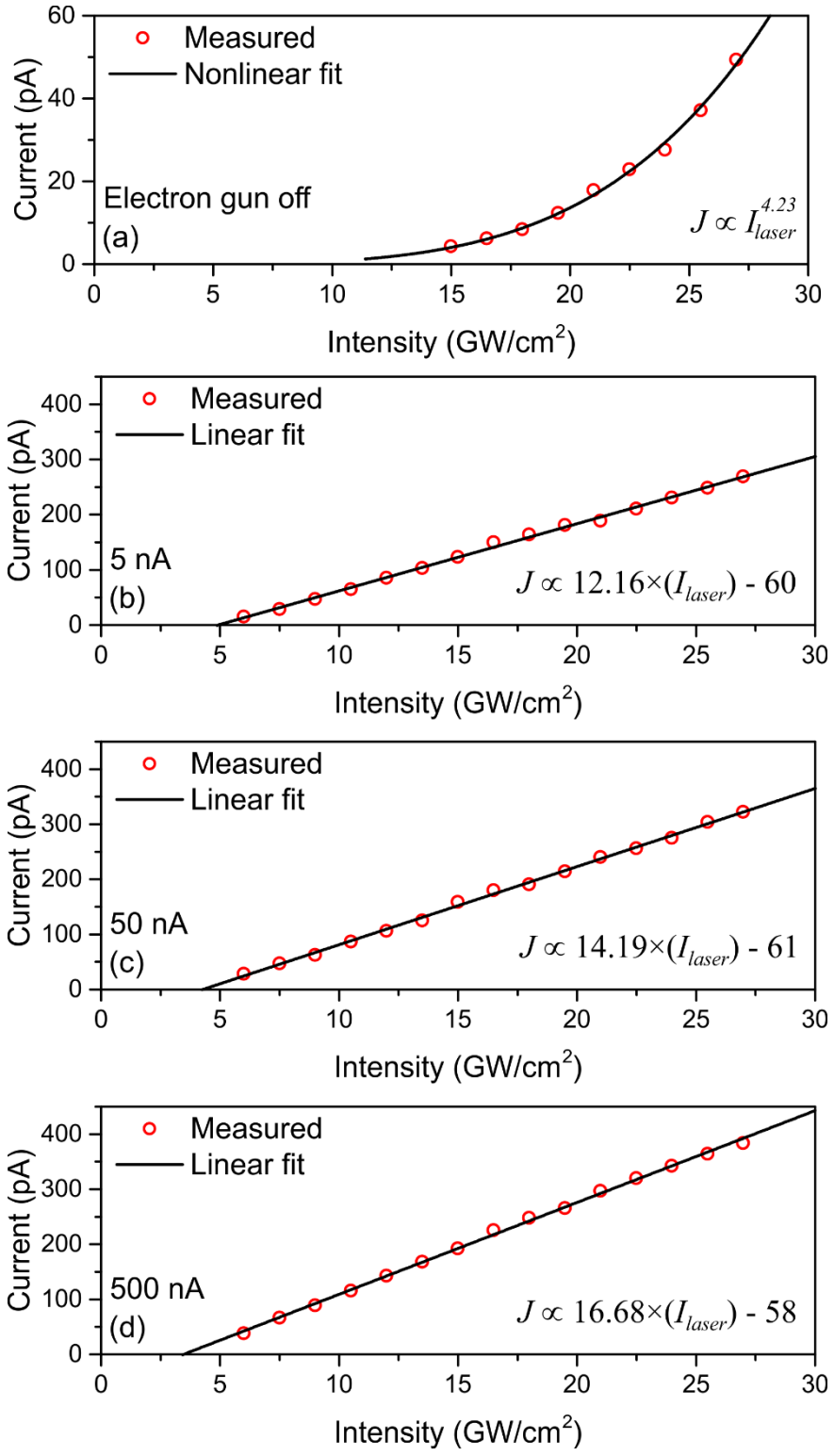

Figure 4.30. Total measured current as a function of incident laser intensity for (a) Electron gun off, and I_{beam} = (b) 5 nA, (c) 50 nA, and (d) 500 nA.

4.4.3. Explanations for Linear Power Scaling

There are multiple explanations for the observed linear power scaling. The first of which has to do with the ponderomotive force of the plasmonic field. Typically, the ponderomotive force is exploited for acceleration of the generated electrons and has been used in the past to achieve high kinetic energies up to 2 keV [6]. However, in this situation, the ponderomotive force will also act in the opposite direction, i.e. towards the metal film, "pulling" electrons into collisions with the Au film. For low energy electrons such as the SP generated electrons, this will negligibly affect the total measured current because their energy is low enough (<30 eV) that the secondary electron yield is low (~0.3) and not many electrons will be generated. Full characterization of the measured electron kinetic energy is presented in section 4.4.6. Also, this phenomenon would be observed even with the electron gun off. On the contrary, for high energy electrons like the 300 eV electrons in our electron beam, their secondary electron yield is quite high (~1.14) and may produce secondary electrons that contribute to the total measured current. As the ponderomotive force scales linearly with laser intensity (equation (2.58)), it is expected that this ponderomotive "pulling" would result in a linear behaviour of the total measured current as a function of incident laser intensity.

To test this theory, particle tracking simulations were conducted. The SP fields are calculated via FDTD, assuming a 45 nm Au film and a 50 fs, λ = 800 nm laser pulse. Due to simulation constraints, the spot size is assumed to have a 5 μm diameter FWHM. Calculated SP electric fields are depicted in Fig. 4.31(a). A primary beam of 300 eV electrons is directed parallel to the direction of propagation of the SP wave and interacts with the SP fields. The primary electrons are placed between 0 and 50 nm above the film

and released at random times to simulate a continuous incoherent electron beam. The total number of electrons colliding with the Au film is recorded at different values of incident laser intensity spanning the experimental intensity range of 5-25 GW/cm^2. Figure 4.31(b) depicts exemplary trajectories of those electrons that have collided with the Au film. Note that the color does not represent anything and is simply to differentiate each individual trajectory. For the simulation it assumed that there is a 25× electric field enhancement and at each intensity 5000 test electrons are used such that the entire interaction process is sampled. The number of electrons that collide with the Au film as a function of incident laser intensity is depicted in Fig. 4.32. Clearly, this does not follow a linear trend as would be expected by the ponderomotive force equation. This is due to the fact that the interaction is not a purely ponderomotive process, similar to sub-cycle acceleration of the nanoplasmonic electron gun in discussed in section 3.4.1.

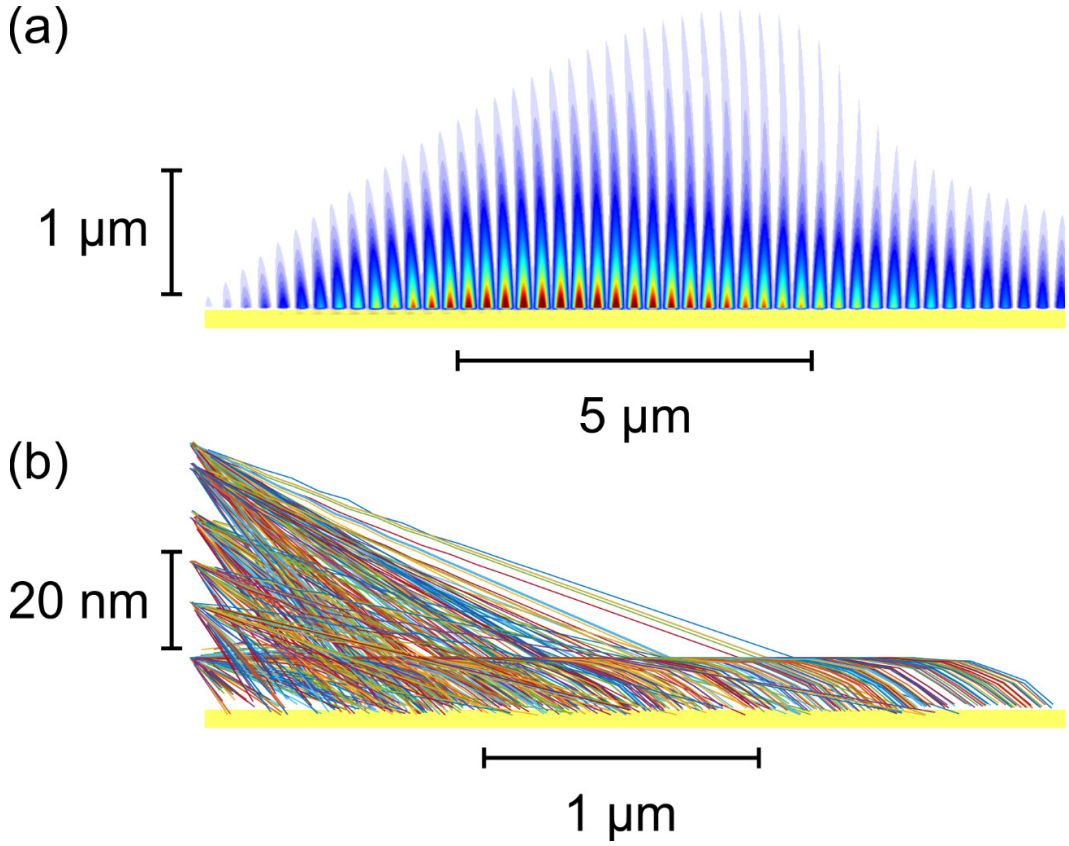

Figure 4.31. (a) SP electric field profile calculated from FDTD. (b) Exemplary electron trajectories of electron beam electrons that collide with the Au film. The color of the electron trajectories does not indicate anything, it is merely added to distinguish each individual trajectory.

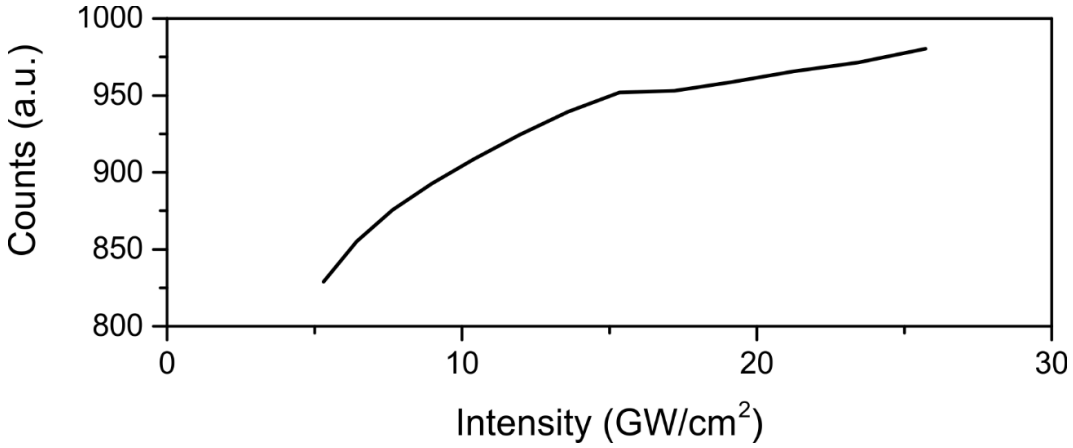

Figure 4.32. Calculated number of primary beam electrons colliding with the Au film as a function of incident laser intensity.

The other possible explanation for the linear power scaling is that of single-photon absorption. Just as with the eC/Au bilayer in the previous section, it is possible that the Au-vacuum potential barrier can be lowered such that electrons can be freed by a single photon. However, when the electron gun is off (and based on the wavelength of the laser used and W_F of Au), the measured current scales with the 4th power of the incident laser intensity indicating that the emission process is strictly in the multi-photon regime. As such, it is pertinent to examine the situation when the external electron beam is present. As previously mentioned, the 300 eV electron beam will induce some electric fields in the Au film with an electric field strength of ~10^6 V/m. Using equation (4.2), this field strength would only lower the barrier by 0.04 eV, which is negligible compared to the incident photon energy. As such, this cannot be responsible for the observed linear power scaling.

This leads to the final scenario, where internal secondary electrons are being excited by an incident laser photon and being freed from the Au film. When secondary electrons are generated within a material, they will have a spread in their kinetic energies depending on the number and type of collisions they undergo as they transit to the material surface. The kinetic energy spectrum of these "internal secondary electrons" can be calculated using the treatment from [81]. The internal secondary electron distribution is given by:

$$\frac{d^2 n(E_i, E_p)}{dE_i dz} = -\frac{d}{d\mu}\left[\frac{\hbar}{\pi a_0 E_p}\frac{1}{n_e}\int_0^{(E_p - E_F)/\hbar}\int_{k_1(\omega)}^{k_2(\omega)} \mathrm{Im}\left\{\frac{-1}{\epsilon(k_p,\omega)}\right\} N\left(\mu, \frac{k_p}{k_F}\right)\frac{dk_p}{k_p}d\omega\right]\frac{1}{2\mu E_F}$$

(4.7)

Where E_i is the internal secondary electron energy in the material, *Ep* is the primary (incident) electron energy, $\hbar$ is the reduced Planck's constant, k_p is the wavenumber of the primary electron, k_F is the Fermi wavenumber, and $\mu = \sqrt{E_0 / E_F}$. Here, $N(\mu, s)$ is given by:

$$N(\mu,s) = \begin{cases} \dfrac{\pi k_F^3}{6s(2\pi)^3}\left[3(\mu^2-1)^2 - 8s(\mu^3-1) + 6s^2(\mu^2+1) - s^4\right], & \text{for} \quad \mu - 1 \le s \le \mu + 1 \\ \dfrac{8\pi k_F^3}{3(2\pi)^3}, & \text{for} \quad \mu + 1 < s \end{cases}$$

(4.8)

and ϵ takes the form of the Lindhard dielectric function [45,46]:

$$\epsilon(k,\omega) = 1 + \frac{\chi^2}{z^2}\{f_1(u,z) + if_2(u,z)\} \tag{4.9}$$

Where the functions f_1 and f_2 are given by:

$$f_1(u,z) = \frac{1}{2} + \frac{1}{8z}\{1-(z-u)^2\}\log\left|\frac{z-u+1}{z-u-1}\right| + \frac{1}{8z}\{1-(z+u)^2\}\log\left|\frac{z+u+1}{z+u-1}\right| \tag{4.10}$$

$$f_2(u,z) = \begin{cases} \dfrac{\pi}{2}u, & \text{for } z+u<1, \\ \dfrac{\pi}{8z}\{1-(z-u)^2\}, & \text{for } |z-u|<1<z+u, \\ 0, & \text{for } |z-u|>1 \end{cases} \tag{4.11}$$

Here *k* and ω are replaced by the dimensionless variables $z = k / 2k_F$, $u = \omega / 2k_F$, and

$$\chi^2 = \frac{q^2}{\pi\hbar v_F} \tag{4.12}$$

Where v_F is the Fermi velocity. The wavenumber integration limits are given by:

$$k_{1,2}(\omega) = \sqrt{2m_e}[E^{1/2} \mp (E - \hbar\omega)^{1/2}] / \hbar \tag{4.13}$$

Solving equation (4.7) numerically for r_s = 3 (for an Au film), the resulting kinetic energy spectrum of the internal secondary electrons is depicted in Fig. 4.33. Note that the energy here is referenced to the Fermi energy as the electrons are still residing within the material itself. Remarkably, 27% of the electrons below the W_F (5.2 eV for the Au film) have energies only a single photon energy ($h\nu$ = 1.55 eV) below W_F. When the electron gun is turned on and the primary electrons are exciting SE in the Au film; it is expected that these generated internal secondary electrons can be freed by absorbing a single incident photon and contribute to the total collected current. Since, this is a single-photon process, the total number of freed electrons will scale linearly with the incident intensity and thus explains the observed linear behaviour.

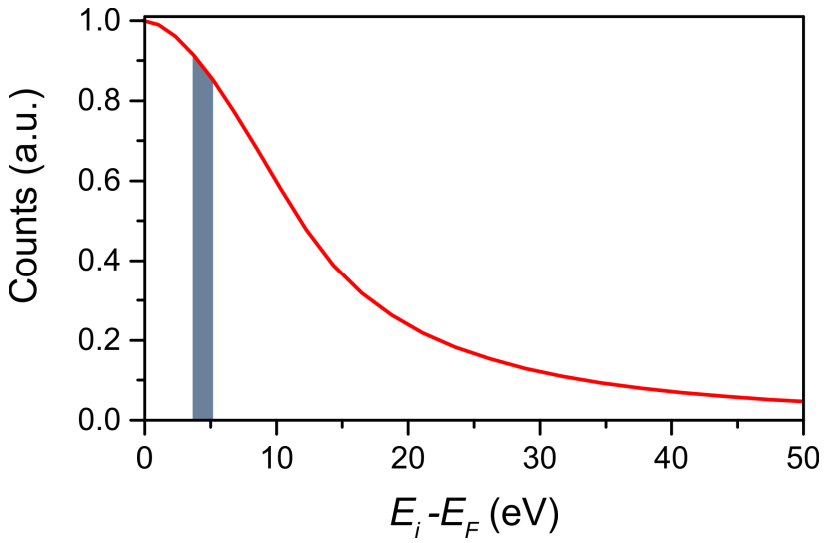

Figure 4.33. Internal secondary electron energy spectrum. Note that the energy presented here is referenced to the Fermi energy. The shaded region indicates the population of electrons having energy between W_F-$h\nu$ and W_F.

4.4.4. Explanation of Angular Beaming

With the linear scaling behaviour explained by single-photon absorption of internal secondary electrons, attention must be paid to explain the origin of the ~30° beaming that is observed in the angular distribution. Again, there are multiple possibilities for the beaming that will be explored in this section.

The first, and possibly most naive explanation is that the SP fields are simply deflecting the 300 eV electrons from the primary beam. To determine if this deflection is happening, particle tracking simulations were performed assuming a 300 eV electron beam is passing ~15 nm above the Au film. Exemplary trajectories along with the corresponding angular distributions are shown in Fig. 4.34 for three peak SP electric field strengths. At the experimental intensity of 25 GW/cm^2, the peak electric field is 0.4 V/nm. Assuming a modest 25× electric field enhancement, the 300 eV electrons trajectories are unaltered as shown in Fig. 4.34(a). Increasing the enhancement to 90× (35 V/nm), the electrons exhibit some deflection between 5-10°. To reproduce the experimentally measured 25° deflection requires an unrealistic 175× enhancement. To further verify that the 300 eV electrons are not being deflected by the SP field another experiment was carried out. This experiment examined the angular distribution of the 300 eV electrons. To do so, a retarding potential grid with an applied voltage of -295 V was added in front of FC1, along with a grounded grid in front to shield the primary 300 eV electrons from the retarding potential. This is depicted schematically in Fig. 4.35. It was determined via finite element simulations that the introduction of this potential grid does not affect the primary electrons within the experimental region in front of the prism. Full simulation results are discussed in Appendix E. The retarding potential grid acts as a high

pass filter, meaning only electrons with kinetic energies above 295 eV would make it to the detector. Figure 4.36 depicts the collected signal as a function of angle for the electron gun being off and an I_{beam} of 5 nA. Within the error of each angular measurement, there are no 300 eV electrons present. Again, it is important to note that by using the lock-in amplifier, only electrons that have interacted with the SP field will be detected. Also note that the experiment was carried out at I_{beam} of 50 and 500 nA which produced the same lack of 300 eV electrons. They are not included in Fig. 4.36 for clarity.

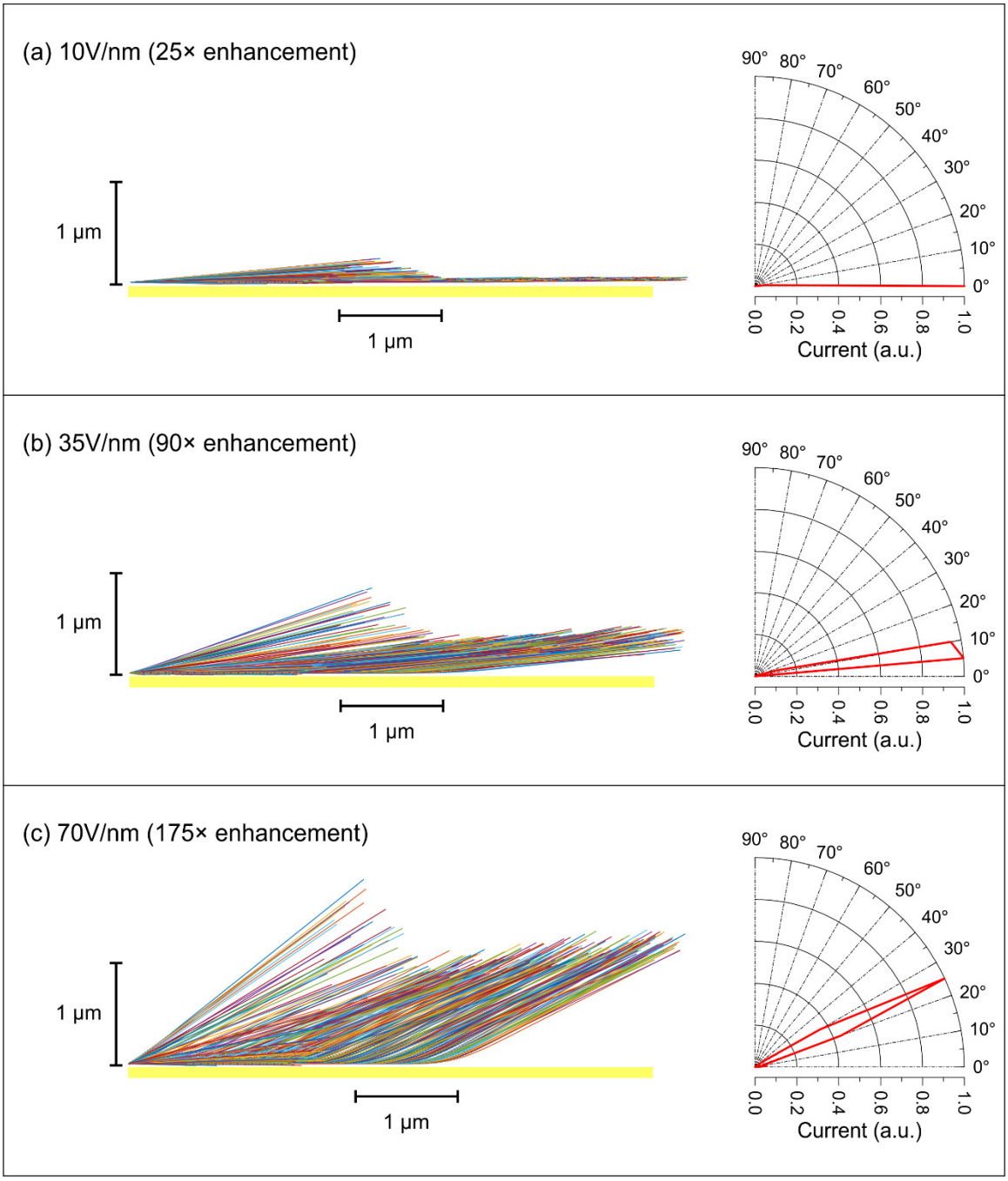

Figure 4.34. Exemplary trajectories of simulated deflected 300 eV electrons and their corresponding angular distributions for E_{SP} = (a) 10V/nm, (b) 35 V/nm, and (c) 70 V/nm.

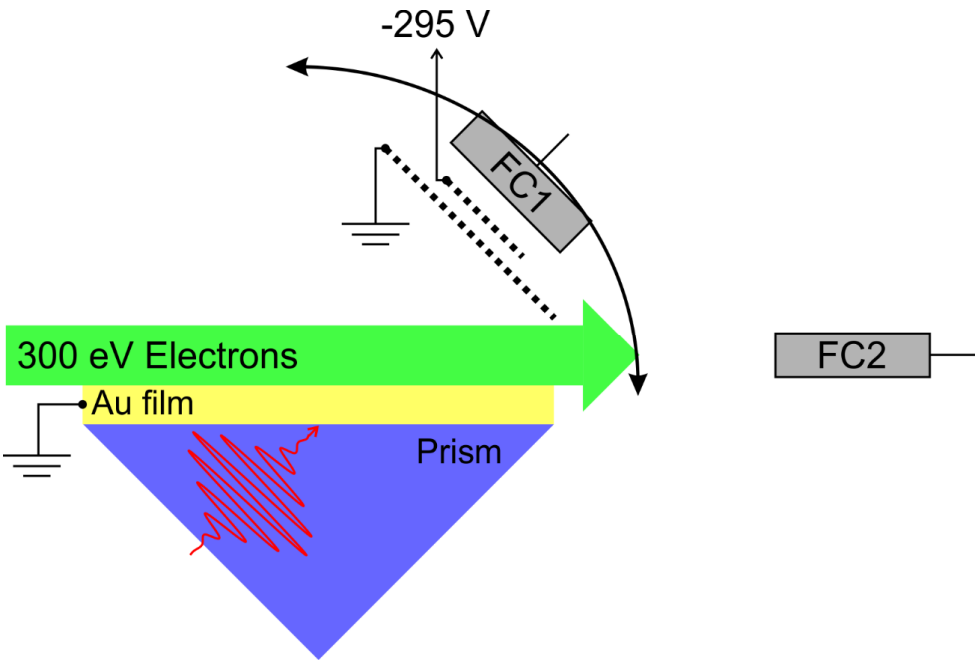

Figure 4.35. Dual grid retarding potential setup for measuring deflected 300 eV electrons.

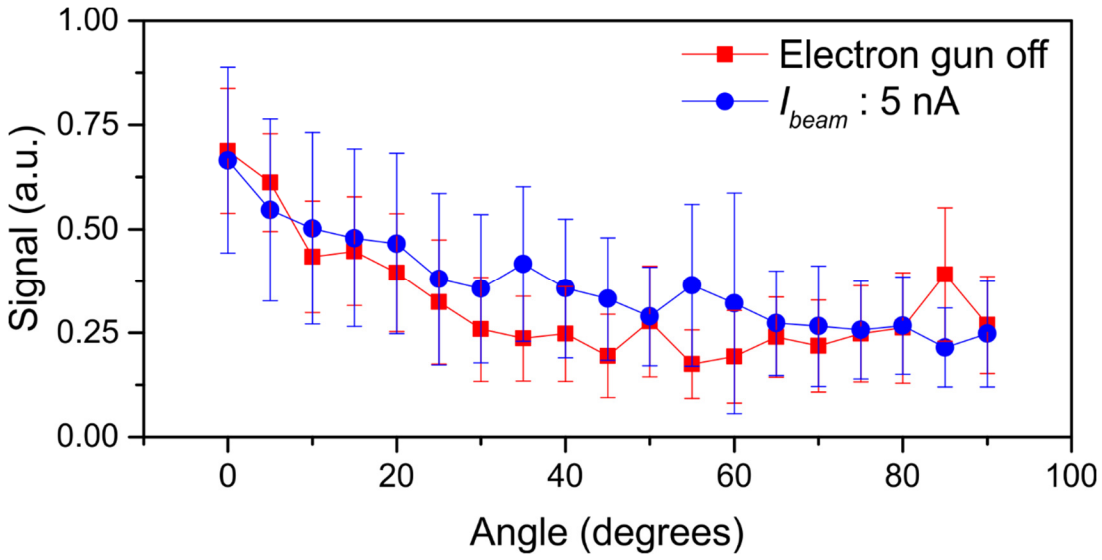

Figure 4.36. Measured angular distribution of filtered electrons indicating the absence of deflected 300 eV electrons. The error bars represent the standard deviation of the signal measured on the lock-in amplifier.

Once it was confirmed that the angular beaming was not originating from simple electron deflection, attention was paid to the generation process of the electrons themselves, both the secondary electrons and the SP generated electrons. It is well known that when an electron beam passes above a metallic surface it can excite a SP wave [82]. In order to excite the SP, there must be phase-matching between the SP and the propagating electron beam. The phase-matching condition can be determined by matching the dispersion curves of surface plasmons in Au and the electron beam. Figure 4.37 depicts the dispersion curve for Au (using permittivity data from [50]), and an electron beam with 300 eV kinetic energy. The dispersion relation for an electron beam is:

$$k_{electron} = \frac{\omega}{\sqrt{2E_p / m_e}} \tag{4.14}$$

From Fig. 4.37, it is determined that at the low-energy that we are using (300 eV), and for a lossy metal (Au), the dispersion curves of the SP and the electron beam never cross. This indicates that the electron beam does not excite a surface plasmon on the Au film. The minimum energy required to excite such a surface plasmon is 15 keV. This result guarantees that we are not exciting a so-called “electron-beam surface plasmon” and thus this cannot be affecting the angular distribution of our electrons.

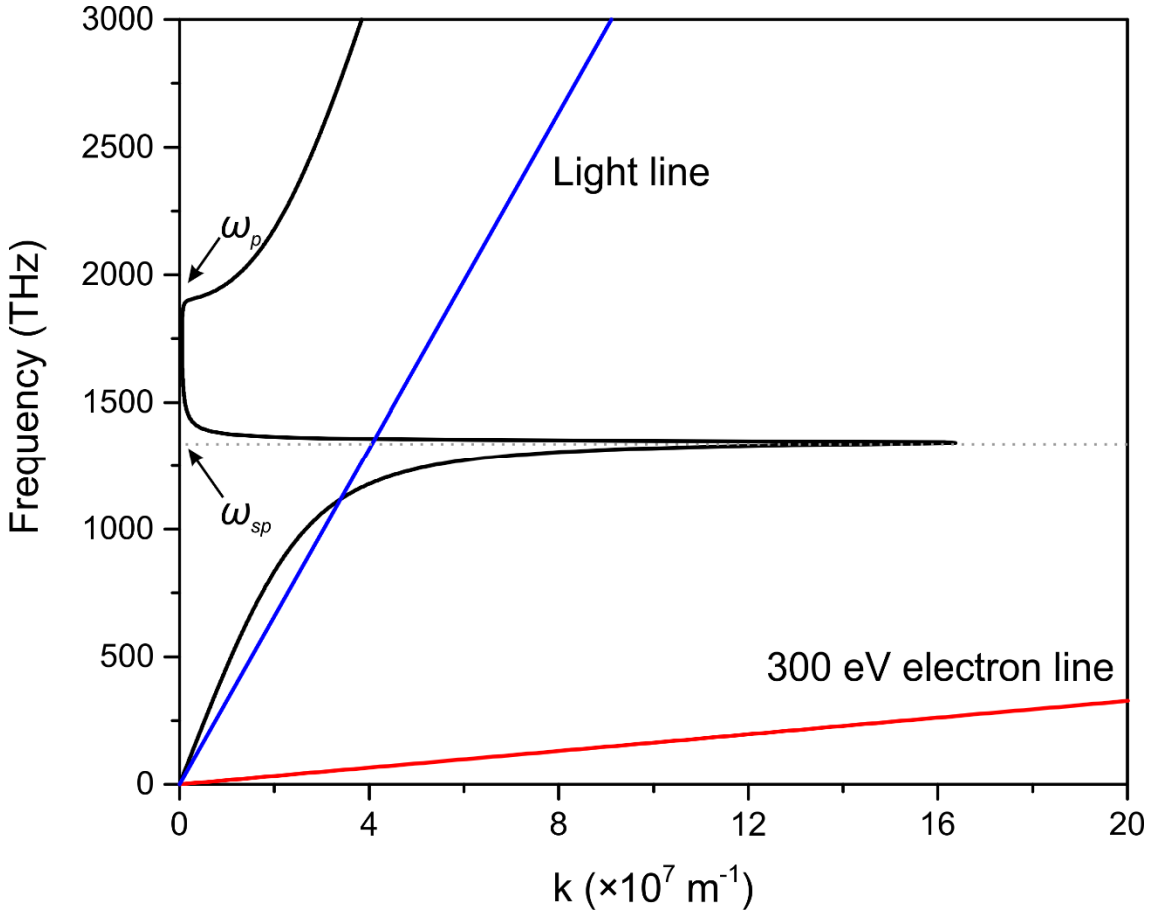

Figure 4.37. Plasmon dispersion curve for a lossy Au film and 300 eV electron beam. Note that the 300 eV electron line does not cross the Au curve indicating no excitation of surface plasmons.

The third possibility is that the low incidence angle of the primary electron beam is causing the secondary electrons to not follow their standard cosine distribution. A software program called CASINO [83,84] was used to perform Monte Carlo simulations of the secondary electron angular distribution for various grazing incidence angles. Figure 4.38 depicts the angular distribution for θ_{beam} of 1°, 2°, 10°, and 90° to confirm the validity of the Monte Carlo simulation when compared to the standard cosine distribution. For grazing incidence (1° up to 10°), the angular distribution does shift slightly towards the direction of electron beam propagation. However, there is no peak at

30° as is observed in the experimental distribution. As such, it can be concluded that the incidence angle of our electron beam is not responsible for the angular beaming.

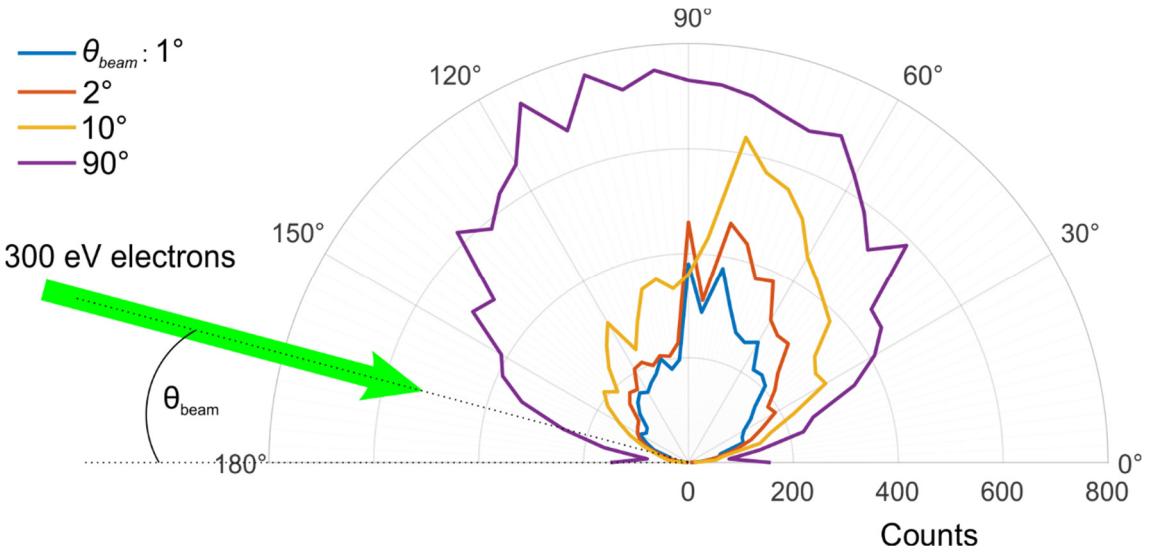

Figure 4.38. Monte Carlo calculated angular distribution for various incident primary electron beam angles.

The final possibility and most likely scenario for the forward scattering of the secondary electrons is scattering from the primary electron beam. The SE will be ejected from the Au film with a cosine distribution and kinetic energies < 50 eV. Simultaneously, the 300 eV primary electrons will be passing through this cloud of SE. A portion of the SE will scatter from the primary electrons and become directed along the direction of propagation. From the calculated SE energy distribution (Fig. 2.10), 51% of the SE will have energies less than 5 eV. As such, only scattered SE with < 5 eV are considered for particle tracking simulations.

4.4.5. Modelling of Plasmon Based High Current Secondary Electron Source

Particle tracking simulations were performed to verify the experimental results. For these particle tracking simulations, secondary electrons were introduced and allowed

to interact with the SP fields. The electrons were given initial kinetic energies corresponding to the SE energy spectrum of Fig. 2.10 and spatially directed in a cosine angular distribution. Figure 4.39 depicts the angular distribution of the electrons once they have interacted with the SP field for varying SP field strengths. Note that there is little change in the distribution as E_{SP} changes, and more importantly, there is no beaming of the SE electrons for E_{sp} < 10 V/nm. It was determined through simulations that in order to achieve electron beaming to 25° requires approximately 35% of the SE electrons with energies below 5 eV to be directed parallel to the direction of SP propagation. Taking this assumption into account, the angular beaming can be reproduced at a peak electric field strength of 17 V/nm (~42× peak electric field enhancement) as depicted in Fig. 4.40. Notably, my model is able to reproduce both the 25° beaming and the increased background of secondary electrons that are observed experimentally. It is also important to note here that the background cosine-like distribution will still be detected even while using the lock-in amplifier due to the single-photon absorption that is responsible for the linear power scaling discussed previously. Clearly, when secondary electrons are excited in the presence of a SP wave, their yield will be increased by absorbing a single photon and being freed from the metal. Subsequently, these SE will be preferentially scattered forward along the direction of propagation of the PE and SP wave where they will be accelerated by the SP field and beamed to 25° from the surface.

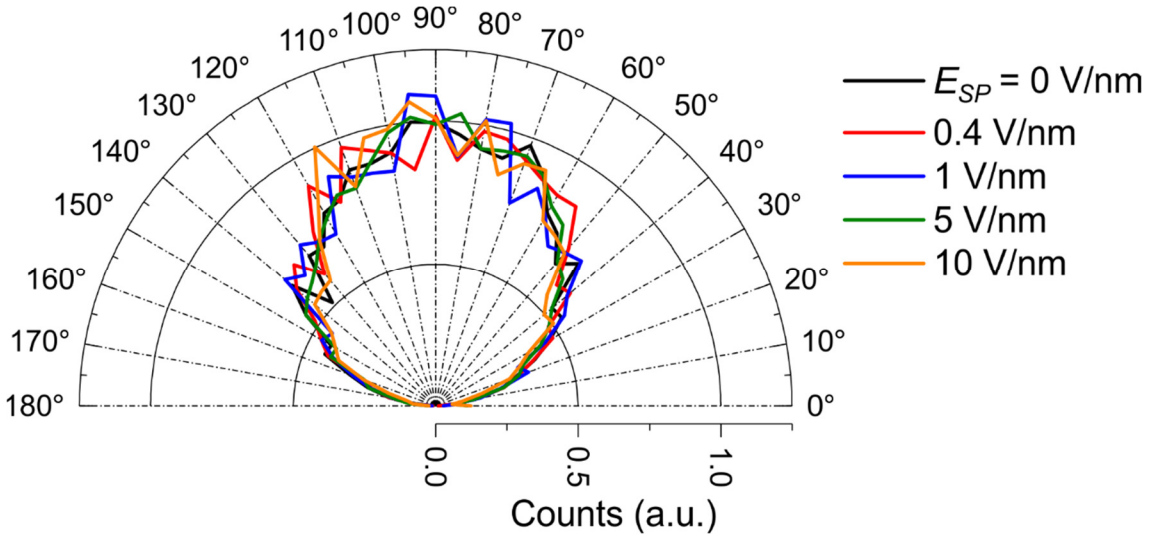

Figure 4.39. Angular distribution of secondary electrons after interacting with various E_{SP} field strengths.

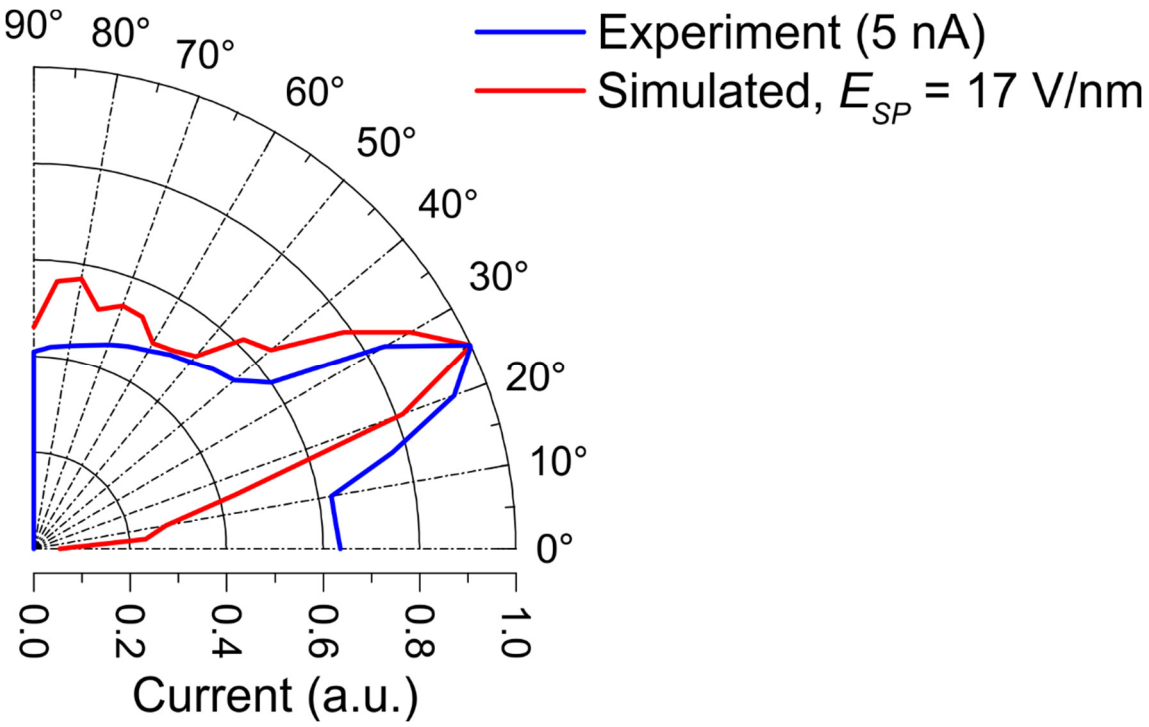

Figure 4.40. Simulated angular distribution assuming that 35% of SE are directed parallel to the direction of propagation.

4.4.6. Kinetic Energy of Surface Plasmon Driven Electrons

The kinetic energy of the collected electrons was also measured using a retarding potential grid setup. FC1 was positioned perpendicular to the Au film with the small aperture removed to provide an acceptance angle of ~90°. Care had to be taken such that the voltage of the retarding potential grid did not affect the electrons from the electron gun as that would alter the outcome of the experiment. To shield the electrons from the stray voltage, a grid was placed in front of the retarding potential grid and connected to ground. The setup is depicted schematically in Fig. 4.41(a) with corresponding photograph in Fig. 4.41(b). A full analysis of the affect of the retarding potential on the 300eV electrons is presented in Appendix E. As the retarding potential setup acts as a high-pass filter for electrons, the measured signal must be differentiated to produce the final kinetic energy spectrum. To get our spectrum, a polynomial was fit to the raw data and then differentiated to produce the final spectra presented in Fig. 4.42. Remarkably, when the electron gun is on, the kinetic energy spectra are quite similar, exhibiting a peak at 0 eV with a majority, ~60%, of their electrons below 10 eV, and a distinct hump around 20 eV. This is to be expected as the single-photon absorption of secondary electrons will produce a large population of low energy, <1.55 eV, electrons that can be subsequently accelerated within the SP field. There will also be electrons that are accelerated to higher kinetic energies depending on the phase of the SP field they are born into. Since the kinetic energy gain is independent of the number of electrons being excited it is expected that the shape of the kinetic energy spectrum does not change with I_{beam}. Only the peak current measured will shift with I_{beam}.

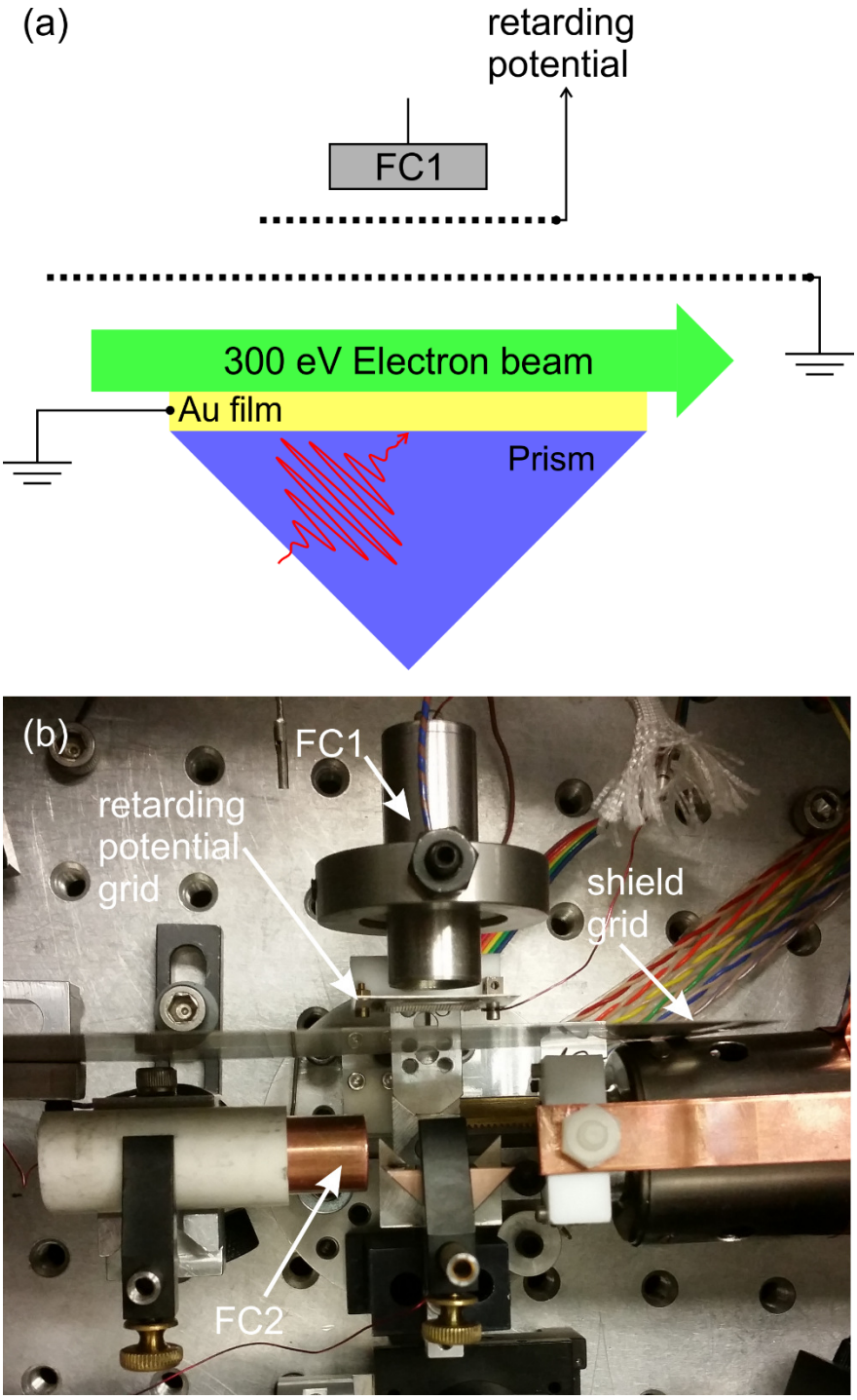

Figure 4.41. (a) Schematic and (b) photograph depiction of double grid retarding potential setup for kinetic energy measurement.

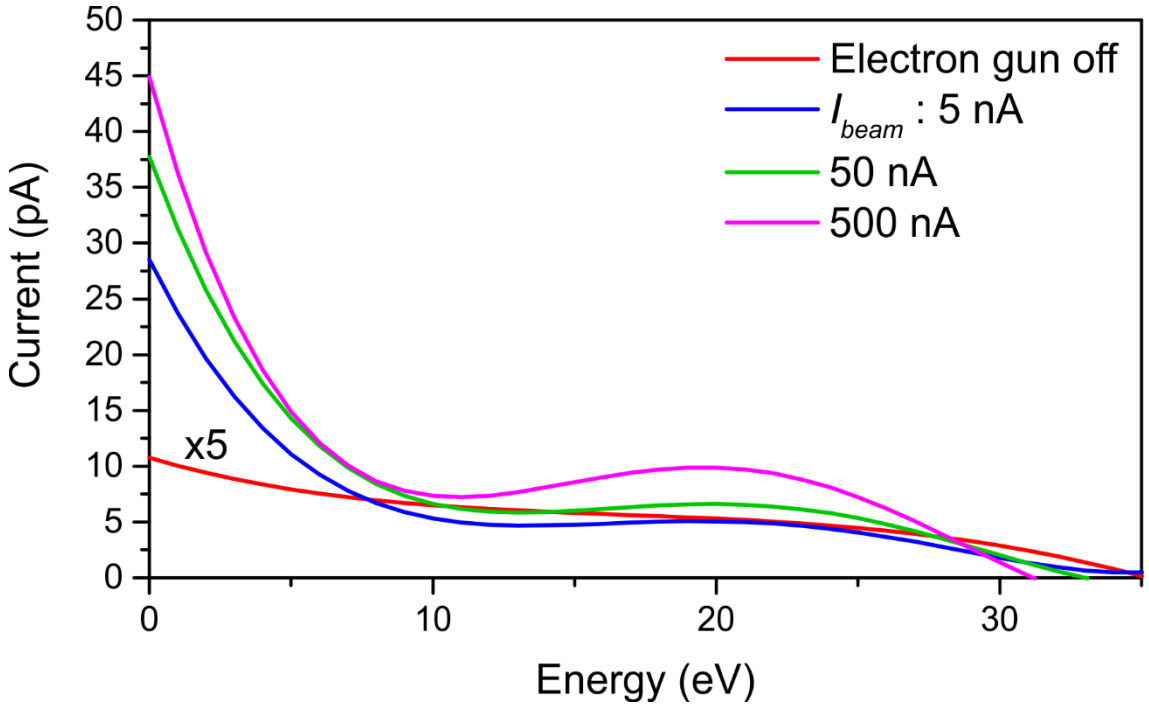

Figure 4.42. Measured kinetic energy spectra for electron gun off and at I_{beam} = 5, 50, and 500 nA. Note that the red Electron gun off curve has been scaled by 5×.

4.5. Summary

The results of this chapter demonstrate multiple methods for increasing the electron current of typical SP based electron sources. Introducing a layer of eCarbon beneath a layer of Au acts as a reservoir of electrons, reducing the nonlinear electron emission order. The eC layer was also shown to not disturb the plasmonic performance of the eC/Au bilayer thus making this a promising candidate for the next generation of ultrafast SP based electron sources driven at low laser intensities. The second half of this chapter investigates the interaction of free electrons with strong plasmonic fields. While this has been greatly studied for SP generated electrons, there had been no previous systematic study of externally injected electrons such as the primary 300 eV or even the SE that are present in this experiment. It was demonstrated that the yield of these SE can

be greatly increased through single photon absorption of the incident laser, resulting in a 10× increase in SP driven electron current. As such, it is envisioned that this can provide a platform for the next generation of truly high current SP driven electron sources.

Chapter 5

Solid-State Ponderomotive Devices

5.1. Introduction

Based on the knowledge gained from the previous chapters on the interaction of electrons with plasmonic fields in a vacuum environment, it was determined that a similar principle could be applied in solid-state devices. This chapter explores the integration of ponderomotive electron acceleration into Si-based devices. The first section details the design and simulation of a nanoplasmonic triode that can be monolithically integrated with current nanoelectronics to bridge the gap between optical and electrical signals. The design of a compact, solid-state CEP detector is detailed in the final section of this chapter.

5.2. Ultrafast Si-based Nanoplasmonic Triode[6]

As the push for increased computation speed and bandwidth continues, the limit achievable with traditional nanoelectronic circuits looms closer. In the short term, the move to photonic integrated circuits (PICs) has been heralded as the next step for information processing. PICs typically fall into the category of silicon photonics such that they can leverage the already mature complementary-metal-oxide-semiconductor (CMOS) fabrication technologies of modern nanoelectronics [85,86]. While PICs represent a significant increase in maximum theoretical speed by operating at optical

[6] A version of this section is published as S.R. Greig and A.Y. Elezzabi, "An Ultrafast Silicon Nanoplasmonic Ballistic Triode," *Appl. Phys. Lett.* **105**, 241115 (2014).

frequencies in the hundreds of THz, they do so at the cost of increased device footprints. Owing to the fact that light cannot be squeezed below the diffraction limit, the typical dimensions of these devices are on the order of hundreds of nanometers compared to the tens of nanometers and below of current and next-gen nanoelectronics [87,88]. In addition, trying to further shrink these dimensions results in the optical modes of the photonic waveguides not being tightly confined to the core and thus introducing a greater risk of cross talk between waveguides [89]. This leads to an overall decrease in integration density. It is for these reasons that nanoplasmonic circuits are being explored as the next step in optical computing.

Nanoplasmonic circuits afford all the benefits of photonic circuits, namely increased speed and bandwidth, while operating with dimensions below the diffraction limit of the operating lightwave [90]. As such, waveguide widths can be reduced 3-4 times [89]. The SP also allows for tighter confinement leading to increased integration density and easier access to nonlinear optical effects for active devices [91]. They are not without their drawbacks though. The requisite metal layers in plasmonic waveguides introduce loss in the circuits that leads to significantly shorter propagation lengths (100 μm vs. 9 cm) [92]. Thus, nanoplasmonic circuits are not ideal for long range on-chip signal routing. Furthermore, the best plasmonic metals are the noble metals (Ag and Au) which are not CMOS compatible and require different fabrication techniques compared to current nanoelectronics. However, by careful selection of materials and design, nanoplasmonic devices can be made to be fully CMOS compatible without a reduction in performance.

The major building block in electronics is the three-terminal transistor which permits switching or amplification of electrical signals. The principle of operation is the control of a current via the application of voltage. The first class of devices exhibiting this behavior and that marked the launch of the modern electronics era are vacuum tubes in a triode configuration [93]. Vacuum tube triodes utilize an evacuated glass tube with an electron source (cathode), an electron collector plate (anode), and a control grid [94]. An example of a vacuum tube triode is shown in Fig. 5.1(a). Figure 5.1(b) depicts a cartoon representation of the vacuum tube triode operation. By thermionic emission of electrons from the cathode and subsequent acceleration in the cathode-anode electric field, current is realized at the anode. To control this current, a negative voltage is applied to the grid which creates an energy barrier. Electrons with energies below the barrier height are rejected, reducing the overall collected current. Vacuum tube triodes still find niche applications in high current modulation and high-power circuits, where they offer far superior performance and reliability compared to semiconductor transistors.

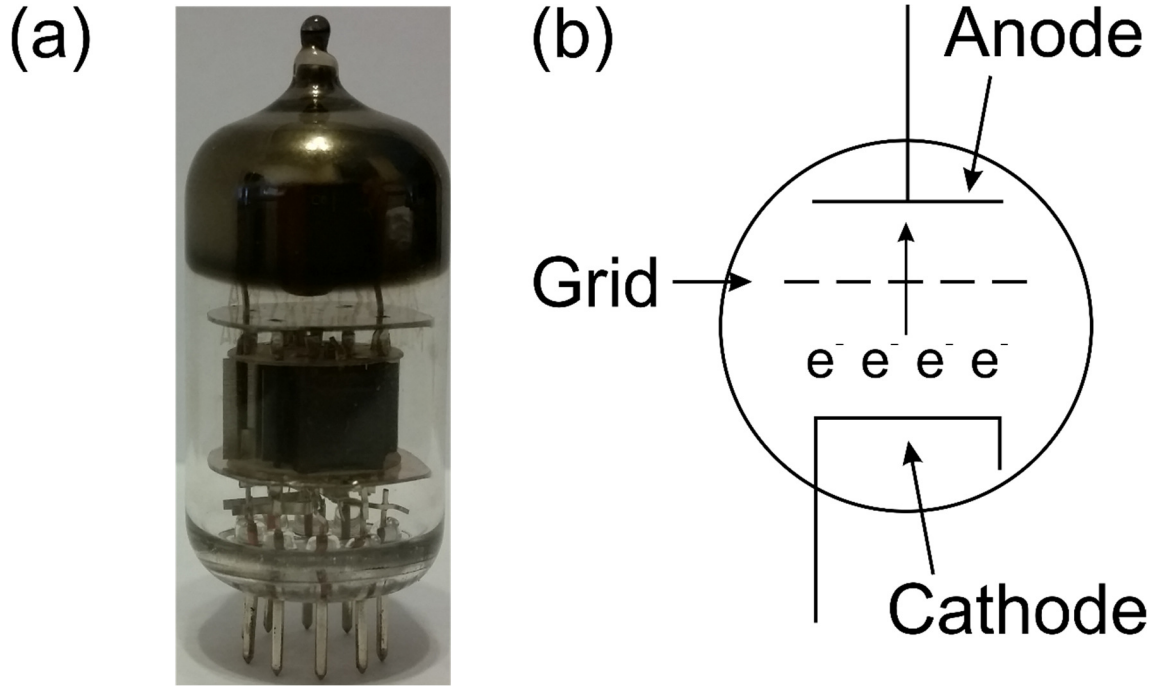

Figure 5.1. (a) Dual triode 12AX7 vacuum tube. (b) Cartoon depiction of vacuum tube triode operation.

The vacuum tube has largely been displaced by the metal-oxide-semiconductor field-effect transistor (MOSFET) due to its high operating speed, ease of fabrication, and large scale integration capability in a silicon based CMOS platform [95]. As such, there has been an ongoing push to create increasingly smaller and faster MOSFETs. An attempt has also been made to create a compact CMOS compatible vacuum tube transistor [96]. As previously mentioned, there exists a limit for the compactness and operational speed of CMOS circuitry. As such, nanoplasmonic devices are being explored to reach higher operating speeds while maintaining nanoscale device footprints and high integration densities [97,98]. To reach the ultimate goal of monolithic integration of nanoelectronics and nanoplasmonics, these structures must be made CMOS compatible.

This section presents a detailed investigation of an ultrafast CMOS compatible Si nanoplasmonic based triode device. The combination of high nanoscale optical field confinement, local nanoplasmonic field enhancement, and the extreme spatial gradient of the electric field act to produce an effective ponderomotive potential that accelerates and dictates the motion of electrons in a Si waveguide core. Through control of a voltage barrier, the nanoplasmonic field-driven current of the device can be modulated, allowing for precise control of the output current behavior, similar to that of a vacuum tube triode.

5.2.1. Nanoplasmonic Triode Device Structure

The design of the silicon plasmonic triode is based on nanoplasmonic waveguides that have been previously fabricated [73], but with materials chosen to maintain compatibility with CMOS fabrication. Copper is chosen for the metallic cladding due to its widespread use in modern CMOS processes and the fact that it can still support the required surface plasmon wave. Utilizing Si for the core allows for nonlinear photogeneration of the electrons due to two photon absorption via Si's high $\chi^{(3)}$ nonlinear coefficient. Tungsten is chosen for the grid metal for two reasons: firstly, it is widely used in CMOS nanoelectronics, and secondly, due to its high optical losses at $\lambda = 1.55$ μm, it does not interfere with the plasmonic mode. As such, the high spatial asymmetry, enhancement, and confinement of the nanoplasmonic field remain unaffected by the W grid. A 3D schematic depicting the device is shown in Fig. 5.2. The nanoplasmonic triode has a width of $w = 200$ nm and a length of $L = 350$ nm, defining a compact footprint of 0.07 μm^2. The upper Cu has a thickness of $h_1 = 60$ nm, the Si core has a thickness of $h_2 = 30$ nm (~ mean-free-path for electron in Si [73]) and the bottom Cu has a thickness of $h_3 = 100$ nm. The grid consists of $w_g = 4$ nm × $h_g = 3$ nm lines spaced $s_g = 4$ nm apart

arrayed throughout the waveguide in both the x and z directions. The W grid is embedded in the Si core 10 nm above the lower Cu. Due to the complex structure of the nanoplasmonic triode, polycrystalline Si is used as the waveguide core material.

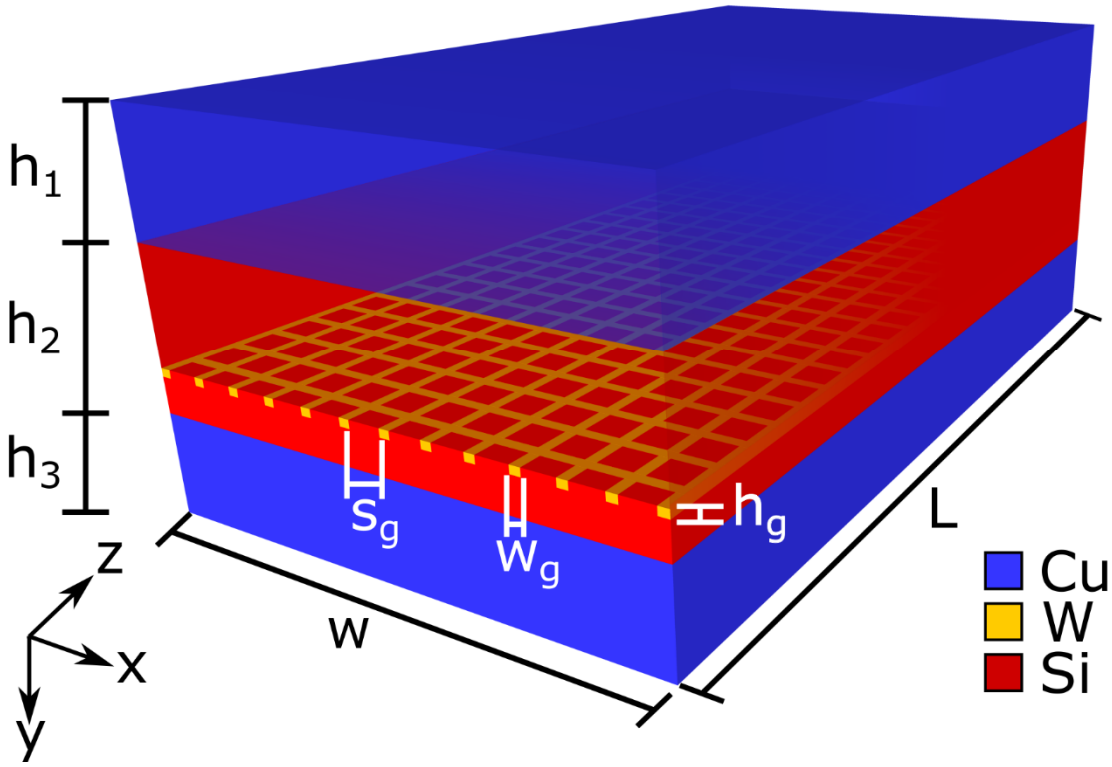

Figure 5.2. 3D schematic of silicon nanoplasmonic triode with dimensions h_1 = 60 nm, h_2 = 30 nm, h_3 = 100 nm, w_g = 4 nm, h_g = 3 nm, s_g = 4 nm, of w = 200 nm, L = 350 nm.

5.2.2. Simulation and Operating Principle of the Nanoplasmonic Triode

FDTD simulations were used to calculate the electromagnetic fields within the nanoplasmonic triode using material data from Palik [51], and Johnson and Christy [99]. Operating at the telecommunications wavelength of λ = 1.55 μm, an 84 fs laser pulse is used to excite a surface plasmon at the upper Cu-Si interface. A depiction of the mode in

the waveguide is represented in Fig. 5.3. The mode is highly confined to the center of the Si core and possesses a high field gradient decaying from the upper Cu towards the W grid, a necessary criterion for the ponderomotive force.

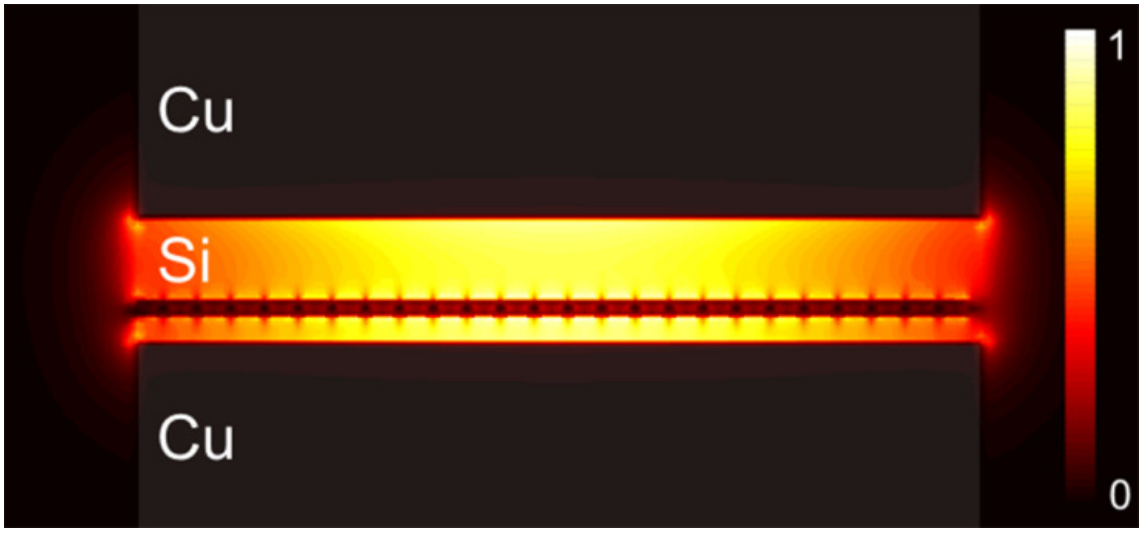

Figure 5.3. Electric field intensity distribution in the *xy*-plane at $\lambda = 1.55$ μm, excited by an 84 fs pulse.

The surface plasmon at the upper Cu-Si interface creates a highly spatially inhomogeneous oscillating electric field profile with electric field strength E_{SP}. Electrons are generated in the Si core via two-photon absorption of this field. As each photon in this process possesses 0.8 eV of energy and the bandgap of Si is 1.1 eV, the 2PA generated electron possesses an excess kinetic energy of 0.5 eV ($2h\nu - E_g$) with velocity, $\vec{v}$, directed in a random direction. The electron is then free to interact with the E_{SP} field. This nonlinear interaction between the electron and the E_{SP} field allows for ponderomotive acceleration of the electron to higher kinetic energies. In the model, approximately 10^5 representative electrons are generated at random spatial and temporal positions within the Si. Each electron is weighted proportionate to the I_{SP}^2 at its temporal and spatial generation position

and subsequently tracked through its interaction with the E_{SP} field. If an electron collides with any surface it is no longer considered in the simulation. Since the extent of the Si region is approximately the mean free path of a free electron in Si, the transport of the electrons is calculated via the equation of motion in a ballistic regime [73]. Throughout the model, the electron effective mass in Si is taken to be $m_e^* = 0.26m_e = 2.37\times10^{-31}$ kg [100], and the two-photon coefficient is taken to be 0.68 cm/GW [101].

The operating principle of the nanoplasmonic triode can be explained through the inhomogeneity of the rapidly oscillating electric field and the ponderomotive force. Here, an ultrafast optical pulse is coupled directly onto the upper Cu-Si interface. The combined upper Cu and adjacent Si layer act like a *cathode* in a typical triode as the Cu layer confines the E_{SP} in the Si layer where free electrons are photogenerated through 2PA. As such, the electron source density is proportional to I_{SP}^2. The E_{SP} field then accelerates and decelerates the electron during its positive and negative half-cycles, respectively, setting up a quasi-DC force directed downwards toward the bottom electrode. The cyclic effect of the ponderomotive potential on the electrons' trajectories is illustrated in Fig. 5.4 where electrons having more oscillations in their trajectory indicate greater interaction with the ponderomotive potential. This ponderomotive force from the nanoplasmonic field plays a similar role to a cathode-anode electric field in a typical vacuum tube triode, providing directional net electron flow (i.e. current). By applying a voltage between the W grid and the upper Cu, an effective electron energy barrier is created, analogous to the grid of a vacuum triode. By modulating the height of this barrier (i.e. varying the applied voltage), the number of electrons passing through it and thus the current can be controlled. This general operating principle of the nanoplasmonic triode can be applied to other

semiconducting materials or other operating wavelengths as long as the electron generation mechanism is a non-linear process and a plasmonic mode can be supported within the structure. Operation at λ = 1.55 μm in a Si waveguide is ideal as it affords a non-linear electron generation process (2PA), as well as compatibility with modern optoelectronic systems and fabrication technologies.

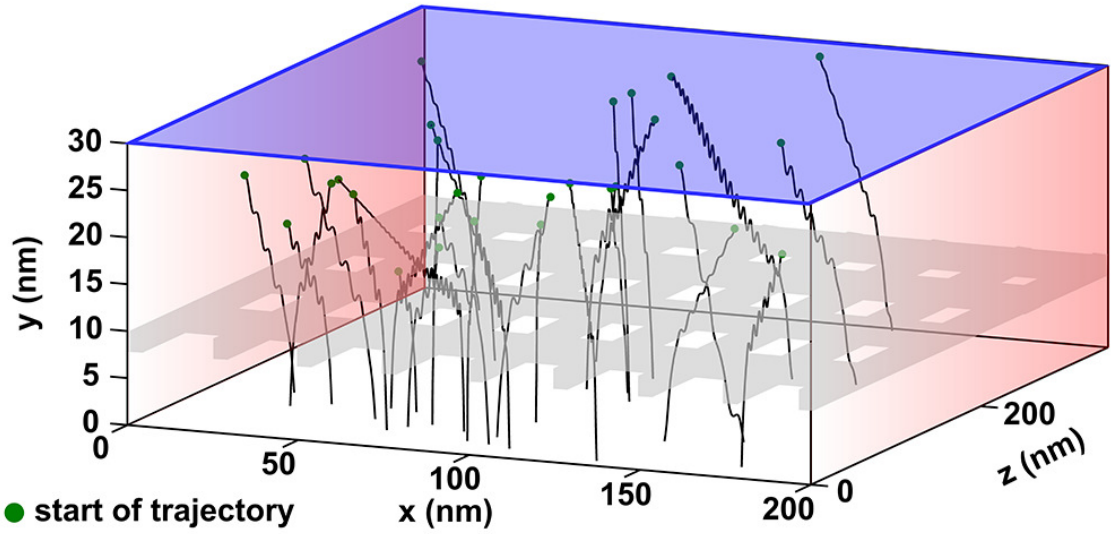

Figure 5.4. Exemplary trajectories of 29 electrons interacting with a ponderomotive potential, a green dot represents the start of the electron's trajectory.

Each generated electron will experience acceleration (deceleration) based on its interaction with the E_{SP} field, resulting in a gain (loss) of kinetic energy. The change in kinetic energy is dependent on the electric field profile the electron experiences as it traverses the waveguide and therefore depends on its spatial and temporal generation point. This allows for a broad distribution of kinetic energies as the electrons reach the W grid. It should be noted that the electron kinetic energies are calculated as $E_k = \frac{1}{2} m_e^* v^2$. Notably, some electrons will be accelerated to energies higher than their initial 0.5 eV, while others may be decelerated to <0.5 eV. The electrons that reach the W grid will either be allowed

through or rejected depending on their acquired kinetic energy and the voltage applied between the W grid and upper Cu. The energy-dependent electron transmission through the grid was calculated using finite element simulations for DC grid voltages, V_g, between 0 and -1 V. At each V_g, an effective energy barrier, $\phi_g = qV_g$, will be created at the grid opening, thus controlling which electrons will pass through. If the electron possesses kinetic energy greater than ϕ_g, it will continue past the grid to the bottom Cu electrode and contribute to the final output current of the device.

5.2.3. Nanoplasmonic Triode Performance

The kinetic energy spectra of the electrons at the bottom Cu anode, with zero voltage applied to the grid, for various values of E_{SP} are depicted in Fig. 5.5. The electron energy distribution is wide spread with a peak centred between 1 to 2 eV for E_{SP} ranging from 1 V/nm to 3 V/nm. Each distribution also includes electrons separated from this main peak that were able to achieve higher kinetic energies through greater interaction with the E_{SP} field. An E_{SP} of 3 V/nm was able to accelerate the electrons to a maximum energy of 18.78 eV over a distance of only 23 nm, while an E_{SP} of 1 V/nm provides a maximum energy of 4.45 eV over the same distance. As each E_{SP} yields a large electron energy distribution between 0 and 1 eV (e.g. 88% of total electrons for 1 V/nm and 23% for 3 V/nm) a V_g of 0 to -1 V can be applied to limit the number of electrons passing through the grid. Fig. 5.5 also illustrates the increase in number of electrons generated and accelerated to higher energies as E_{SP} increases.

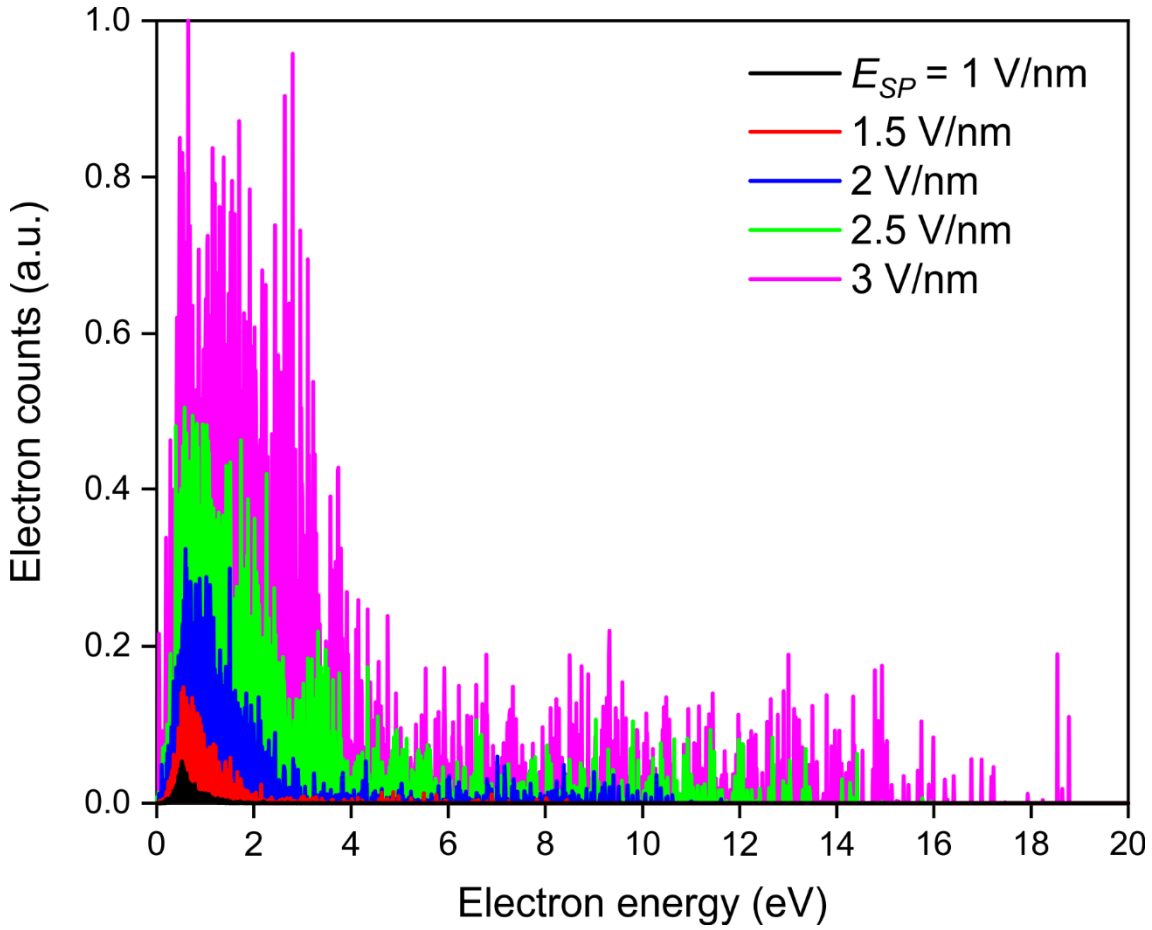

Figure 5.5. Electron kinetic energy spectra for different E_{SP} values at $V_g = 0$ calculated at the bottom Cu electrode.

To fully describe the ultrafast nature of the nanoplasmonic triode the arrival times of the electrons at the bottom Cu electrode for various E_{SP} need to be examined. Fig. 5.6 shows the arrival times for three different E_{SP} field strengths, 5×10^8 V/m, 1×10^9 V/m and 1.5×10^9 V/m at $V_g = 0$ V. Each time response has a similar shape but as E_{SP} increases, a double-peaked signature begins to arise. The first peak is dominated by the higher energy electrons of the increased E_{SP} field. For an E_{SP} field strength of 1.5×10^9 V/m, 67% of the electrons arrive within the first 75 fs and the rest arrive over the next 75 fs, demonstrating an effective current switching time of 150 fs. For an E_{SP} of 5.0×10^8 V/m, only 61% of the

electrons arrive within the first 75 fs. The arrival time of electrons for higher field strengths is directly related to the higher energies acquired with higher field strengths as seen in Fig. 5.5. Higher E_{SP} leads to greater acceleration, thus higher velocities which in turn allows for faster operation.

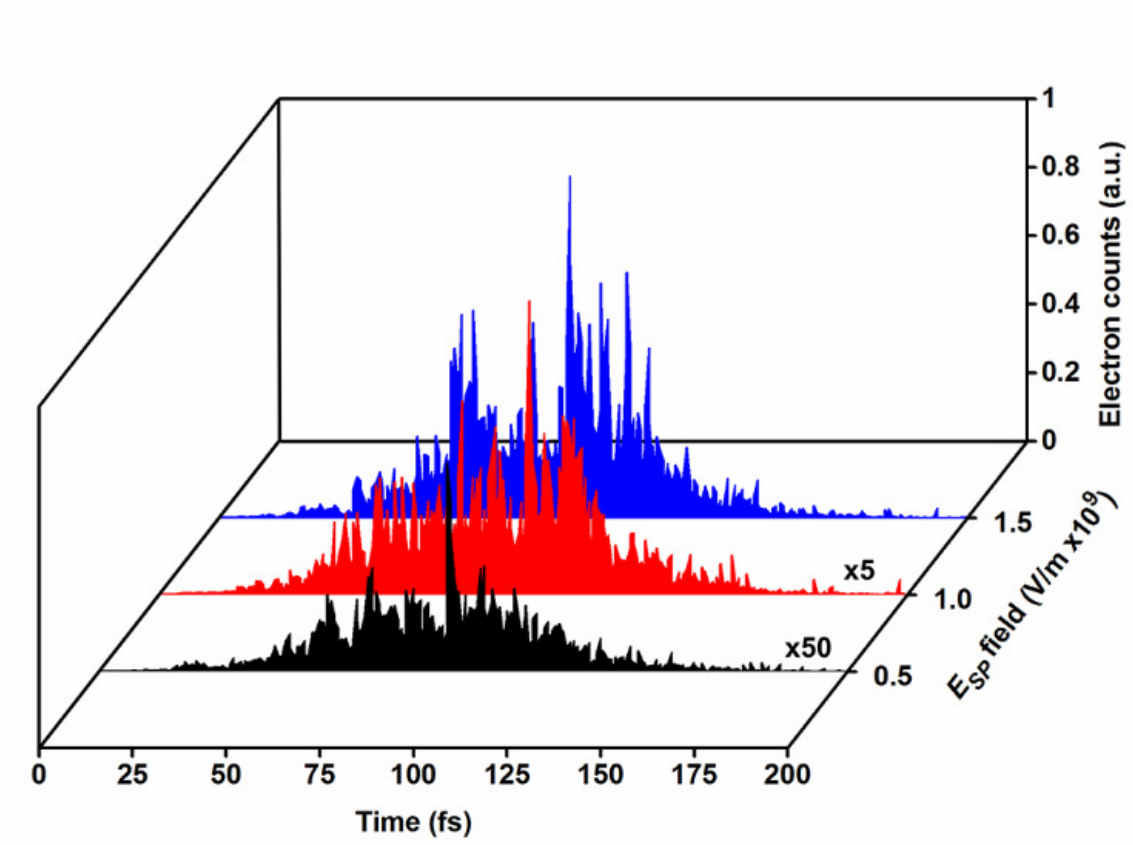

Figure 5.6. Electron arrival times at bottom Cu electrode for E_{SP} field strengths of 5.0×10^8 V/m, 1.0×10^9 V/m, and 1.5×10^9 V/m illustrating a current switching time of 150 fs.

When characterizing conventional three terminal devices the most important measure of performance is the current-voltage characteristic curves that demonstrate how the output current of a device responds to externally applied voltages. However, for the case of an optical device there is no applied voltage and thus it is more accurate to

examine the change in output current as a function of E_{SP} field strength. Then, by varying E_{SP}, the total number of photogenerated electrons can be controlled, as well as the distribution of kinetic energies of the electrons at the grid. When this is combined with a varying energy barrier at the grid, due to V_g, the output current characteristics can be precisely manipulated.

Figure 5.7 depicts the nonlinear characteristic curves of the output current with respect to varying E_{SP} at various V_g indicating a triode-like behaviour in a nanoplasmonic structure. Clearly, by increasing E_{SP}, the current increases nonlinearly due to a greater number of electrons being generated via 2PA. As a more negative V_g is applied, the current decreases, thus allowing for both amplification and switching operations. Amplification can be achieved by superimposing an AC signal on V_g which will be amplified in the output current. Initial results showed that the device can operate at a high pulsed current output up to 628 mA/μm for an E_{SP} of 1×10^9 V/m. From this it was determined that the operating point should be lowered to operate below an E_{SP} field of 2.5×10^8 V/m and a V_g between 0 and -0.75 V. Operation in this region allows for lower laser power, as well as voltage and current compatibility with modern MOSFETs [102]. At an E_{SP} of 2.5×10^8 V/m, the nanoplasmonic triode device can achieve a maximum output current of 11.7 mA/μm. Decreasing Vg from 0 to -0.75 V the maximum output current drops to 0.2 mA/μm, indicating switching operation.

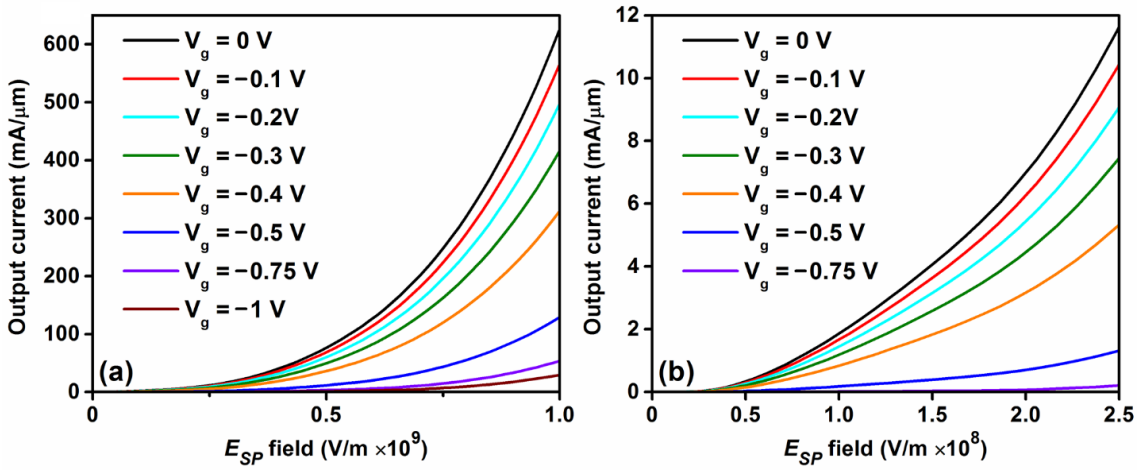

Figure 5.7. Characteristic output current curves of the Si nanoplasmonic triode. Descending curves represent decreasing current for increasing negative grid voltage, V_g. (a) High current operation with maximum output current of 628 mA/ μm for an E_{SP} of 1×10^9 V/m and $V_g = 0$. (b) Low current operation with maximum output current of 11.7 mA/μm for E_{SP} of 2.5×10^8 V/m and $V_g = 0$.

5.3. Ultracompact Solid-State Detector for Ultrafast Metrology[7]

Realizing that ponderomotive acceleration is sensitive to the CEP of few-cycle pulses (Chapter 3) and that ponderomotive acceleration can be applied to a Si-based nanoplasmonic platform, the idea for developing a solid-state CEP detector was born. When working with ultrashort laser pulses that are comprised of only a few cycles of the oscillating electric field, the CEP becomes important. The most widely used CEP detection method is the *f*-to-*2f* interferometric measurement, which measures the CEP offset between subsequent pulses within a mode-locked pulse train [103]. More recently, Wittmann *et al* [104] have developed a single shot method using photoionization of Xe gas to directly measure the CEP of a single laser pulse. Their device operates by using the

[7] A version of this section is published in S. Sederberg, C.J. Firby, S.R. Greig, and A.Y. Elezzabi, "Integrated Nanoplasmonic Waveguides for Magnetic, Nonlinear, and Strong-Field Devices," *Nanophotonics* 6, (2017).

laser pulse to generate electrons within the Xe gas and then subsequently observing the difference in current between left and right electron detectors. Another highly sensitive and simple technique to measure the absolute CEP of pulses spanning the telecommunications to terahertz spectral regions is electro-optic sampling, whereby a high-frequency probe pulse is used to measure the temporal structure of a low-frequency waveform [105].

This section investigates a solid-state equivalent that utilizes a semiconductor for the electron generation medium. Figure 5.8(a) depicts a cartoon illustration of the device that consists of a 50 nm thick Au antenna embedded in the top layer of a Si substrate, with a 20 nm gap between the antenna point and the transmission line. The device operates on a similar principle to the nanoplasmonic triode previously discussed. Electrons are generated in the Si within the gap by 5 fs, $\lambda = 800$ nm laser pulses. These electrons are then subsequently accelerated towards either the left or the right electrode, due to the asymmetry of the electric field at the tip of the nanoantenna. Exemplary trajectories for two values of CEP, $\varphi_{CEP} = 0$ and π, are depicted in Fig. 5.9. As the interaction is highly dependent on the CEP of the driving laser pulse, a difference in current between the two electrodes is obtained for varying values of CEP. Figure 5.8(b) depicts this difference in output current as a function of CEP, indicating that the detected current follows the expected sinusoidal behavior. This device represents a compact method for direct measurement of the CEP of a laser pulse from low intensity oscillators.

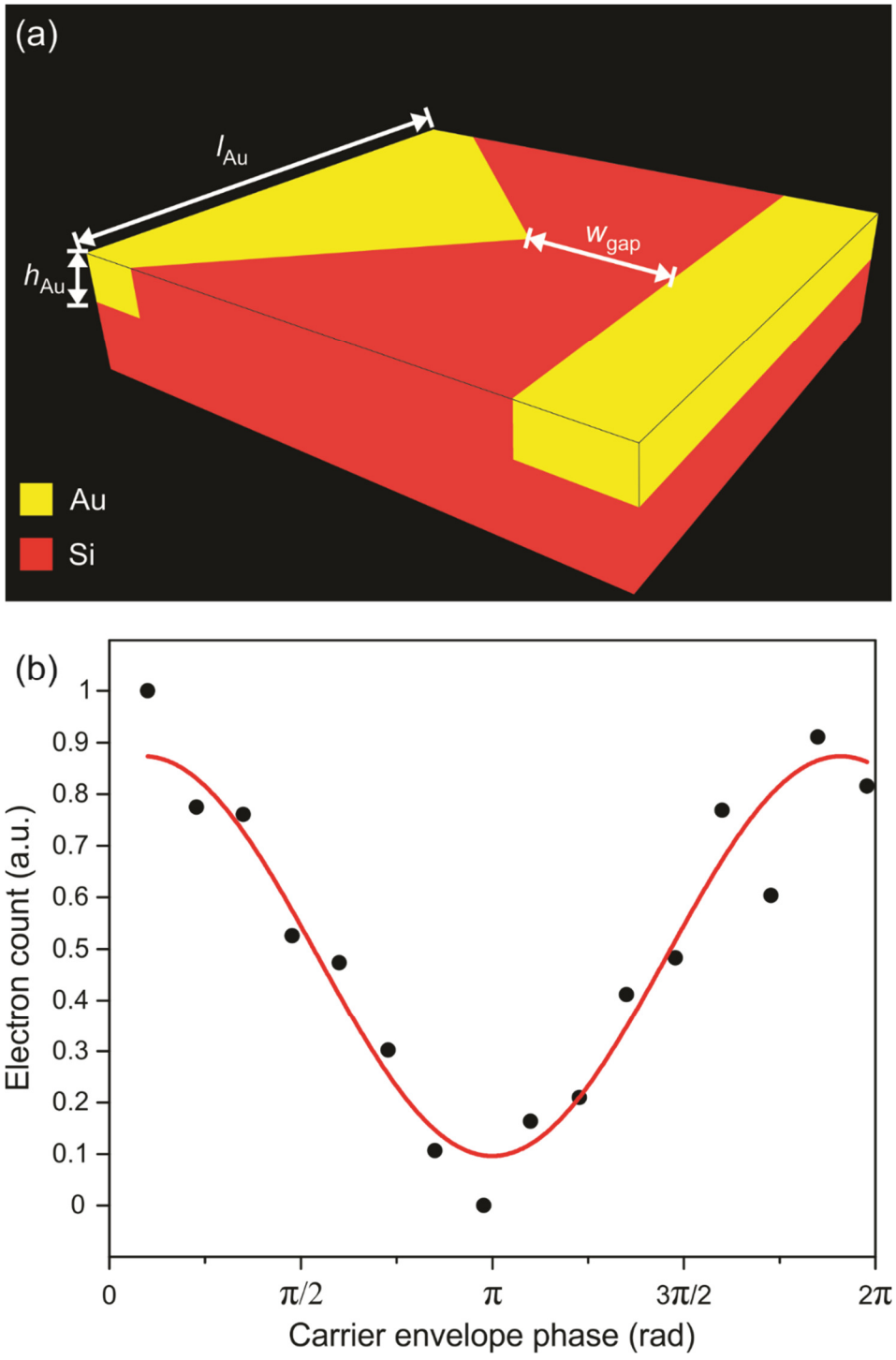

Figure 5.8. (a) 3D schematic of silicon CEP detector with dimensions w_{gap} = 20 nm, h_{Au} = 50 nm, and l_{Au} = 200 nm. (b) Output current response as a function of CEP for a 5 fs, λ = 800 nm laser pulse. The red line represents a sinusoidal fit.

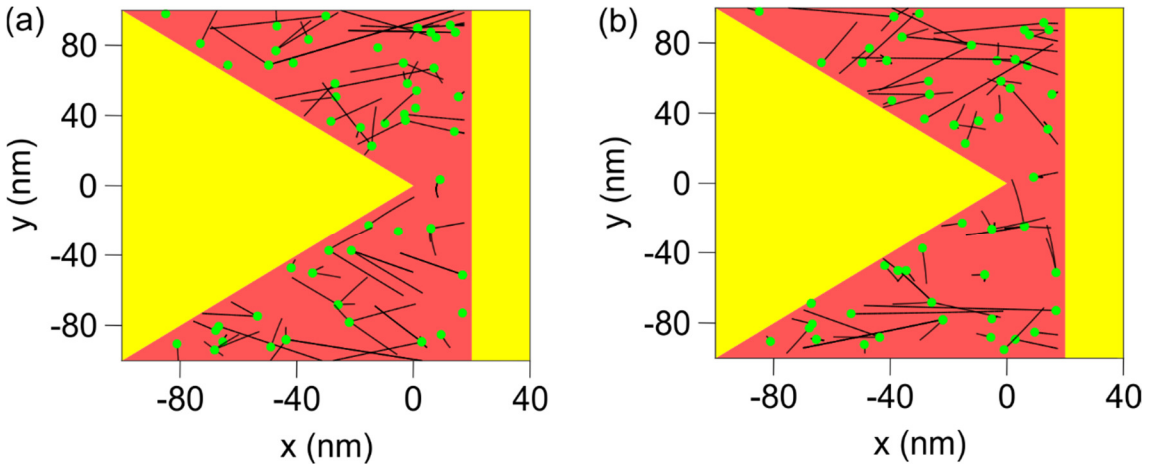

Figure 5.9. Exemplary electron trajectories within the gap for (a) $\varphi_{CEP} = 0$ and (b) $\varphi_{CEP} = \pi$.

A similar approach using wide-bandgap insulators such as quartz has been demonstrated by Kwon et al. [106]. The drawback to using an insulator over a semiconductor is that it requires the use of high laser intensities due to the generation process being multi-photon in nature compared to the linear absorption in the semiconductor. Not only does this have the issue of the reaching the laser damage threshold, it is also possible that the current in the insulator conduction band can lead to optical breakdown of the insulator.

5.4. Summary

This chapter demonstrates the application of the knowledge gained about vacuum based ponderomotive electron acceleration to compact solid-state devices. The nanoplasmonic triode is envisioned to help interface current nanoelectronics and nanoplasmonics for the next generation of high performance optical computers. The CEP detector can be used to replace current bulky interferometer setups to allow for measurement of the CEP at the exact location of the experiment.

Chapter 6

Modulation of the High Frequency Conductivity of Au[8]

Chapter 3 of this thesis explores how THz electric fields can be used to modulate the energy, directivity and angular spread of SP generated electrons. Here, the THz electric field modifies the electron's energy and momentum after they have left the metal. However, as was demonstrated in Chapter 4 it is beneficial to modify the material parameters and influence the electrons prior to leaving the metallic film. As such, it would be advantageous to allow the THz electric fields to interact with the conduction electrons in the film, thereby modifying the metal's dielectric properties. SP electric field enhancement, coupling, and photoemission is governed by a metal's dielectric function. We want to employ THz electric fields to alter the metal properties such that the photoemission properties of the metal can be controlled in the near-infrared (λ = 800 nm) regime. Furthermore, by generating the THz electric fields using the same driving laser as the photoemission, time-synchronization and thus low timing jitter is guaranteed.

Before the influence on photoemission can be studied it is important to understand how the metal dielectric function is altered in the presence of a THz electric field. To this end, this chapter details the investigation of THz plasmonically induced conductivity modulation in Au. Operating in the THz frequency regime affords a few major benefits

[8] A version of this chapter is published as A.Y. Elezzabi, P. Maraghechi, and S.R. Greig, "Terahertz Plasmonic Field-Induced Conductivity Modulation in Gold," *Sci. Rep.* 6 (2015).

including the ability to access and measure the amplitude and phase of the THz electric field through electro-optic sampling. The THz frequency regime is also far from any SP or intraband resonances in the metal.

6.1. Introduction

The behaviour of free and bound electrons in solids is one of the most fundamental areas of study in condensed matter physics. Understanding many critical, intricate mechanisms of interaction of electrons within materials is often revealed by introducing an external electric field. Electrical conductivity modulation, $\Delta\sigma$, by an electric field, serves as core for many semiconductor electronic devices [5]. Particularly, electric field conductivity modulation of a field effect transistor channel is the heart of modern day high-speed semiconductor electronics. In these classes of devices, the electric field varies the charge concentration in the semiconducting channel and, subsequently, controls the amount of electrical current passing through it. On the contrary, for metals, the electric field induced $\Delta\sigma$ is extremely low. This is due to the presence of a high density ($n_e \sim 10^{23}$ cm^{-3}) of conduction electron screening. A small DC conductivity modulation of $\Delta\sigma \approx 0.1\%$ from a 10 nm thick Au film at an electric field of 10^6 V/cm, was first reported by Bonfiglioli et al. [107–109]. Subsequent experiments by Stadler showed a slightly higher $\Delta\sigma \approx 2\%$ at 3×10^8 V/cm [110]. In these pioneering experiments, the electrical conductivity, σ, was shown to vary linearly with the electric field-induced surface charge.

When a metal is exposed to an electric field, conduction electrons are displaced within a femtosecond timescale to counteract the presence of the perturbing electric field

inside the conductor, thus leaving behind immobile positively charged ions (holes). The spatial extent (i.e. skin depth), ζ, over which this field is screened depends on the frequency of the applied electric field. For a DC electric field, due to the abrupt surface discontinuity of the normal component of the displacement field and the high density of conduction electrons, an infinitesimal conductivity change occurs within the first few atomic layers. As such, the phenomenon could only be observed at a high field $E = 10^6$-10^8 V/cm, and for a metal thickness of $d \leq \Lambda$, where Λ is the electron's mean free path. At these extreme conditions, ballistic electron transport and scattering from *d*-level states dominate the electron transport [111]. Furthermore, size effects, ascribed to grain boundary scattering, produce noticeable deviations from the conduction bulk behavior [112–114]. However, for time-varying electric fields, the scenario is less restrictive. Here, the field screening length scale, $\zeta(\omega)$ (i.e. skin depth), ranges from 10-100 nm. As charges accumulate within $\zeta(\omega)$, the induced surface charge density, ρ_s, modifies the electronic density of states. Accordingly, the non-equilibrium surface charge accumulation maps itself as a local change in the metal's surface conductivity, $\sigma_s(\omega)$.

Owing to the large density of background electrons, the high magnitude of the electric field required, and the distortion of the metallic band structure due to charge transfer between the metal film and the supporting substrate, it remains a challenge to isolate the electric field-induced conduction from other dominate contributing backgrounds. Nonetheless, these can be overcome by exploiting THz plasmonic field interaction, which has provided a stimulating domain for studying conduction electron interaction in metals such as photonic magnetoresistance [115], spinplasmonic electron transport [116], metal-metal contact resistance [117], and Schottky barrier conduction

[118]. THz conductivity modulation has also been observed in optically pumped Au-Si metamaterials [119].

This chapter discusses the experimental observation of THz field-induced conductivity modulation in a metallic gold plasmonic medium using phase-controlled THz-pump/THz-probe time-resolved transmission spectroscopy. By virtue of the metal's high THz frequency permittivity, ε_m, and plasmonic near-field enhancement, ultrafast intensified THz radiation transmission modulation is observed at a low THz field of 12 V/cm. The enhanced THz radiation energy transport is attributed to the presence of induced surface charges and the large surface-to-volume near-field interaction region provided by the localized THz plasmonic field. Evidence of the coherence of the phenomenon is revealed via in-phase and out-of-phase THz-pump/THz-probe time-resolved spectroscopy. These findings offer a new platform for studying charge dynamics in metallic surfaces and open the door to technological applications and fundamental studies of new photonic materials based on ultrafast all-THz plasmonic field modulation of metallic structures.

6.2. Interaction of Terahertz and Metallic Particles

The key aspects in observing such a weak phenomenon are: (*i*) modifying the electronic density of states in ζ by having a high surface-to-volume ratio to affect $\sigma_s(\omega)$, and (*ii*) ensuring that the applied field is below the breakdown strength or field emission threshold. To satisfy these criteria, a THz plasmonic near-field coupling to a sub-wavelength size metallic surface is employed. By taking advantage of the large $\zeta \approx 90$ nm [120], and field enhancement, an augmented $\Delta\sigma_s(\omega)$ signature can be realized.

The interaction of metals with electromagnetic radiation is dictated by the free conduction electrons at the surface of the metal. Consider a single spherical metallic particle of radius $R_{particle}$ ($R_{particle} << \lambda_{THz}$) placed in free space of permittivity ε_0. Within the framework of the quasi-static approximation, a time-varying THz field, $\vec{E}(\vec{r},t) = \mathrm{Re}\{\vec{E}_0(\vec{r},\omega)e^{-i\omega t}\}$ polarizes the particle to induce a time-varying Hertzian dipole moment [121]:

$$\vec{p}(\vec{r},t) = 4\pi\varepsilon_0 R_{particle}{}^3 \left(\frac{\varepsilon_m - 1}{\varepsilon_m + 2}\right)\vec{E}(\vec{r},t) \tag{6.1}$$

Accordingly, the conduction electron current density, $\vec{J}(\vec{r},t) = \mathrm{Re}\{\vec{J}_0(\vec{r},\omega)e^{-i\omega t}\}$, in ζ(ω) is governed by,

$$\frac{d\vec{J}(\vec{r},t)}{dt} + \tau_e^{-1}\vec{J}(\vec{r},t) = \left(\frac{n_e q^2}{m_e^*}\right)\vec{E}(\vec{r},t) \tag{6.2}$$

and one customarily writes the current density as: $\vec{J}_0(\vec{r},\omega) = \tilde{\sigma}(\omega)\vec{E}_0(\vec{r},\omega)$.

Where

$$\tilde{\sigma}(\omega) = \left(\frac{n_e q^2}{m_e^*}\right)\frac{\tau_e}{1 - i\omega\tau_e} \tag{6.3}$$

is the complex conductivity, and τ_e is electron relaxation time. Within the region ζ(ω) of the polarized metallic particle, the induced current density is dependent on $\tilde{\sigma}(\omega)$ and hence, the radiated *plasmonic* depolarization electric field, $\vec{E}_{pl}(\vec{r},t)$, from the oscillating dipole moment, $\vec{p}(\vec{r},t)$ is given by,

$$\vec{E}_{pl}(\vec{r},t)=\frac{1}{4\pi\varepsilon_0}\left\{\frac{\vec{p}(\vec{r},t)}{r^3}+\left(\frac{1}{r^2c}\right)\frac{d\vec{p}(\vec{r},t)}{dt}+\left(\frac{1}{rc^2}\right)\frac{d^2\vec{p}(\vec{r},t)}{dt^2}\right\} \tag{6.4}$$

The terms $\left(\propto\frac{1}{\mathrm{r}^3}\right)$, $\left(\propto\frac{1}{\mathrm{r}^2}\right)$, and $\left(\propto\frac{1}{\mathrm{r}}\right)$ in equation (6.4) represent the near, the intermediate, and the far-fields, respectively. Clearly, since $\vec{J}\left(\vec{r},t\right)\propto\frac{d\vec{p}(\vec{r},t)}{dt}$, the radiated far-field THz field strongly depends on $\tilde{\sigma}(\omega)$.

When the metallic surface is subjected to an additional weaker THz electric field, $\vec{E}^a(\vec{r},t)=\mathrm{Re}\{\vec{E}^a(\vec{r},\omega)e^{-i\omega t}\}$, the effective conductivity, $\tilde{\sigma}_{eff}\left(\omega\right)$, becomes the sum of $\tilde{\sigma}(\omega)$ and the additional conductivity due to the induced surface charge density, ρ_s, by the perturbing electric field, $\vec{E}^a(\vec{r},t)$. This effect is further enhanced in an ensemble of sub-λ size metallic particles where the surface electric field enhancement increases from 3× for a single particle to 85× for the ensemble. This enhancement is due to particle plasmons in micro- and nano-cavities that exist between the particles. A detailed analysis of the surface electric field enhancement can be found in Appendix F.

6.3. Terahertz Pump-Probe Measurements

To measure the change in conductivity due to induced charges, a sample consisting of three layers of randomly distributed and closely-packed 99.99% pure Au microparticles having a mean diameter of ~100 μm is placed on top of a thin THz-transparent polystyrene substrate. The choice of such plasmonic configuration combined with THz probe radiation has been shown to be sensitive to small changes in conductivity [115–118].

A THz pump-THz probe time-domain spectroscopy system was employed to measure the transmission through the ensemble of Au particles. Figure 6.1 shows a schematic depiction of the experimental setup. It consists of two independently addressable photoconductive (PC) THz emitters, Fig. 6.1(b). The PC THz emitters consist of 2 mm long, 10 μm wide Cr/Au (20 nm/100 nm) coplanar transmission lines with a 70 μm gap fabricated on a 500 μm thick GaAs substrate. Each THz emitter is independently biased with a 20 $V_{pk\text{-}pk}$ square wave at frequency f_1 (pump) and f_2 (probe). The THz emitters are excited by 10 fs, λ = 800 nm laser pulses from a Ti:Sapphire laser oscillator at a repetition rate of 80 MHz. The THz time domain signal is acquired via electro-optic sampling in a 500 μm thick <111> ZnSe electro-optic crystal by collecting the THz radiation and co-linearly focusing it with an optical probe pulse (λ = 800 nm) on the ZnSe crystal. A balanced photodetection setup consisting of a quarter-wave plate, Wollaston prism and a balanced photodetector (New Focus Nirvana Detector Model 2007) extracts the THz induced polarization modulation of the optical probe pulse, and lock-in detection is carried out at the bias voltage modulation frequency of the THz probe pulse (f_2) with a lock-in amplifier. This system has been extensively characterized to verify that there are no non-linear effects or harmonics that would result in incorrect measurements [122]. Operating the system at the worst case scenario of $f_1 = 2 \times f_2$, this setup is able to achieve a signal to noise ratio of greater than 10^4:1. Further details of the experimental setup can be found in [122].

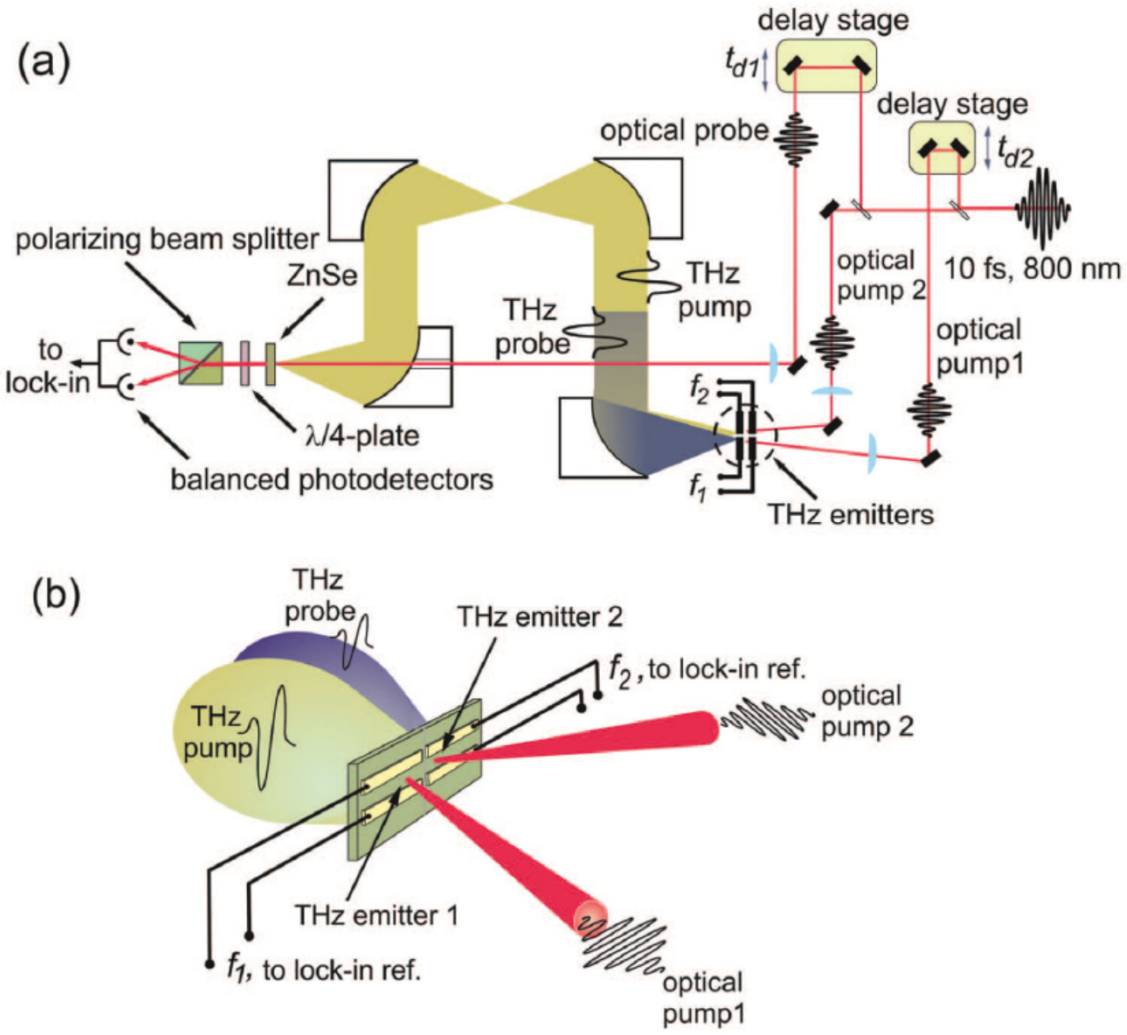

Figure 6.1. (a) Schematic of the THz pump-THz probe time-domain spectroscopy system. (b) Schematic of the two THz emitters. [122]

The Au sample is placed at the 0.8 mm diameter focal spot of the THz-PP setup and is excited by a THz pump pulse with an electric field ($\vec{E}(t)$) magnitude of 12 V/cm (see discussion in Appendix F for the calculation of the THz electric field strength) and pulse duration of 1 ps. To ensure no coupling between $\vec{E}(t)$ and the probe electric field pulse, ($\vec{E}^a(t)$), throughout the experiment, the ratio $|\boldsymbol{E}|/|\boldsymbol{E}^a|$ is set at 10:1. The THz field-induced charge effect on particle plasmon formation is recorded as a function of the THz

pump-probe pulses relative delay time, Δt, by lock-in detection of the time-dependent THz transmission of the radiated THz plasmonic field, $\vec{E}^{a}_{pl}(t)$, resulting from the coupling of the probe $\vec{E}^{a}(t)$ pulse to the ensemble. The transport of THz electromagnetic energy through this ensemble of particles is governed by nearest-neighbour plasmonic field coupling and has been studied extensively through THz radiation transmission in a variety of different media [115–118,120–128]. It should be noted that the THz pump and THz probe pulses are modulated at different frequencies, allowing for lock-in detection of only the radiated THz $\vec{E}^{a}_{pl}(t)$ probe pulse electric field. Since the degree of THz $\vec{E}^{a}(t)$ probe pulse electric field signal acquired at the modulation frequency of the THz probe pulse is directly proportional to $\tilde{\sigma}_{eff}(\omega)$ of the Au sample, any change in transmission due to THz pump pulse $\vec{E}(t)$ can only be attributed to the induced ρ_s by the THz pump pulse electric field.

Figure 6.2(a) depicts the time-domain electric field of the THz probe pulse transmitted through the Au particles at various time delays (Δt=0, 1, 2, 3, 5 and 7 ps) along with the case when there is no THz $\vec{E}(t)$ pump pulse.

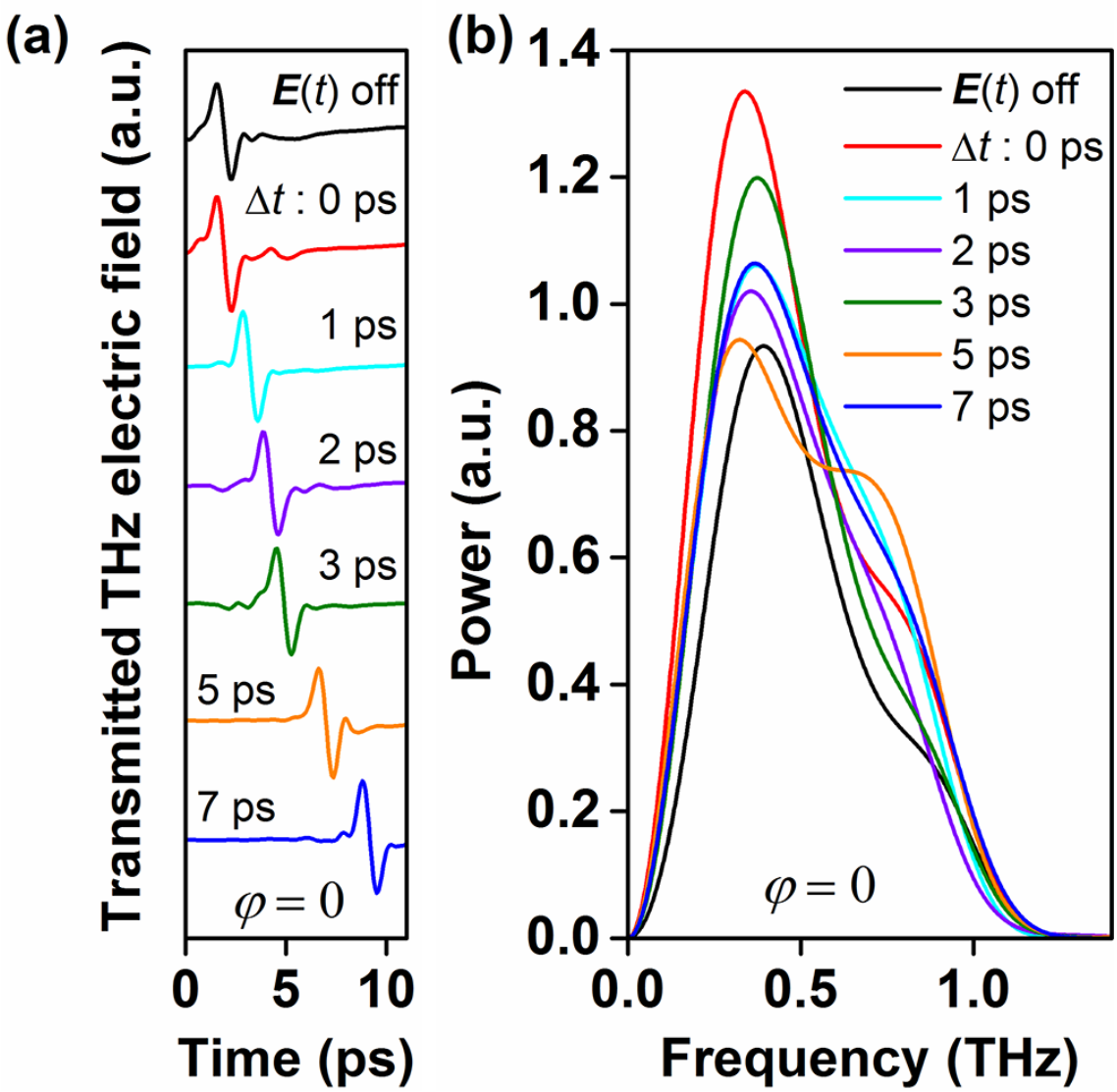

Figure 6.2. (a) In-phase (φ=0) time-domain reradiated THz probe electric field signals transmitted through the plasmonic sample at various delay times (Δt). (b) The corresponding spectral power plots at various delay times (Δt).

Here, the probe electric field, $\vec{E}^{a}(t)$ is set to be in-phase (φ=0) with $\vec{E}(t)$. Interestingly, examining the transmitted THz $\vec{E}^{a}_{pl}(t)_{\varphi=0}$ waveforms, for all delays, reveals that their amplitudes are higher than when the THz pump pulse is turned off. The $\vec{E}^{a}_{pl}(t)_{\varphi=0}$ transmission enhancement is better illustrated by comparing the change in the

pulse's spectral power density for each time-resolved signal. As shown in Fig. 6.2(b), the transmitted THz probe pulse power is lowest when there is no THz pump pulse and the shape of its spectral content is modified in the presence of $\vec{E}(t)$. The transmitted THz probe pulse power is the highest at $\Delta t = 0$, when the THz probe pulse interacts with the sample at the same time as the THz pump pulse. The spectral reshaping is an indication that the presence of charges induced by the THz pump pulse and their time dynamics act to distort the phase of the probe THz pulse. Minor spectral reshaping will also be present based on the size and structure of the Au particles themselves.

While changing the relative Δt between the pump and probe THz pulses and detecting $\vec{E}^{a}_{pl}(t)_{\varphi=0}$ effectively samples the surface charge effects as a function of time, such time-sampling process does not permit probing $\tilde{\sigma}_{eff}$ at various phases of the time-domain THz $\vec{E}(t)$ field cycles since the two THz fields have the same duration and the electrons are induced almost instantaneously within a few femtoseconds by the THz $\vec{E}(t)$ field. Nonetheless, the phase-dependency of the observed phenomenon can be distinguished at $\Delta t = 0$ where $\vec{E}^{a}(t)$ traverses and probes, in a travelling wave fashion, the sample at the same instant and locations where electrons are induced by the THz $\vec{E}(t)$ field. To ascertain this premise, the $\vec{E}^{a}(t)$ probe pulse electric field polarity is reversed such that it is out of phase ($\varphi = \pi$) with respect to $\vec{E}(t)$ pump pulse [122]. As shown in Fig. 6.3(a)-(b), similar to the $\varphi = 0$ situation, the $\vec{E}^{a}_{pl}(t)_{\varphi=\pi}$ waveform amplitudes and spectral powers are higher in the presence of $\vec{E}(t)$ pump pulse; though, the degree of enhancement is less than that for $\vec{E}^{a}(t)_{\varphi=0}$. This suggests that even though, in both

situations, the same amount ρ_s is induced by $\vec{E}(t)$ (amounting to the same $\tilde{\sigma}_{eff}(\omega)$), the coupling of $\vec{E}^a(t)$ to the ensemble and the formation of the particle plasmon currents is sensitive to the phase dynamics of the induced ρ_s.

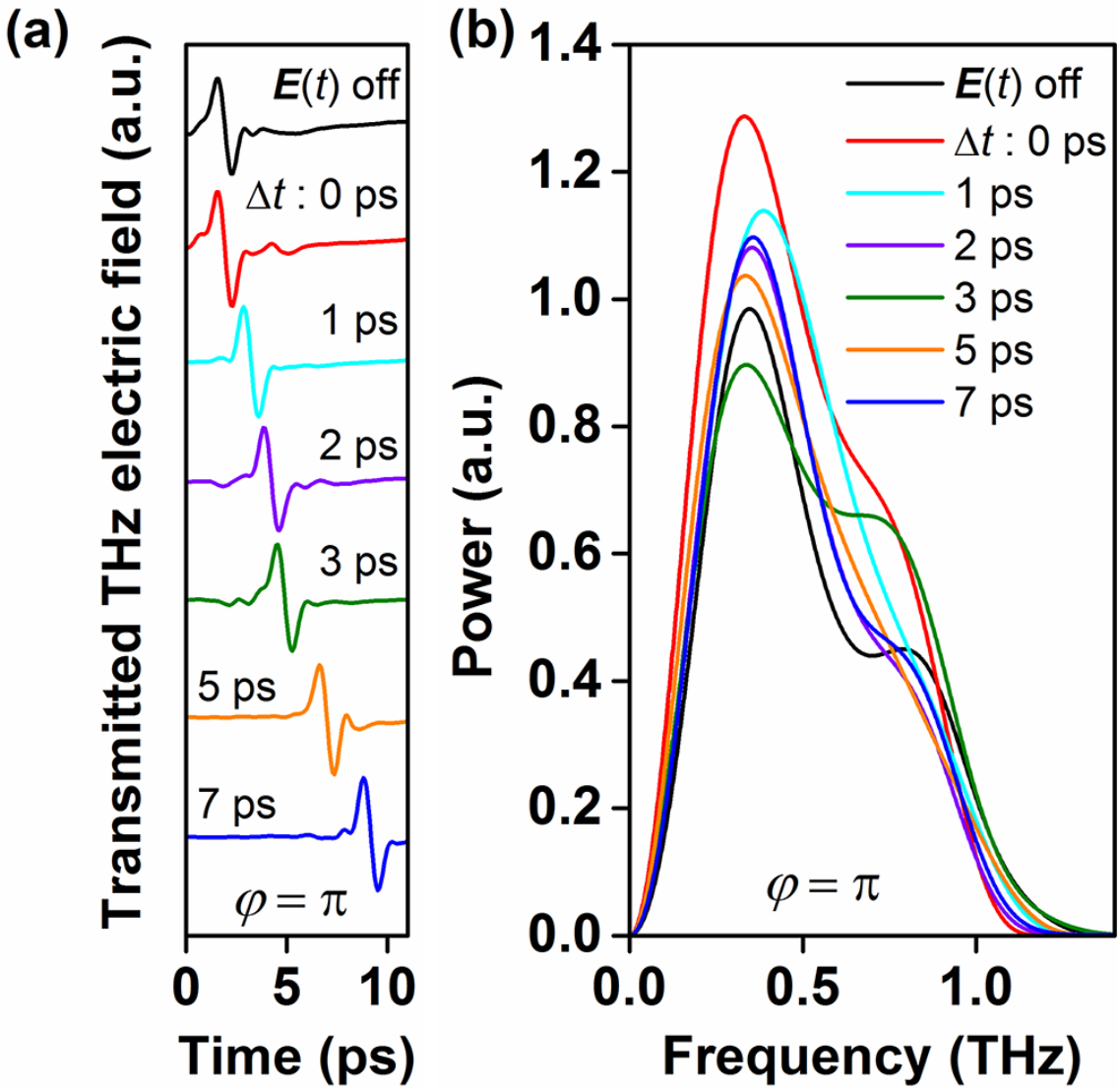

Figure 6.3. (a) Out-of-phase ($\varphi = \pi$) time-domain reradiated THz probe electric field signals transmitted through the plasmonic sample at various delay times (Δt). (b) The corresponding spectral power plots at various delay times (Δt).

To estimate the change in the conductivity, one can invoke the quasi-static approximation for a polarized metallic sphere. At the surface boundary between metal

and free space ($r = R_{particle}$), ρ_s can be evaluated at any point on the surface by the discontinuity of the normal components of the electric flux densities to obtain:

$$\varepsilon_0 \left(\tilde{\varepsilon}_m \vec{E}_{in}(R_{particle}, \omega) - 3\vec{E}(R_{particle}, \omega) \right) \cos\theta = \rho_s \tag{6.5}$$

where $\vec{E}_{in}(R_{particle}, \omega)$ is the THz electric field inside the metal surface and θ is the angle between the fields and normal unit vector. The relative magnitude $\vec{E}_{in}(R_{particle}, \omega) / \vec{E}(R_{particle}, \omega)$ is calculated to be ~0.95 within 5 nm from the surface [120]. For $\vec{E}(R_{particle}, \omega)$ = 12 V/cm, with a plasmonic field enhancement of ≈ 85 at $R_{particle}$, and $\varepsilon_m \approx -1.12\times10^5 + i\ 7.22\times10^5$ [129], ρ_s is estimated to be 1×10^{-5} C/cm^2. Notably, this value is comparable to Stadler's estimation of 4.8×10^{-5} C/cm^2 [110]. Therefore, at this THz electric field magnitude, $\Delta\sigma_s(\omega)$ is estimated to be 1%.

To further quantify the THz field induced effect on the THz probe pulse, Fig. 6.4(a) depicts the percent change of the integrated spectral power at each Δt, $S(\Delta t) = \int \left(\left| \tilde{E}^a_{pl}(\omega) \right|^2 d\omega \right)_{\Delta t} \Big/ \int \left(\left| \tilde{E}^a_{pl}(\omega) \right|^2 d\omega \right)_{THz \text{ pump off}}$, normalized to the integrated spectral power in the absence of the THz pump pulse. Remarkably, for φ=0, at Δt = 0, S is measured to be 46% higher than when the THz pump $\vec{E}(t)$ pulse is absent. The transmission enhancement is reduced at Δt =2 ps to a minimum of 20% and increases again, for $\Delta t \geq$ 3ps, to reach a constant steady state value of 27%. While S at φ=0 and φ =π exhibits a similar trend for all Δt, there is a notable offset of ~15% between the two

curves. For $\varphi=\pi$, at $\Delta t=0$, S is greatly reduced to 34%, where at Δt = 2 ps, it exhibits a minimum of 5% and for $\Delta t \geq 3$ ps, a steady state value of 10% is reached.

In the absence of the $\vec{E}(t)$ pump pulse, the free surface electrons within the $\zeta(\omega)$ layer carry the plasmonic conduction currents from the probe $\vec{E}^a(t)$ pulse. Here, $\tilde{\sigma}(\omega)$ is constant and is determined by the background electron density n_e in the metal; making the near-field coupling efficiency between $\vec{E}^a(t)$ and the radiated THz plasmonic field, $\vec{E}^a_{pl}(t)$, conductivity-dependent. However, in the presence of the pump $\vec{E}(t)$ electric field, additional electrons are drawn into the $\zeta(\omega)$ region at the surface to screen $\vec{E}(t)$. Within a few femtoseconds, the electrons distribute themselves over the metallic surface in accordance with the local $\vec{E}(t)$ magnitude. This distribution is spatially nonuniform, being higher at the gaps between adjacent particles and at localized spots at surface crevices.

When the probe $\vec{E}^a(t)_{\varphi=0}$ field is in-phase with the $\vec{E}(t)$ field, its induced electrons are displaced also in-phase with the electrons induced and driven by the pump $\vec{E}(t)$ electric field. Collectively, the presence of additional coherently-driven electrons in the $\zeta(\omega)$ layer makes a notable increase to $\tilde{\sigma}_{eff}(\omega)$ (or accordingly the surface plasmon currents) and thus the radiated THz $\vec{E}^a_{pl}(t)$ field. In particular, at a delay of Δt = 0 ps, where the two THz fields are phase-synchronized and propagate in a travelling wave manner, the instantaneous-modulation of the local $\tilde{\sigma}_{eff}(\omega)$ is *sampled* locally by the $\vec{E}^a(t)_{\varphi=0}$ probe field pulse as enhanced surface conductance. This is evidenced as the

maximum contribution to the $\vec{E}^{a}_{pl}(t)$ field occurs at this time where the induced background conductivity is coherently oscillating with the probing $\vec{E}^{a}(t)_{\varphi=0}$. However, when $\vec{E}^{a}(t)_{\varphi=\pi}$ is out of-phase with $\vec{E}(t)$, whilst the same number of electrons are induced by both THz fields as in the THz pump-probe arrangement, the induced electrons due to $\vec{E}^{a}(t)_{\varphi=\pi}$ are displaced out of-phase with those induced by the $\vec{E}(t)$ field. Effectively, the local conductivity in ζ(ω) is still enhanced by the additional electrons; however, since these are oscillating out of-phase, they introduce more damping on the oscillating plasmonic currents. As such the radiated $\vec{E}^{a}_{pl}(t)$ far-field is expected to be lower than the $\varphi = 0$ case.

Through this picture of the physical processes involved, the transmission enhancement of the probe pulse with the presence of the THz pump pulse can be described for all delays. At $0 < \Delta t < 1.7$ ps and for both cases when $\varphi = 0$ and $\varphi = \pi$, the $\vec{E}^{a}(t)$ probes $\tilde{\sigma}_{eff}(\omega)$ at various phases. This is evident by the observed similarity between $S(\Delta t)_{\varphi=0}$ and $S(\Delta t)_{\varphi=\pi}$. For $\varphi = 0$ and at $\Delta t = 0.7$ ps, the probe $\vec{E}^{a}(t)_{\varphi=0}$ positive field half cycle overlaps with the negative field half cycle of the pump $\vec{E}(t)$ creating a situation equivalent to the $\varphi = \pi$ pump-probe configuration at $\Delta t = 0$ where the sample interacts with a unipolar field that dampens the oscillating plasmonic currents. As evidenced from Fig. 6.4(a), $S(\Delta t = 0.7 \text{ ps})_{\varphi=0} \approx S(\Delta t = 0 \text{ ps})_{\varphi=\pi}$. Since the propagation speed of the $\vec{E}(t)$ pump electric field pulse inside the sample is ≈0.62c [123,124] and the effective sample thickness is ≈ 300 μm (~λ_{THz}), the main $\vec{E}(t)$ pulse traverses the entire

sample and exits within ~1.7 ps. Thus, for delay times > 1.7 ps, the probe $\vec{E}^{a}(t)$ pulse sojourns and samples charge distribution due to circulating plasmonic surface currents and reflections from the end face. These plasmonic surface currents persist for ~ 20 ps, during which the induced charges spread through the entire sample, as such the $S(\Delta t > 7\text{ ps})_{\varphi=0,\pi}$ exhibits a steady state value.

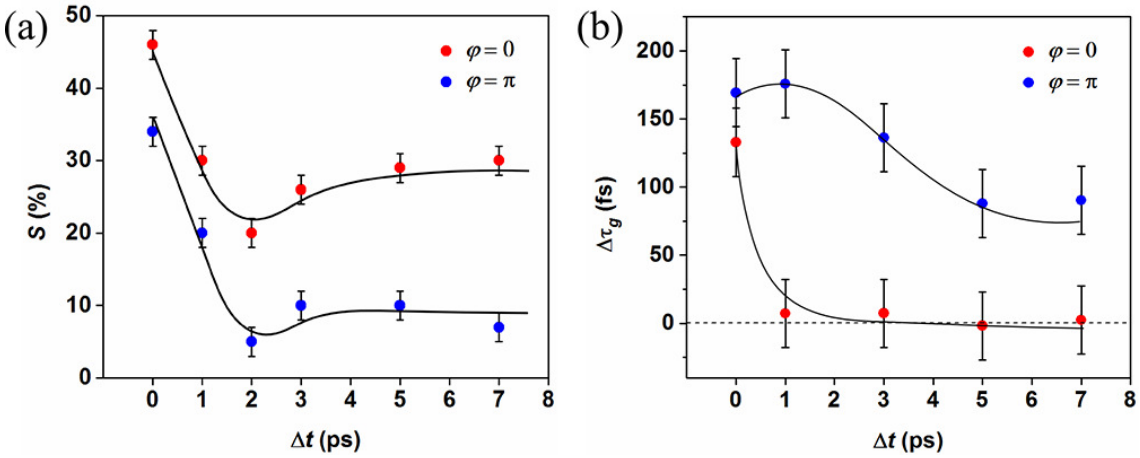

Figure 6.4. (a) Normalized integrated spectral power as a function of various delay times (Δt) for in-phase and out-of-phase THz probe electric field pulse. (b) Frequency-average group delay difference as a function of various delay times (Δ*t*) for in-phase and out-of-phase THz probe electric field pulse. Note that the black lines are inserted to guide the eye.

Examining the time-domain $\vec{E}^{a}_{pl}(t)$ pulse reveals a noticeable pulse reshaping of the electric field signal in the presence of $\vec{E}(t)$. Any change associated with the imaginary part of the impedance of the system is contained in the phase of the transmitted THz pulse. The ascribed relative phase distortion, $\Delta\Omega(\omega)$ (relative to $\vec{E}(t)$ being off), represents the time-dependent ρ_s induced dispersion in the plasmonic ensemble. An accurate parameter influenced by $\Delta\Omega(\omega)$, is the frequency-average group delay

difference, $\left\langle \Delta\tau_g \right\rangle = -\left(\left\langle \frac{\partial \Delta\Omega(\omega)}{\partial \omega} \right\rangle \right)$, which quantifies the average retardation time for $\vec{E}^a_{pl}(t)$ emission from the whole polarized ensemble. The exact shape of the $\left\langle \Delta\tau_g \right\rangle$ curve depends on the polarity and where the charges are induced in the ensemble. As depicted in Fig. 6.4(b), for $\left\langle \Delta\tau_g \right\rangle$ at $\varphi = 0$, the only significant $\left\langle \Delta\tau_g \right\rangle$ (= 140 fs), occurs at $\Delta t = 0$, reaffirming that the induced background ρ_s spatial distribution in the sample readjusts within ~140 fs in response to the $\vec{E}^a_{pl}(t)$ oscillations. At this time delay (i.e. $\Delta t = 0$), a maximum THz field transmission is observed. At delays of $\Delta t > 0$, $\left\langle \Delta\tau_g \right\rangle \approx 0$, indicating that ρ_s in the ensemble relaxes to a steady state which oscillates in unison with $\vec{p}(\vec{r},t)$. However, the situation is strikingly different for $\varphi = \pi$. While it takes a slightly longer time ($\left\langle \Delta\tau_g \right\rangle$ = 170 fs) for the induced background ρ_s to redistribute in response to the $\vec{E}^a_{pl}(t)$ oscillations at $\Delta t = 0$ and for $\Delta t > 0$, the emission is delayed by several picoseconds. As ρ_s oscillates in opposite phase with respect to $\vec{E}^a_{pl}(t)$, and at $\Delta t > 0$, the THz probe field experiences regions where the conductivity varies both in time and space along the path traversed. Each conductivity region can be oscillating in-phase or out of phase with the probe field. As such, the redistribution of ρ_s can only reach a steady state when the entire ensemble oscillates collectively in unison where all the $\vec{p}(\vec{r},t)$ are coherently-coupled. However, the time to reach this state corresponds to the sojourn time of $\vec{E}^a_{pl}(t)$ which is several picoseconds. This leads to a lower emission efficiency, as observed in $S(\Delta t)_{\varphi=\pi}$, in Fig. 6.4(a).

6.4. Summary

The results of this chapter reveal a new THz electric field-dependent modulation of the conductivity of Au. This modulation opens a pathway for control of the photoemission process operating in the near infrared regime, much like the work presented in Chapter 4. As the THz electric fields will be synchronized with the SP photoemission, this can be utilized for all-optical THz electric field enhanced electron pulse generation.

Chapter 7

Conclusion

The work presented in this thesis demonstrates important steps towards the creation of compact, ultrafast, SP based electron sources that can generate and tailor electron pulses for specific time-resolved applications. Specifically, it explores ways to improve SP coupling, enhance photoemission, and provide means to control ultrafast electrons.

Preliminary studies of SP generated electron pulse interaction with ultrafast THz fields revealed that both the kinetic energy and the angular directivity of the electron pulse can be controlled. And by carefully selecting the time delay between two THz pulses, kinetic energies up to 3.5 keV can be achieved. These electron pulses were found to be sensitive to the carrier-envelope-phase of the driving laser, making this a unique platform to study electron pulse generation with few-cycle laser pulses. The kinetic energy of the electron pulses was still broad though, indicating long pulse durations. To overcome this broad kinetic energy spectrum, investigations combining multiple filtering techniques, such as spatial and magnetic filtering, were conducted. It was determined that these two filtering methods, combined with a conical SP field can generate attosecond electron pulses with kinetic energies of ~0.5 keV in an extremely compact footprint.

Experiments in the second half of this thesis focused on techniques to generate a higher number of electrons at a given laser intensity. First studies of a dielectric layer,

eCarbon, beneath the plasmonic Au film indicated that the nonlinear emission order can be controlled such that a fewer number of photons are required to free a single electron from the bilayer film. The next step was to use the SP field to control externally injected free electrons such that the current of the ultrafast electron source could be greatly increased. For this it was important to understand the interaction of the externally injected electrons and the SP field. It was determined that at modest laser intensities of 25 GW/cm^2, secondary electrons ejected from the plasmonic film could be affected. The number of these secondary electrons that are ejected can be significantly increased by single photon absorption of the incident laser, thus producing a high current ultrafast electron source. Furthermore, it was found that these secondary electrons are preferentially scattered forward by the primary electron beam and then subsequently beamed to ~30° from the surface. These results represent a stepping stone to ultrafast, high current, tuneable, SP based electron sources.

Harnessing the understanding of the laser-electron interaction in vacuum, two devices were explored that exploit this interaction in a solid-state Si-based platform. The first device is a nanoplasmonic triode that represents the optically excited, solid-state analogue to the vacuum tubes of the early 20^{th} century. The nanoplasmonic triode is envisioned to merge current nanoelectronics with ultrafast nanoplasmonics in a monolithic nanoscale chip. Exploiting the fact that ponderomotive acceleration is sensitive to CEP effects, a solid-state device was designed that would allow for the measurement of the CEP in a compact, solid-state manner. This represents a significant step forward for the miniaturization of CEP detectors.

With the understanding that altering the free electrons within a film can greatly affect the properties of a plasmonic system, modulation of the conductivity of an ensemble of Au particles using THz electric fields was demonstrated. This all-optical modulation of the conduction electron density in Au is the first step towards controlling the SP coupling and photoemission properties in the near-infrared, such that THz electric field enhanced photoemission can be realized. Furthermore, as an additional benefit, this field-driven conductivity modulation provides an all-optical platform the next generation of computing devices operating at THz frequencies.

7.1. Outlook and Future Directions

The work presented in this thesis introduces numerous methods to control and tailor ultrafast electron pulses for time-resolved electron microscopy, and it lays the groundwork for the next generation of research endeavours. This section details future research directions for ultrafast electron acceleration and strong-field devices.

7.1.1. Surface Plasmon Gating of Continuous Electron Beams

The work presented in Chapter 4 on the beaming of secondary electrons is merely the beginning to a broader range of experiments for controlling continuous electron beams. While the work explores the interaction of free electrons and plasmonic fields, the ultimate goal has not yet been achieved. By utilizing a lower energy electron beam (<10 eV), it will be possible to fully deflect the incident beam on the timescale of the SP, thus generating electron pulses on the order of 10's of fs. Further, by introducing a high-pass energy filter, only those electrons that are accelerated by the SP field will contribute to the final electron pulse, resulting in even shorter duration electron pulses. A similar concept can also be applied on the nanoscale to route electron pulses based on the

incident laser intensity. This represents a possible solution for addressing/seeding multiple nanoscale particle accelerators or experiments.

7.1.2. Seeding of Nanoscale Particle Accelerators

Due to the compact nature of the nanoplasmonic attosecond electron gun developed in Chapter 3, it represents a perfect source for seeding nanoscale particle accelerators. By having the particle accelerator directly after the spatial aperture, the attosecond electron pulses can be accelerated to high kinetic energies while maintaining their low kinetic energy spread. The combination of these two elements would allow for time resolved electron experiments to be carried out in an extremely compact volume with high spatial and temporal resolution.

7.1.3. Pulse Shaping of Terahertz Fields for Optimal Electron Acceleration

The THz pulses considered in Chapter 3 are typical single-cycle pulses that one would achieve with a standard photoconductive antenna. While these pulses work for electron acceleration and angular control, it would be possible to better tailor the THz pulses such that the temporal acceleration profile for the electrons can be better controlled. This is briefly touched on in Chapter 3, when two THz pulses are used to effectively generate a unipolar THz pulse that provides constant acceleration and thus higher kinetic energy gain. The control of the THz pulses can be achieved by altering the properties of the femtosecond laser filament used in THz generation from an air plasma [130,131].

7.1.4. Outlook on Strong Field Devices

The solid-state devices of Chapter 5 illustrate the next step for nanoscale strong field devices. The understanding of acceleration and control of electrons in vacuum, such as those ideas explored in this thesis, can and should be transferred to integrated devices. Nanoscale devices harnessing strong-field laser-electron interactions in semiconductors show promise for the next generation of optical computing devices [73]. Semiconductor ponderomotive electron acceleration allows for increased switching speeds by moving free carriers via light instead of a conventional, externally applied, electrical bias. This, in turn, opens up a new platform that revisits the operating principles of the original vacuum tubes, except operating at significantly increased speeds (terahertz), owing to the electrons being driven by surface plasmon fields.

7.1.5. Outlook on Ultrafast Surface Plasmon Based Electron Pulse Generation

Although the majority of ultrafast electron microscopes are currently operating with direct laser-driven electron sources, their fastest achievable time resolution is on the order of 100's of fs. SP based sources have been demonstrated to achieve sub-10 fs [3] and even speculated to reach sub-fs resolutions using energy filtering [2,39]. Clearly, the next generation of ultrafast electron sources will be SP based. Not only do they provide higher time resolution, but they can also be implemented in a more compact manner without the need for a standard TEM/SEM imaging column. By combining current SP nanotip based electron sources with the understanding gained from the secondary electron beaming presented in this thesis, compact, high brightness electron sources with sub-10 fs temporal resolution can be achieved. This would enable ultrafast single-shot

electron microscopy with atomic resolution laying the groundwork for the next generation of UEM and the greater understanding of fundamental physical processes.

References

[1] M. von Ardenne, "Das elektronen-rastermikroskop," *Zeitschrift Für Phys.* **109**, 553 (1938).

[2] P. Baum and A.H. Zewail, "Attosecond electron pulses for 4d diffraction and microscopy," *Proc. Natl. Acad. Sci. U. S. A.* **104**, 18409 (2007).

[3] M. Müller, V. Kravtsov, A. Paarmann, M.B. Raschke, and R. Ernstorfer, "Nanofocused plasmon-driven sub-10 fs electron point source," *ACS Photonics* **3**, 611 (2016).

[4] J. Vogelsang et al., "Ultrafast electron emission from a sharp metal nanotaper driven by adiabatic nanofocusing of surface plasmons," *Nano Lett.* **15**, 4685 (2015).

[5] Sze, *Physics of semiconductor devices*, 2nd ed. (Wiley, New York, 1981).

[6] S.E. Irvine and A.Y. Elezzabi, "Ponderomotive electron acceleration using surface plasmon waves excited with femtosecond laser pulses," *Appl. Phys. Lett.* **86**, 264102 (2005).

[7] B.J. Siwick, J.R. Dwyer, R.E. Jordan, and R.J.D. Miller, "An atomic-level view of melting using femtosecond electron diffraction," *Science* **302**, (2003).

[8] B.J. Siwick, J.R. Dwyer, R.E. Jordan, and R.J.D. Miller, "Femtosecond electron diffraction studies of strongly driven structural phase transitions," *Chem. Phys.* **299**, 285 (2004).

[9] V.A. Lobastov, R. Srinivasan, and A.H. Zewail, "Four-dimensional ultrafast electron microscopy.," *Proc. Natl. Acad. Sci. U. S. A.* **102**, 7069 (2005).

[10] T. Tajima and J.M. Dawson, "Laser electron accelerator," *Phys. Rev. Lett.* **43**, 267 (1979).

[11] M.Z. Mo et al., "Generation of 500 mev–1 gev energy electrons from laser wakefield acceleration via ionization induced injection using co2 mixed in he," *Appl. Phys. Lett.* **102**, 134102 (2013).

[12] O. Lundh et al., "Few femtosecond, few kiloampere electron bunch produced by a laser–plasma accelerator," *Nat. Phys.* **7**, 219 (2011).

[13] S. Payeur et al., "Generation of a beam of fast electrons by tightly focusing a radially polarized ultrashort laser pulse," *Appl. Phys. Lett.* **101**, 041105 (2012).

[14] C. Varin and M. Piché, "Relativistic attosecond electron pulses from a free-space laser-acceleration scheme," *Phys. Rev. E* **74**, 045602 (2006).

[15] C. Varin et al., "Direct electron acceleration with radially polarized laser beams," *Appl. Sci.* **3**, 70 (2013).

[16] V. Marceau, C. Varin, T. Brabec, and M. Piché, "Femtosecond 240-kev electron pulses from direct laser acceleration in a low-density gas," *Phys. Rev. Lett.* **111**, 224801 (2013).

[17] J. Zawadzka, D. A. Jaroszynski, J. J. Carey, and K. Wynne, "Evanescent-wave acceleration of femtosecond electron bunches," *Nucl. Instruments Methods Phys. Res. Sect. A Accel. Spectrometers, Detect. Assoc. Equip.* **445**, 324 (2000).

[18] J. Zawadzka, D.A. Jaroszynski, J.J. Carey, and K. Wynne, "Evanescent-wave acceleration of ultrashort electron pulses," *Appl. Phys. Lett.* **79**, 2130 (2001).

[19] S.E. Irvine, A. Dechant, and A.Y. Elezzabi, "Generation of 0.4-kev femtosecond electron pulses using impulsively excited surface plasmons," *Phys. Rev. Lett.* **93**, 184801 (2004).

[20] P. Dombi et al., "Observation of few-cycle, strong-field phenomena in surface plasmon fields," *Opt. Express* **18**, 24206 (2010).

[21] J. Kupersztych, P. Monchicourt, and M. Raynaud, "Ponderomotive acceleration of photoelectrons in surface-plasmon-assisted multiphoton photoelectric emission," *Phys. Rev. Lett.* **86**, 5180 (2001).

[22] J. Kupersztych and M. Raynaud, "Anomalous multiphoton photoelectric effect in ultrashort time scales," *Phys. Rev. Lett.* **95**, 147401 (2005).

[23] P.M. Nagel et al., "Surface plasmon assisted electron acceleration in photoemission from gold nanopillars," *Chem. Phys.* **414**, 106 (2013).

[24] P. Dombi et al., "Ultrafast strong-field photoemission from plasmonic nanoparticles," *Nano Lett.* **13**, 674 (2013).

[25] T. Tsang, T. Srinivasan-Rao, and J. Fischer, "Surface-plasmon field-enhanced multiphoton photoelectric emission from metal films," *Phys. Rev. B* **43**, 8870 (1991).

[26] B. Barwick et al., "Laser-induced ultrafast electron emission from a field emission tip," *New J. Phys.* **9**, 142 (2007).

[27] P. Hommelhoff, Y. Sortais, A. Aghajani-Talesh, and M.A. Kasevich, "Field emission tip as a nanometer source of free electron femtosecond pulses," *Phys. Rev. Lett.* **96**, 077401 (2006).

[28] M. Schenk, M. Krüger, and P. Hommelhoff, "Strong-field above-threshold photoemission from sharp metal tips," *Phys. Rev. Lett.* **105**, 257601 (2010).

[29] S. Li and R.R. Jones, "High-energy electron emission from metallic nano-tips driven by intense single-cycle terahertz pulses," *Nat. Commun.* **7**, 13405 (2016).

[30] J. Breuer and P. Hommelhoff, "Laser-based acceleration of nonrelativistic electrons at a dielectric structure," *Phys. Rev. Lett.* **111**, 134803 (2013).

[31] J. McNeur et al., "A miniaturized electron source based on dielectric laser accelerator operation at higher spatial harmonics and a nanotip photoemitter," *J. Phys. B At. Mol. Opt. Phys.* **49**, 034006 (2016).

[32] B.-L. Qian and H.E. Elsayed-Ali, "Electron pulse broadening due to space charge effects in a photoelectron gun for electron diffraction and streak camera systems," *J. Appl. Phys.* **91**, 462 (2002).

[33] A. Gahlmann, S. Tae Park, and A.H. Zewail, "Ultrashort electron pulses for diffraction, crystallography and microscopy: theoretical and experimental resolutions," *Phys. Chem. Chem. Phys.* **10**, 2894 (2008).

[34] P. Dombi and P. Rácz, "Ultrafast monoenergetic electron source by optical waveform control of surface plasmons," *Opt. Express* **16**, 2887 (2008).

[35] M.T. Hassan, J.S. Baskin, B. Liao, and A.H. Zewail, "High-temporal-resolution

electron microscopy for imaging ultrafast electron dynamics," *Nat. Photonics* **11**, 425 (2017).

[36] T. van Oudheusden et al., "Electron source concept for single-shot sub-100 fs electron diffraction in the 100 kev range," *J. Appl. Phys.* **102**, 093501 (2007).

[37] T. van Oudheusden et al., "Compression of subrelativistic space-charge-dominated electron bunches for single-shot femtosecond electron diffraction," *Phys. Rev. Lett.* **105**, 264801 (2010).

[38] A.Y. Elezzabi and S.E. Irvine, "Femtosecond electron pulse gating using surface plasmons," *Opt. Express* **14**, 4115 (2006).

[39] M. Kozák et al., "Optical gating and streaking of free electrons with sub-optical cycle precision," *Nat. Commun.* **8**, 14342 (2017).

[40] J. McNeur et al., "Elements of a dielectric laser accelerator," *Optica* **5**, 687 (2018).

[41] C. Kealhofer et al., "All-optical control and metrology of electron pulses.," *Science* **352**, 429 (2016).

[42] M. Kozák, N. Schönenberger, and P. Hommelhoff, "Ponderomotive generation and detection of attosecond free-electron pulse trains," *Phys. Rev. Lett.* **120**, 103203 (2018).

[43] P. Drude, "Zur elektronentheorie der metalle," *Ann. Phys.* **306**, 566 (1900).

[44] P. Drude, "Zur elektronentheorie der metalle; ii. teil. galvanomagnetische und thermomagnetische effecte," *Ann. Phys.* **308**, 369 (1900).

[45] J. Lindhard, "On the properties of a gas of charged particles," *Dan. Mat. Fys.*

Medd. **28**, 1 (1954).

[46] J. Lindhard and A. Winther, "Stopping power of electron gas and equipartition rule," *Mat. Fys. Medd. Dan. Vid. Selsk.* **34**, 1 (1964).

[47] N.W. Ashcroft and N.D. Mermin, *Solid state physics* (Holt, Rinehart and Winston, 1976).

[48] J. Daniels, C. v. Festenberg, H. Raether, and K. Zeppenfeld, in *Springer Tracts Mod. Phys.* (Springer, Berlin, Heidelberg, 1970), pp. 77–135.

[49] H. Raether, *Surface plasmons on smooth and rough surfaces and on gratings* (Springer Berlin Heidelberg, 1988).

[50] A.D. Rakić, A.B. Djurišić, J.M. Elazar, and M.L. Majewski, "Optical properties of metallic films for vertical-cavity optoelectronic devices," *Appl. Opt.* **37**, 5271 (1998).

[51] E.D. Palik, *Handbook of optical constants of solids* (Academic Press, 1998).

[52] H.E. Bennett, R.L. Peck, D.K. Burge, and J.M. Bennett, "Formation and growth of tarnish on evaporated silver films," *J. Appl. Phys.* **40**, 3351 (1969).

[53] L.V. Keldysh, "Ionization in the field of a strong electromagnetic wave," *Sov. Phys. JETP* **20**, 1307 (1965).

[54] M.S. Chung and T.E. Everhart, "Simple calculation of energy distribution of low-energy secondary electrons emitted from metals under electron bombardment," *J. Appl. Phys.* **45**, 707 (1974).

[55] H. Seiler, "Secondary electron emission in the scanning electron microscope," *J.*

Appl. Phys. **54**, R1 (1983).

[56] J.J. Scholtz, D. Dijkkamp, and R.W.A. Schmitz, "Secondary electron emission properties," *Philips J. Res* **50**, 375 (1996).

[57] G.F. Dionne, "Effects of secondary electron scattering on secondary emission yield curves," *J. Appl. Phys.* **44**, 5361 (1973).

[58] J.R. Young, "Penetration of electrons and ions in aluminum," *J. Appl. Phys.* **27**, 1 (1956).

[59] R.L. Petry, "Secondary electron emission from tungsten, copper and gold," *Phys. Rev.* **28**, 362 (1926).

[60] Y. Lin and D.C. Joy, "A new examination of secondary electron yield data," *Surf. Interface Anal.* **37**, 895 (2005).

[61] K. Kanaya and H. Kawakatsu, "Secondary electron emission due to primary and backscattered electrons," *J. Phys. D. Appl. Phys.* **5**, 330 (1972).

[62] J.L.H. Jonker, "The angular distribution of the secondary electrons of nickel," *Philips Res. Rep.* **6**, 372 (1951).

[63] Lumerical Inc., (https://www.lumerical.com/).

[64] S.E. Irvine and A.Y. Elezzabi, "Surface-plasmon-based electron acceleration," *Phys. Rev. A* **73**, 013815 (2006).

[65] S.E. Irvine, P. Dombi, G. Farkas, and A.Y. Elezzabi, "Influence of the carrier-envelope phase of few-cycle pulses on ponderomotive surface-plasmon electron acceleration," *Phys. Rev. Lett.* **97**, 146801 (2006).

[66] S.D. Johnson, M.M. El-Gomati, and L. Enloe, "High-resolution retarding field analyzer," *J. Vac. Sci. Technol. B Microelectron. Nanom. Struct.* **21**, 350 (2003).

[67] C.L. Enloe, "High-resolution retarding potential analyzer," *Rev. Sci. Instrum.* **65**, 507 (1994).

[68] D.N. McIlroy, P.A. Dowben, A. Knop, and E. Rühl, "A novel design for a small retractable cylindrical mirror analyzer," *J. Vac. Sci. Technol. B Microelectron. Nanom. Struct.* **13**, 2142 (1995).

[69] C.M. Teodorescu et al., "Retractable miniature double pass cylindrical mirror analyzers," *Rev. Sci. Instrum.* **69**, 3805 (1998).

[70] A. Morteza Najarian, B. Szeto, U.M. Tefashe, and R.L. McCreery, "Robust all-carbon molecular junctions on flexible or semi-transparent substrates using “process-friendly” fabrication," *ACS Nano* **10**, 8918 (2016).

[71] J. Robertson, "Diamond-like amorphous carbon," *Mater. Sci. Eng. R Reports* **37**, 129 (2002).

[72] S. Coulombe and J.-L. Meunier, "Thermo-field emission: a comparative study," *J. Phys. D. Appl. Phys.* **30**, 776 (1997).

[73] S. Sederberg and A.Y. Elezzabi, "Ponderomotive electron acceleration in a silicon-based nanoplasmonic waveguide," *Phys. Rev. Lett.* **113**, 167401 (2014).

[74] R.L. Olmon et al., "Optical dielectric function of gold," *Phys. Rev. B* **86**, 235147 (2012).

[75] J.T. Titantah and D. Lamoen, "Determination of the electron effective band mass

in amorphous carbon from density-functional theory calculations," *Phys. Rev. B* **70**, 033101 (2004).

[76] J.D. Carey, R.D. Forrest, and S.R.P. Silva, "Origin of electric field enhancement in field emission from amorphous carbon thin films," *Appl. Phys. Lett.* **78**, 2339 (2001).

[77] J.D. Carey, R.D. Forrest, R.U.A. Khan, and S.R.P. Silva, "Influence of sp^2 clusters on the field emission properties of amorphous carbon thin films," *Appl. Phys. Lett.* **77**, 2006 (2000).

[78] A. Ilie, A.C. Ferrari, T. Yagi, and J. Robertson, "Effect of sp^2-phase nanostructure on field emission from amorphous carbons," *Appl. Phys. Lett.* **76**, 2627 (2000).

[79] N.S. Xu, Y. Tzeng, and R. V Latham, "Similarities in the “cold” electron emission characteristics of diamond coated molybdenum electrodes and polished bulk graphite surfaces," *J. Phys. D. Appl. Phys.* **26**, 1776 (1993).

[80] H.-S. Hsu, S.-P. Ju, S.-J. Sun, H. Chou, and C.H. Chia, "Gold nanoparticles promote amorphous carbon to be ammonia gas sensor," *Europhys. Lett.* **114**, 40001 (2016).

[81] T. Kaneko, "Energy distribution of secondary electrons emitted from solid surfaces under electron bombardment: i. theory," *Surf. Sci.* **237**, 327 (1990).

[82] S. Gong et al., "Electron beam excitation of surface plasmon polaritons," *Opt. Express* **22**, 19252 (2014).

[83] D. Drouin et al., "CASINO v2.42—a fast and easy-to-use modeling tool for

scanning electron microscopy and microanalysis users," *Scanning* **29**, 92 (2007).

[84] H. Demers, N. Poirier-Demers, M.R. Phillips, N. de Jonge, and D. Drouin, "Three-dimensional electron energy deposition modeling of cathodoluminescence emission near threading dislocations in gan and electron-beam lithography exposure parameters for a pmma resist," *Microsc. Microanal.* **18**, 1220 (2012).

[85] R. Soref, "The past, present, and future of silicon photonics," *IEEE J. Sel. Top. Quantum Electron.* **12**, 1678 (2006).

[86] L.C. Kimerling et al., in *Top. Appl. Phys.* (Springer, Berlin, Heidelberg, 2004), pp. 89–120.

[87] S. Narasimha et al., in *2017 IEEE Int. Electron Devices Meet.* (IEEE, 2017), p. 29.5.1-29.5.4.

[88] C. Auth et al., in *2017 IEEE Int. Electron Devices Meet.* (IEEE, 2017), p. 29.1.1-29.1.4.

[89] S. Sederberg, C.J. Firby, S.R. Greig, and A.Y. Elezzabi, "Integrated nanoplasmonic waveguides for magnetic, nonlinear, and strong-field devices," *Nanophotonics* **6**, (2017).

[90] E. Ozbay, "Plasmonics: merging photonics and electronics at nanoscale dimensions.," *Science* **311**, 189 (2006).

[91] S. Sederberg, V. Van, and A.Y. Elezzabi, "Monolithic integration of plasmonic waveguides into a complimentary metal-oxide-semiconductor- and photonic-compatible platform," *Appl. Phys. Lett.* **96**, 121101 (2010).

[92] S. Sun, A.-H.A. Badawy, V. Narayana, T. El-Ghazawi, and V.J. Sorger, "The case for hybrid photonic plasmonic interconnects (hyppis): low-latency energy-and-area-efficient on-chip interconnects," *IEEE Photonics J.* **7**, 1 (2015).

[93] Lee De Forest, "The audion; a new receiver for wireless telegraphy," *Trans. Am. Inst. Electr. Eng.* **XXV**, 735 (1906).

[94] K.R. Spangenberg, *Vacuum tubes* (McGraw-Hill, 1948).

[95] W.F. Brinkman, D.E. Haggan, and W.W. Troutman, "A history of the invention of the transistor and where it will lead us," *IEEE J. Solid-State Circuits* **32**, 1858 (1997).

[96] J.-W. Han, J. Sub Oh, and M. Meyyappan, "Vacuum nanoelectronics: back to the future?—gate insulated nanoscale vacuum channel transistor," *Appl. Phys. Lett.* **100**, 213505 (2012).

[97] M.P. Nielsen and A.Y. Elezzabi, "Nanoplasmonic distributed bragg reflector resonators for monolithic integration on a complementary metal-oxide-semiconductor platform," *Appl. Phys. Lett.* **103**, 051107 (2013).

[98] S. Sederberg, D. Driedger, M. Nielsen, and A.Y. Elezzabi, "Ultrafast all-optical switching in a silicon-based plasmonic nanoring resonator," *Opt. Express* **19**, 23494 (2011).

[99] P.B. Johnson and R.W. Christy, "Optical constants of the noble metals," *Phys. Rev. B* **6**, 4370 (1972).

[100] R.N. Dexter, H.J. Zeiger, and B. Lax, "Cyclotron resonance experiments in silicon

and germanium," *Phys. Rev.* **104**, 637 (1956).

[101] A.R. Motamedi, A.H. Nejadmalayeri, A. Khilo, F.X. Kärtner, and E.P. Ippen, "Ultrafast nonlinear optical studies of silicon nanowaveguides," *Opt. Express* **20**, 4085 (2012).

[102] S. Yang et al., in *Int. Electron Devices Meet. 1998. Tech. Dig. (Cat. No.98CH36217)* (IEEE, 1998), pp. 197–200.

[103] D.J. Jones et al., "Carrier-envelope phase control of femtosecond mode-locked lasers and direct optical frequency synthesis," *Science* **288**, 635 (2000).

[104] T. Wittmann et al., "Single-shot carrier–envelope phase measurement of few-cycle laser pulses," *Nat. Phys.* **5**, 357 (2009).

[105] S. Keiber et al., "Electro-optic sampling of near-infrared waveforms," *Nat. Photonics* **10**, 159 (2016).

[106] O. Kwon et al., "Semimetallization of dielectrics in strong optical fields," *Sci. Rep.* **6**, 21272 (2016).

[107] G. Bonfiglioli and R. Malvano, "Surface states in metals," *Phys. Rev.* **115**, 330 (1959).

[108] G. Bonfiglioli, E. Coen, and R. Malvano, "Modulation of conductivity by surface charges in metals," *Phys. Rev.* **101**, 1281 (1956).

[109] G. Bonfiglioli, E. Coen, and R. Malvano, "Modulation of the electrical conductivity by surface charges in metals," *Nuovo Cim.* **2**, 334 (1955).

[110] H.L. Stadler, "Changing properties of metals by ferroelectric polarization

charging," *Phys. Rev. Lett.* **14**, 979 (1965).

[111] A. Sekiyama et al., "The prominent 5d-orbital contribution to the conduction electrons in gold," *New J. Phys.* **12**, 043045 (2010).

[112] H.. Juretschke, "Mean free path and boundary influences in the metallic field effect," *Surf. Sci.* **2**, 40 (1964).

[113] H.J. Juretschke, "Influence of the surface scattering of electrons on the metallic field effect in thin layers," *Surf. Sci.* **5**, 111 (1966).

[114] E.C. McIrvine, "Influence of boundary scattering on the metallic field effect," *Surf. Sci.* **5**, 171 (1966).

[115] K.J. Chau and A.Y. Elezzabi, "Photonic anisotropic magnetoresistance in dense co particle ensembles," *Phys. Rev. Lett.* **96**, 033903 (2006).

[116] K.J. Chau, M. Johnson, and A.Y. Elezzabi, "Electron-spin-dependent terahertz light transport in spintronic-plasmonic media," *Phys. Rev. Lett.* **98**, 133901 (2007).

[117] K.J. Chau and A.Y. Elezzabi, "Effect of interface resistance on terahertz pulses in bimetallic microparticles," *Phys. Rev. B* **73**, 085419 (2006).

[118] C.A. Baron et al., "The effect of a semiconductor-metal interface on localized terahertz plasmons," *Appl. Phys. Lett.* **98**, 111106 (2011).

[119] I. Al-Naib et al., "Effect of local field enhancement on the nonlinear terahertz response of a silicon-based metamaterial," *Phys. Rev. B* **88**, 195203 (2013).

[120] K.J. Chau, K.M. Rieckmann, and A.Y. Elezzabi, "Subsurface probing of terahertz particle plasmons," *Appl. Phys. Lett.* **90**, 131114 (2007).

[121] C.J.E. Straatsma, M. Johnson, and A.Y. Elezzabi, "Terahertz spinplasmonics in random ensembles of ni and co microparticles," *J. Appl. Phys.* **112**, 103904 (2012).

[122] A.Y. Elezzabi and P. Maraghechi, "A versatile and reconfigurable setup for all-terahertz time-resolved pump-probe spectroscopy," *Rev. Sci. Instrum.* **83**, 053107 (2012).

[123] K.J. Chau, G.D. Dice, and A.Y. Elezzabi, "Coherent plasmonic enhanced terahertz transmission through random metallic media," *Phys. Rev. Lett.* **94**, 173904 (2005).

[124] K.J. Chau and A.Y. Elezzabi, "Terahertz transmission through ensembles of subwavelength-size metallic particles," *Phys. Rev. B* **72**, 075110 (2005).

[125] A.Y. Elezzabi, K.J. Chau, C.A. Baron, and P. Maraghechi, "A plasmonic random composite with atypical refractive index," *Opt. Express* **17**, 1016 (2009).

[126] P. Maraghechi, C. Straatsma, Z. Liu, V. Zhao, and A.Y. Elezzabi, "Plasmon-assisted terahertz imaging inside metal-filled media," *Opt. Express* **17**, 16456 (2009).

[127] C.A. Baron and A.Y. Elezzabi, "A magnetically active terahertz plasmonic artificial material," *Appl. Phys. Lett.* **94**, 071115 (2009).

[128] C.A. Baron and A.Y. Elezzabi, "Active plasmonic devices via electron spin," *Opt. Express* **17**, 7117 (2009).

[129] M.A. Ordal, R.J. Bell, R.W. Alexander, L.L. Long, and M.R. Querry, "Optical properties of fourteen metals in the infrared and far infrared: al, co, cu, au, fe, pb, mo, ni, pd, pt, ag, ti, v, and w," *Appl. Opt.* **24**, 4493 (1985).

[130] Y. Bai et al., "Waveform-controlled terahertz radiation from the air filament produced by few-cycle laser pulses," *Phys. Rev. Lett.* **108**, 255004 (2012).

[131] T.-J. Wang et al., "Waveform control of enhanced thz radiation from femtosecond laser filament in air," *Appl. Phys. Lett.* **110**, 221102 (2017).

[132] COMSOL Multiphysics Modeling Software, (https://www.comsol.com/).

[133] M. Tani, S. Matsuura, K. Sakai, and S. Nakashima, "Emission characteristics of photoconductive antennas based on low-temperature-grown gaas and semi-insulating gaas," *Appl. Opt.* **36**, 7853 (1997).

Appendix A

Particle Tracking Code

The model discussed in Chapter 3 is implemented using MATLAB and takes input electromagnetic field files from a commercial FDTD software package (*Lumerical FDTD solutions* [63]). Table A.1 lists the MATLAB and Lumerical script files and a short description of their purpose. The overall flow of the program is depicted in the flowchart in Fig. A.1.

Filename	**Description**
add_date.m	Adds input time in seconds to current time and returns it as a string in the format "mmm dd HH:MM:SS."
allcomb.m	Calculates all possible combinations of simulation parameters.
calc_angles.m	Calculates various parameters (including angle) for the electrons that did not recollide with the metal film.
check_auto_shutoff.m	Checks whether there are still active electrons in the simulation region, if not it ends the simulation.
clear_results.m	Deletes all old result files from the current folder.
combine_fields_time.m	Takes the output field files generated from FDTD using export_fields_time.lsf and combines them if necessary. Also finds the max fields as described below.
controller.m	Controls the local loop of the simulation, sets up the random number generator.
duplicate_folder.m	Duplicates all the MATLAB (*.m) files in the current folder to a new folder with the same base name. Optionally, it can copy to multiple new folders.
electron_source.m	Generates the injected electrons based on the source type selected in update_global_settings.m.
electron2D.m	The main 2D electron class. Each electron that is tracked in the simulation is an object of this class. This class contains the main particle tracking code.
electron3D.m	The main 3D electron class.
find_esp.m	Calculates a linear equation for the location of the metal film and the 1/e edge of the SP field.

find_max.m	Finds the location in space and time of the maximum electric fields.
intensity_movie.m	Generates a time domain movie of the SP intensity over a specific range of times.
main_controller.m	The entry point to the particle tracking code.
parse_args.m	Parse input arguments to functions into a nice, useable structure.
parse_seconds.m	Converts time in seconds to a string of the format “00h 00m 00s.”
propagate.m	Propagates electrons through free space with no electromagnetic fields.
thz_source.m	Calculates the electromagnetic fields of a 2D THz pulse.
track_trajectories.m	The main time loop for the particle tracking code.
update_file.m	Updates the file in destination folder with 'file' from the current directory. Two optional parameters can be specified to indicate a start and end for the number of folders to update.
update_global_settings.m	The main settings file. All of the necessary settings for the simulation are set in this file.
update_local_settings.m	This sets the settings for the specific set of simulation parameters for the current loop iteration.
v2struct.m	Converts between a group of variables and a structure, and vice versa.
export_fields_time.lsf	Runs the FDTD simulation and exports E & H fields from the time monitor. Combine_fields_time.m must be run after to generate field files that are useable by the MATLAB code. This script can handle looping to export E & H fields that would normally require more memory than is available on the local computer.

Table A.1. Simulation files and their description.

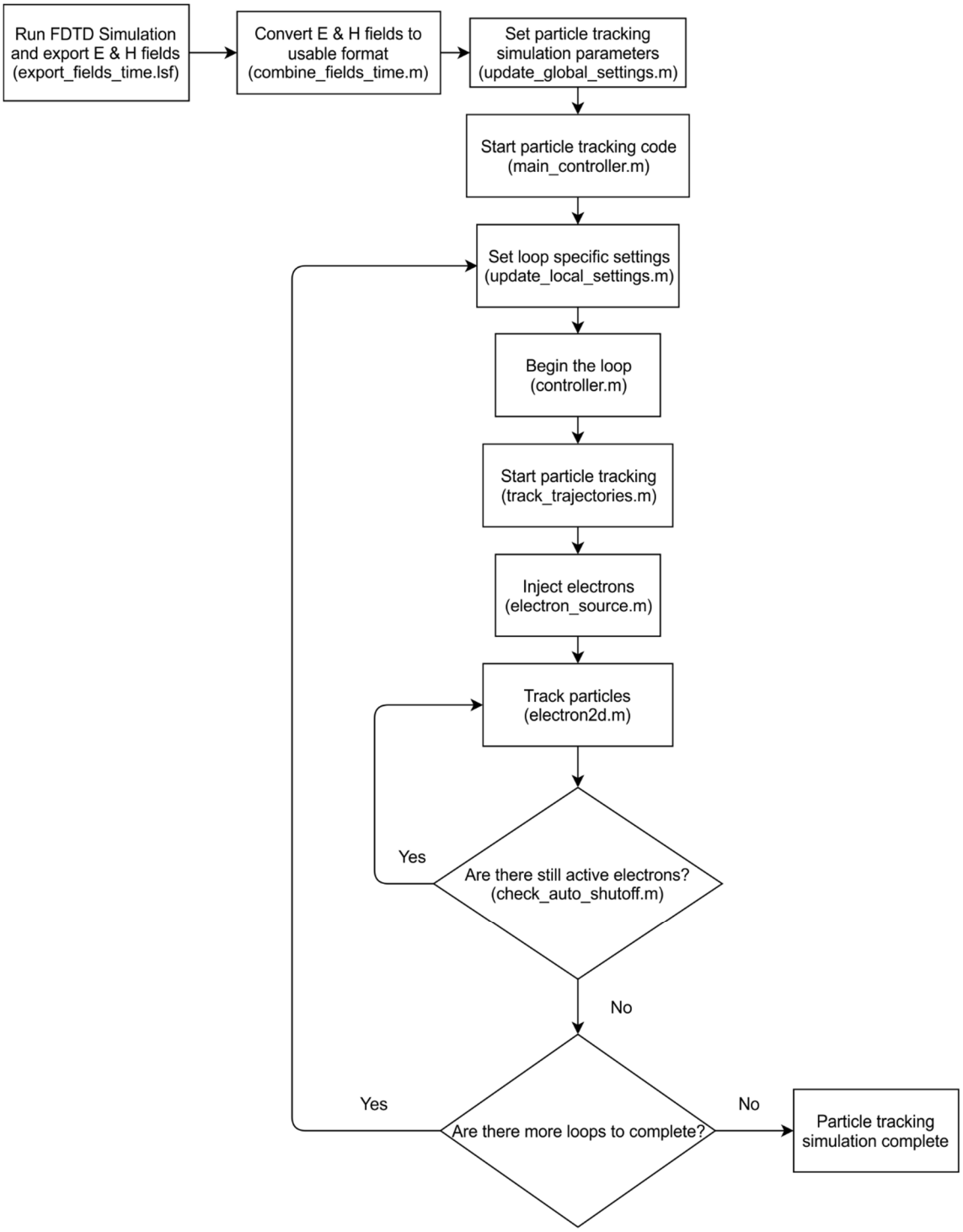

Figure A.1. Flowchart outlining the steps necessary to carry out a simulation from FDTD to particle tracking. The filenames responsible for each appropriate step are included in parentheses.

Appendix B

Vacuum Chamber Electrical Connections

There are three separate electrical feedthroughs mounted on the vacuum chamber for making connections to the various electrical components in the chamber. This appendix includes the pinouts of these feedthroughs as well as the wiring diagrams for correctly connecting and biasing the channeltron or the electron multiplier.

B.1. Main Electrical Feedthrough

The main electrical feedthrough carries the connections for the electron detectors as well as for the retarding potential setup. The feedthrough has 6 pins and is connected to a ribbon cable with individual colors on the vacuum and air side. The wiring diagram for the channeltron is depicted in Fig. B.1. The channeltron bias box provides the necessary biasing for the channeltron and includes a 10 nF, 3 kV capacitor to decouple the signal output from the high voltage (HV) input. The 1n4148 diodes provide transient protection on the signal output line. The electrical connections for the electron multiplier are depicted in Fig. B.2. The electron multiplier bias box does not contain resistors, but a 2 MΩ resistor can be attached from the green connector to ground to increase the gain of the first stage of the electron multiplier.

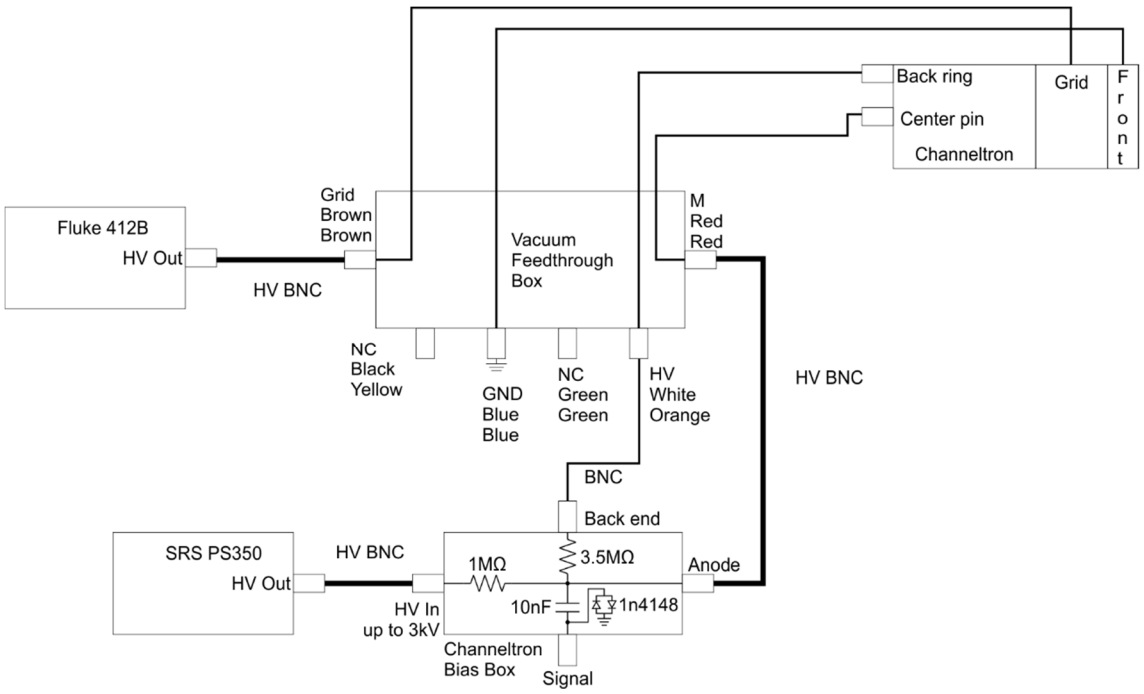

Figure B.1. Channeltron wiring diagram. The vacuum feedthrough box is connected to the vacuum feedthrough by a 6 pin Amphenol connector. Connections are listed with air-side wire color on top and vacuum-side on the bottom.

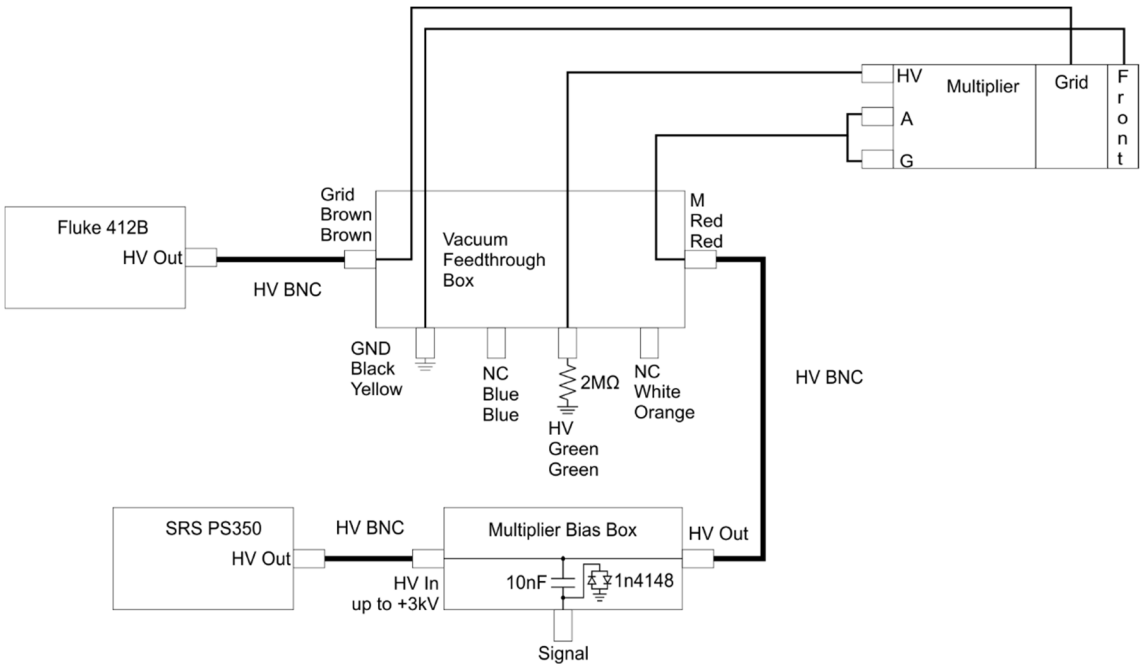

Figure B.2. Electron multiplier wiring diagram. The vacuum feedthrough box is connected to the vacuum feedthrough by a 6 pin Amphenol connector. Connections are listed with air-side wire color on top and vacuum-side on the bottom.

B.2. Motor Mike Feedthrough

The second electrical feedthrough is a seven-pin screw terminal connector that connects to an Oriel Motor Mike motor with integral encoder in the vacuum chamber. The air-side connections connect to an Oriel 18009 dual Motor Mike controller which provides 1 μm resolution. The pinout of the Motor Mike connector is depicted in Fig. B.3.

NC	Brown	Red	Orange
NC	Yellow	Green	Blue

Figure B.3. Motor Mike connection pinout.

B.3. 20-pin Multipurpose Feedthrough

The final electrical feedthrough is a multipurpose 20-pin feedthrough that currently has 12 wires terminated in a ribbon cable on both the vacuum- and air-side connections. The pinout for the feedthrough as well as the ribbon cables is depicted in Fig. B.4 with the connections listed in Table B.1.

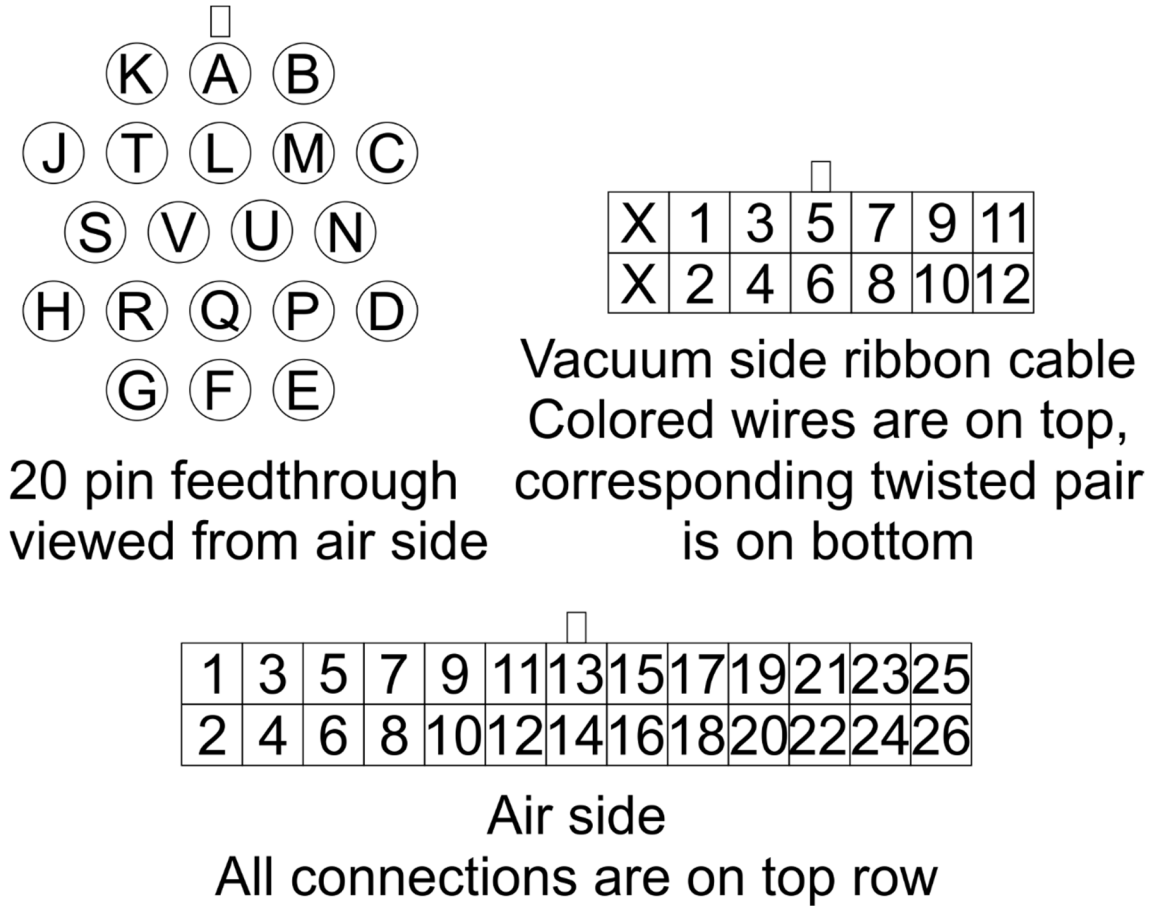

Figure B.4. 20-pin electrical feedthrough pinout. Table B.1 lists the corresponding air-feedthrough-vacuum connection list.

Air side connection	Feedthrough pin	Vacuum side connection	Vacuum side color
1	A	1	Red
3	B	2	Red/White
5	C	3	Orange
7	M	4	Orange/White
9	N	5	Yellow
11	D	6	Yellow/White
13	E	7	Green
15	F	8	Green/White
17	G	9	Blue
19	H	10	Blue/White
21	J	11	Purple
23	K	12	Purple/White

Table B.1. 20-pin feedthrough electrical connection list.

Appendix C

Retarding Potential Analyzer Mechanical Design

To improve the resolution of the retarding potential energy measurements and simplify the setup, I designed and built a contained retarding potential analyzer (RPA) based on the designs from [66,67]. The complete mechanical drawings are included in the following section

C.1. Mechanical Drawings

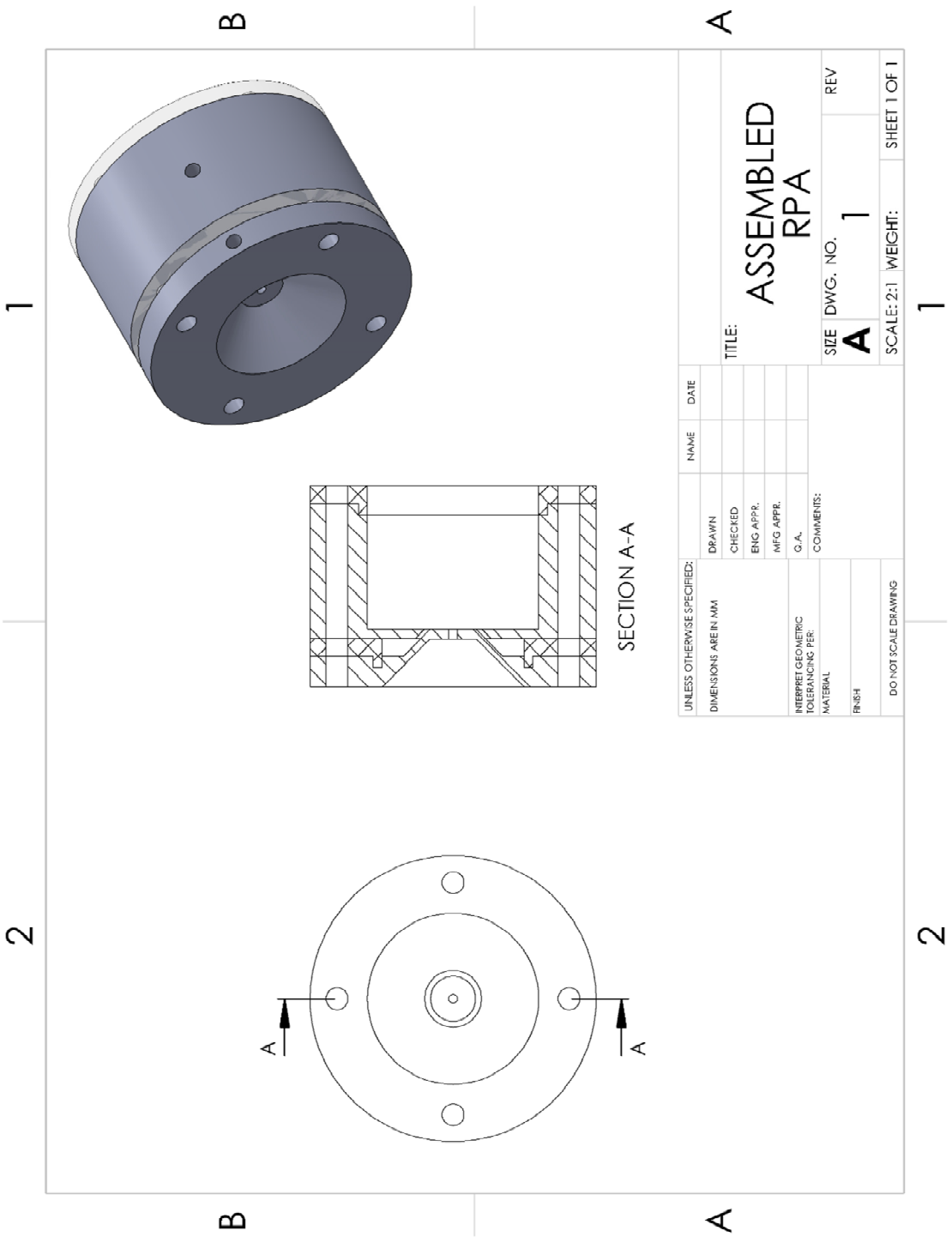

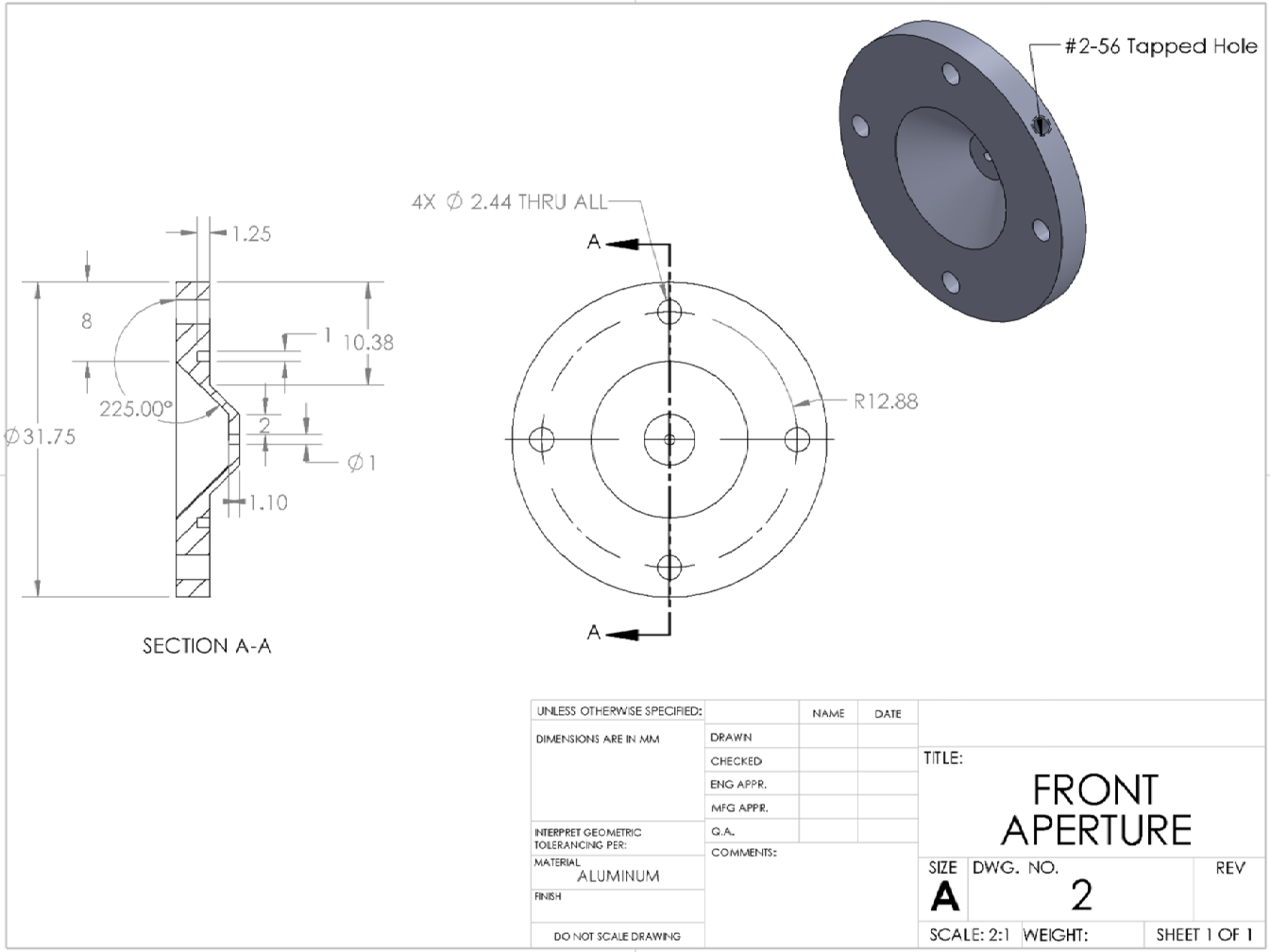
#2-56 Tapped Hole
4X ∅ 2.44 THRU ALL
A
A
R12.88
1.25
8
1
10.38
225.00°
2
∅31.75
∅1
1.10
SECTION A-A
UNLESS OTHERWISE SPECIFIED:
DIMENSIONS ARE IN MM
INTERPRET GEOMETRIC TOLERANCING PER:
MATERIAL
ALUMINUM
FINISH
DO NOT SCALE DRAWING
NAME
DATE
DRAWN
CHECKED
ENG APPR.
MFG APPR.
Q.A.
COMMENTS:
TITLE:
FRONT APERTURE
SIZE
A
DWG. NO.
2
REV
SCALE: 2:1
WEIGHT:
SHEET 1 OF 1

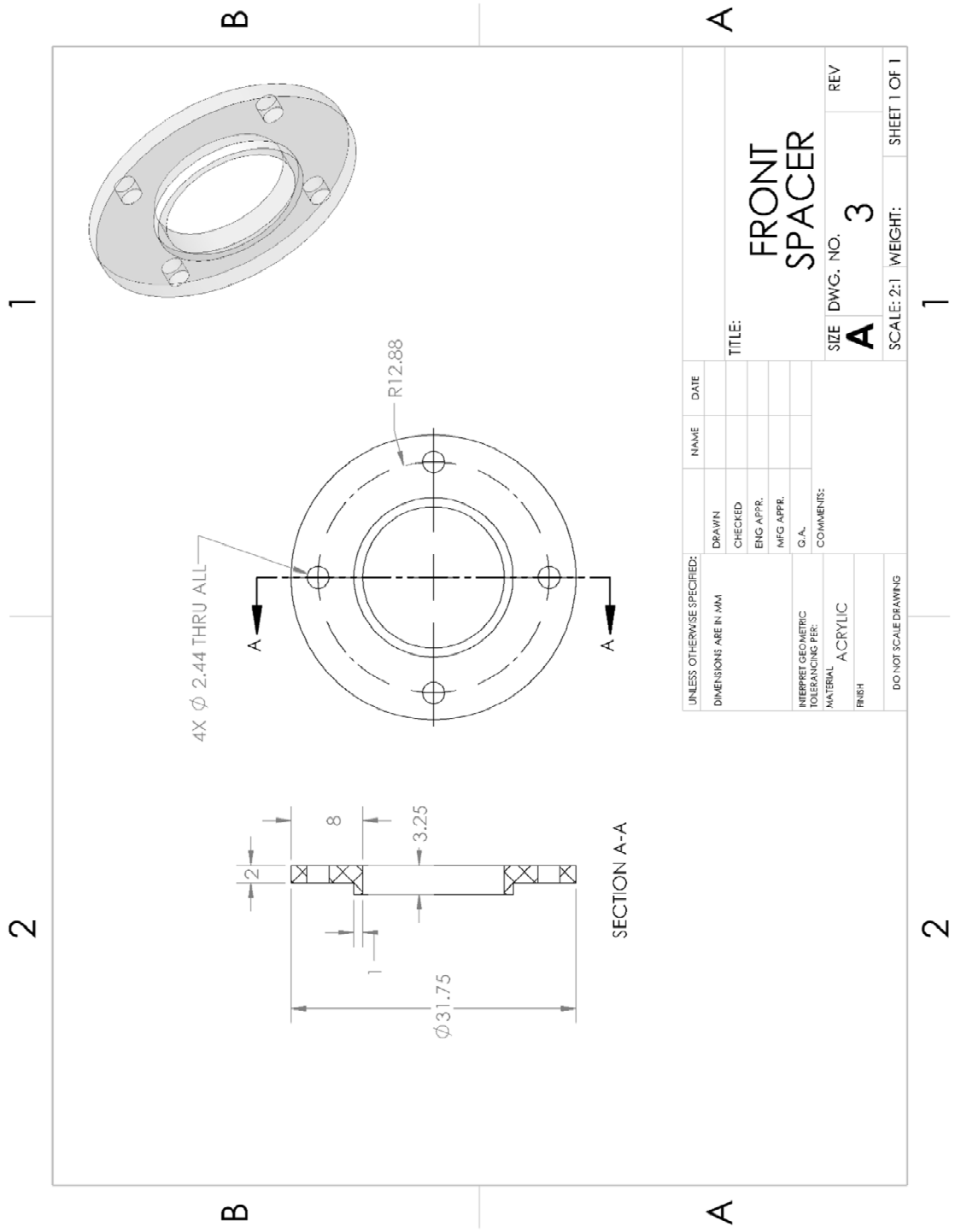
R12.88
4X ⌀ 2.44 THRU ALL
A
A
SECTION A-A
2
8
3.25
1
⌀31.75
UNLESS OTHERWISE SPECIFIED:
DIMENSIONS ARE IN MM
INTERPRET GEOMETRIC TOLERANCING PER:
MATERIAL ACRYLIC
FINISH
DO NOT SCALE DRAWING
NAME
DATE
DRAWN
CHECKED
ENG APPR.
MFG APPR.
Q.A.
COMMENTS:
TITLE:
FRONT SPACER
SIZE A
DWG. NO. 3
REV
SCALE: 2:1
WEIGHT:
SHEET 1 OF 1
1
2
A
B

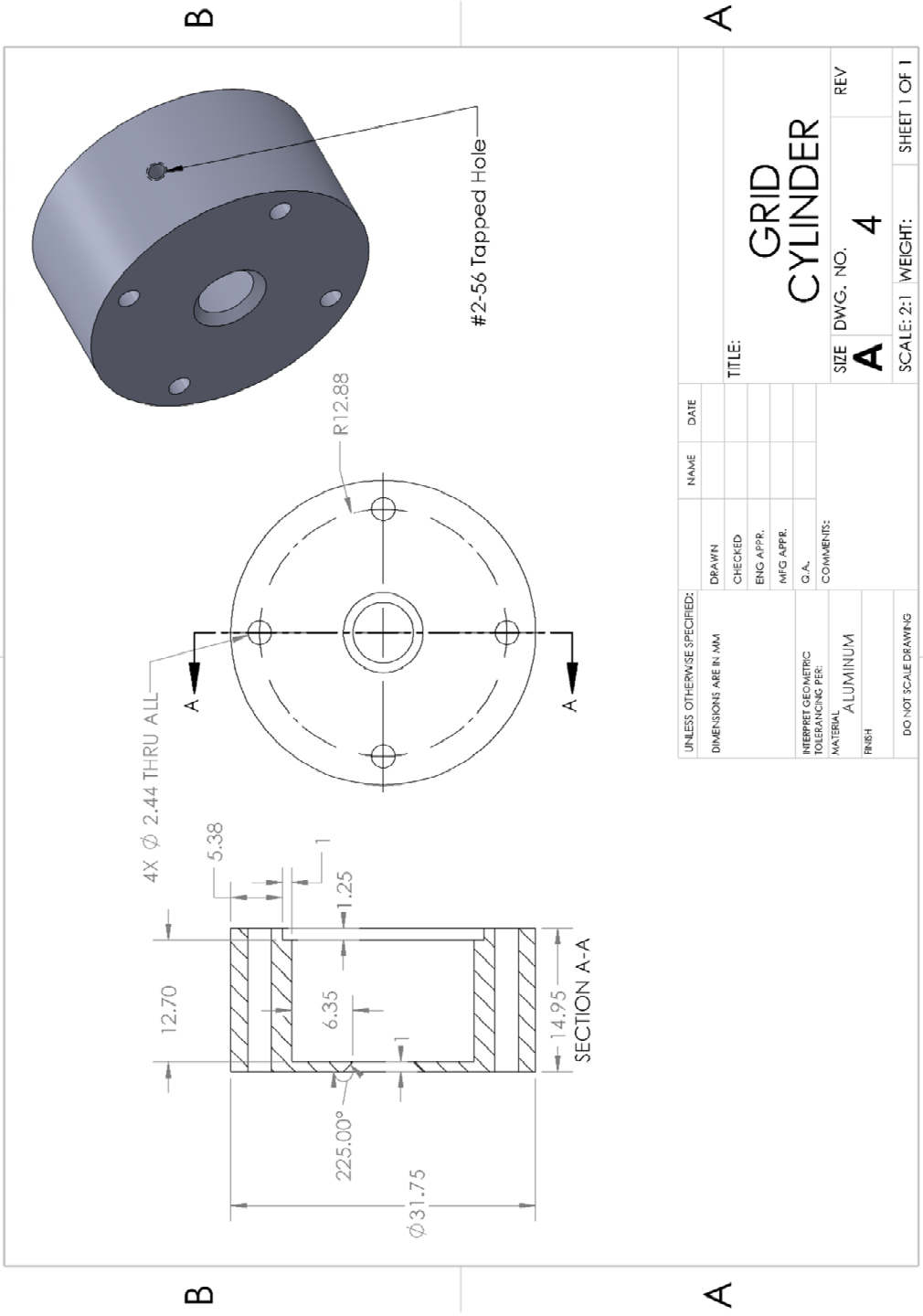
#2-56 Tapped Hole
R12.88
4X Ø 2.44 THRU ALL
5.38
1
1.25
12.70
6.35
1
14.95
225.00°
Ø31.75
SECTION A-A
A
A
UNLESS OTHERWISE SPECIFIED:
DIMENSIONS ARE IN MM
INTERPRET GEOMETRIC TOLERANCING PER:
MATERIAL
ALUMINUM
FINISH
DO NOT SCALE DRAWING
NAME
DATE
DRAWN
CHECKED
ENG APPR.
MFG APPR.
Q.A.
COMMENTS:
TITLE:
GRID CYLINDER
SIZE
A
DWG. NO.
4
REV
SCALE: 2:1
WEIGHT:
SHEET 1 OF 1

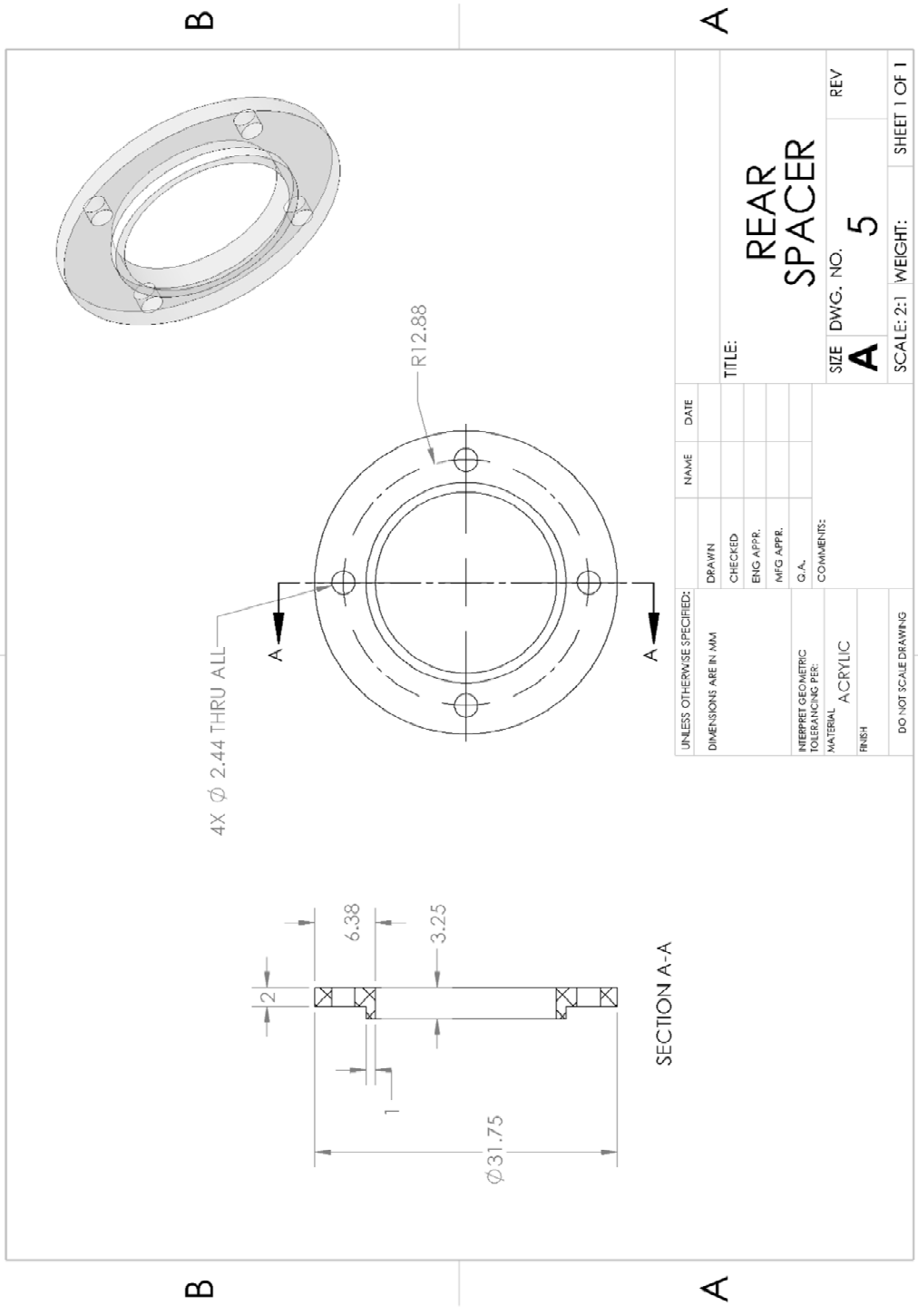
R12.88
4X Ø 2.44 THRU ALL
A
A
SECTION A-A
6.38
3.25
2
1
Ø31.75
REAR SPACER
TITLE:
SIZE A
DWG. NO. 5
REV
SCALE: 2:1
WEIGHT:
SHEET 1 OF 1
UNLESS OTHERWISE SPECIFIED:
DIMENSIONS ARE IN MM
DRAWN
CHECKED
ENG APPR.
MFG APPR.
Q.A.
COMMENTS:
NAME
DATE
INTERPRET GEOMETRIC TOLERANCING PER:
MATERIAL ACRYLIC
FINISH
DO NOT SCALE DRAWING

Appendix D

Design and Simulation of Double-pass Cylindrical Mirror Analyzer

To achieve higher energy resolution when measuring the kinetic energy of the generated electron pulses, I designed and built an electron spectrometer based on designs from [68,69].The design is a double-pass cylindrical mirror analyzer (CMA) that incorporates two cascaded stages to achieve a higher energy resolution as well as a defined image plane 6 mm from the first slit. The mechanical designs for the entire CMA can be found in the next section. To help with the design, I used finite element simulations in COMSOL Multiphysics [132] to verify the design and expected energy resolution. Figure D.1 depicts a side view cut-away of the CMA. The pass energy (energy of the electrons that are able to traverse from the input of the CMA to the detector) is controlled by varying the voltage applied to the outer cylinder with respect to the grounded inner cylinder. From simulations, and based on the dimensions of the outer and inner cylinders, the required voltage is given by:

$$V_{outer} = -0.58 \times \frac{E_{pass}}{q} \tag{D.1}$$

Where, V_{outer} is the voltage applied to the outer cylinder, and E_{pass} is the pass energy of the CMA. Figure D.2 depicts the number of electrons that reach the detector as a function of kinetic energy for a fixed E_{pass} = 1 eV, indicating a FWHM resolution of 0.01 eV and a full resolution of 0.03 eV. Figure D.3(a) depicts exemplary trajectories of electrons

passing from the input to the output of the CMA. Here, the electrons have a kinetic energy of 1 eV, and the outer cylinder is held at -0.58 V. Slightly changing the energy to be 1.02 eV, the electrons do not make it through the first pass of the CMA as illustrated in Fig. D.3(b).

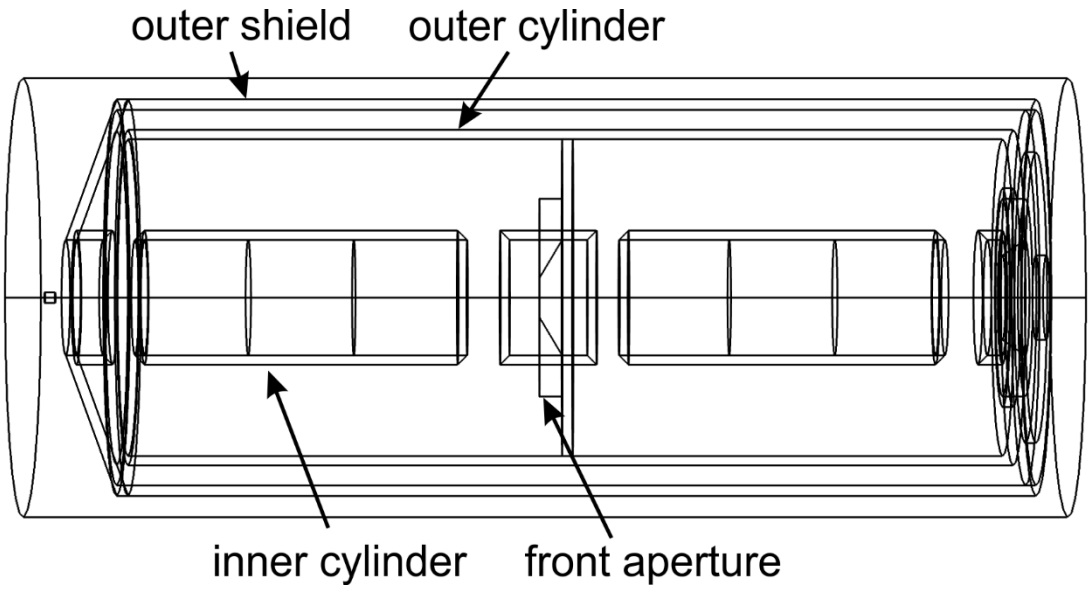

Figure D.1. Side view cut away of double-pass cylindrical mirror analyzer.

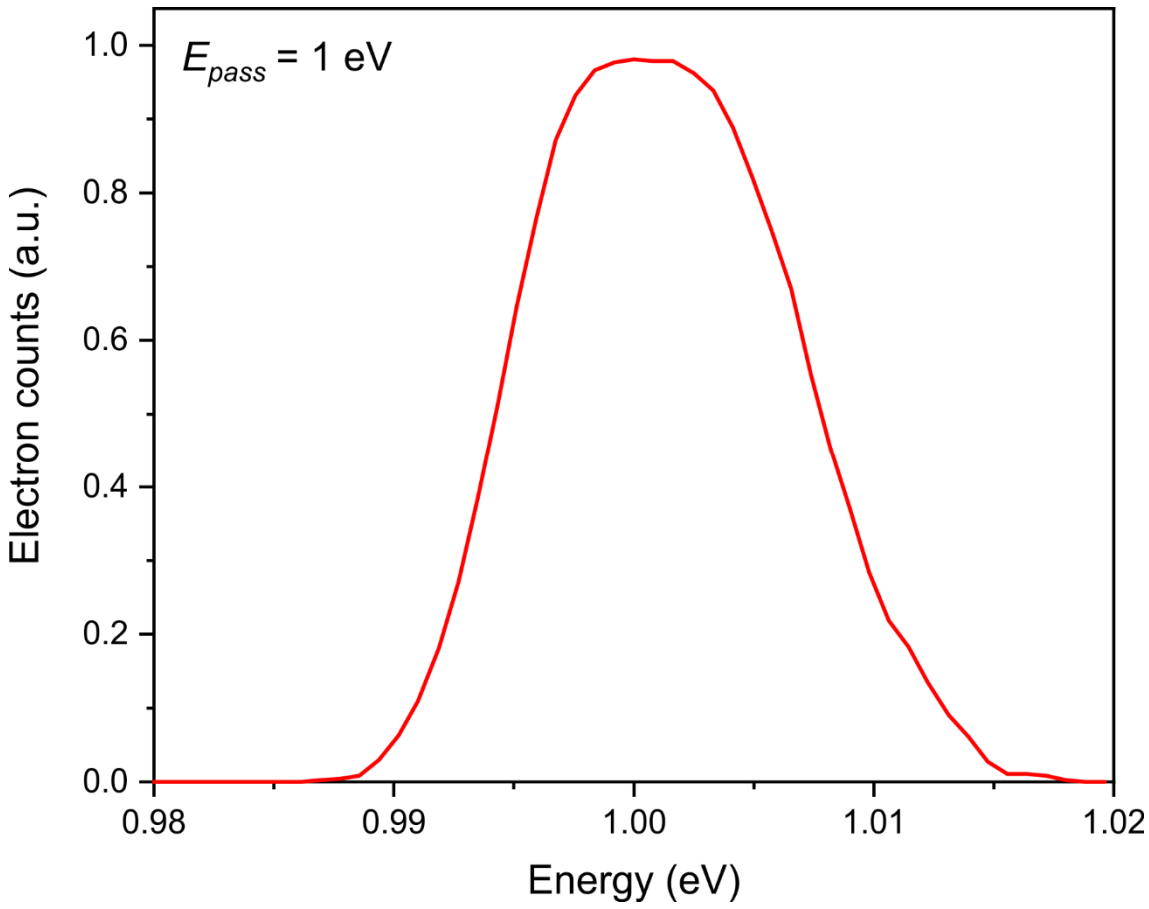

Figure D.2. Simulated number of electrons passing through the double-pass CMA as a function of initial kinetic energy for E_{pass} = 1 eV.

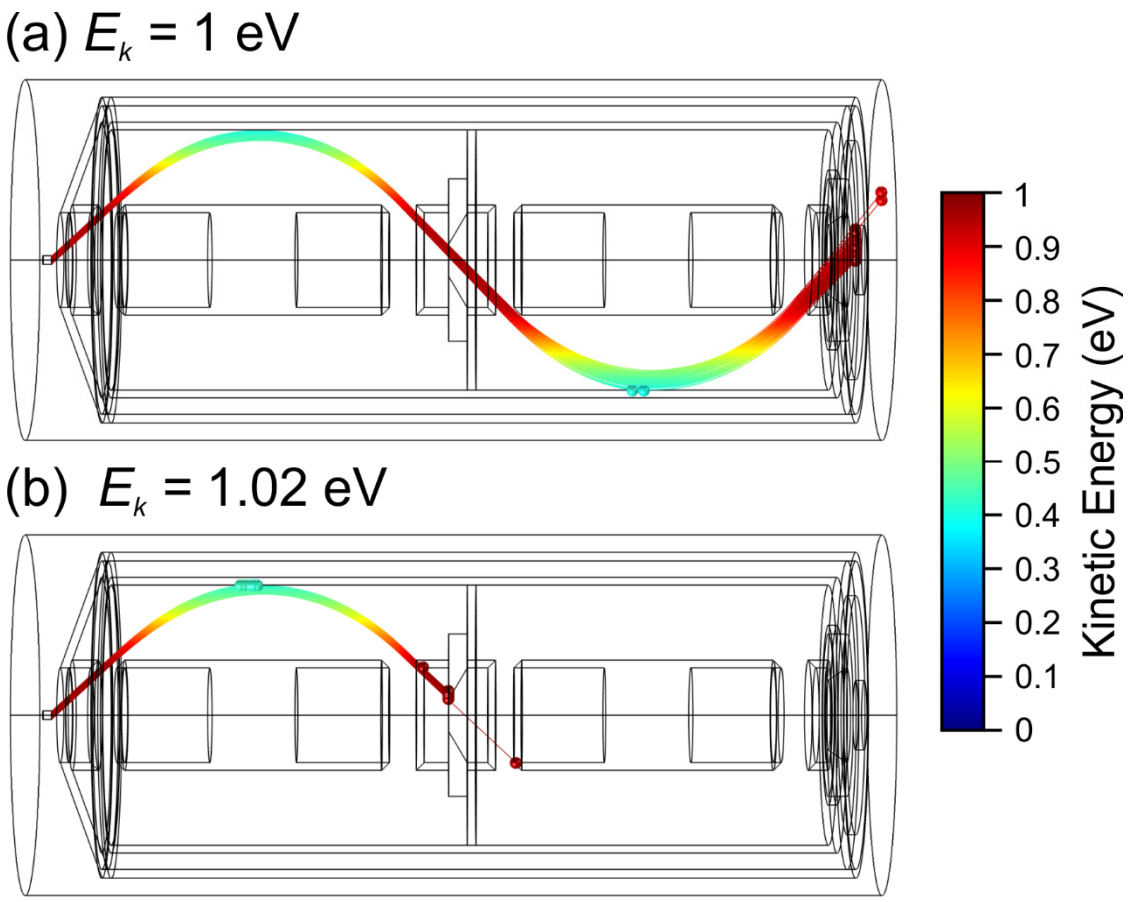

Figure D.3. Exemplary trajectories of electrons traversing through the CMA with E_{pass} = 1 eV at a kinetic energy of (a) 1 eV, and (b) 1.02 eV. The color of the trajectory indicates the electron kinetic energy.

The complete mechanical design drawings are found in the next section.

D.1. Mechanical Drawings

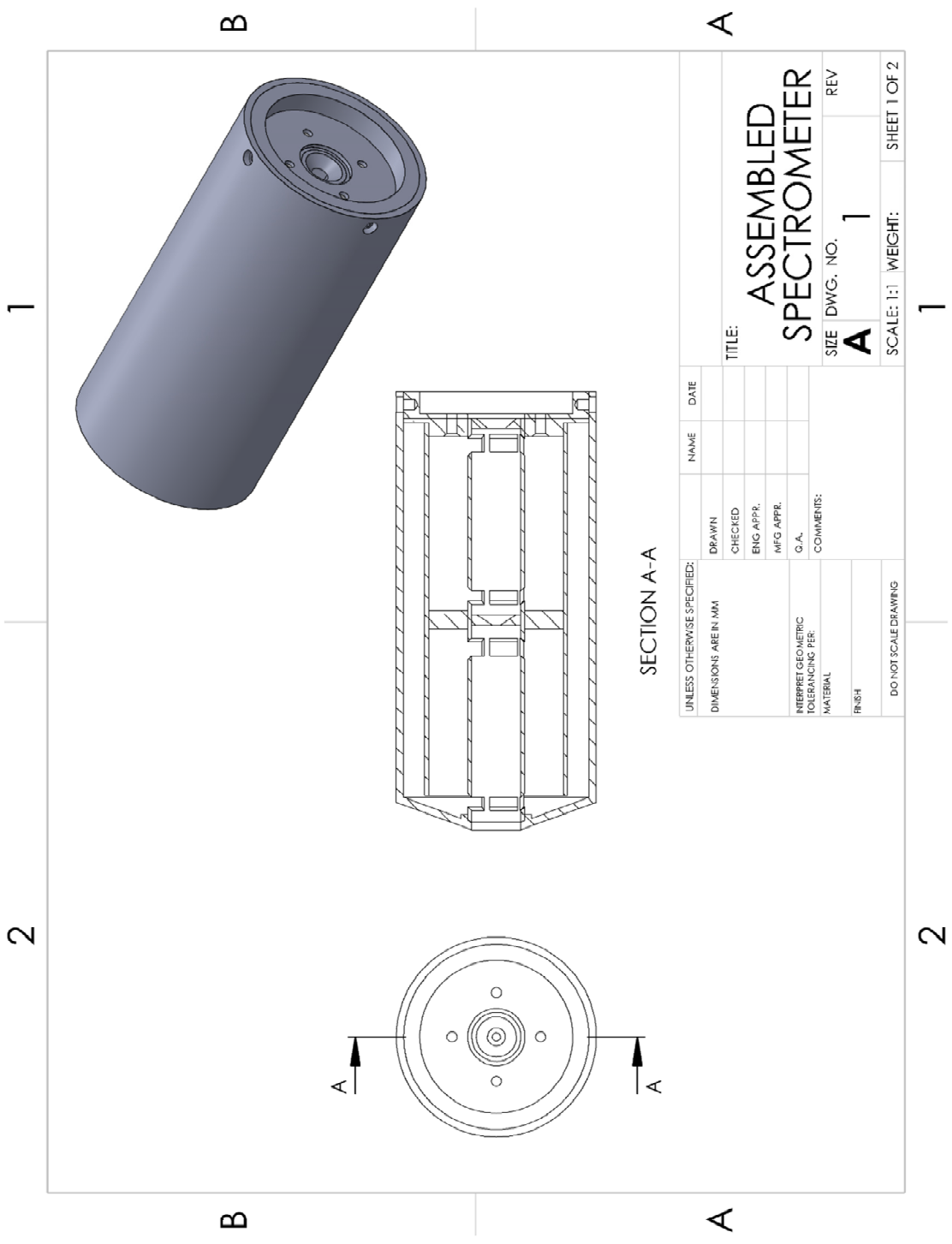

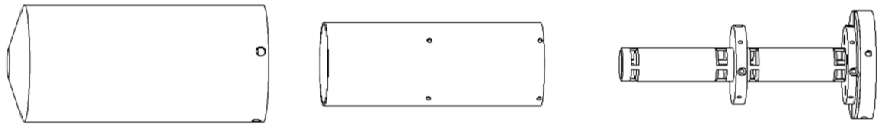

		NAME	DATE
UNLESS OTHERWISE SPECIFIED:			
DIMENSIONS ARE IN MM	DRAWN		
	CHECKED		
	ENG APPR.		
	MFG APPR.		
INTERPRET GEOMETRIC TOLERANCING PER:	Q.A.		
MATERIAL	COMMENTS:		
FINISH			
DO NOT SCALE DRAWING			

TITLE:

ASSEMBLED SPECTROMETER

SIZE	DWG. NO.	REV
A	1	
SCALE: 1:2	WEIGHT:	SHEET 2 OF 2

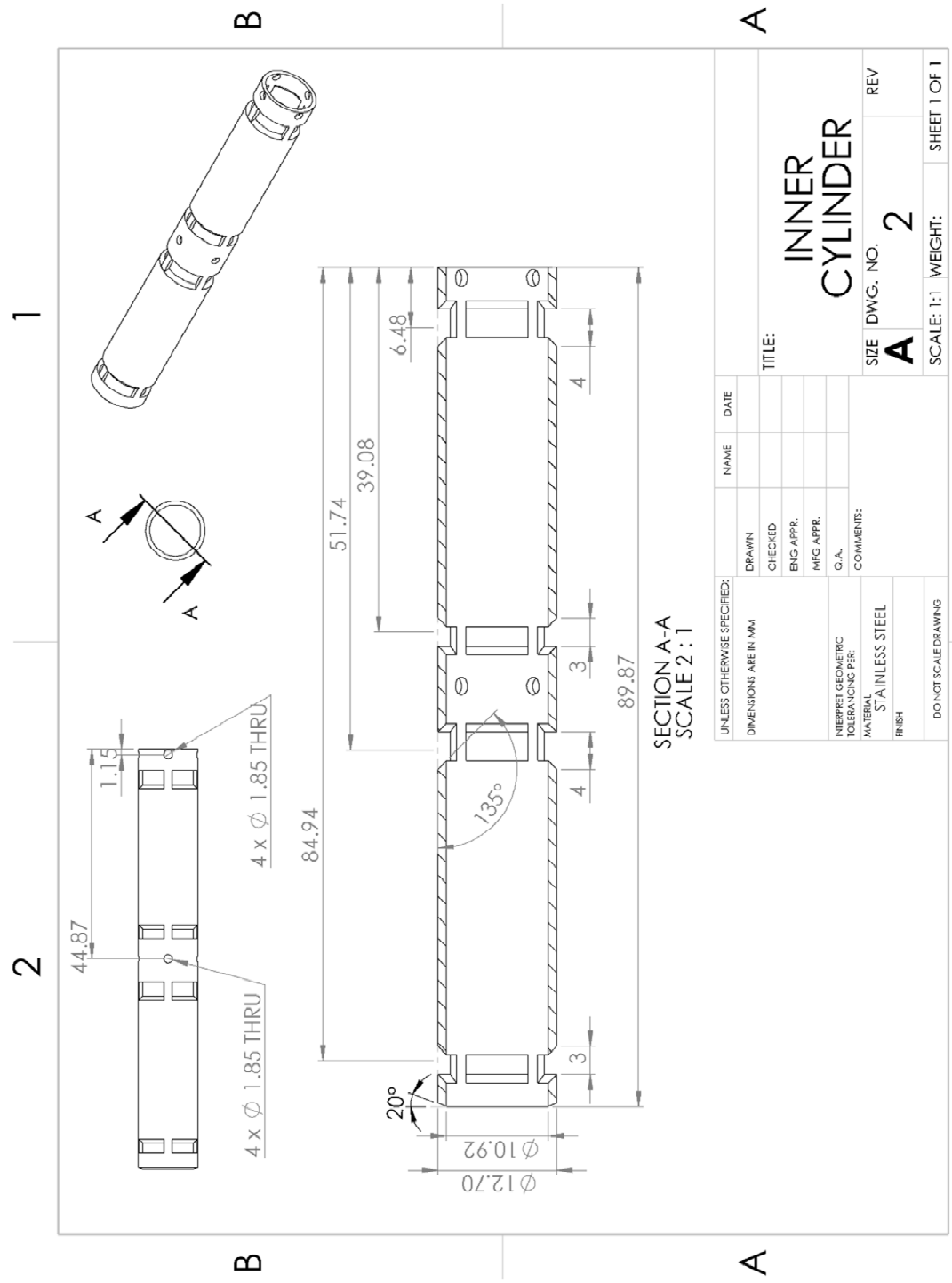
INNER CYLINDER
SECTION A-A
SCALE 2 : 1
4 x ∅ 1.85 THRU
4 x ∅ 1.85 THRU
44.87
1.15
84.94
51.74
39.08
6.48
89.87
4
4
3
3
135°
20°
∅10.92
∅12.70
A
A
UNLESS OTHERWISE SPECIFIED:
DIMENSIONS ARE IN MM
INTERPRET GEOMETRIC TOLERANCING PER:
MATERIAL
STAINLESS STEEL
FINISH
DO NOT SCALE DRAWING
NAME
DATE
DRAWN
CHECKED
ENG APPR.
MFG APPR.
G.A.
COMMENTS:
TITLE:
SIZE
A
DWG. NO.
2
REV
SCALE: 1:1
WEIGHT:
SHEET 1 OF 1

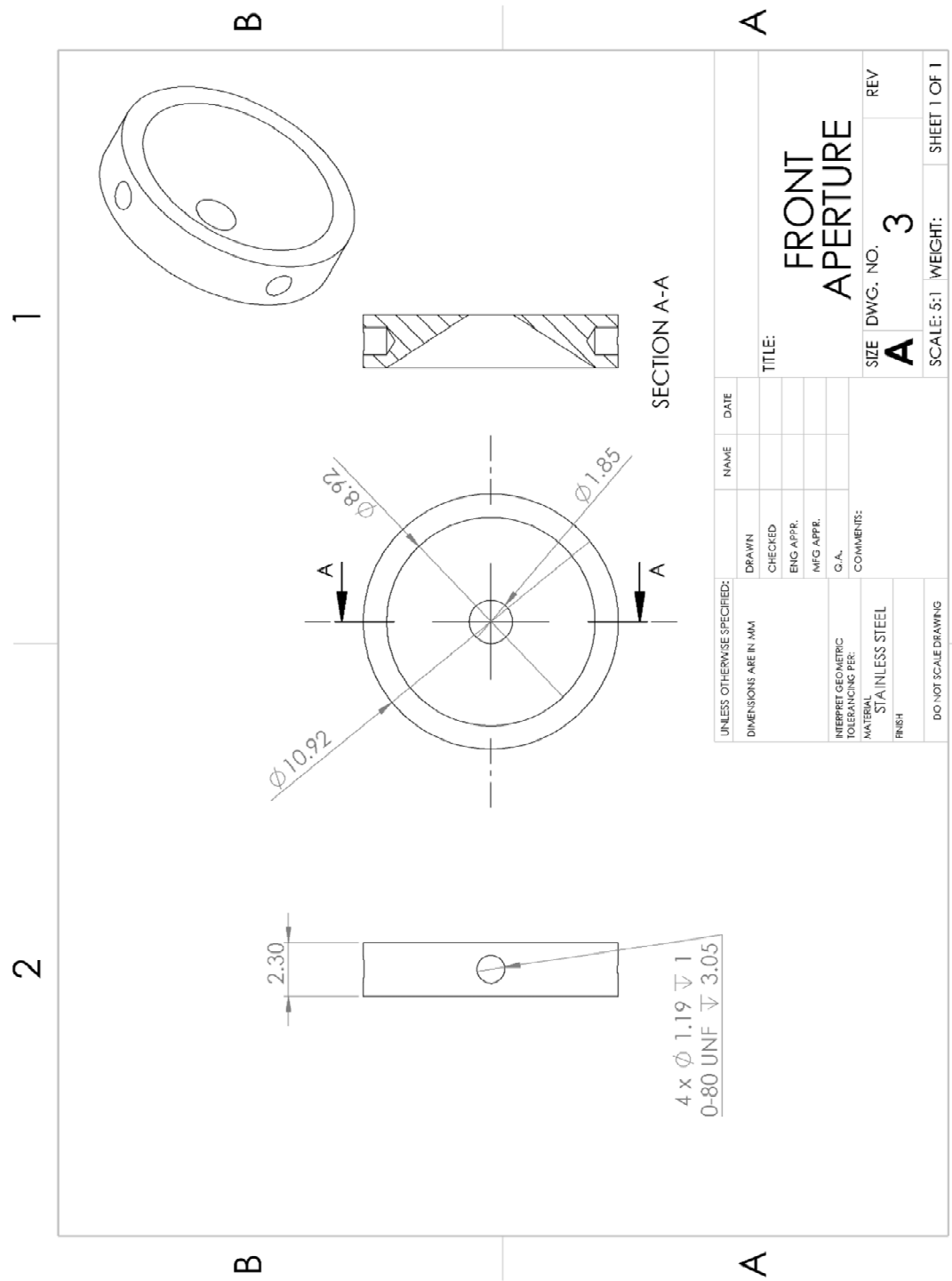
SECTION A-A
Ø8.92
Ø1.85
Ø10.92
2.30
4 x Ø 1.19 ↧ 1
0-80 UNF ↧ 3.05
UNLESS OTHERWISE SPECIFIED:
DIMENSIONS ARE IN MM
INTERPRET GEOMETRIC TOLERANCING PER:
MATERIAL
STAINLESS STEEL
FINISH
DO NOT SCALE DRAWING
NAME
DATE
DRAWN
CHECKED
ENG APPR.
MFG APPR.
Q.A.
COMMENTS:
TITLE:
FRONT APERTURE
SIZE
A
DWG. NO.
3
REV
SCALE: 5:1
WEIGHT:
SHEET 1 OF 1

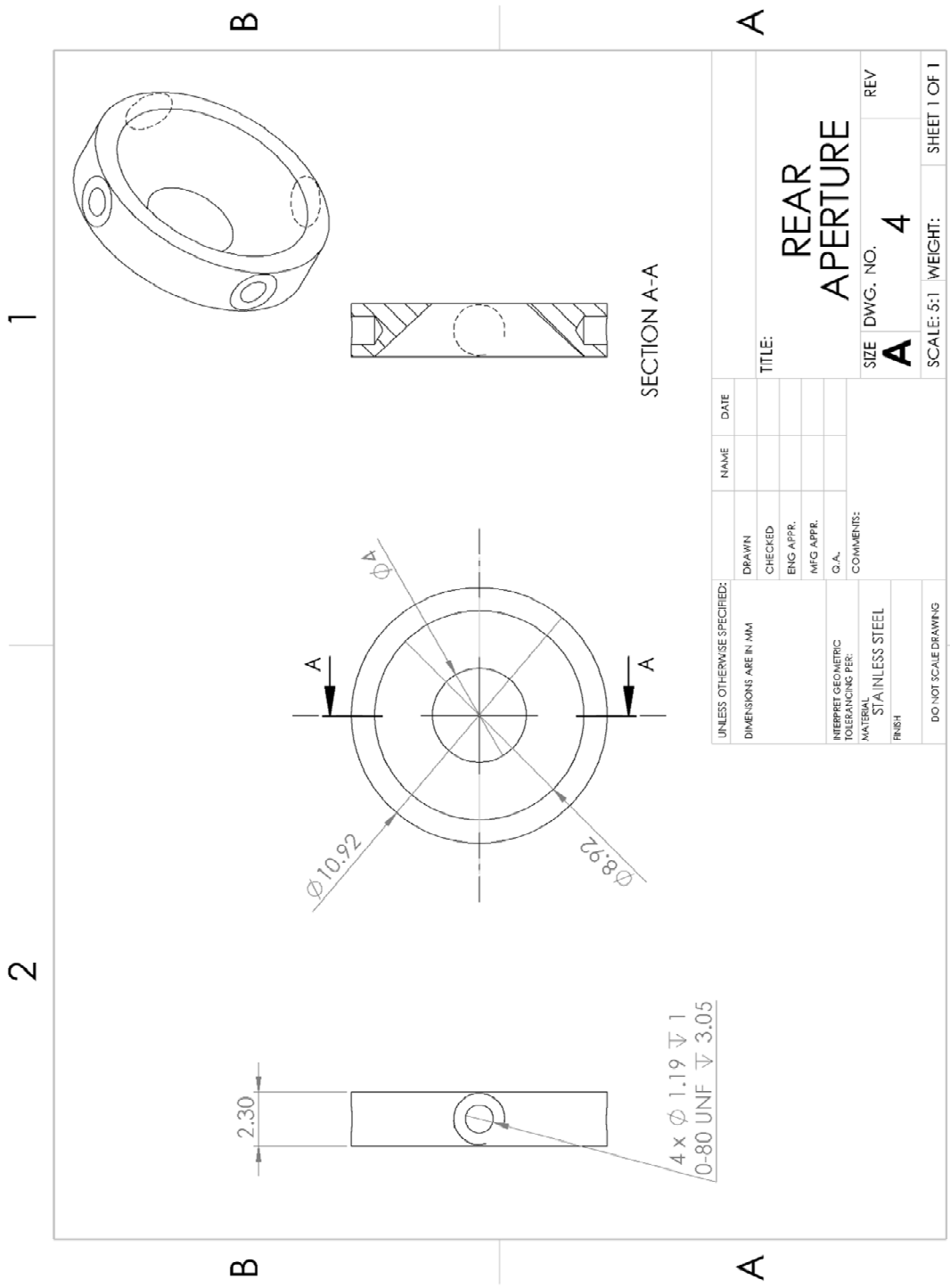
SECTION A-A
REAR APERTURE
SIZE A
DWG. NO. 4
REV
SCALE: 5:1
WEIGHT:
SHEET 1 OF 1
UNLESS OTHERWISE SPECIFIED:
DIMENSIONS ARE IN MM
DRAWN
CHECKED
ENG APPR.
MFG APPR.
Q.A.
COMMENTS:
NAME
DATE
INTERPRET GEOMETRIC TOLERANCING PER:
MATERIAL
STAINLESS STEEL
FINISH
DO NOT SCALE DRAWING
TITLE:
2.30
4 x ⌀ 1.19 ↧ 1
0-80 UNF ↧ 3.05
⌀10.92
⌀8.92
A
A

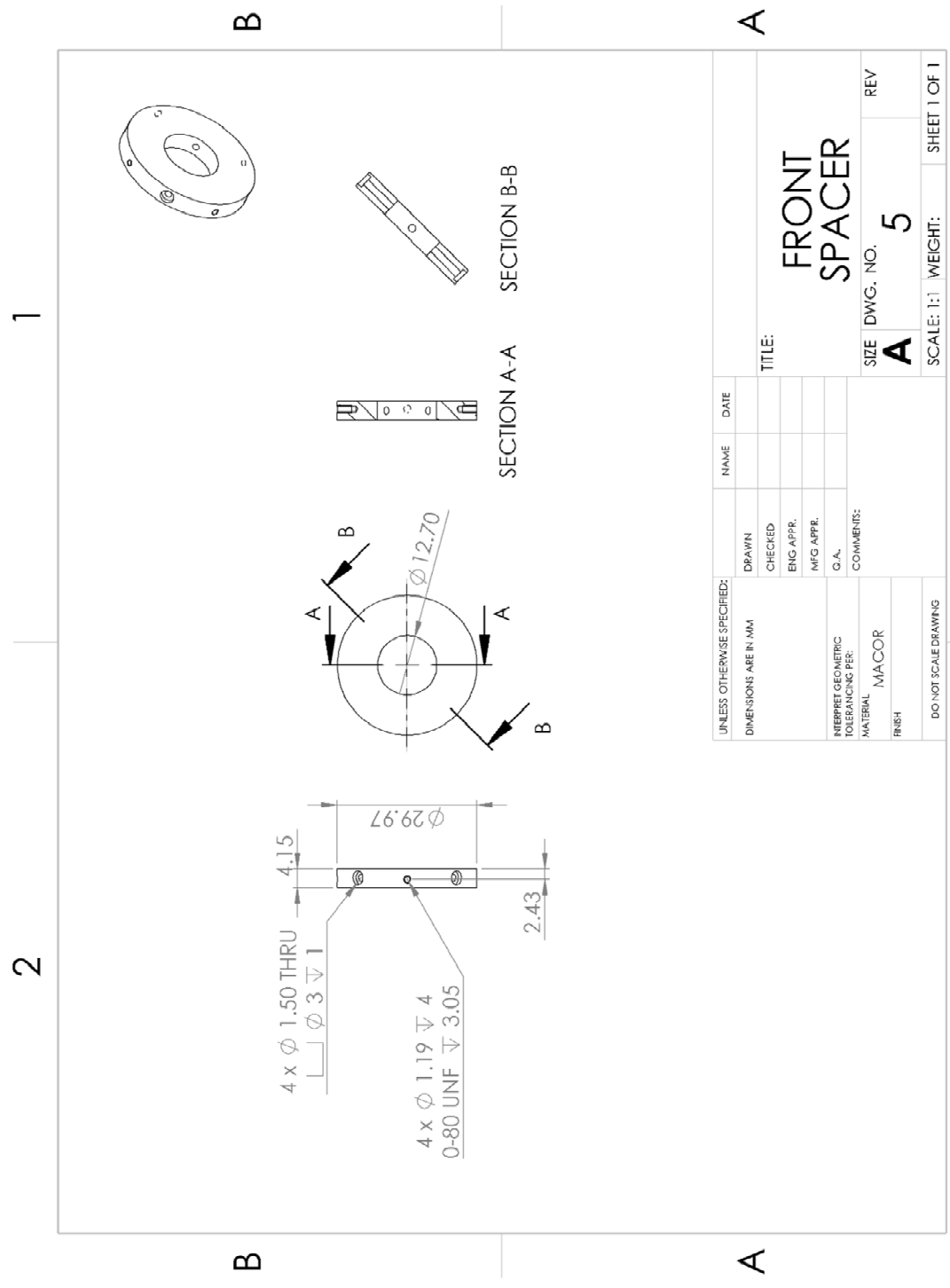
SECTION A-A
SECTION B-B
Ø12.70
Ø29.97
4.15
2.43
4 x Ø 1.50 THRU
⌴ Ø 3 ∓ 1
4 x Ø 1.19 ∓ 4
0-80 UNF ∓ 3.05
UNLESS OTHERWISE SPECIFIED:
DIMENSIONS ARE IN MM
INTERPRET GEOMETRIC TOLERANCING PER:
MATERIAL
MACOR
FINISH
DO NOT SCALE DRAWING
DRAWN
CHECKED
ENG APPR.
MFG APPR.
Q.A.
COMMENTS:
NAME
DATE
TITLE:
FRONT SPACER
SIZE
A
DWG. NO.
5
REV
SCALE: 1:1
WEIGHT:
SHEET 1 OF 1

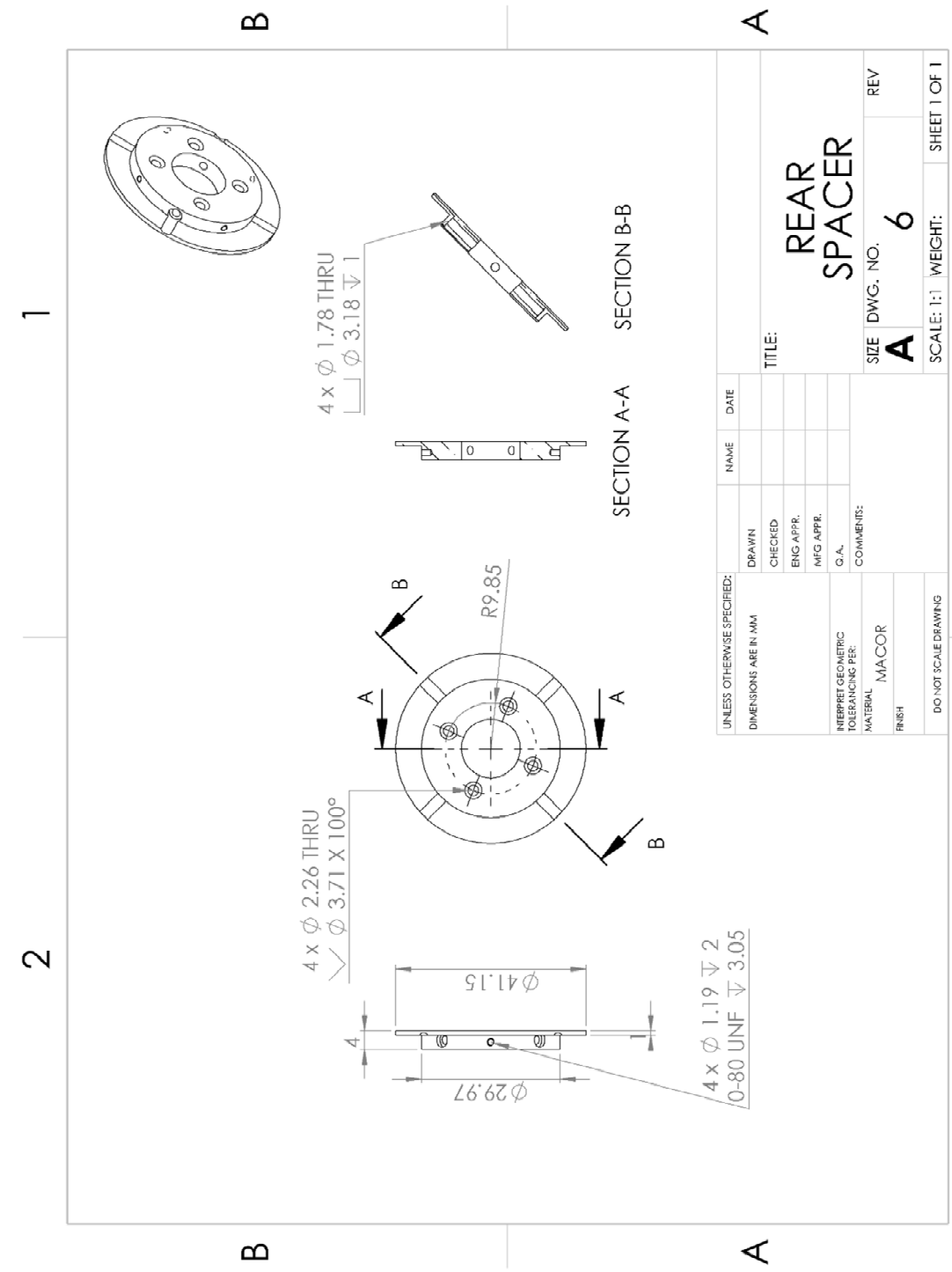
REAR SPACER
SECTION A-A
SECTION B-B
4 x ⌀ 1.78 THRU
⌴ ⌀ 3.18 ↧ 1
4 x ⌀ 2.26 THRU
⌵ ⌀ 3.71 X 100°
R9.85
⌀41.15
⌀29.97
4 x ⌀ 1.19 ↧ 2
0-80 UNF ↧ 3.05
UNLESS OTHERWISE SPECIFIED:
DIMENSIONS ARE IN MM
INTERPRET GEOMETRIC TOLERANCING PER:
MATERIAL MACOR
FINISH
DO NOT SCALE DRAWING
DRAWN
CHECKED
ENG APPR.
MFG APPR.
Q.A.
COMMENTS:
NAME
DATE
TITLE:
SIZE A
DWG. NO. 6
REV
SCALE: 1:1
WEIGHT:
SHEET 1 OF 1

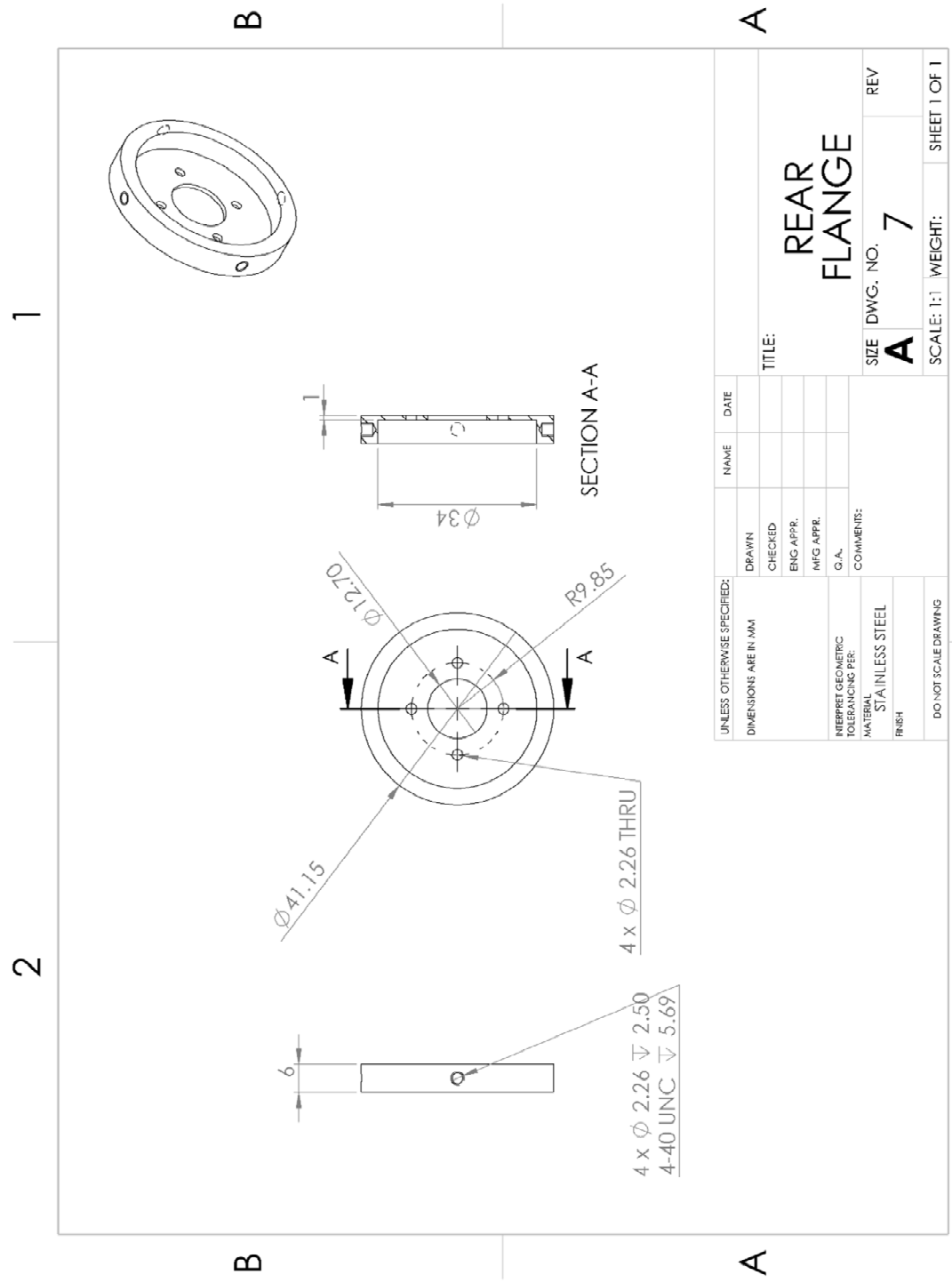
REAR FLANGE
SECTION A-A
Ø34
1
Ø12.20
R9.85
Ø41.15
4 x Ø 2.26 THRU
4 x Ø 2.26 ⩛ 2.50
4-40 UNC ⩛ 5.69
6
UNLESS OTHERWISE SPECIFIED:
DIMENSIONS ARE IN MM
INTERPRET GEOMETRIC TOLERANCING PER:
MATERIAL
STAINLESS STEEL
FINISH
DO NOT SCALE DRAWING
NAME
DATE
DRAWN
CHECKED
ENG APPR.
MFG APPR.
G.A.
COMMENTS:
TITLE:
SIZE
A
DWG. NO.
7
REV
SCALE: 1:1
WEIGHT:
SHEET 1 OF 1

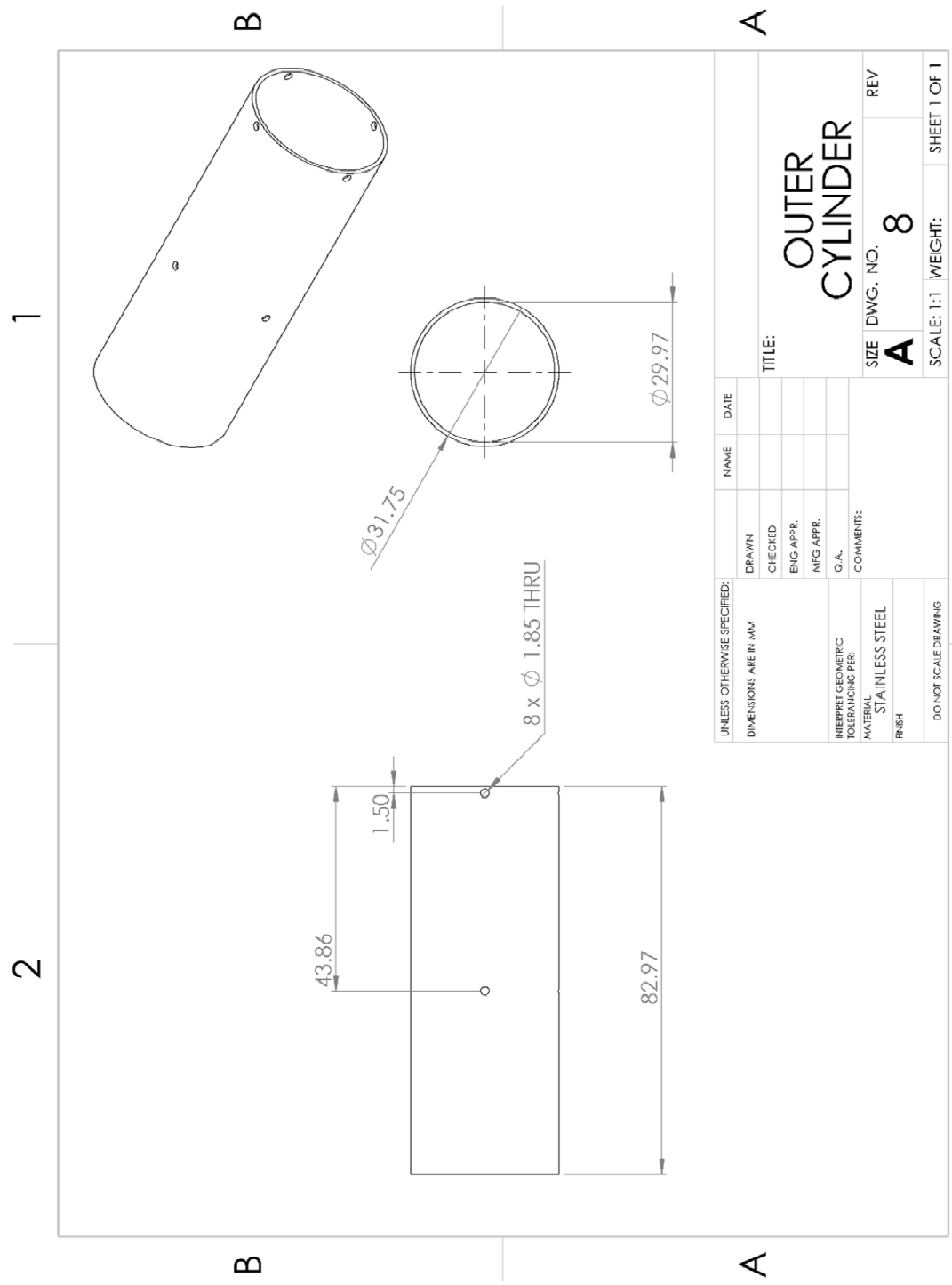
OUTER CYLINDER
8
A
SIZE
DWG. NO.
REV
SCALE: 1:1
WEIGHT:
SHEET 1 OF 1
TITLE:
NAME
DATE
DRAWN
CHECKED
ENG APPR.
MFG APPR.
G.A.
COMMENTS:
UNLESS OTHERWISE SPECIFIED:
DIMENSIONS ARE IN MM
INTERPRET GEOMETRIC TOLERANCING PER:
MATERIAL
STAINLESS STEEL
FINISH
DO NOT SCALE DRAWING
8 x Ø 1.85 THRU
Ø31.75
Ø29.97
1.50
43.86
82.97

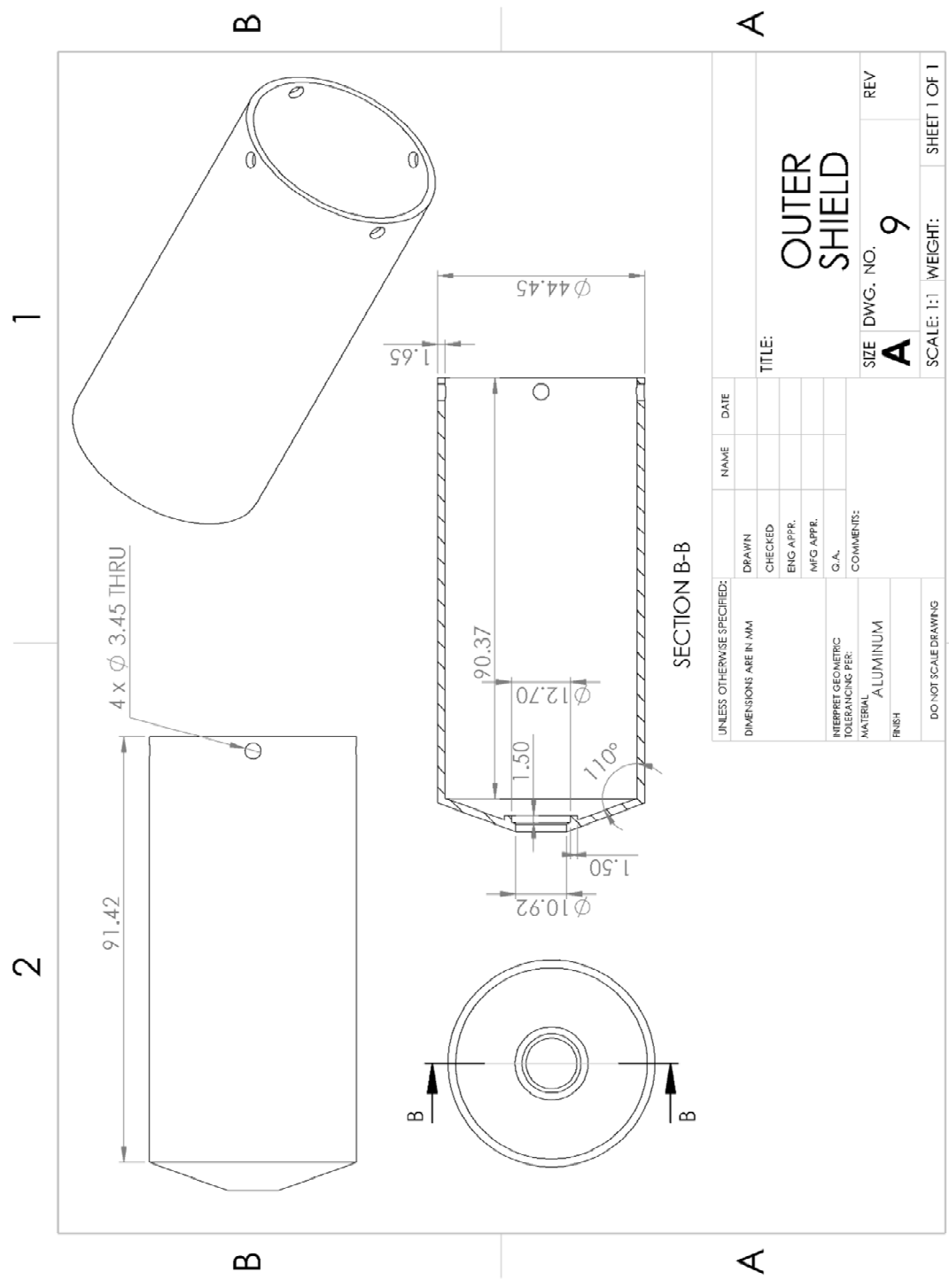
4 x ∅ 3.45 THRU
91.42
SECTION B-B
∅44.45
1.65
90.37
∅12.70
1.50
110°
1.50
∅10.92
B
B
UNLESS OTHERWISE SPECIFIED:
DIMENSIONS ARE IN MM
INTERPRET GEOMETRIC TOLERANCING PER:
MATERIAL
ALUMINUM
FINISH
DO NOT SCALE DRAWING
NAME
DATE
DRAWN
CHECKED
ENG APPR.
MFG APPR.
Q.A.
COMMENTS:
TITLE:
OUTER SHIELD
SIZE
A
DWG. NO.
9
REV
SCALE: 1:1
WEIGHT:
SHEET 1 OF 1

Appendix E

Finite Element Simulations of Retarding Potential Setup

This appendix details the simulations necessary to design the retarding potential setup used to measure the kinetic energy spectra for the secondary electron beaming results presented in Chapter 4. During the initial experiments, it was quickly determined that introducing any voltage into the vacuum chamber, such as the retarding potential grid, could alter the trajectories of the 300 eV primary electrons coming from the electron gun. As such, the following finite element simulations were performed with COMSOL Multiphysics [132] to determine the best possible experimental configuration.

Figure E.1 depicts a schematic of the simulation setup. Here, 300 eV electrons traverse from right to left, just above the surface of the prism. Faraday cup FC1 is located normal to the prism surface for these simulations. For all of the simulations, the prism face and face of the electron gun is grounded, and FC1 is left floating. Figure E.2(a) depicts a surface map of the electrical potential within the simulation region. Clearly, due to the absence of any additional voltage grids, the electrical potential is zero everywhere. As such, the 300 eV electrons are not affected and travel from right to left, as depicted in Fig. E.2(b).

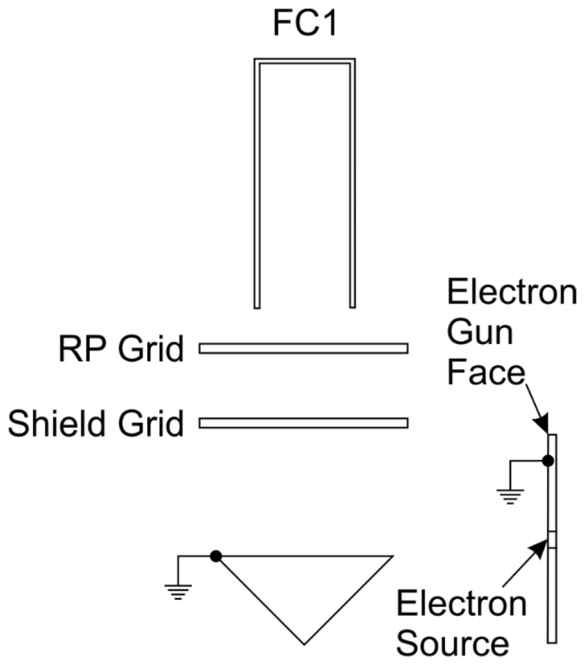

Figure E.1. Finite element simulation setup.

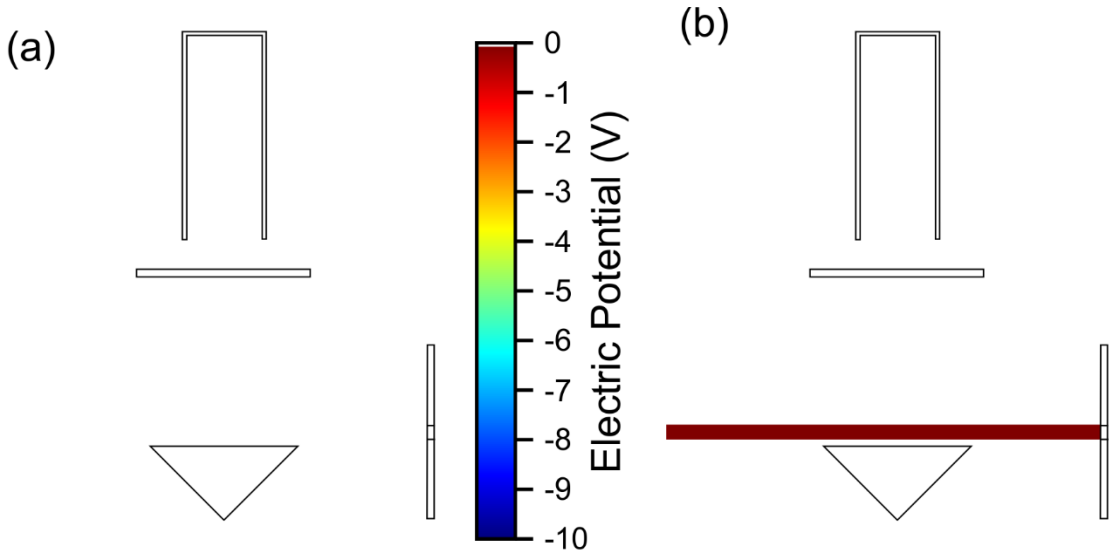

Figure E.2. (a) Electric potential with no grids. (b) 300 eV electron trajectories in the absence of any retarding potential.

Introducing a retarding potential grid alters the electrical potential, even with a retarding potential voltage, V_{RP} of only -10 V (Fig. E.3(a)). Now, with a voltage gradient

between the retarding potential grid and the grounded prism, electrons are pushed towards the prism as depicted in Fig. E.3(b).

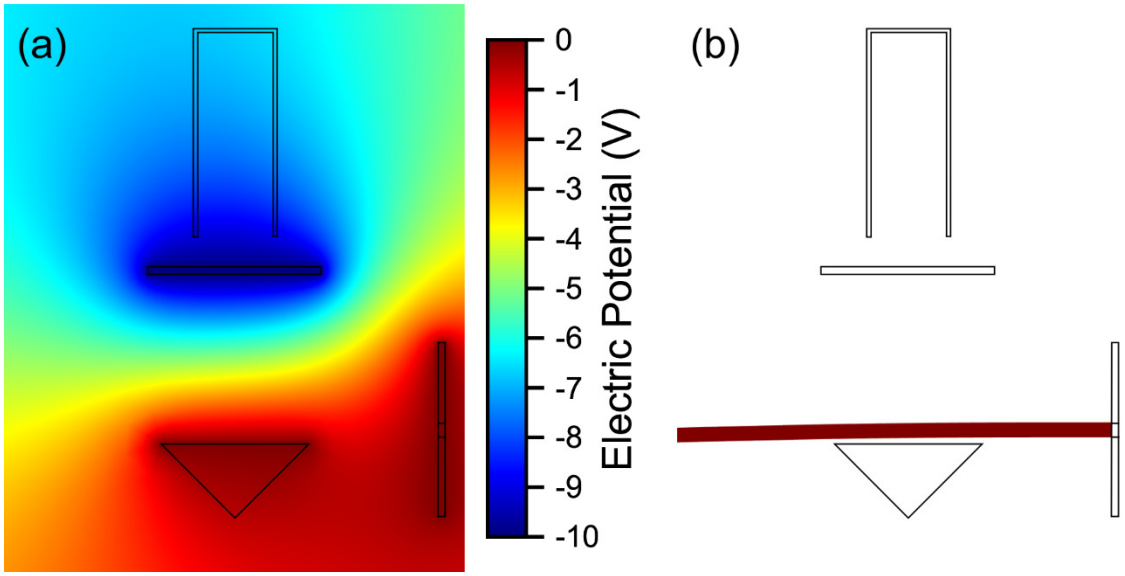

Figure E.3. (a) Electric potential with retarding potential grid at V_{RP} = -10V. (b) Deflected 300 eV electron trajectories due to V_{RP}.

In order to compensate for the retarding potential voltage, it is necessary to place a grounded grid in front of it. This effectively shields the 300 eV electrons from V_{RP} and creates a field free region in front of the prism depicted in Fig. E.4(a). This allows the 300 eV electrons to travel their normal path unaffected as illustrated in Fig. E.4(b). Shielding the V_{RP} = -295 V that is used in Chapter 4 to monitor for deflection of 300 eV electrons requires a slightly larger grounded grid, as depicted in Fig. E.5.

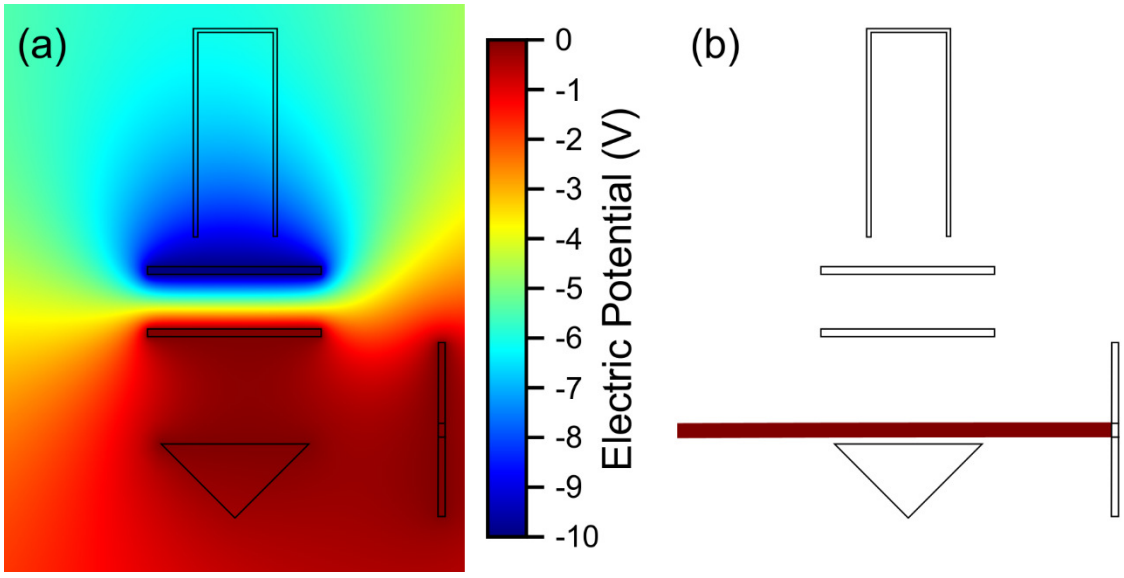

Figure E.4. (a) Electric potential with retarding potential grid at V_{RP} = -10V and grounded shield grid. (b) Unaffected 300 eV electron trajectories due shielding of V_{RP}.

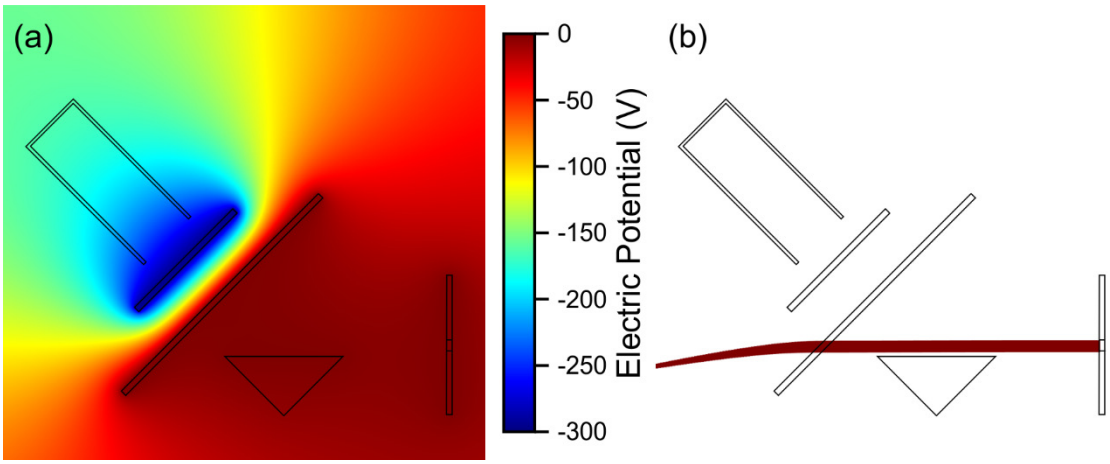

Figure E.5. (a) Electric potential with retarding potential grid at V_{RP} = -295 V and grounded shield grid. (b) Unaffected 300 eV electron trajectories in the experimental region in front of the prism. Note that a larger grounded shield grid is required to fully shield V_{RP}.

Appendix F

Terahertz Electric Fields in Particle Ensembles

This appendix includes the calculations performed to estimate the electric field strength of the THz pulses used for the THz pump probe experiment in Chapter 6. Numerical simulations are also included to determine the THz surface electric field enhancement in the ensemble of Au particles.

F.1. Estimation of the Terahertz Pump Electric Field Strength

The THz pump pulse used in these experiments is generated from a 70 μm gap photoconductive stripline antenna patterned on a LT-GaAs substrate biased with 20 V (~2.86 kV/cm) and illuminated with a 60 mW, 10 fs, λ = 800 nm optical pulse.

The magnitude of the THz pump electric field can be estimated from the differential power of the optical probe beam at the input to the balanced photodetector, which can be obtained from the time domain signal detected by the lock-in amplifier. Knowing this, the THz pump electric field can be estimated via the following equation:

$$E_{THz} = 2\frac{\Delta P}{P_{probe}}\sqrt{\frac{3}{8}}\frac{c}{2\pi\nu n^3 r_{41} L} \tag{F.1}$$

Where:

ΔP = differential power at the photodetector (54 nW)

P_{probe} = power of the optical probe pulse (0.5 mW)

c = speed of light in vacuum

ν = frequency of optical probe pulse (375 THz)

n = refractive index of ZnSe electro-optic crystal (2.5295)

r_{41} = electro-optic coefficient of ZnSe (2 pm/V)

L = thickness of ZnSe crystal (500 μm)

With these parameters, and this equation, the THz pump electric field is estimated to be 10 V/cm.

Additionally, the THz electric field strength can also be estimated from the conversion efficiency of the photoconductive antenna. Here, the THz electric field strength at the focus is given by:

$$E_{THz} = \sqrt{\frac{2\eta_{THz} P_{optical}}{f_{rep}\tau_{THz}\varepsilon_0 c\pi x_f y_f}} \tag{F.2}$$

Where:

η_{THz} = optical to THz conversion efficiency (5×10^{-6})

$P_{optical}$ = average power of the optical pump pulse (60 mW)

f_{rep} = repetition rate of the laser (80 MHz)

τ_{THz} = pulse length of the THz pump pulse (1 ps)

ε_0 = permittivity of free space

c = speed of light in vacuum

x_f = full-width-at-half-maximum of the THz focal region in the x direction (510 μm)

y_f = full-width-at-half-maximum of the THz focal region in the y direction (740 μm)

To estimate η_{THz}, one can compare our geometry to that of a similar geometry with a known conversion efficiency [133]. The geometry employed in [133] is that of an 80 μm gap stripline antenna patterned on LT-GaAs and biased with 100 V, leading to a bias electric field strength of 12.5 kV/cm. A THz pulse of 0.09 μW is produced from this geometry when illuminated by a 15 mW optical pulse, signifying a conversion efficiency of 6×10^{-6}. As the THz power scales quadratically with both bias electric field strength and optical pump power [133], our bias electric field strength is 4.37× lower than [133], and our optical pump power is 4× higher than [133], we estimate our conversion efficiency to be 5×10^{-6}. Utilizing this conversion efficiency as well as the other parameters for our setup [122], the estimated THz electric field strength at the focus is found to be 15 V/cm.

Based on these two estimations (upper and lower limits), we arrive at a THz pump electric field strength of 12 V/cm.

F.2. Calculation of Local Electric Field Enhancement

The THz plasmon current dynamics, localized plasmonic field strength, and the radiated depolarization THz plasmonic field (i.e. $\vec{E}^a_{pl}(\vec{r},t)$ due to $\vec{E}^a(\vec{r},t)$ coupling), are strongly influenced by collective surface conductivity, the interparticle separation, *s*, and the THz plasmon field evanescent decay distance, ℓ. For $s/\ell > 1$, the interparticle

interaction is governed by far-field dipolar or multipolar absorption and reradiation, whereas, for closely packed metallic particles $s/\ell << 1$, high evanescent fields result in a strong near-field coupling [123]. It is evident that any changes in σ due to electric-field induced charges will map itself on the radiated THz electric field.

Using FDTD calculations, it was determined that in an ensemble of sub-λ size metallic particles the surface electric field enhancement increases from 3× for a single particle to 85× for the ensemble, as shown in Fig. F.1. Thus, the incident 12 V/cm THz electric field is enhanced to 1 kV/cm within the 10 nm gap between the particles.

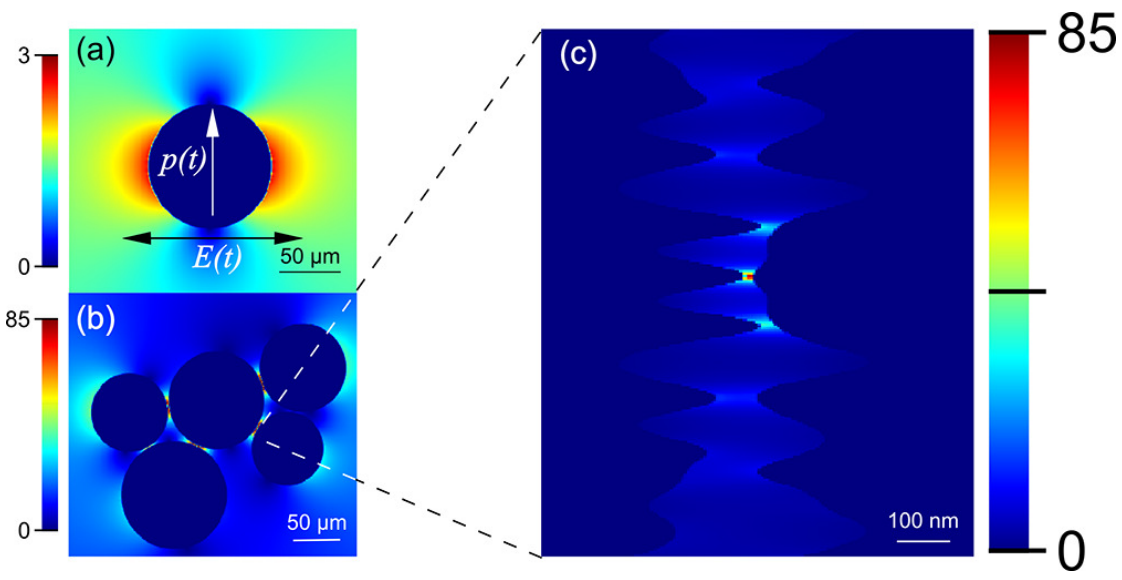

Figure F.1. (a) Surface electric field enhancement for a single particle excited with *E(t)*. The two-headed arrow represents the polarization direction of the incident THz electric field and *p(t)* represents the induced Hertzian dipole moment. (b) Surface electric field enhancement for an ensemble of particles showing inter-particle THz field enhancement of 85 times. (c) Enlarged image showing the electric field enhancement between two particles.